THE UNIVERSITY OF CHICAGO

PHOTOCHEMICALLY AND ELECTROCHEMICALLY DRIVEN HOMOGENEOUS CATALYSTS FOR HYDROGEN OXIDATION AND CARBON DIOXIDE REDUCTION

A DISSERTATION SUBMITTED TO

THE FACULTY OF THE DIVISION OF THE PHYSICAL SCIENCES

IN CANDIDACY FOR THE DEGREE OF

DOCTOR OF PHILOSOPHY

DEPARTMENT OF CHEMISTRY

BY

MARK WESTWOOD

CHICAGO, ILLINOIS

JUNE 2018

For our gaggle

TABLE OF CONTENTS

LIST OF FIGURES ix

LIST OF SCHEMES xvii

LIST OF TABLES xviii

ACKNOWLEDGEMENTS xx

ABSTRACT xxii

CHAPTER 1: Introduction 1

1.1. Background 1

1.2. Target Complexes for Photocatalytic H_2 Oxidation. 6

1.3. Target Complexes for Photocatalytic CO_2 Reduction. 7

1.4. Chapter Summary 10

1.5. References 12

CHAPTER 2: X-Ray Crystallographic, Multifrequency EPR, and DFT Characterization of the $Ni(P^{Cy}_2N^{tBu}_2)_2^{n+}$ Hydrogen Oxidation Catalyst in the Ni(I) Oxidation State 24

2.1. Introduction 24

2.2. Experimental Section 27

2.2.1. General Procedures for Synthesis and Characterization 27

2.2.2. Preparation of **1**[BF_4] 27

2.2.3. Multi-Frequency EPR Studies 28

2.2.4. Density Functional Theory (DFT) Calculations. 30

2.3. Results and Discussion 31

2.3.1. Molecular Structure of **1**$^{+}$ 31

2.3.2. Multi-Frequency EPR Study of **1**[BF_4] in Frozen Solution. 33

2.3.3. Density Functional Theory (DFT) Calculations on [Ni($P^{R}_2N^{R'}_2$)$_2$]$^{+}$ Complexes. ... 39

2.4. Conclusions 45

2.5. Acknowledgements 46

2.6. References 46

CHAPTER 3: Driving Catalytic Hydrogen Oxidation with Light 52

3.1. Introduction 52

3.2. Experimental 55

3.3. Results and Discussion 58

3.3.1. Mechanistic Considerations of Photocatalytic H_2 Oxidation. 58

3.3.2. Light-driven Activation and Cleavage of H_2. 61

3.3.3. Light-Driven Oxidation and Deprotonation of **1H**$^{+}$. 66

3.3.4. Photoelectrocatalytic 70

3.4. Conclusions 74

3.5. References 74

CHAPTER 4: Electrochemical Development of a System Competent for the Light-Driven 80

Reverse Water-Gas-Shift Reaction 80

4.1. Introduction 80

4.2. Experimental 82

4.3. Results and Discussion 82

4.3.1. Design Criteria. 82

4.3.2. Electrochemical Studies of the Acid/Base Pair for Inter-Catalyst Proton Transfer. 90

4.3.3. Studies of the Photochemical RWGS Reaction 100

4.4. Conclusions 103

4.5. References 103

CHAPTER 5: Ligand Effects on Electrocatalytic CO_2 Reduction by Ruthenium–Bipyridyl Complexes. Characterization of a Photostable, non-CO-Bearing Catalyst 109

5.1. Introduction 109

5.2. Experimental Section 112

5.3. Results and Discussion 114

5.3.1. Photochemistry of **1** with Visible Light 114

5.3.2. Electrochemistry of **1**, **2*t***, **3**, and $\mathbf{4}^{+}$. 116

5.3.3. Electrocatalytic CO_2 and proton reduction by **1**, **2*t***, **3**, and $\mathbf{4}^{+}$ 118

5.4. Conclusions 123

5.5. References 123

CHAPTER 6: A Photostable, Selective Ruthenium–Bipyridyl Electrocatalyst for CO_2 Reduction 131

6.1. Introduction 131

6.2. Experimental Section 134

6.3. Results and Discussion 136

6.3.1. Photochemistry of **1** and Synthesis and Characterization of $\mathbf{2}^+$. 136

6.3.2. Photochemistry of $\mathbf{2}^+$. 140

6.3.3. Electrochemistry of $\mathbf{2}^+$. 141

6.3.4. Electrocatalytic Reduction of CO_2 by $\mathbf{2}^+$. 143

6.4. Conclusions 148

6.5. References 149

CHAPTER 7: Supplementary Information 155

7.1. Chapter 2 Supplementary Information 155

7.1.1. Definitions 155

7.1.2. Single-Crystal X-ray Diffraction Study of $\mathbf{1}[BF_4]$. 155

7.1.3. Electron Paramagnetic Spectroscopy 159

7.1.4. Density Function Theory Calculations 163

7.2. Chapter 3 Supplementary Information 169

7.2.1. Definitions 169

7.2.2. Synthesis and Characterization of Compounds 169

7.2.3. Photochemical and Photophysical Experiments 172

7.2.4. Electrochemical Experiments 179

7.3. Chapter 4 Supplementary Information..... 181

7.3.1. Definitions..... 181

7.3.2. General Procedures..... 181

7.3.3. Electrochemistry..... 182

7.3.4. Photochemistry..... 184

7.3.5. Gas Chromatography..... 184

7.3.6. Synthesis and Characterization 185

7.4. Supplementary Information for Chapter 5 191

7.4.1. Definitions..... 191

7.4.2. Synthesis, Characterization, and Photochemistry of Compounds..... 191

7.4.3. Single Crystal X-Ray Diffraction Study of **4Cl**•$2H_2O$..... 195

7.4.4. Electrochemical Experiments..... 201

7.5. Chapter 6 Supplementary Information..... 208

7.5.1. Definitions..... 208

7.5.2. Synthesis and Characterization of Compounds..... 208

7.5.3. Single Crystal X-Ray Diffraction Study of **2[PF_6]**•$CHCl_3$..... 211

7.5.4. Electrochemical Experiments 216

7.6. References 220

LIST OF FIGURES

Figure 1.1. Schematic representation of the light-driven reverse water-gas shift reaction. 3

Figure 1.2. Depictions of the catalysts discussed in this chapter. 7

Figure 1.3. The reported photochemical reactivity of **Ru-1** in CH_3CN (λ_{ex} = 366 nm). 10

Figure 2.1. $[Ni(P^R_2N^{R'}_2)_2]^+$ complexes discussed in this Chapter. 25

Figure 2.2. Thermal-ellipsoid representation of the $\mathbf{1}^+$ ion of **1**$[BF_4]$ 32

Figure 2.3. Electron paramagnetic resonance spectra (X-, Q-, and D-band) of a 2 mM solution of **1**$[BF_4]$ in butyronitrile at 10 K. 34

Figure 2.4. Field swept Echo-detected EPR and Davies ENDOR spectra of **1**$[BF_4]$ in butyronitrile at 15 K. 38

Figure 2.5. X-band HYSCORE spectra of **1**$[BF_4]$ in butyronitrile at 20 K recorded at magnetic field position 336.5 mT. 39

Figure 2.6. Calculated electron spin densities for complexes $\mathbf{1}^+$ and $\mathbf{4b}^+$ at the 0.002 e/a_0^3 isosurface level. 45

Figure 3.1. The primary $Ni(P^R_2N^{R'}_2)_2^+$ compound discussed in this chapter and the chromophore $Ru(bpy)_3^{2+}$ used for demonstrating photocatalytic H_2 oxidation. 54

Figure 3.2. Stern-Volmer analysis of the luminescence quenching of $\mathbf{2}^{2+}$ by $\mathbf{1}^+$ in CH_3CN. 62

Figure 3.3. Electronic-absorption spectra of a PhCN solution containing $\mathbf{1}^+$, $\mathbf{2}^{2+}$, and PCy_3O in PhCN solution under H_2 before and during photolysis (λ_{ex} = 455 nm). 63

Figure 3.4. $^{31}P\{^1H\}$ NMR spectra of a PhCN solution containing $\mathbf{1}^+$, $\mathbf{2}^{2+}$, and PCy_3O during photolysis (λ_{ex} = 455 nm). 64

Figure 3.5. $^{31}P\{^{1}H\}$ NMR spectra showing the deprotonation of **1-H$_2$**$^{2+}$ by **1**. 65

Figure 3.6. Stern-Volmer analysis of the luminescence quenching of **2**$^{2+}$ by **1H**$^{+}$ in CH_3CN. 68

Figure 3.7. $^{31}P\{^{1}H\}$ NMR spectra of a CD_3CN solution containing **1H**$^{+}$, **2**$^{2+}$ and pyrrolidine during photolysis (λ_{ex} = 455 nm). 69

Figure 3.8. Schematic of the H-cell used for controlled-potential electrolysis experiments. 72

Figure 3.9. Traces of current *vs.* time for CPE (E = –1.0 V) of a benzonitrile solution containing [^{n}Bu$_4$N][PF_6], **1**$^{+}$, **2**$^{2+}$, and pyrrolidine under a H_2 atmosphere. 73

Figure 4.1. The catalysts discussed in this chapter. 81

Figure 4.2. Electronic-absorption spectra of (A) **2** in CH_3CN during photolysis (λ_{ex} = 565 nm), (B) **2** in CH_3CN during photolysis (λ_{ex} = 590 nm), and (C) ZnTPP in PhCN and CH_3CN. 89

Figure 4.3. $^{31}P\{^{1}H\}$ NMR spectra in CD_3CN of **1**$^{2+}$ in CD_3CN, after addition of NaOPh (40 mM), and after subsequent addition of H_2. 93

Figure 4.4. CV of **2** in 0.1 M [NBu$^{n}_4$][PF_6] CH_3CN with PhOH under N_2, CO_2 and with titration of pyrrolidine under CO_2. 94

Figure 4.5. The sterically-hindered pyrrolidines examined in this chapter. 95

Figure 4.6. CV of **2** with PhOH in 0.1 M [NBu$^{n}_4$][PF_6] CH_3CN under N_2 (black) and CO_2 (blue) with titration of *N*-(*o*-tolyl)pyrrolidine (**3**). 96

Figure 4.7. $^{31}P\{^{1}H\}$ NMR spectra in CD_3CN of 1 mM **1**$^{2+}$ in CD_3CN, after addition of H_2, and after subsequent addition of 70 mM **3**. 97

Figure 4.8. Cyclic voltammograms of **2** with PhOH in 0.1 M [NBu$^{n}_4$][PF_6] CH_3CN under N_2 (black) and CO_2 (blue) with titration of **4**. 98

Figure 4.9. $^{31}P\{^{1}H\}$ NMR spectra in CD_3CN of $\mathbf{1}^{2+}$ in CD_3CN, after addition of H_2, and after subsequent addition of **4**. 99

Figure 4.10. Cyclic voltammograms of $\mathbf{1}^{+}$ in CH_3CN under H_2 with titration of **4**. 100

Figure 4.11. Electronic-absorption and $^{31}P\{^{1}H\}$ NMR spectra of a solution containing $\mathbf{1}^{+}$), PhOH, **4**, and ZnTPP in CH_3CN under H_2/CO_2 (28:72) during photolysis (λ_{ex} = 590 nm). 101

Figure 5.1. The reported photochemical reactivity of **1** under 366 nm irradiation in CH_3CN, and depictions of related compounds (mes = 2,4,6-trimethylphenyl)..... 111

Figure 5.2. Electronic-absorption spectra during the photolysis of **1** in CH_3CN..... 116

Figure 5.3. Cyclic voltammograms of ***2t*** in CH_3CN containing 0.1 M $[NBu^{n}_4][PF_6]$..... 118

Figure 5.4. Cyclic voltammograms of **1**, ***2t***, **3**, and $\mathbf{4}^{+}$ in CH_3CN containing 0.1 M $[NBu^{n}_4][PF_6]$ in the absence and presence of substrates. 120

Figure 6.1. Compounds discussed in this study. 132

Figure 6.2. Electronic-absorption spectra of **1** and its photolysis products in CH_3CN.. 138

Figure 6.3. Thermal-ellipsoid representation of the $\mathbf{2}^{+}$ core of **2**$[PF_6]$. 139

Figure 6.4. Electronic-absorption spectra of **2Cl** in 4% H_2O-CH_3CN (v/v) in the dark, and under ambient laboratory lighting. 140

Figure 6.5. Cyclic voltammograms of $\mathbf{2}^{+}$-containing compounds in CH_3CN solution. 142

Figure 6.6. Cyclic voltammograms of **2Cl** in CH_3CN containing 0.1 M $[NBu^{n}_4][PF_6]$ with different combinations of substrates. 145

Figure 7.1.1. The compounds discussed in Section 7.1..... 155

Figure 7.1.2. Thermal-ellipsoid representation of one crystallographically unique $P^{Cy}{}_2N^{tBu}{}_2$ ligand about the Ni center of **1**[BF_4], showing the full numbering scheme. 157

Figure 7.1.3. Comparison of CW X-band EPR spectra of **1**[BF_4] in butyronitrile at 5 K (black), 40 K (red), and 100 K (green). 159

Figure 7.1.4. Comparison of CW and pulsed X-band EPR spectra of **1**[BF_4] in butyronitrile at 5–15 K. 159

Figure 7.1.5. X-band inversion recovery time trace of **1**[BF_4] in butyronitrile at 336.5 mT. X-band 2-Pulse ESEEM time trace of **1**[BF_4] in butyronitrile at 336.5 mT at 15 K. 160

Figure 7.1.6. Comparison of EPR spectra of **1**[BF_4] in butyronitrile (black) and 1:2 CH_3CN:CH_2Cl_2 (green) at 5–15 K. 160

Figure 7.1.7. Field-swept echo-detected X-band EPR spectrum of **1**[BF_4] in butyronitrile at 15 K. Arrows indicate the magnetic field positions where the ENDOR spectra were recorded. ^{31}P X-band Mims ENDOR spectra (inverted) of **1**[BF_4] in butyronitrile at 15 K. 161

Figure 7.1.8. Field-swept echo-detected X-band EPR spectrum of **1**[BF_4]. ^{31}P X-band Mims ENDOR spectrum, ^{31}P X-band Davies ENDOR spectrum, and ELDOR-detected NMR spectrum of **1**[BF_4]. 161

Figure 7.1.9. Pulsed X-band EPR and Davies ENDOR spectra of **1**[BF_4] in fully protonated and fully deuterated 1:2 CH_3CN:CH_2Cl_2 mixtures at 15 K. 162

Figure 7.1.10. (*Left*) HYSCORE spectrum of **1**[BF_4] recorded at magnetic field position 336.5 mT (butyronitrile, 20 K). (*Middle*) Simulation of HYSCORE spectrum with one ^{14}N nucleus. (*Right*) Simulation of HYSCORE spectrum with two ^{13}C nuclei. 163

Figure 7.1.11. Numbering system for phosphorus nuclei of $\mathbf{1}^+$. 164

Figure 7.1.13. Calculated structures of complexes $\mathbf{1}^+$ and $\mathbf{4b}^+$. 167

Figure 7.1.14. Calculated electron spin densities for $\mathbf{1}^+$ and a representative $\mathbf{4}^+$ structure ($\mathbf{4b}^+$) at the 0.001 e/a_0^3 isosurface level. 168

Figure 7.1.15. Calculated electron spin densities for $\mathbf{1}^+$ and a representative $\mathbf{4}^+$ structure ($\mathbf{4b}^+$) at the 0.0001 e/a_0^3 isosurface level. 168

Figure 7.2.1. The compounds discussed in Section 7.2. For clarity, the phosphine (cyclohexyl) and amine (*tert*-butyl) substituents of the nickel compounds are not shown. 169

Figure 7.2.2. ^{1}H NMR spectrum of **1H**[BF_4] (CD_3CN, 400 MHz). The Ni–H resonance is shown in the inset. 170

Figure 7.2.3. Expansion of Figure 7.2.2. 171

Figure 7.2.4. $^{31}P\{^1H\}$ NMR spectrum of **1H**[BF_4] in CD_3CN solution. 171

Figure 7.2.5. Electronic-absorption spectrum of $\mathbf{1}^+$ in CH_3CN solution. 172

Figure 7.2.6. Electronic-absorption spectra of a CH_3CN solution of $\mathbf{1}^+$ (0.9 mM) during photolysis (λ_{ex} = 455 nm). 176

Figure 7.2.7. Electronic-absorption spectra of a CH_3CN solution of $\mathbf{1}^{2+}$ (1.0 mM) during photolysis (λ_{ex} = 455 nm). 176

Figure 7.2.8. Electronic-absorption spectra of $\mathbf{1H}^+$ (1.0 mM) in CH_3CN during photolysis (λ_{ex} = 455 nm). The rising band at $\lambda \geq 700$ nm is consistent with the production of $\mathbf{1}^+$. 177

Figure 7.2.9. Electronic absorption spectra during photolysis (λ_{ex} = 455 nm) of a PhCN solution containing $\mathbf{1}^+$ (1.9 mM), $\mathbf{2}^{2+}$ (70 μM), and PCy_3O (4.7 mM), under N_2. 178

Figure 7.2.10. A white precipitate that is seen upon photolysis (λ_{ex} = 455 nm) under H_2 of a CD_3CN solution containing $\mathbf{1}^+$ (2.0 mM) and $\mathbf{2}^{2+}$ (70 μM). 178

Figure 7.2.11. A white precipitate that is seen upon photolysis (λ_{ex} = 455 nm) of a CD_3CN solution containing $\mathbf{1H}^+$, $\mathbf{2}^{2+}$ and pyrrolidine. 178

Figure 7.2.12. Photographs of the H-Cell setup used for controlled potential electrolysis experiments. (*Left*) Under ambient conditions. (*Right*) Under LED irradiation. 179

Figure 7.2.13. CPE at –1.0 V of a PhCN solution containing 0.1 M [^{n}Bu$_4$N][PF_6]. 180

Figure 7.2.14. CPE at −1.0 V of a PhCN solution under N_2 containing $\mathbf{1}^+$, $\mathbf{2}^{2+}$, pyrrolidine and [^{n}Bu$_4$N][PF_6]..... 181

Figure 7.3.1. The compounds discussed in Section 7.3. For clarity, the phosphine (cyclohexyl) and amine (*tert*-butyl) substituents of the nickel compounds are not shown. 181

Figure 7.3.2. ^{1}H NMR spectrum of *N*-(*o*-tolyl)pyrrolidine (**3**) in $(CD_3)_2CO$..... 188

Figure 7.3.3. ^{1}H NMR spectrum of pyrrolidinium tetrafluoroborate in CD_3CN. 188

Figure 7.3.4. CV responses of 2 mM **2** in 0.1 M [NBu$^n_4$][PF_6] CH_3CN at 0.1 V/s with titration of TFE. 189

Figure 7.3.5. CV responses of 0.6 mM $\mathbf{1}^+$ with 0.5 M PhOH in 0.1 M [NBu$^n_4$][PF_6] CH_3CN at 0.1 V/s under H_2 with titration of **4**. 190

Figure 7.3.6. Example FID trace from a bulk photolysis headspace sample. 190

Figure 7.4.1. The compounds discussed in Section 7.4. 191

Figure 7.4.2. ^{1}H NMR spectrum of ***2t*** in CD_3CN..... 192

Figure 7.4.3. Expansion of the ^{1}H NMR spectrum ***2t*** in CD_3CN..... 193

Figure 7.4.4. Electronic-absorption spectrum of ***2t*** in CH_3CN. 193

Figure 7.4.5. ^1H NMR spectrum of **4Cl** in CD_3CN. 194

Figure 7.4.6. Expansion of the ^1H NMR spectrum of **4Cl** in CD_3CN. 194

Figure 7.4.7. Electronic-absorption spectrum of **4Cl** in CH_3CN. 195

Figure 7.4.8. Thermal-ellipsoid representation (40% probability ellipsoids) of **4Cl**•$2H_2O$. 198

Figure 7.4.9. Cyclic voltammograms of **1** in CH_3CN solution. 202

Figure 7.4.10. Cyclic voltammograms of **3** in CH_3CN solution. 203

Figure 7.4.11. Cyclic voltammograms of **4Cl** in CH_3CN solution. 203

Figure 7.4.12. Cyclic voltammograms of ***2t*** in CH_3CN solution. 204

Figure 7.4.13. Cyclic-voltammetric measurements showing proton reduction from phenol in CH_3CN in the absence (black traces) and presence (red traces) of **1**, ***2t***, **3**, and $\mathbf{4}^+$ 205

Figure 7.4.14. Cyclic voltammograms of **1** in CH_3CN as a function of PhOH concentration. .. 206

Figure 7.4.15. Cyclic voltammograms of ***2t*** in CH_3CN as a function of PhOH concentration .. 206

Figure 7.4.16. Cyclic voltammograms of **4Cl** in CH_3CN as a function of PhOH concentration. 207

Figure 7.4.17. Cyclic voltammograms of **1** in CH_3CN solution, rinse test. 207

Figure 7.5.1. The compounds discussed in Section 7.5. 208

Figure 7.5.2. ^1H NMR spectrum of **2Cl** in CD_2Cl_2. 209

Figure 7.5.3. Expansion of the ^1H NMR spectrum of **2Cl** in CD_2Cl_2. 209

Figure 7.5.4. $^{13}C\{^1H\}$ NMR spectrum of **2Cl** in CD_2Cl_2. 210

Figure 7.5.5. ESI mass spectrum of **2Cl**. 210

Figure 7.5.6. Electronic-absorption spectrum of **2Cl** in CH_3CN. 211

Figure 7.5.7. Thermal ellipsoid representation (40% probability ellipsoids) of **2[PF_6]**•$CHCl_3$. 216

Figure 7.5.8. Cyclic voltammograms of **2[PF_6]** in CH_3CN. 218

Figure 7.5.9. Cyclic voltammograms of **2Cl** in CH_3CN..... 218

Figure 7.5.10. Differential pulse voltammogram of **2Cl** in CH_3CN. 219

Figure 7.5.11. Cyclic voltammograms of **1** in CH_3CN..... 219

Figure 7.5.12. Cyclic voltammograms of **2Cl** in CH_3CN containing varying concentrations of PhOH. 220

LIST OF SCHEMES

Scheme 3.1. Proposed pathway for the electrocatalytic oxidation of dihydrogen by a $Ni(P^R_2N^{R'}_2)_2^{n+}$ catalyst. 59

Scheme 3.2. The proposed mechanism by which $\mathbf{1}^+$ is converted into $\mathbf{1H}^+$ photochemically..... 66

Scheme 3.3. The proposed mechanism for light-driven conversion of $\mathbf{1H}^+$ to **1**. 70

Scheme 4.1. Schematic representation of the light-driven reverse water-gas-shift reaction. 84

Scheme 4.2. The mechanism of H_2 oxidation by $\mathbf{1}^+$. 85

Scheme 4.3. The mechanism of electrocatalytic CO_2 reduction by **2**. 86

Scheme 4.4. Proof-of-concept stoichiometric system that prepares $ZnTPP^-$ from H_2-sourced reducing equivalents to drive photocatalytic CO_2 reduction. 93

LIST OF TABLES

Table 2.1. Electron Paramagnetic Resonance Parameters of $[Ni(P^R_2N^{R'}_2)_2]^+$ Complexes. 35

Table 2.2. Calculated Bond Distances (Å) and Angles (°) for 1^+, 2^+, 3^+, and 4^+. 41

Table 2.3. Calculated and Experimental EPR Parameters for $[Ni(P^R_2N^{R'}_2)_2]^+$ Complexes 43

Table 4.1. Photophysical Data for the Chromophores Discussed in this Chapter..... 88

Table 4.2. CPE Experiments of CO_2 Reduction by 2 and Different Acids. 91

Table 4.3. Efficiency and Product Selectivity of Electrocatalytic CO_2 Reduction by **2** Using Various Bases. 96

Table 4.4. Conditions and Results from Photochemical RWGS Experiments with ZnTPP, $\mathbf{1}^+$, **2**, and **4**, under CO_2/H_2. 102

Table 5.1. Redox Potentials (V *vs*. $FeCp_2^{0/+}$) of **1**, **2*t***, **3**, and $\mathbf{4}^+$ from Cyclic Voltammetry. 117

Table 5.2. Faradaic Efficiency and Product Selectivity of Ruthenium Electrocatalysts. 121

Table 6.1. Redox Potentials (V *vs*. $FeCp_2^{0/+}$) of **1** and $\mathbf{2}^+$. 141

Table 6.2. Electrocatalytic Faradaic Efficiency for CO_2 and Proton Reduction by **1** and $\mathbf{2}^+$. 147

Table 7.1.1. Crystallographic Data for $[Ni(P^{Cy}_2N^{tBu}_2)_2][BF_4]$ (**1**[BF_4]). 156

Table 7.1.2. Selected Bond Lengths (Å) and Angles (°) for **1**[BF_4] as Determined by X-ray Crystallography. 158

Table 7.1.3. Effect of Functional and Basis Set on Calculated EPR Parameters for $\mathbf{1}^+$. 163

Table 7.1.4. Effect of Functional and Basis Set used for Geometry Optimization on the Calculated EPR Parameters for $\mathbf{1}^+$. 164

Table 7.1.5. Calculated (BP86|3-21G) Ni–P Bond Lengths of $Ni(P^{R}_{2}N^{R'}_{2})_{2}^{+}$ Complexes. 164

Table 7.1.6. Calculated (BP86|3-21G) NiP_4 Bond Angles of $Ni(P^{R}_{2}N^{R'}_{2})_{2}^{+}$ Complexes. 165

Table 7.1.7. Calculated (BP86|3-21G) Bond Angles about the Pendant Amines of $Ni(P^{R}_{2}N^{R'}_{2})_{2}^{+}$ Complexes. 166

Table 7.2.1. The Emission Lifetime of $\mathbf{2}^{2+}$ in CH_3CN with Various Concentrations of Pyrrolidine. 177

Table 7.2.2. Experimental Conditions Used for CPE Experiments. 179

Table 7.2.3. The Schedule of Illumination for CPE Experiment 5. 180

Table 7.4.1. ^{1}H-NMR Chemical Shift Data for **2*c***, **2*t***, and **4Cl**. 195

Table 7.4.2. Crystal Data and Structure Refinement for **4Cl**•$2H_2O$..... 197

Table 7.4.3. Bond Lengths and Angles for **4Cl**•$2H_2O$. 199

Table 7.4.4. Selected Bond Lengths (Å) and Angles (°) for **4Cl** from Two Nonisomorphous Crystal Structures. 200

Table 7.4.5. Comparison of Redox Potentials from This Work with Literature Values. 204

Table 7.5.1. Crystal Data and Structure Refinement for **2[PF$_6$]**•$CHCl_3$. 213

Table 7.5.2. Bond Lengths and Angles for **2[PF$_6$]**•$CHCl_3$. 214

ACKNOWLEDGEMENTS

My successful navigation of graduate school would not have been possible without the support of a great number of people. I would like to thank Prof. Mike Hopkins for being a wonderful advisor. I truly appreciate his support and patience—the latter was fully utilized during my first few weeks in the lab as I failed (many, many times) to prepare $[Re(bpy)(CO)_3(CH_3CN)][PF_6]$. During my time working with him I have greatly improved both as a scientist (see above) and a teacher, and I am very grateful for all he has taught me. I'd like to thank Prof's Simon Clarke and Peter Battle not only for their mentorship throughout my undergraduate degree, but for their encouragement and support as I applied for graduate school. I would never have made it to Chicago without them. I also wouldn't have done this without Dr. Phil, my A-level teacher. His passion and enthusiasm are the principal reasons I further pursued the study of chemistry. I would like to thank my dissertation committee, Professors Rich Jordan and John Anderson, who were great sources of support throughout my time in the department.

The Hopkins group was a great place to be, and I would like to thank everyone that I have been so incredibly lucky to work alongside. Davis Moravec, for taking the time to pretty much teach me how to do everything. Nathan La Porte, for all his great work on this project before me and for his insight and support when I (inevitably) struggled, and Dan O'Hanlon, for teaching me the finer points of electrochemistry. I would also like to thank Hunter Vibbert for being one of the few to take the inorganic classes with me in first year, for teaching 227 together, and for being a generally excellent chemist and labmate. Thank you, Chris Hansen, for getting lunch every day and for greatly enhancing my knowledge of beer. Also, thanks to Wayne Lau and Judith Kamm for being great to be around, and for always being up to get coffee. All of you made this such a

fun experience. I'm also grateful to have met all of the other wonderful people in this lab: Andrew Grorud, Ayush Gupta, Dylan Lynch, Mollye Levin, Noah Lewis, and Hannah Friedman.

I'd very much like to thank all of my friends and family that helped me get through it all. Alicia, for having me over for delicious bowls of chili, and Jamie for helping me sample all that the Printer's Row Wine Shop and Kasey's had to offer. Andrew for hanging out in New Grad during my (brief) time there. I would like to thank the Peeles for helping me feel at home so far from my own, and for all the things—both big and small—they have done for me. I especially would like to thank my family, for always being proud of me and for all their support through everything. Thank you for making me feel so loved. Lastly, I owe this to Sarabeth. Thank you for marrying me (twice), and for being my partner and better half. I am so proud to have shared this experience with you.

ABSTRACT

The development of renewable, carbon-neutral energy sources is compelled by the devastating environmental consequences that will result from the continued combustion of fossil fuels. Solar energy provides the capacity to easily meet our projected energy demand, but it must be converted to a form more easily stored and distributed. This can be achieved through artificial photosynthesis, which converts solar energy to chemical fuels. One attractive energy-storing artificial photosynthetic reaction is the light-driven reverse water-gas shift reaction (RWGS, $CO_2 + H_2 \rightarrow CO + H_2O$), which requires the successful marrying of photocatalytic hydrogen oxidation and carbon dioxide reduction. Prior work in our group elucidated a comprehensive kinetic and mechanistic picture of the photosensitization of a system capable for achieving the light-driven RWGS reaction, but greater understanding of catalytic H_2 oxidation and CO_2 reduction is required in order to develop a functionally competent system.

Firstly, a molecular nickel hydrogen oxidation catalyst is studied through a combination of electron paramagnetic resonance techniques, X-ray crystallography, and density functional theory calculations. Photocatalytic hydrogen oxidation with the same catalyst is then detailed, with an initial stepwise approach determining that every process necessary for accomplishing catalysis is achievable with photochemical sensitization. Catalytic turnover is demonstrated in a photoelectrocatalytic system, with an electrode acting as an electron acceptor.

Secondly, molecular catalysts for CO_2 reduction are studied with the aim of understanding how catalytic activity is influenced by the nature of the monodentate ligands. Whether efficient catalysis requires the routinely employed but photolabile CO ligand is explored. The electrocatalytic reduction of CO_2 by Ru–bipyridyl compounds is investigated and their visible-light photochemistry is also discussed.

Finally, the development of a functional system for the light-driven RWGS reaction is discussed. The key design criteria for a system are elucidated and the use of promising nickel and ruthenium catalysts is probed. Electrochemical techniques are utilized to efficiently screen reaction conditions. Although key steps of the reaction are demonstrated, the photochemical experiments intended to demonstrate the light-driven RWGS reaction yielded no more than trace production of CO. Additional research is required to develop a fully functional system for the light-driven RWGS reaction.

CHAPTER 1: Introduction

1.1. Background

From the advent of the industrial revolution, the anthropogenic combustion of fossil fuels such as coal and oil has led to a dramatic increase in the atmospheric concentration of carbon dioxide,[1-2] with potentially devastating environmental consequences.[3-7] Compounding this threat is the rapid growth in global energy consumption,[8] which is estimated[9] to increase by 42% from 2012 to 2040. This makes the development of renewable, carbon-neutral energy sources of vital importance.

Among renewable sources of energy that could replace fossil fuels, such as geothermal, tidal, solar, hydroelectric, wind, and biomass, only solar energy offers the capacity to meet the projected growth in energy consumption,[8] with the total insolation of the earth able to meet our current demand approximately 10,000 times over.[10] For solar energy to become our principal energy source, methods are required to convert it to a form more easily stored and distributed.[11-12] The form of energy that is most compatible with our current energy-distribution infrastructure is chemical fuels. This conversion can be achieved through artificial photosynthesis, which mimics the natural processes that convert solar energy into high-energy chemical bonds. [10, 13-18]

Two key objectives of modern artificial photosynthesis have been the development of systems capable of (1) the splitting of water into H_2 and O_2,[16, 19-28] and (2) the reduction of CO_2 to yield renewable carbonaceous fuels.[29-38] The production of H_2 is desirable as it can either generate heat through combustion or clean electrical power upon oxidation, without the concomitant production of greenhouse gases.[39-41] However, hydrogen is both less energy-dense and more difficult to store and transport than conventional fuels.[42] Contrastingly, the reduction of CO_2 can yield carbon-based fuels such as CO, CH_4, and CH_3OH that are both more readily-liquefied and

more compatible with our existing energy infrastructure. Although the subsequent power-generating combustion of carbon-fuels will lead to the production of CO_2, the conversion of CO_2 back into fuels will—provided an efficient artificial photosynthetic process—lead to a closing of the fuel cycle and the stabilization of atmospheric CO_2 concentrations.

As demonstrated by water-splitting, artificial photosynthesis consists of both oxidative and reductive components[23, 25-26, 35] but, for simplicity and practicality, work on molecular processes such as CO_2 reduction have focused primarily on the reductive half-reaction with reducing equivalents sourced (with very few exceptions[43]) from the oxidation of sacrificial electron donors.[10, 13-14, 31, 44] Such reagents are utilized because they undergo rapid decomposition subsequent to photoinitiated oxidation, which suppresses back-electron transfer and enables substrate transformation. Offsetting the practical advantages offered by sacrificial electron donors, however, is that their stoichiometric consumption negates their energy-storing potential and prevents systems that utilize them from being renewable and energy storing. Sacrificial donors must be replaced with a renewable source of reducing equivalents in order to perform energy-storing reactions.

One prospective source of renewable reducing equivalents for artificial photosynthetic processes is hydrogen, which can be oxidized to generate electrons and protons ($H_2 \rightarrow 2H^+ + 2e^-$).[39-41] Despite hydrogen being a non-renewable resource as it is currently produced through steam-reformation of natural gas,[45] as discussed above solar water splitting could yield renewable H_2 in the future.[13-14, 25] One major impediment for utilizing hydrogen oxidation has been the development of efficient and inexpensive catalysts for the process as the most active catalyst known is platinum,[46] which is limited in its application by its expense and rarity. This might be overcome through recent advances that have yielded highly active molecular catalysts

incorporating earth-abundant metals such as iron and nickel (vide infra).[47-48] However, despite its potential value as an oxidative half-reaction in artificial photosynthesis, photocatalytic hydrogen oxidation with a molecular catalyst has yet to be demonstrated.

A potential energy-storing artificial photosynthetic reaction is the reverse water-gas shift reaction (RWGS, $CO_2 + H_2 \rightarrow CO + H_2O$), which is an attractive target for solar fuel production.[43, 49-50] The process involves the successful marrying of two renewable half-reactions, photocatalytic hydrogen oxidation and carbon dioxide reduction, to yield a net energy-storing (41.2 kJ/mol) reaction.[51] The RWGS reaction is a desirable target because CO, the carbonaceous product, can be subsequently transformed into an array of industrially useful compounds through the Fischer-Tropsch process.[52] Fischer-Tropsch chemistry can convert CO into liquid hydrocarbon fuels identical to the oil-sourced fuels currently utilized, meaning that solar fuels can be utilized with no significant modification to our existing energy distribution infrastructure. The key steps required of a photodriven RWGS reaction are outlined in Figure 1.1. The reaction proceeds though the reductive quenching of an excited chromophore (Chr^*) by a H_2 oxidation catalyst (Cat_{H2}), activating the catalyst towards H_2 binding and oxidation. The thus-generated reduced chromophore (Chr^-) can then reduce a CO_2 reduction catalyst (Cat_{CO2}), activating that catalyst towards CO_2 binding and reduction and returning the chromophore to its ground state.

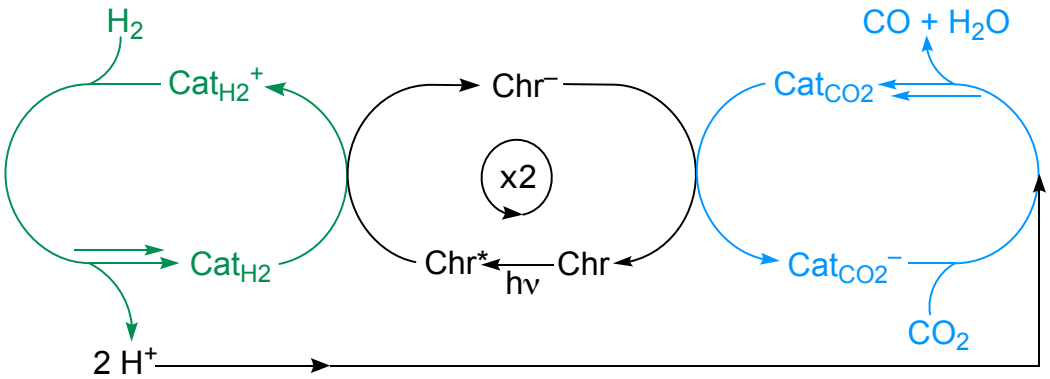

Figure 1.1. Schematic representation of the light-driven reverse water-gas shift reaction (Chr = chromophore, Cat_{H2} = H_2 oxidation catalyst, Cat_{CO2} = CO_2 reduction catalyst).

A key aspect that will determine whether such a system is functional is the lifetime of the doubly-sensitized state (where both catalysts are activated for substrate binding and transformation), which is determined through the relative kinetics of forward and back electron transfer. The required lifetime of the state is dependent upon the rate of substrate binding/activation for the specific catalysts used. The supramolecular assembly of a chromophore with electron acceptor and/or electron donor components has been heavily studied,[9, 30, 53-54] and offers precise tuning of electron transfer kinetics through linkage variation. However, the synthesis of such assemblies is often very complex and is a low-yield process. In addition, the synthesis of an entirely new supramolecular assembly is required in order to change even one component, making it difficult to screen different compositions, and the nature of an assembly places restrictions on the relative stoichiometries allowed of individual components. For these reasons, the artificial photosynthetic systems studied herein consist of freely-diffusing molecular species in homogeneous solution.

Prior work by our group[49-50] has demonstrated that, energetically, the energy-storing reverse-water-gas-shift reaction ($CO_2 + H_2 \rightarrow CO + H_2O$) can be driven photochemically by a single chromophore. In an initial study,[50] a proof-of-concept system established for the first time that in a freely diffusing solution, two catalysts can be sensitized by an electron transfer initiated by the absorption of a single photon by a chromophore. The chromophore zinc tetraphenylporphyrin (ZnTPP) was used, as were H_2 oxidation catalysts of the form $[Cp^RCr(CO)_3]^-$ (R = H, CH_3), and CO_2 reduction catalysts of the type Re(bpy-4,4′-R_2)$(CO)_3Cl$ (R = H, Me, *t*Bu, $COOCH_3$). Upon excitation of ZnTPP, rapid reductive quenching of the porphyrin S1 and T1 excited states by Cat_{H2} was observed, producing Cat_{H2}^+ and $ZnTPP^-$; the latter then thermally reduced Cat_{CO2} to Cat_{CO2}^-. This was the first example of photoredox-sensitized electron transfer

between two freely diffusing redox-active catalysts in solution. The catalytically competent state was observed to decay with a second-order half-life of approximately 15 μs, which is of a sufficient magnitude for substrate-trapping of sensitized catalyst intermediates. However, the specific catalysts of the proof-of-concept system were not active enough to successfully demonstrate the light-driven RWGS reaction.

Subsequent work by our group[49] expanded on this by employing catalysts that possess improved catalytic function. The H_2 oxidation catalyst $[Ni(P^{Cy}_2N^{tBu}_2)]^+$ and the CO_2 reduction catalyst $[Co(HMD)]^{2+}$ were used, again with ZnTPP as chromophore. Transient-absorption experiments confirmed the production of Cat_{CO2}^- and its subsequent trapping by CO_2. However, despite the use of improved catalysts, bulk photolysis experiments achieved the production of sub-stoichiometric amounts of CO.

This body of work suggests that greater understanding of specific H_2 oxidation and CO_2 reduction catalysts is required in order to develop a system functionally competent for the photocatalytic RWGS reaction. Firstly, to understand more fully the requirements of each component in the artificial photosynthetic system, it is necessary to independently probe and demonstrate photocatalytic hydrogen oxidation, which is yet to be achieved with a molecular catalyst. Only with insight into the specific requirements of the photocatalytic hydrogen oxidation half-reaction can a system be rationally developed to achieve the RWGS reaction. Secondly, though photocatalytic CO_2 reduction has been investigated in depth using several classes of efficient CO_2-reduction catalysts of the broad type $M(bpy^R)_a(CO)_bL_c^{n+}$ (M = Ru, Re, Mn; bpy^R = bipyridine and its derivatives),[55-57] the influence of L substitution within these classes has been little explored. Although not necessarily an impediment to electrocatalytic applications of these complexes, the photoinstability of metal–carbonyl complexes is of concern in light-driven systems.

Thus, the development of CO-free molecular catalysts is vital for artificial photosynthetic systems. With these pieces in place, integrated light-driven dual-catalyst systems for the energy-storing RWGS reaction can be rationally developed.

1.2. Target Complexes for Photocatalytic H_2 Oxidation.

Demonstrating photocatalytic hydrogen oxidation requires an active catalyst, and in recent years much has been accomplished in the rational development of earth-abundant metal electrocatalysts for the oxidation of H_2. Taking cues from the active site structure of the hydrogenase enzymes,[41, 58-62] naturally-occurring compounds that can oxidize H_2 with rates comparable to Pt but which only contain earth-abundant metals (principally Fe or Ni), researchers have found great success by incorporating biomimetic motifs into catalyst design.[63-67] Recent work by DuBois, Bullock, Shaw and co-workers[47-48, 66, 68-71] has led to the development of an efficient class of molecular catalysts for hydrogen oxidation and production that feature low-cost earth-abundant metals such as nickel and iron. Among the most promising of the catalysts developed are nickel diphosphine complexes of general form $Ni(P^R_2N^{R'}_2)_2^{n+}$, where $P^R_2N^{R'}_2$ (1,5-di(R)-3,7-di(R′)-1,5-diaza-3,7-diphosphacyclooctane) is an heterocyclic diphosphine ligand featuring two functionalized, non-coordinating pendant amines.[47, 66, 69, 72-77] These amines aid catalysis by assisting in the binding and cleaving of hydrogen and in the movement of protons to and from the nickel center. Usefully, the catalytic behavior of these compounds is tunable through varying the identity of the substituent groups (R and R′).[78-80] The nature of the amine R′ substituent primarily affects the basicity of the pendant amine and the nature of the phosphine R group affects the Ni–P bond distance and the redox properties of the Ni center, which impacts the hydricity of the compound.[81-82]

Whereas there have been many recent reports of photocatalytic H_2 production with $Ni(P^R_2N^{R'}_2)_2^{n+}$ catalysts, there has been no corresponding investigation of light-driven H_2 oxidation. The aggregated H_2 production findings detail sensitization by homogeneous organometallic chromophores,[83-84] organic dyes,[84-85] nanoparticles,[86-87] proteins,[88] and in a supramolecular system,[89] among others,[23, 90-92] demonstrating the versatility of $Ni(P^R_2N^{R'}_2)_2^{n+}$ compounds for photochemical applications. The specific compound studied in this thesis, $Ni(P^{Cy}_2N^{tBu}_2)_2^{+}$ (**Ni**$^+$; Figure 1.2), is utilized because it is among the fastest molecular H_2 oxidation electrocatalysts known and is particularly amenable to use as a photocatalyst because of its large thermodynamic driving force for H_2 binding ($\Delta G = -33$ kJ mol^{-1}).[66, 72] This means that it is highly favorable for the photogenerated active state to bind H_2 and that it is more likely to be irreversibly trapped before back-electron transfer.

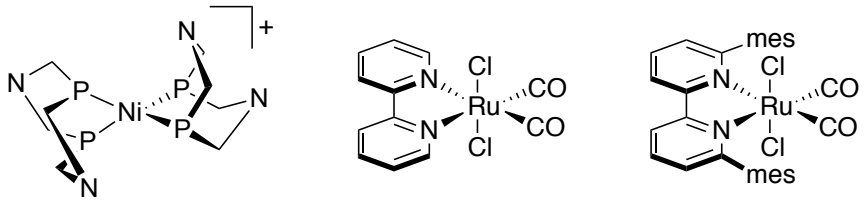

Ni$^+$ **Ru-1** **Ru-2**

Figure 1.2. Depictions of the catalysts discussed in this chapter. The R and R′ groups of Ni^+ are not shown for clarity (R = cyclohexyl, R′ = *tert*-butyl)

1.3. Target Complexes for Photocatalytic CO_2 Reduction.

A system competent for achieving the light-driven RWGS reaction requires a molecular photocatalyst for the reduction of CO_2 to CO. In contrast with hydrogen oxidation, catalytic CO_2 reduction has been extensively studied—particularly as a potential half-reaction for artificial photosynthetic systems..[1-2, 29, 32-38, 44, 48, 53, 55-57, 93-124] Photocatalytic studies of CO_2 reduction typically utilize, in addition to a molecular catalyst and a chromophore, a sacrificial electron donor (*e.g.* triethylamine, ascorbate, 1-benzyl-1,4-dihydronicotinamide) that provides reducing equivalents (vide supra).

Catalysts that accomplish the conversion of CO_2 to energy-rich compounds need to coordinate multiple proton-coupled electron-transfer reactions,[56] with the reduction of CO_2 to CO that is required for the RWGS reaction necessitating the controlled delivery of two electrons and two protons. One method of directing electron-transfer and proton-transfer events in molecular catalysts is through utilizing π-unsaturated redox-active ligands,[33, 38, 44, 55-56, 98, 107, 123-124] where reduction of the ligand facilitates rapid intramolecular electron transfer to the metal in sequence with protonation steps.[55] Common redox-active ligands include such examples as porphyrins[33, 93, 107, 125-126] and polypyridines, with metal-bipyridyl compounds in particular being extensively investigated as electro- and photocatalysts for CO_2 reduction; a recent review described the properties of over 80 different polypyridyl catalysts.[55] The most common architecture among these catalysts is of the form $M(bpy^R)(CO)_nX_{4-n}$, where bpy^R is 2,2′-bipyridine or a derivative in which R substituents are employed to modify its electronic or steric properties, and X typically is an anionic ligand. Intuitively, the preponderance of CO as a ligand within metal-polypyridyl catalysts is logical because of its ability to stabilize the low metal oxidation states that are produced during CO_2 reduction reactions. Indeed, many highly active catalysts bear multiple CO ligands, as illustrated by the extensively studied $Re(bpy^R)(CO)_3Cl$, $Mn(bpy^R)(CO)_3Cl$, and $Ru(bpy^R)(CO)_2Cl_2$ catalyst families.[38, 55-57] Efforts to improve the catalytic properties of these compounds have largely focused on understanding the effects of varying the bpy^R substituents.[38, 55-57, 97-99, 116, 123-124] In contrast, the question of whether neutral ligands other than CO will support comparable catalytic activity has been much less explored.[55-56] Of particular relevance to artificial photosynthesis, CO-free catalysts are of interest because metal–carbonyl compounds are often light sensitive, making photoinduced CO loss a potential catalyst degradation pathway.[127]

Discussed in this work are the CO-bearing catalysts *trans(Cl)*-Ru(bpy)$(CO)_2Cl_2$ (**Ru-1**, Figure 1.2)[128] and Ru(bpy^{mes})$(CO)_2Cl_2$ (**Ru-2**, Figure 1.2; bpy^{mes} = 6,6′-dimesityl-2,2′-bipyridine)[129], which are highly selective for the conversion of CO_2 to CO and are promising catalysts for accomplishing the RWGS reaction. **Ru-1**, in addition to being an active electrocatalyst for the reduction of CO_2 to CO and formate under a variety of reaction conditions,[128, 130-131] has been successfully employed in artificial-photosynthetic systems for CO_2 reduction, wherein the electrons are supplied from a photoredox chromophore and sacrificial reductant.[31, 132-133] The derivative **Ru-2** has been found to possess improved stability and electrocatalytic properties owing to its sterically hindering mesityl groups,[129] and has also been utilized in light-driven systems.[133]

However, despite its success in a photocatalytic system, **Ru-1** is photosensitive.[134-145] Photolysis of **Ru-1** with near-UV light in acetonitrile (a common solvent for catalytic CO_2 reduction reactions) is reported to sequentially produce the photosensitive compounds *cis(Cl)*-Ru(bpy)$(CO)(CH_3CN)Cl_2$ and *trans(*CH_3CN*)*-Ru(bpy)$(CH_3CN)_2Cl_2$, with prolonged irradiation yielding *mer*-$[Ru(bpy)(CH_3CN)_3Cl]^+$ (Figure 1.3).[143-144] If **Ru-1** is also sensitive to *visible light*, it would have potential implications for the suitability of its use in artificial-photosynthetic systems that employ common transition-metal photoredox chromophores,[31, 132-133] and raise the question of whether photoproducts of **Ru-1** formed by adventitious photolysis in room light are active in and contribute to electrocatalytic CO_2 reduction in studies of this compound. Additionally, this behavior raises the question of whether **Ru-2** is also photosensitive, which is similarly relevant both with regard to the potential contribution of photoproducts to measurements of its electrocatalytic properties and its use in photoredox-sensitized catalytic systems. A literature procedure for the synthesis of **Ru-2** specifies that it should be carried out in the dark,[129] suggesting that its photoinstability was a potential concern.

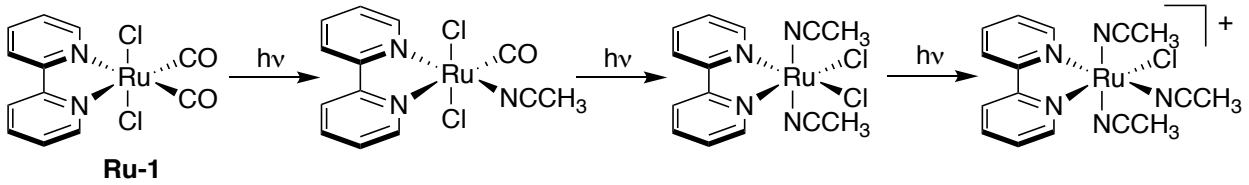

Figure 1.3. The reported photochemical reactivity of **Ru-1** in CH_3CN (λ_{ex} = 366 nm).[143-144]

The question of how the catalytic function of these $Ru(bpy^R)(CO)_2Cl_2$ compounds, with respect to CO_2 reduction, is affected by replacement of CO with other neutral ligands has only been investigated computationally thus far.[146] This question is pertinent because substitution of CO could yield highly-active, yet photostable, catalysts that are well suited for application in artificial photosynthetic systems, such as for accomplishing the light-driven RWGS reaction. Further, such a question is of fundamental interest in the development of CO_2-reduction catalysts, especially regarding whether CO is an essential ligand for catalytic function or whether variation of the monodentate ligands within $Ru^{II}(bpy)L_n$ complexes is a route to improve catalytic performance.

1.4. Chapter Summary

Herein we report work that aims to address three key issues in solar-fuel generation: (1) the demonstration of photocatalytic hydrogen oxidation; (2) the influence of neutral-ligand substitution on catalytic CO_2 reduction and the subsequent development of photostable molecular catalysts suitable for use in artificial photosynthetic systems; and (3) the photoredox integration of H_2 oxidation and CO_2 reduction to yield a functional system for the light-driven RWGS reaction.

Chapters 2 and 3 are directed towards the first issue—the demonstration of photocatalytic H_2 oxidation. Chapter 2 describes the study of $\mathbf{Ni}^+$ through a combination of electron paramagnetic resonance (EPR) techniques, X-ray crystallography, and density functional theory (DFT) calculations. Crystallographic and DFT studies detail the molecular structure of $\mathbf{Ni}^+$, and EPR reveals that the Ni(I) center does not interact strongly with potentially coordinating solvents. DFT

calculations on derivatives in which the R and R′ groups are systematically varied allow elucidation of structure/substituent relationships. Chapter 3 depicts a demonstration of photocatalytic hydrogen oxidation with **Ni**$^{+}$. An initial stepwise approach determines that every process necessary for accomplishing catalysis is achievable with photochemical sensitization. Catalysis is demonstrated in a photoelectrocatalytic system, with an electrode acting as an electron acceptor.

Chapters 5 and 6 detail the study of molecular catalysts for CO_2 reduction, with the dual aims of understanding how catalytic activity is influenced by the nature of the monodentate ligands and whether efficient reduction requires the routinely employed but photolabile CO ligand. In Chapter 5, the electrocatalytic reduction of CO_2 by **Ru-1**, *trans(Cl)*-Ru(bpy)(CO)(CH_3CN)Cl_2, *trans(CH₃CN)*-Ru(bpy)(CH_3CN)$_2Cl_2$, and *mer*-[Ru(bpy)(CH_3CN)$_3$Cl]$^{+}$ is investigated. The visible-light photochemistry of **Ru-1** is also discussed. In Chapter 6, the synthesis, structure, photochemistry, electrochemistry, and electrocatalytic CO_2 reduction chemistry of the ruthenium–bipyridyl complex mer-[Ru(bpy^{mes})(CH_3CN)$_3$Cl]$^{+}$ are described and compared to **Ru-2**.

The development of a functional system for the RWGS reaction is discussed in Chapter 4. The use of **Ni**$^{+}$ and **Ru-2** are discussed, and electrochemical techniques are utilized to screen reaction conditions to ensure that catalysis is not inhibited. It is found that with all components of a potential RWGS system present, excepting **Ru-2**, the light-induced activation of H_2 by **Ni**$^{+}$ is still achievable—even under only a partial H_2 atmosphere. Unfortunately, the photochemical experiments intended to demonstrate the light-driven RWGS reaction yielded no substantial production of CO. Additional research will be required to make this a fully functional system for the light-driven RWGS reaction.

1.5. References

1. Mikkelsen, M.; Jørgensen, M.; Krebs, F. C. The Teraton Challenge. A Review of Fixation and Transformation of Carbon Dioxide. *Energy Environ. Sci.* **2010**, *3*, 43–81.

2. Appel, A. M.; Bercaw, J. E.; Bocarsly, A. B.; Dobbek, H.; DuBois, D. L.; Dupuis, M.; Ferry, J. G.; Fujita, E.; Hille, R.; Kenis, P. J.; Kerfeld, C. A.; Morris, R. H.; Peden, C. H.; Portis, A. R.; Ragsdale, S. W.; Rauchfuss, T. B.; Reek, J. N.; Seefeldt, L. C.; Thauer, R. K.; Waldrop, G. L. Frontiers, Opportunities, and Challenges in Biochemical and Chemical Catalysis of CO_2 Fixation. *Chem. Rev.* **2013**, *113*, 6621–6658.

3. Thomas, C. D.; Cameron, A.; Green, R. E.; Bakkenes, M.; Beaumont, L. J.; Collingham, Y. C.; Erasmus, B. F.; De Siqueira, M. F.; Grainger, A.; Hannah, L.; Hughes, L.; Huntley, B.; Van Jaarsveld, A. S.; Midgley, G. F.; Miles, L.; Ortega-Huerta, M. A.; Peterson, A. T.; Phillips, O. L.; Williams, S. E. Extinction Risk from Climate Change. *Nature* **2004**, *427*, 145–148.

4. Parmesan, C.; Yohe, G. A Globally Coherent Fingerprint of Climate Change Impacts Across Natural Systems. *Nature* **2003**, *421*, 37–42.

5. Nerem, R. S.; Beckley, B. D.; Fasullo, J. T.; Hamlington, B. D.; Masters, D.; Mitchum, G. T. Climate-Change-Driven Accelerated Sea-Level Rise Detected in the Altimeter Era. *Proc. Natl. Acad. Sci. U. S. A.* **2018**, *115*, 2022–2025.

6. Screen, J. A. Arctic Sea Ice at 1.5 and 2 °C. *Nat. Clim. Change* **2018**.

7. Solomon, S.; Plattner, G. K.; Knutti, R.; Friedlingstein, P. Irreversible Climate Change Due to Carbon Dioxide Emissions. *Proc. Natl. Acad. Sci. U. S. A.* **2009**, *106*, 1704–1709.

8. Lewis, N. S.; Nocera, D. G. Powering the Planet: Chemical Challenges in Solar Energy Uilization. *Proc. Natl. Acad. Sci. U. S. A.* **2006**, *103*, 15729–15735.

9. Ashford, D. L.; Gish, M. K.; Vannucci, A. K.; Brennaman, M. K.; Templeton, J. L.; Papanikolas, J. M.; Meyer, T. J. Molecular Chromophore-Catalyst Assemblies for Solar Fuel Applications. *Chem. Rev.* **2015**, *115*, 13006–13049.

10. Concepcion, J. J.; House, R. L.; Papanikolas, J. M.; Meyer, T. J. Chemical Approaches to Artificial Photosynthesis. *Proc. Natl. Acad. Sci. U. S. A.* **2012**, *109*, 15560–15564.

11. Nocera, D. G. Solar Fuels and Solar Chemicals Industry. *Acc. Chem. Res.* **2017**, *50*, 616–619.

12. Cook, T. R.; Dogutan, D. K.; Reece, S. Y.; Surendranath, Y.; Teets, T. S.; Nocera, D. G. Solar Energy Supply and Storage for the Legacy and Nonlegacy Worlds. *Chem. Rev.* **2010**, *110*, 6474–6502.

13. Kim, D.; Sakimoto, K. K.; Hong, D.; Yang, P. Artificial Photosynthesis for Sustainable Fuel and Chemical Production. *Angew. Chem., Int. Ed.* **2015**, *54*, 3259–3266.

14. Kärkäs, M. D.; Verho, O.; Johnston, E. V.; Åkermark, B. Artificial Photosynthesis: Molecular Systems for Catalytic Water Oxidation. *Chem. Rev.* **2014**, *24*, 11863–12001.

15. Frischmann, P. D.; Mahata, K.; Würthner, F. Powering the Future of Molecular Artificial Photosynthesis with Light-Harvesting Metallosupramolecular Dye Assemblies. *Chem. Soc. Rev.* **2013**, *42*, 1847–1870.

16. Bard, A. J.; Fox, M. A. Artificial Photosynthesis: Solar Splitting of Water to Hydrogen and Oxygen. *Acc. Chem. Res.* **1995**, *28*.

17. Gust, D.; Moore, T. A.; Moore, A. L. Solar Fuels via Artificial Photosynthesis. *Acc. Chem. Res.* **2009**, *42*, 1890–1898.

18. Barber, J. Photosynthetic Energy Conversion: Natural and Artificial. *Chem. Soc. Rev.* **2009**, *38*, 185–196.

19. Du, P.; Eisenberg, R. Catalysts Made of Earth-Abundant Elements (Co, Ni, Fe) for Water Splitting: Recent Progress and Future Challenges. *Energy Environ. Sci.* **2012**, *5*, 6012–6021.

20. Dempsey, J. L.; Brunschwig, B. S.; Winkler, J. R.; Gray, H. B. Hydrogen Evolution Catalyzed by Cobaloximes. *Acc. Chem. Res.* **2009**, *42*, 1995–2004.

21. Tachibana, Y.; Vayssieres, L.; Durrant, J. R. Artificial Photosynthesis for Solar Water-Splitting. *Nat. Photonics* **2012**, *6*, 511–518.

22. You, B.; Sun, Y. Innovative Strategies for Electrocatalytic Water Splitting. *Acc. Chem. Res.* **2018**.

23. Rosser, T. E.; Gross, M. A.; Lai, Y.-H.; Reisner, E. Precious-Metal Free Photoelectrochemical Water Splitting with Immobilised Molecular Ni and Fe Redox Catalysts. *Chem. Sci.* **2016**, *7*, 4024–4035.

24. Han, Z.; Eisenberg, R. Fuel from Water: The Photochemical Generation of Hydrogen from Water. *Acc. Chem. Res.* **2014**, *47*, 2537–2544.

25. Walter, M. G.; Warren, E. L.; McKone, J. R.; Boettcher, S. W.; Mi, Q.; Santori, E. A.; Lewis, N. S. Solar Water Splitting Cells. *Chem. Rev.* **2010**, *110*, 6446–6473.

26. Kudo, A.; Miseki, Y. Heterogeneous Photocatalyst Materials for Water Splitting. *Chem. Soc. Rev.* **2009**, *38*, 253–278.

27. Nocera, D. G. The Artificial Leaf. *Acc. Chem. Res.* **2012**, *45*, 767–776.

28. Eckenhoff, W. T.; McNamara, W. R.; Du, P.; Eisenberg, R. Cobalt Complexes as Artificial Hydrogenases for the Reductive side of Water Splitting. *Biochim. Biophys. Acta* **2013**, *1827*, 958–973.

29. Yamazaki, Y.; Takeda, H.; Ishitani, O. Photocatalytic Reduction of CO_2 Using Metal Complexes. *J. Photochem. Photobiol., C* **2015**, *25*, 106–137.

30. Sahara, G.; Ishitani, O. Efficient Photocatalysts for CO_2 Reduction. *Inorg. Chem.* **2015**, *54*, 5096–5104.

31. Sekizawa, K.; Maeda, K.; Domen, K.; Koike, K.; Ishitani, O. Artificial Z-scheme Constructed with a Supramolecular Metal Complex and Semiconductor for the Photocatalytic Reduction of CO_2. *J. Am. Chem. Soc.* **2013**, *135*, 4596–4599.

32. Takeda, H.; Ishitani, O. Development of Efficient Photocatalytic Systems for CO_2 Reduction Using Mononuclear and Multinuclear Metal Complexes Based on Mechanistic Studies. *Coord. Chem. Rev.* **2010**, *254*, 346–354.

33. Bonin, J.; Maurin, A.; Robert, M. Molecular Catalysis of the Electrochemical and Photochemical Reduction of CO_2 with Fe and Co Metal Based Complexes. Recent Advances. *Coord. Chem. Rev.* **2017**, *334*, 184–198.

34. Benson, E. E.; Kubiak, C. P.; Sathrum, A. J.; Smieja, J. M. Electrocatalytic and Homogeneous Approaches to Conversion of CO_2 to Liquid Fuels. *Chem. Soc. Rev.* **2009**, *38*, 89–99.

35. White, J. L.; Baruch, M. F.; Pander Iii, J. E.; Hu, Y.; Fortmeyer, I. C.; Park, J. E.; Zhang, T.; Liao, K.; Gu, J.; Yan, Y.; Shaw, T. W.; Abelev, E.; Bocarsly, A. B. Light-Driven Heterogeneous Reduction of Carbon Dioxide: Photocatalysts and Photoelectrodes. *Chem. Rev.* **2015**, *115*, 12888–12935.

36. Liu, X.; Inagaki, S.; Gong, J. Heterogeneous Molecular Systems for Photocatalytic CO_2 Reduction with Water Oxidation. *Angew. Chem., Int. Ed.* **2016**, *55*, 14924–14950.

37. Morris, A. J.; Meyer, G. J.; Fujita, E. Molecular Approaches to the Photocatalytic Reduction of Carbon Dioxide for Solar Fuels. *Acc. Chem. Res.* **2009**, *42*, 1983–1994.

38. Windle, C. D.; Perutz, R. N. Advances in Molecular Photocatalytic and Electrocatalytic CO_2 Reduction. *Coord. Chem. Rev.* **2012**, *256*, 2562–2570.

39. Armstrong, F. A.; Belsey, N. A.; Cracknell, J. A.; Goldet, G.; Parkin, A.; Reisner, E.; Vincent, K. A.; Wait, A. F. Dynamic Electrochemical Investigations of Hydrogen Oxidation and Production by Enzymes and Implications for Future Technology. *Chem. Soc. Rev.* **2008**, *38*, 36–51.

40. Turner, J. A. Sustainable Hydrogen Production. *Science* **2004**, *305*, 972–974.

41. Ogo, S. H_2 and O_2 Activation–A Remarkable Insight into Hydrogenase. *Chem. Rec.* **2014**, *14*, 397–409.

42. Sakintuna, B.; Lamaridarkrim, F.; Hirscher, M. Metal Hydride Materials for Solid Hydrogen Storage: A Review. *Int. J. Hydrogen Energy* **2007**, *32*, 1121–1140.

43. Ettedgui, J.; Diskin-Posner, Y.; Weiner, L.; Neumann, R. Photoreduction of Carbon Dioxide to Carbon Monoxide with Hydrogen Catalyzed by a Rhenium(I) Phenanthroline−Polyoxometalate Hybrid Complex. *J. Am. Chem. Soc.* **2011**, *133*, 188–190.

44. Inglis, J. L.; MacLean, B. J.; Pryce, M. T.; Vos, J. G. Electrocatalytic Pathways Towards Sustainable Fuel Production from Water and CO_2. *Coord. Chem. Rev.* **2012**, *256*, 2571–2600.

45. Palo, D. R.; Dagle, R. A.; Holladay, J. D. Methanol Steam Reforming for Hydrogen Production. *Chem. Rev.* **2007**, *107*, 3992–4021.

46. Sheng, W.; Gasteiger, H. A.; Shao-Horn, Y. Hydrogen Oxidation and Evolution Reaction Kinetics on Platinum: Acid vs Alkaline Electrolytes. *J. Electrochem. Soc.* **2010**, *157*, B1529–B1536.

47. Bullock, R. M.; Helm, M. L. Molecular Electrocatalysts for Oxidation of Hydrogen Using Earth-Abundant Metals: Shoving Protons Around with Proton Relays. *Acc. Chem. Res.* **2015**, *48*, 2017–2026.

48. DuBois, D. L. Development of Molecular Electrocatalysts for Energy Storage. *Inorg. Chem.* **2014**, *53*, 3935–3960.

49. La Porte, N. T. Photosensitizing the Reverse Water-Gas Shift Reaction. Ph.D. Thesis, The University of Chicago, 2015.

50. La Porte, N. T.; Moravec, D. B.; Hopkins, M. D. Electron-Transfer Sensitization of H_2 Oxidation and CO_2 Reduction Catalysts Using a Single Chromophore. *Proc. Natl. Acad. Sci. U. S. A.* **2014**, *111*, 9745–9750.

51. Xiaoding, X.; Moulijn, J. A. Mitigation of CO_2 by Chemical Conversion: Plausible Chemical Reactions and Promising Products. *Energy Fuels* **1996**, *10*, 305–325.

52. Dry, M. E. The Fischer–Tropsch Process: 1950–2000. *Catal. Today* **2002**, *71*, 227–241.

53. Tamaki, Y.; Ishitani, O. Supramolecular Photocatalysts for the Reduction of CO_2. *ACS Catal.* **2017**, *7*, 3394–3409.

54. Schulz, M.; Karnahl, M.; Schwalbe, M.; Vos, J. G. The Role of the Bridging Ligand in Photocatalytic Supramolecular Assemblies for the Reduction of Protons and Carbon Dioxide. *Coord. Chem. Rev.* **2012**, *256*, 1682–1705.

55. Elgrishi, N.; Chambers, M. B.; Wang, X.; Fontecave, M. Molecular Polypyridine-Based Metal Complexes as Catalysts for the Reduction of CO_2. *Chem. Soc. Rev.* **2017**, *46*, 761–796.

56. Francke, R.; Schille, B.; Roemelt, M. Homogeneously Catalyzed Electroreduction of Carbon Dioxide-Methods, Mechanisms, and Catalysts. *Chem. Rev.* **2018**.

57. Qiao, J.; Liu, Y.; Hong, F.; Zhang, J. A Review of Catalysts for the Electroreduction of Carbon Dioxide to Produce Low-Carbon Fuels. *Chem. Soc. Rev.* **2014**, *43*, 631–675.

58. Gloaguen, F.; Rauchfuss, T. B. Small Molecule Mimics of Hydrogenases: Hydrides and Redox. *Chem. Soc. Rev.* **2009**, *38*, 100–108.

59. Lubitz, W.; Ogata, H.; Rudiger, O.; Reijerse, E. Hydrogenases. *Chem. Rev.* **2014**, *114*, 4081–4148.

60. Ogo, S. H_2 and O_2 activation by [NiFe] Hydrogenases – Insights from Model Complexes. *Coord. Chem. Rev.* **2017**, *334*, 43–53.

61. Del Barrio, M.; Sensi, M.; Orain, C.; Baffert, C.; Dementin, S.; Fourmond, V.; Leger, C. Electrochemical Investigations of Hydrogenases and Other Enzymes That Produce and Use Solar Fuels. *Acc. Chem. Res.* **2018**, *51*, 769–777.

62. Schilter, D.; Camara, J. M.; Huynh, M. T.; Hammes-Schiffer, S.; Rauchfuss, T. B. Hydrogenase Enzymes and Their Synthetic Models: The Role of Metal Hydrides. *Chem. Rev.* **2016**, *116*, 8693–8749.

63. Yuki, M.; Sakata, K.; Kikuchi, S.; Kawai, H.; Takahashi, T.; Ando, M.; Nakajima, K.; Nishibayashi, Y. Catalytic Activity of Thiolate-Bridged Diruthenium Complexes Bearing Pendent Ether Moieties in the Oxidation of Molecular Dihydrogen. *Chem. Eur. J.* **2017**, *23*, 1007–1012.

64. Yuki, M.; Sakata, K.; Nakajima, K.; Kikuchi, S.; Sekine, S.; Kawai, H.; Nishibayashi, Y. Dicationic Thiolate-Bridged Diruthenium Complexes for Catalytic Oxidation of Molecular Dihydrogen. *Organometallics* **2017**, *36*, 4499–4506.

65. Ogo, S.; Ichikawa, K.; Kishima, T.; Matsumoto, T.; Nakai, H.; Kusaka, K.; Ohhara, T. A Functional [NiFe]-Hydrogenase Mimic That Catalyzes Electron and Hydride Transfer from H_2. *Science* **2013**, *339*, 682–684.

66. Shaw, W. J.; Helm, M. L.; DuBois, D. L. A Modular, Energy-Based Approach to the Development of Nickel Containing Molecular Electrocatalysts for Hydrogen Production and Oxidation. *Biochim. Biophys. Acta* **2013**, *1827*, 1123–1139.

67. Ho, M. H.; O'Hagan, M.; Dupuis, M.; DuBois, D. L.; Bullock, R. M.; Shaw, W. J.; Raugei, S. Water-Assisted Proton Delivery and Removal in Bio-Inspired Hydrogen Production Catalysts. *Dalton Trans.* **2015**, *44*, 10969–10979.

68. Helm, M. L.; Stewart, M. P.; Bullock, R. M.; DuBois, M. R.; DuBois, D. L. A Synthetic Nickel Electrocatalyst with a Turnover Frequency Above 100,000 s^{-1} for H_2 Production. *Science* **2011**, *333*, 863–866.

69. Priyadarshani, N.; Dutta, A.; Ginovska, B.; Buchko, G. W.; O'Hagan, M.; Raugei, S.; Shaw, W. J. Achieving Reversible H_2/H^+ Interconversion at Room Temperature with

Enzyme-Inspired Molecular Complexes: A Mechanistic Study. *ACS Catal.* **2016**, *6*, 6037–6049.

70. Darmon, J. M.; Kumar, N.; Hulley, E. B.; Weiss, C. J.; Raugei, S.; Bullock, R. M.; Helm, M. L. Increasing the Rate of Hydrogen Oxidation Without Increasing the Overpotential: A Bio-Inspired Iron Molecular Electrocatalyst with an Outer Coordination Sphere Proton Relay. *Chem. Sci.* **2015**, *6*, 2737–2745.

71. Liu, T.; Dubois, D. L.; Bullock, R. M. An Iron Complex with Pendent Amines as a Molecular Electrocatalyst for Oxidation of Hydrogen. *Nat. Chem.* **2013**, *5*, 228–233.

72. Yang, J. Y.; Smith, S. E.; Liu, T.; Dougherty, W. G.; Hoffert, W. A.; Kassel, W. S.; DuBois, M. R.; DuBois, D. L.; Bullock, R. M. Two Pathways for Electrocatalytic Oxidation of Hydrogen by a Nickel Bis(diphosphine) Complex with Pendant Amines in the Second Coordination Sphere. *J. Am. Chem. Soc.* **2013**, *135*, 9700–9712.

73. Yang, J. Y.; Chen, S.; Dougherty, W. G.; Kassel, W. S.; Bullock, R. M.; DuBois, D. L.; Raugei, S.; Rousseau, R.; Dupuis, M.; DuBois, M. R. Hydrogen Oxidation Catalysis by a Nickel Diphosphine Complex with Pendant *tert*-Butyl Amines. *Chem. Commun.* **2010**, *46*, 8618–8620.

74. Boralugodage, N. P.; Arachchige, R. J.; Dutta, A.; Buchko, G. W.; Shaw, W. J. Evaluating the Role of Acidic, Basic, and Polar Amino Acids and Dipeptides on a Molecular Electrocatalyst for H_2 Oxidation. *Catal. Sci. Technol.* **2017**, *7*, 1108–1121.

75. Stolley, R. M.; Darmon, J. M.; Das, P.; Helm, M. L. Nickel Bis-Diphosphine Complexes: Controlling the Binding and Heterolysis of H_2. *Organometallics* **2016**, *35*, 2965–2974.

76. Stolley, R. M.; Darmon, J. M.; Helm, M. L. Solvent and Electrolyte Effects on $Ni(P^R_2N^{R'}_2)_2$-Catalyzed Electrochemical Oxidation of Hydrogen. *Chem. Commun.* **2014**, *50*, 3681–3684.

77. Das, P.; Stolley, R. M.; van der Eide, E. F. A Ni(II)–Bis(diphosphine)–Hydride Complex Containing Proton Relays –Structural Characterization and Electrocatalytic Studies. *Eur. J. Inorg. Chem.* **2014**, 4611–4618.

78. Kilgore, U. J.; Roberts, J. A.; Pool, D. H.; Appel, A. M.; Stewart, M. P.; DuBois, M. R.; Dougherty, W. G.; Kassel, W. S.; Bullock, R. M.; DuBois, D. L. $[Ni(P^{Ph}_2N^{C6H4X})_2)_2]^{2+}$ Complexes as Electrocatalysts for H_2 Production: Effect of Substituents, Acids, and Water on Catalytic Rates. *J. Am. Chem. Soc.* **2011**, *133*, 5861–5872.

79. Kilgore, U. J.; Stewart, M. P.; Helm, M. L.; Dougherty, W. G.; Kassel, W. S.; DuBois, M. R.; DuBois, D. L.; Bullock, R. M. Studies of a Series of $[Ni(P^R_2N^{Ph}_2)_2(CH_3CN)]^{2+}$ Complexes as Electrocatalysts for H_2 Production: Substituent Variation at the Phosphorus Atom of the P_2N_2 Ligand. *Inorg. Chem.* **2011**, *50*, 10908–10918.

80. Chen, S.; Rousseau, R.; Raugei, S.; Dupuis, M.; DuBois, D. L.; Bullock, R. M. Comprehensive Thermodynamics of Nickel Hydride Bis(Diphosphine) Complexes: A Predictive Model through Computations. *Organometallics* **2011**, *30*, 6108–6118.

81. DuBois, M. R.; DuBois, D. L. The Roles of the First and Second Coordination Spheres in the Design of Molecular Catalysts for H_2 Production and Oxidation. *Chem. Soc. Rev.* **2009**, *38*, 62–72.

82. Raugei, S.; DuBois, D. L.; Rousseau, R.; Chen, S.; Ho, M.-H.; Bullock, R. M.; Dupuis, M. Toward Molecular Catalysts by Computer. *Acc. Chem. Res.* **2015**, *48*, 248–255.

83. Gross, M. A.; Reynal, A.; Durrant, J. R.; Reisner, E. Versatile Photocatalytic Systems for H_2 Generation in Water Based on an Efficient DuBois-Type Nickel Catalyst. *J. Am. Chem. Soc.* **2014**, *136*, 356–366.

84. McLaughlin, M. P.; McCormick, T. M.; Eisenberg, R.; Holland, P. L. A Stable Molecular Nickel Catalyst for the Homogeneous Photogeneration of Hydrogen in Aqueous Solution. *Chem. Commun.* **2011**, *47*, 7989–7991.

85. Kamire, R. J.; Majewski, M. B.; Hoffeditz, W. L.; Phelan, B. T.; Farha, O. K.; Hupp, J. T.; Wasielewski, M. R. Photodriven Hydrogen Evolution by Molecular Catalysts Using Al_2O_3-Protected Perylene-3,4-Dicarboximide on NiO Electrodes. *Chem. Sci.* **2017**, *8*, 541–549.

86. Martindale, B. C. M.; Hutton, G. A. M.; Caputo, C. A.; Reisner, E. Solar Hydrogen Production Using Carbon Quantum Dots and a Molecular Nickel Catalyst. *J. Am. Chem. Soc.* **2015**, *137*, 6018–6025.

87. Martindale, B. C.; Joliat, E.; Bachmann, C.; Alberto, R.; Reisner, E. Clean Donor Oxidation Enhances the H_2 Evolution Activity of a Carbon Quantum Dot-Molecular Catalyst Photosystem. *Angew. Chem., Int. Ed.* **2016**, *55*, 9402–9406.

88. Silver, S. C.; Niklas, J.; Du, P.; Poluektov, O. G.; Tiede, D. M.; Utschig, L. M. Protein Delivery of a Ni Catalyst to Photosystem I for Light-Driven Hydrogen Production. *J. Am. Chem. Soc.* **2013**, *135*, 13246–13249.

89. Weingarten, A. S.; Kazantsev, R. V.; Palmer, L. C.; McClendon, M.; Koltonow, A. R.; Samuel, A. P. S.; Kiebala, D. J.; Wasielewski, M. R.; Stupp, S. I. Self-Assembling Hydrogel Scaffolds for Photocatalytic Hydrogen Production. *Nat. Chem.* **2014**, *6*, 964–970.

90. Caputo, C. A.; Gross, M. A.; Lau, V. W.; Cavazza, C.; Lotsch, B. V.; Reisner, E. Photocatalytic Hydrogen Production using Polymeric Carbon Nitride with a Hydrogenase and a Bioinspired Synthetic Ni Catalyst. *Angew. Chem., Int. Ed.* **2014**, *53*, 11538–11542.

91. Moore, G. F.; Sharp, I. D. A Noble-Metal-Free Hydrogen Evolution Catalyst Grafted to Visible Light-Absorbing Semiconductors. *J. Phys. Chem. Lett.* **2013**, *4*, 568–572.

92. Kasap, H.; Caputo, C. A.; Martindale, B. C.; Godin, R.; Lau, V. W.; Lotsch, B. V.; Durrant, J. R.; Reisner, E. Solar-Driven Reduction of Aqueous Protons Coupled to Selective Alcohol Oxidation with a Carbon Nitride-Molecular Ni Catalyst System. *J. Am. Chem. Soc.* **2016**, *138*, 9183–9192.

93. Costentin, C.; Robert, M.; Saveant, J. M. Catalysis of the Electrochemical Reduction of Carbon Dioxide. *Chem. Soc. Rev.* **2013**, *42*, 2423–2436.

94. Jones, J.-P.; Prakash, G. K. S.; Olah, G. A. Electrochemical CO_2 Reduction: Recent Advances and Current Trends. *Isr. J. Chem.* **2014**, *54*, 1451–1466.

95. Kortlever, R.; Shen, J.; Schouten, K. J.; Calle-Vallejo, F.; Koper, M. T. Catalysts and Reaction Pathways for the Electrochemical Reduction of Carbon Dioxide. *J. Phys. Chem. Lett.* **2015**, *6*, 4073–4082.

96. Rakowski DuBois, M.; DuBois, D. L. Development of Molecular Electrocatalysts for CO_2 Reduction and H_2 Production/Oxidation. *Acc. Chem. Res.* **2009**, *42*, 1974–1982.

97. Finn, C.; Schnittger, S.; Yellowlees, L. J.; Love, J. B. Molecular Approaches to the Electrochemical Reduction of Carbon Dioxide. *Chem. Commun.* **2012**, *48*, 1392–1399.

98. Takeda, H.; Cometto, C.; Ishitani, O.; Robert, M. Electrons, Photons, Protons and Earth-Abundant Metal Complexes for Molecular Catalysis of CO_2 Reduction. *ACS Catal.* **2016**, *7*, 70–88.

99. Saveant, J. M. Molecular Catalysis of Electrochemical Reactions. Mechanistic Aspects. *Chem. Rev.* **2008**, *108*, 2348–2378.

100. Goeppert, A.; Czaun, M.; Jones, J. P.; Surya Prakash, G. K.; Olah, G. A. Recycling of Carbon Dioxide to Methanol and Derived Products—Closing the Loop. *Chem. Soc. Rev.* **2014**, *43*, 7995–8048.

101. Voiry, D.; Shin, H. S.; Loh, K. P.; Chhowalla, M. Low-Dimensional Catalysts for Hydrogen Evolution and CO_2 Reduction. *Nat. Rev. Chem.* **2018**, *2*, 0105.

102. Artz, J.; Muller, T. E.; Thenert, K.; Kleinekorte, J.; Meys, R.; Sternberg, A.; Bardow, A.; Leitner, W. Sustainable Conversion of Carbon Dioxide: An Integrated Review of Catalysis and Life Cycle Assessment. *Chem. Rev.* **2018**, *118*, 434–504.

103. Song, Q.-W.; Zhou, Z.-H.; He, L.-N. Efficient, Selective and Sustainable Catalysis of Carbon Dioxide. *Green Chem.* **2017**, *19*, 3707–3728.

104. Hernández, S.; Amin Farkhondehfal, M.; Sastre, F.; Makkee, M.; Saracco, G.; Russo, N. Syngas Production from Electrochemical Reduction of CO_2: Current Status and Prospective Implementation. *Green Chem.* **2017**, *19*, 2326–2346.

105. Zhu, D. D.; Liu, J. L.; Qiao, S. Z. Recent Advances in Inorganic Heterogeneous Electrocatalysts for Reduction of Carbon Dioxide. *Adv. Mater.* **2016**, *28*, 3423–3452.

106. Daza, Y. A.; Kuhn, J. N. CO2 Conversion by Reverse Water Gas Shift Catalysis: Comparison of Catalysts, Mechanisms and their Consequences For CO_2 Conversion to Liquid Fuels. *RSC Adv.* **2016**, *6*, 49675–49691.

107. Costentin, C.; Robert, M.; Saveant, J. M. Current Issues in Molecular Catalysis Illustrated by Iron Porphyrins as Catalysts of the CO_2-to-CO Electrochemical Conversion. *Acc. Chem. Res.* **2015**, *48*, 2996–3006.

108. Maeda, C.; Miyazaki, Y.; Ema, T. Recent Progress in Catalytic Conversions of Carbon Dioxide. *Catal. Sci. Technol.* **2014**, *4*, 1482–1497.

109. Lanzafame, P.; Centi, G.; Perathoner, S. Catalysis for Biomass and CO_2 Use Through Solar Energy: Opening New Scenarios for A Sustainable and Low-Carbon Chemical Production. *Chem. Soc. Rev.* **2014**, *43*, 7562–7580.

110. Kondratenko, E. V.; Mul, G.; Baltrusaitis, J.; Larrazábal, G. O.; Pérez-Ramírez, J. Status and Perspectives of CO_2 Conversion Into Fuels and Chemicals by Catalytic, Photocatalytic and Electrocatalytic Processes. *Energy Environ. Sci.* **2013**, *6*, 3112–3135.

111. Reithmeier, R.; Bruckmeier, C.; Rieger, B. Conversion of CO_2 via Visible-Light Promoted Homogeneous Redox Catalysis. *Catalysts* **2012**, *2*, 544–571.

112. Mori, K.; Yamashita, H.; Anpo, M. Photocatalytic Reduction of CO_2 with H_2O on Various Titanium Oxide Photocatalysts. *RSC Adv.* **2012**, *2*, 3165–3172.

113. Kumar, B.; Llorente, M.; Froehlich, J.; Dang, T.; Sathrum, A.; Kubiak, C. P. Photochemical and Photoelectrochemical Reduction of CO_2. *Annu. Rev. Phys. Chem.* **2012**, *63*, 541–569.

114. Whipple, D. T.; Kenis, P. J. A. Prospects of CO_2 Utilization via Direct Heterogeneous Electrochemical Reduction. *J. Phys. Chem. Lett.* **2010**, *1*, 3451–3458.

115. Roy, S. C.; Varghese, O. K.; Paulose, M.; Grimes, C. A. Toward Solar Fuels: Photocatalytic Conversion of Carbon Dioxide to Hydrocarbons. *ACS Nano* **2010**, *4*, 1259–1278.

116. Stanbury, M.; Compain, J.-D.; Chardon-Noblat, S. Electro and Photoreduction of CO_2 Driven by Manganese-Carbonyl Molecular Catalysts. *Coord. Chem. Rev.* **2018**, *361*, 120–137.

117. Omae, I. Recent Developments in Carbon Dioxide Utilization for the Production of Organic Chemicals. *Coord. Chem. Rev.* **2012**, *256*, 1384–1405.

118. Grice, K. A. Carbon Dioxide Reduction with Homogenous Early Transition Metal Complexes: Opportunities and Challenges for Developing CO_2 Catalysis. *Coord. Chem. Rev.* **2017**, *336*, 78–95.

119. Lim, R. J.; Xie, M.; Sk, M. A.; Lee, J.-M.; Fisher, A.; Wang, X.; Lim, K. H. A Review on the Electrochemical Reduction of CO_2 in Fuel Cells, Metal Electrodes and Molecular Catalysts. *Catal. Today* **2014**, *233*, 169–180.

120. Manbeck, G. F.; Fujita, E. A Review of Iron and Cobalt Porphyrins, Phthalocyanines and Related Complexes for Electrochemical and Photochemical Reduction of Carbon Dioxide. *J. Porphyrins Phthalocyanines* **2015**, *19*, 45–64.

121. Taheri, A.; Berben, L. A. Making C–H Bonds with CO_2: Production of Formate by Molecular Electrocatalysts. *Chem. Commun.* **2016**, *52*, 1768–1777.

122. Schneider, J.; Jia, H.; Muckerman, J. T.; Fujita, E. Thermodynamics and Kinetics of CO_2, CO, and H^+ Binding to the Metal Centre of CO_2 Reduction Catalysts. *Chem. Soc. Rev.* **2012**, *41*, 2036–2051.

123. Grice, K. A.; Kubiak, C. P. In *Advances in Inorganic Chemistry*, Aresta, M., van Eldik, R., Eds. Academic Press: Waltham, MA, 2014; Vol. 66, pp 163–188.

124. Apaydin, D. H.; Schlager, S.; Portenkirchner, E.; Sariciftci, N. S. Organic, Organometallic and Bioorganic Catalysts for Electrochemical Reduction of CO_2. *ChemPhysChem* **2017**, *18*, 3094–3116.

125. Rao, H.; Schmidt, L. C.; Bonin, J.; Robert, M. Visible-Light-Driven Methane Formation From CO_2 with a Molecular Iron Catalyst. *Nature* **2017**, *548*, 74–77.

126. Costentin, C.; Drouet, S.; Robert, M.; Saveant, J. M. A Local Proton Source Enhances CO_2 Electroreduction to CO by a Molecular Fe Catalyst. *Science* **2012**, *338*, 90–94.

127. Wrighton, M. Photochemistry of Metal Carbonyls. *Chem. Rev.* **1974**, *74*, 401–430.

128. Collomb-Dunand-Sauthier, M.-N.; Deronzier, A.; Ziessel, R. Electrocatalytic Reduction of Carbon Dioxide with Mono(bipyridine)carbonylruthenium Complexes in Solution or as Polymeric Thin Films. *Inorg. Chem.* **1994**, *33*, 2961–2967.

129. Machan, C. W.; Sampson, M. D.; Kubiak, C. P. A Molecular Ruthenium Electrocatalyst for the Reduction of Carbon Dioxide to CO and Formate. *J. Am. Chem. Soc.* **2015**, *137*, 8564–8571.

130. Chardon-Noblat, S.; Deronzier, A.; Ziessel, R.; Zsoldos, D. Selective Synthesis and Electrochemical Behavior of *trans(Cl)*- and *cis(Cl)*- [Ru(bpy)$(CO)_2Cl_2$] Complexes (bpy = 2,2'-Bipyridine). Comparative Studies of Their Electrocatalytic Activity Toward the Reduction of Carbon Dioxide. *Inorg. Chem.* **1997**, *36*, 5384–5389.

131. Ishida, H.; Fujiki, K.; Ohba, T.; Ohkubo, K.; Tanaka, K.; Terada, T.; Tanaka, T. Ligand Effects of Ruthenium 2,2′ -Bipyridine and 1,10-Phenanthroline Complexes on the Electrochemical Reduction of CO_2. *J. Chem. Soc., Dalton Trans.* **1990**, 2155‑2160.

132. Lehn, J.-M.; Ziessel, R. Photochemical Reduction of Carbon Dioxide to Formate Catalyzed by 2,2'-Bipyridine- or 1,10-Phenanthroline-Ruthenium(II) Complexes. *J. Organomet. Chem.* **1990**, *382*, 157–173.

133. Kuramochi, Y.; Itabashi, J.; Fukaya, K.; Enomoto, A.; Yoshida, M.; Ishida, H. Unexpected Effect of Catalyst Concentration on Photochemical CO_2 Reduction by *trans(Cl)*-$Ru(bpy)(CO)_2Cl_2$: New Mechanistic Insight into the $CO/HCOO^-$ Selectivity. *Chem. Sci.* **2015**, *6*, 3063–3074.

134. Eskelinen, E.; Kinnunen, T.-J. J.; Haukka, M.; Pakkanen, Tapani A. Photochemical Studies of *cis*(CO),*trans*(Cl)-[$Ru(bpy)(CO)_2Cl_2$] (bpy = 2,2′ -bipyridine): Ligand Exchange Reactions in Methanol. *Eur. J. Inorg. Chem.* **2002**, *2002*, 1169‑1173.

135. Gabrielsson, A.; Zalis, S.; Matousek, P.; Towrie, M.; Vlcek, A., Jr. Ultrafast Photochemical Dissociation of an Equatorial CO Ligand From *trans(X,X)*-[$Ru(X)_2(CO)_2(bpy)$] (X = Cl, Br, I): A Picosecond Time-Resolved Infrared Spectroscopic and DFT Computational Study. *Inorg. Chem.* **2004**, *43*, 7380–7388.

136. Bokach, N. A.; Haukka, M.; Hirva, P.; Guedes Da Silva, M. F. C.; Kukushkin, V. Y.; Pombeiro, A. J. L. Photoinduced Synthesis and Electrochemical Properties of New Ruthenium(Mono)Bipyridine Dialkylcyanamide and Propiononitrile Complexes. *J. Organomet. Chem.* **2006**, *691*, 2368–2377.

137. Deacon, G. B.; Kepert, C. M.; Sahely, N.; Skelton, B. W.; Spiccia, L.; Thomas, N. C.; White, A. H. Synthesis and Structures of Photodecarbonylated Ruthenium(II) Complexes—Potential Intermediates for Mixed Ligand Complexes. *J. Chem. Soc., Dalton Trans.* **1999**, 275–277.

138. Mulhern, D.; Brooker, S.; Gorls, H.; Rau, S.; Vos, J. G. Synthesis of Mononuclear and Dinuclear Ruthenium(II) Tris(heteroleptic) Complexes via Photosubstitution in Bis(carbonyl) Precursors. *Dalton Trans.* **2006**, 51–57.

139. Kubeil, M.; Vernooij, R. R.; Kubeil, C.; Wood, B. R.; Graham, B.; Stephan, H.; Spiccia, L. Studies of Carbon Monoxide Release from Ruthenium(II) Bipyridine Carbonyl Complexes Upon UV-Light Exposure. *Inorg. Chem.* **2017**, *56*, 5941–5952.

140. Kepert, C. M.; Deacon, G. B.; Sahely, N.; Spiccia, L.; Fallon, G. D.; Skelton, B. W.; White, A. H. Synthesis of Heteroleptic Bis(diimine)carbonylchlororuthenium(II) Complexes from Photodecarbonylated Precursors. *Inorg. Chem.* **2004**, *43*, 2818–2827.

141. Spiccia, L.; Deacon, G. B.; Kepert, C. M. Synthetic Routes to Homoleptic and Heteroleptic Ruthenium(II) Complexes Incorporating Bidentate Imine Ligands. *Coord. Chem. Rev.* **2004**, *248*, 1329–1341.

142. Chen, Z.; Chen, C.; Weinberg, D. R.; Kang, P.; Concepcion, J. J.; Harrison, D. P.; Brookhart, M. S.; Meyer, T. J. Electrocatalytic Reduction of CO_2 to CO by Polypyridyl Ruthenium Complexes. *Chem. Commun.* **2011**, *47*, 12607–12609.

143. Eskelinen, E.; Haukka, M.; Venäläinen, T.; Pakkanen, T. A.; Wasberg, M.; Chardon-Noblat, S.; Deronzier, A. Light-Induced Decarbonylation, Solvolysis, and Isomerization of $Ru(L)(CO)_2Cl_2$ (L = 2,2'-Bipyridine and 4,4'-Dimethyl-2,2'-bipyridine) in Acetonitrile. *Organometallics* **2000**, *19*, 163–169.

144. Collomb-Dunand-Sauthier, M.-N.; Deronzier, A. Photochemical Reactivity of $[Ru^{II}(L)(CO)_2Cl_2]$ and $[Me_4N]$ $[Ru^{III}(L)(CO)Cl_3]$ (L = 2,2'-Bipyridine or 4,4'-Di(isopropoxycarbonyl)-2,2'-Bipyridine) in CH_3CN and the Redox Properties of the Resulting New Complexes. *J. Organomet. Chem.* **1993**, *444*, 191–198.

145. Hartl, F.; Aarnts, M. P.; Nieuwenhuis, H. A.; van Slageren, J. Electrochemistry of Different Types of Photoreactive Ruthenium(II) Dicarbonyl α-Diimine Complexes. *Coord. Chem. Rev.* **2002**, *230*, 107–125.

146. Ramakrishnan, S.; Chidsey, C. E. D. Initiation of the Electrochemical Reduction of CO_2 by a Singly Reduced Ruthenium(II) Bipyridine Complex. *Inorg. Chem.* **2017**, *56*, 8326–8333.

CHAPTER 2: X-Ray Crystallographic, Multifrequency EPR, and DFT Characterization of the Ni($P^{Cy}_2N^{tBu}_2$)$_2^{n+}$ Hydrogen Oxidation Catalyst in the Ni(I) Oxidation State

NOTE: This work has previously been published in an alternative format as Niklas, J.; Westwood, M.; Mardis, K. L.; Brown, T. L.; Pitts-McCoy, A. M.; Hopkins, M. D.; Poluektov, O. G. *Inorg. Chem.* **2015**, *54*, 6226–6234

2.1. Introduction

The environmental and social impacts of fossil fuel consumption require that we develop renewable sources of energy.[1-3] The prospect of using molecular hydrogen as a renewable fuel has motivated considerable research into the development of efficient homogeneous catalysts for the reduction of protons to H_2 and for the corresponding reverse H_2-oxidation reaction.[4-10] In general, catalysts that employ first-row transition metals are especially attractive targets owing to their greater natural abundance and potential lower cost relative to traditional catalysts comprised of rare and expensive metals like platinum. Relevant to this goal, DuBois, Bullock and coworkers have pioneered the development of highly active and tunable nickel–phosphine electrocatalysts of the general form [Ni($P^R_2N^{R'}_2$)$_2$]$^{n+}$.[11-14] These catalysts, examples of which are shown schematically in Figure 2.1 (for n = 1), contain second-coordination-sphere amine groups that are integral to the H–H bond forming and cleavage processes.[13, 15-16] The nature of the R and R′ substituents on the phosphine and amine units, respectively, governs whether these catalysts operate for proton reduction, hydrogen oxidation, or the bidirectional redox interconversion of protons and hydrogen.[11, 17] Extensive studies of these catalysts have provided detailed insights into how the phosphine and amine substituents affect the redox potentials, Brønsted acidity, substrate binding free energies, and other underlying thermodynamic factors that control catalyst function. These

details are particularly rich for catalyst intermediates in the Ni(II) and Ni(0) oxidation states, which are amenable to study by multinuclear NMR spectroscopic methods.[18]

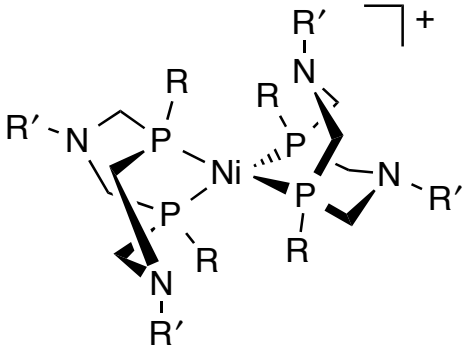

Compound	R	R′
1^{+}	Cy	*t*-Bu
2^{+}	Ph	*t*-Bu
3^{+}	Cy	Ph
4^{+}	Ph	Ph
5^{+}	Ph	$C_6H_4CH_2P(O)(OEt)_2$

Figure 2.1. $[Ni(P^R{}_2N^{R'}{}_2)_2]^+$ complexes discussed in this Chapter.

It has been found that complexes of form $[Ni(P^R{}_2N^{R'}{}_2)_2]^+$, which possess the Ni(I) oxidation state, are key intermediates in the catalytic cycles for both proton reduction and hydrogen oxidation by this class of catalysts.[15, 18-19] In the catalytic oxidation of hydrogen, the one-electron oxidation of $[Ni(P^R{}_2N^{R'}{}_2)_2]^+$ compounds produces the $[Ni(P^R{}_2N^{R'}{}_2)_2]^{2+}$ species that coordinate dihydrogen, while in catalytic proton reduction, $[Ni(P^R{}_2N^{R'}{}_2)_2]^+$ species initiate the cycle by binding the first proton. Because $[Ni(P^R{}_2N^{R'}{}_2)_2]^+$ compounds are paramagnetic (d^9 electron configuration), their structures and properties are not fruitfully probed by NMR spectroscopic techniques. In contrast, electron paramagnetic resonance (EPR) spectroscopy is an excellent tool for characterizing the electronic structures of paramagnetic metal complexes and studying changes due to the variation of ligands and the surroundings.[20-23] Recently, two EPR studies on $[Ni(P^R{}_2N^{R'}{}_2)_2]^+$ proton-reduction catalysts **4**$^{+}$ [24] and **5**$^{+}$ [25] (Figure 2.1) have been reported. Among several observations, it

was found that the phosphorus nuclei of these complexes are inequivalent. Further, it was noted that there is appreciable delocalization of the unpaired electron spin density onto the ligands. These and related[26] studies show that EPR spectroscopy is a sensitive and useful probe for Ni(I) species in the $[Ni(P^{R}_2N^{R'}_2)_2]^{n+}$ family of catalysts.

There have not yet been corresponding EPR spectroscopic studies of $[Ni(P^{R}_2N^{R'}_2)_2]^{+}$ complexes that function as hydrogen-oxidation catalysts. These catalysts, of which the complex $[Ni(P^{Cy}_2N^{tBu}_2)_2][BF_4]$ (**1**[BF_4]; $P^{Cy}_2N^{tBu}_2$ = 1,5-di(*tert*-butyl)-3,7-dicyclohexyl-1,5-diaza-3,7-diphosphacyclooctane) has been found to exhibit particularly high activity,[18, 27] generally possess more strongly electron-donating phosphine R groups than do proton-reduction catalysts (e.g., R = cyclohexyl for $\mathbf{1}^+$ vs. R = Ph for $\mathbf{4}^+$ and $\mathbf{5}^+$). In addition to governing catalytic activity through control of the thermodynamic factors noted above, these different substituents also likely affect the molecular structures of the catalyst, the interaction of the Ni center with the solvent (which can influence catalytic activity),[28] and the delocalization of the unpaired electron. The contributions to these effects from catalytic intermediates in the Ni(I) state have not been directly probed.

Here we report a study of **1**[BF_4] using X-ray crystallography, density functional theory (DFT) calculations, and EPR spectroscopic methods. We use EPR spectroscopy at X-band (9 GHz), Q-band (34 GHz), and D-band (130 GHz) microwave frequencies to distinguish clearly between field-dependent and field-independent parameters. The multifrequency approach allows us to determine **g** tensor anisotropy and hyperfine splitting due to the ^{31}P, ^{14}N, and ^{1}H magnetic nuclei of the ligands. The crystallographic, computational, and EPR spectroscopic studies all indicate that the structure of the $\mathbf{1}^+$ ion is highly symmetric. This contrasts with the structure of $\mathbf{4}^+$, which is inferred to be less symmetrical and to possess several energetically accessible conformers. It is additionally found that the Ni(I) center of $\mathbf{1}^+$ interacts only weakly with solvent, and that the

magnitude of the hyperfine coupling of the Ni(I) electron spin with the phosphorus nuclei differs significantly from those observed previously for $\mathbf{4}^+$. Computational studies of $[Ni(P^R{}_2N^{R'}{}_2)_2]^+$ compounds in which the phosphine R and amine R′ substituents of $\mathbf{1}^+$ and $\mathbf{4}^+$ are systematically interchanged ($\mathbf{2}^+$ and $\mathbf{3}^+$, Figure 2.2) allow delineation of their individual and collective effects on the molecular structures and magnetic parameters of the catalysts.

2.2. Experimental Section

2.2.1. General Procedures for Synthesis and Characterization. All experiments were performed under a nitrogen atmosphere using standard Schlenk and glovebox techniques. Solvents used for syntheses were HPLC grade; they were further purified by passing them under nitrogen pressure through an anaerobic, stainless-steel system consisting of either two 4.5 in. × 24 in. (1 gal) columns of activated A2 alumina (CH_3CN, Et_2O, and CH_2Cl_2) or one column of activated A2 alumina and one column of activated BASF R3-11 catalyst (*n*-pentane).[29] Butyronitrile and CD_3CN were stored under nitrogen over activated 4 Å molecular sieves. The compounds **1**[18] and $\mathbf{1}[BF_4]_2$[27] were prepared by standard procedures. ^1H- and $^{31}P\{^1H\}$-NMR spectra were recorded at room temperature with a Bruker DRX 400 NMR spectrometer. Chemical shifts were measured relative to the solvent resonance (^1H)[30] or an external standard of 85% H_3PO_4 (^{31}P). Single-crystal X-ray diffraction studies were performed using a Bruker D8 Venture system; full details are available in Chapter 7.1.

2.2.2. Preparation of $\mathbf{1}[BF_4]$. This compound was prepared by a modified version of the previously reported procedure.[18] A mixture of **1** (0.100 g, 0.11 mmol) and $\mathbf{1}[BF_4]_2$ (0.107 g, 0.099 mmol) in CH_3CN (10 mL) was stirred at room temperature for 30 min. The $^{31}P\{^1H\}$-NMR spectrum of the reaction mixture showed that $\mathbf{1}[BF_4]_2$ had been completely consumed and exhibited a weak signal due to the small excess quantity of **1** employed in the starting mixture. The

solvent was removed under reduced pressure and the remaining orange residue was stirred for 1 h whilst suspended in *n*-pentane (30 mL) to extract unreacted **1**. An orange powder was collected by filtration, washed with pentane (3 × 10 mL), and dried under vacuum. The product was recrystallized by vapor diffusion of Et_2O into a concentrated solution of the compound in CH_3CN (*ca*. 3 mL); this provided, after 3 days, green crystals of **1**[BF_4] (0.130 g, 63% yield) suitable for single-crystal X-ray diffraction experiments. ^{1}H NMR (400.1 Hz, CD_3CN): δ3.99 (v br), 1.70 (br), 1.42 (br), 0.96 (br).

2.2.3. Multi-Frequency EPR Studies. EPR experiments were performed and analyzed by Dr. Oleg Poluektov and Dr. Jens Niklas at Argonne National Laboratory. All samples were prepared under a nitrogen atmosphere. Solutions of **1**[BF_4] (~2 mM) were contained in Suprasil quartz capillaries; X-band sample tubes had 4 mm outside diameter (o.d.), Q-band sample tubes 2 mm o.d., and D-band sample tubes 0.6 mm o.d. The filled EPR sample tubes were sealed under nitrogen to prevent exposure to air; however, in the case of the fine-bore D-band tubes, which are difficult to seal, some exposure to oxygen could not be avoided; this resulted in generation of a trace paramagnetic impurity (see Results and Discussion). Continuous wave (CW) X-band (9–10 GHz) EPR experiments were carried out with a Bruker ELEXSYS E580 EPR spectrometer (Bruker Biospin, Rheinstetten, Germany), equipped with a TE_{102} rectangular EPR resonator (Bruker ER 4102st) and a helium gas-flow cryostat (ICE Oxford, UK). An intelligent temperature controller (ITC503) from Oxford Instruments (Oxford, UK) was used.

Pulsed X-band experiments were performed on the same spectrometer, using a Flexline dielectric ring resonator (Bruker ER 4118X-MD5-W1 or Bruker EN 4118X-MD4-W1) and a helium gas-flow cryostat (CF935, Oxford Instruments, UK). The temperature was controlled by an ITC503 (Oxford Instruments, UK). Pulsed ENDOR experiments were performed on the same

spectrometer using a Bruker EN 4118X-MD4-W1 resonator and a BT01000-AlphaSA 1 kW RF amplifier (TOMCO Technologies, Stepney, Australia). The Davies ENDOR sequence[31-32] (π–t–π /2–t–π–t–echo) with an inversion π pulse of 148 ns, t = 10 μs, and the Mims ENDOR sequence[32-33] (π /2–t–π /2–t–π /2–t–echo) with a π/2 pulse of 24 ns, t = 10 μs, were employed. The rf pulse was 6 μs long.

Continuous wave (CW) Q-band (34 GHz) EPR experiments were carried out with the same EPR spectrometer, equipped with a Q-band bridge (Bruker ER 051 QG), a cylindrical EPR resonator (Bruker ER 5106 QT-W) and a helium gas-flow cryostat (CF935, Oxford Instruments). The temperature was controlled by an ITC503 (Oxford Instruments, UK). The microwave (MW) frequency was monitored by a frequency counter (5352B, Hewlett Packard). The spectra were recorded under saturating conditions, yielding absorption-type line shapes, and were then pseudomodulated[34] to yield derivative-type line shapes.

High frequency EPR measurements were performed on a home-built D-band (130 GHz) spectrometer equipped with a single mode TE_{011} cylindrical cavity.[35-36] The spectrometer was controlled by a PC using the SpecMan4EPR program.[37] EPR spectra were recorded in pulsed mode in order to remove the microwave phase distortion due to fast-passage effects. The absorption line shape of the EPR spectra was recorded by monitoring the electron spin echo (ESE) intensity from a two-microwave-pulse sequence as a function of magnetic field. The duration of a π/2 microwave pulse was 40–60 ns, and typical separation times between microwave pulses were 150–300 ns. All D-band spectra have been pseudo-modulated to yield derivative-type line shapes.[34]

Data processing was done as described previously[38] using Xepr (Bruker BioSpin, Rheinstetten) and Matlab 7.11.2 (MathWorks, Natick, MA) software. The magnetic parameters were obtained from theoretical simulation of the EPR and ENDOR spectra. The simulations were

performed using the EasySpin software package (version 4.5.5).[39] The accuracy in determination of the electronic **g** tensor for the set of multi-frequency EPR spectra is estimated to be ±0.001.

2.2.4. Density Functional Theory (DFT) Calculations. Density functional theory calculations were performed by Prof. Kristy Mardis and students Tiara Brown and Anthony Pitts-McCoy of Chicago State University. The molecular structures of $\mathbf{1}^+$, $\mathbf{2}^+$, $\mathbf{3}^+$, and $\mathbf{4}^+$ were optimized *in vacuo* using PQS v 2.0-3.[40] Basis sets and functionals used for geometry optimizations were selected on the basis of a benchmarking study described below. In all cases frequency calculations were performed to ensure, by the absence of imaginary frequencies, that the stationary points obtained in the geometry optimizations were energetic minima. EPR parameters were calculated using the computational package Orca 2.9.1.[41] The principal *g*-values were calculated employing the coupled-perturbed Kohn-Sham equations.[42] The anisotropic magnetic dipole and the isotropic Fermi contact contributions to the hyperfine coupling were calculated for all ^{1}H, ^{14}N and ^{31}P atoms. Second-order spin-orbit hyperfine contributions were included for ^{31}P atoms. Calculations of the EPR parameters employed the B3LYP functional,[43-46] the EPRII basis set[47-48] for C, N, and H, the IGLOII basis set[49] for P, and Wachters basis set[50-52] for Ni. To test for influence of basis set on the calculated EPR parameters, additional single point calculations were performed using the def2-TZVP basis set[53] for all atoms; these showed only minor differences in the magnetic parameters (**g** tensors, hyperfine interaction tensors; see Chapter 7, Table 7.1.3).

To determine the best method for geometry optimization, the structure of $\mathbf{1}^+$ was optimized *in vacuo* using multiple basis sets (3-21G, 6-31G) and functionals (B3LYP, BP86, PBE); in each case, the geometry from the crystal structure of **1**[BF_4] served as the starting point. In general, these methods provided Ni–P bond distances slightly longer than those determined from the crystal structure of $\mathbf{1}^+$ (Chapter 7, Table 7.1.4), with the 3-21G basis set providing closer agreement than

6-31G for a given functional. Subsequent calculation of the EPR parameters (*g*-values and ^{31}P isotropic hyperfine coupling constants) for each structure showed that the results for the structures provided by the functionals BP86 and PBE are very similar to each other and close to experimental values. The structures provided by calculations using the B3LYP functional give larger *g*-values and smaller hyperfine constants in the subsequent EPR parameter calculations. As a consequence of these considerations, the BP86 functional and 3-21G basis set were used for geometry optimizations of $\mathbf{1}^+$, $\mathbf{2}^+$, $\mathbf{3}^+$, and $\mathbf{4}^+$ because they provide a good balance of speed and accuracy. The starting structures for $\mathbf{2}^+$, $\mathbf{3}^+$, and $\mathbf{4}^+$ were obtained by substituting R and R′ in the optimized structure of complex $\mathbf{1}^+$. Atomic coordinates of optimized structures and calculated hyperfine couplings constants are given in Chapter 7 (Tables 7.1.8–13).

2.3. Results and Discussion

2.3.1. Molecular Structure of $\mathbf{1}^+$. The molecular structures of $\mathbf{1}^+$ in the solid state and gas phase were determined using X-ray crystallography and DFT calculations, respectively. The X-ray crystal structure of $\mathbf{1}[BF_4]$ shows the presence of discrete $\mathbf{1}^+$ and BF_4^- ions; the former is displayed in Figure 2.2. The Ni(I) center of $\mathbf{1}^+$ exhibits a distorted tetrahedral geometry, with an intra-ligand P–Ni–P bite angle of 81.8˚ and with the P–Ni–P planes of the two ligands offset by a dihedral angle (α) of 62.1˚ (where α = 90˚ characterizes a NiP_4 subunit with D_{2d} symmetry). The NiP_4 subunit is quite symmetric: the $\mathbf{1}^+$ ion resides at a site of 2-fold rotational symmetry, and the non-symmetry-equivalent Ni–P bonds differ in length by less than 2σ (2.2175(7) and 2.2195(7) Å). The high symmetry about the Ni center of $\mathbf{1}^+$ may be contrasted with findings for the related Ni(I) compound $[Ni(P^{tBu}{}_2N^{Bn}{}_2)_2][BF_4]$,[54] the crystal-structure of which exhibits statistically significant differences among the Ni–P bond lengths (2.2113(15), 2.2124(17), 2.2289(15) and 2.2292(16) Å), and for structures calculated for $\mathbf{4}^+$ using DFT (see below). In $\mathbf{1}[BF_4]$ the four six-membered

[$NiPCH_2NCH_2P$] rings formed by the chelating ligands are in the boat conformation. The long Ni•••N distances (Ni–N(1) = 3.412 Å, Ni–N(2) = 3.411 Å) indicate that the pendant amine groups are not bonded to the nickel center.

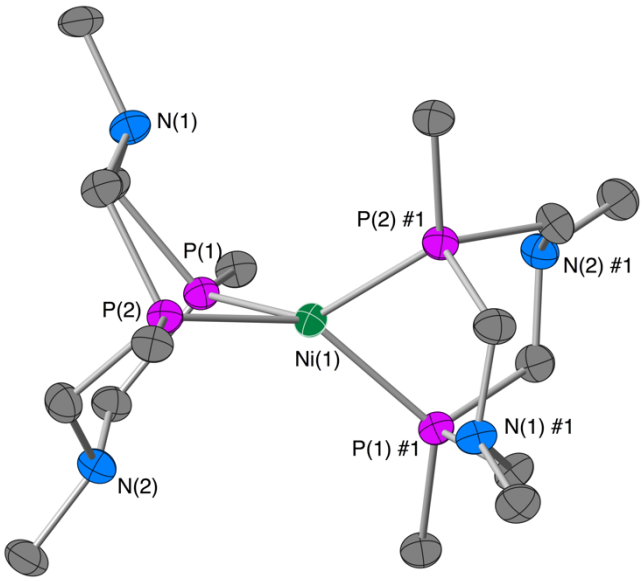

Figure 2.2. Thermal-ellipsoid representation of the $\mathbf{1}^+$ ion of **1**[BF_4] (50% probability ellipsoids). Carbon (grey), phosphorus (purple), nitrogen (blue) and nickel (green) atoms are shown; hydrogen atoms are omitted for clarity and only the first carbon atoms of the cyclohexyl and *tert*-butyl groups are shown. Selected bond lengths (Å) and bond angles (˚): Ni(1)–P(1) = 2.2175(7), Ni(1)–P(2) = 2.2195(7), P(1)–Ni(1)–P(2) = 81.83(3), P(1)–Ni(1)–P(1)#1 = 111.36(4), P(2)–Ni(1)–P(2)#1 = 112.13(3), P(1)–Ni(1)–P(2)#1 = 140.49(2), α = 62.1˚. Complete metrical data are provided in Chapter 7.1 (Table 7.1.2 and Figure 7.1.2).

The gas-phase molecular structure of $\mathbf{1}^+$ provided by DFT calculations (Chapter 7, Table 7.1.5) is in essential agreement with the solid-state structure of **1**[BF_4] described above. The calculated Ni–P bond distance, intra-ligand P–Ni–P bond angle, and inter-ligand dihedral angle all differ slightly from those observed in the crystal structure (calculated/experimental values: Ni–P = 2.225/2.2185_{avg} Å; P–Ni–P = 83.3/81.8˚; α = 69.1/62.1˚), which in part may reflect the effects of crystal packing. Importantly, though, the calculated structure very nearly conforms to idealized D_2 symmetry, with the phosphorus nuclei residing in chemically equivalent positions. This is consistent with the observation from the crystal structure of a highly symmetric structure, and

contrasts with observations for $\mathbf{4}^{+}$ described below. The six-membered rings formed by the chelating ligands are all computed to adopt boat conformation, as found in the crystal structure.

The geometry about the Ni(I) center of **1**[BF_4] may be compared with those previously determined by X-ray crystallography for the redox-congeneric Ni(II) and Ni(0) compounds [Ni($P^{Cy}_2N^{tBu}_2$)$_2$][BF_4]$_2$ (**1**[BF_4]$_2$)[27] and Ni($P^{Cy}_2N^{tBu}_2$)$_2$ (**1**),[18] respectively. The inter-ligand dihedral angles of these compounds vary with d^n configuration in the expected manner, with the geometry of d^{10} **1** lying closer to the tetrahedral limit ($\alpha = 85^\circ$) than that of d^9 $\mathbf{1}^{+}$ ($\alpha = 62.1^\circ$), and d^8 $\mathbf{1}^{2+}$ lying closer to the square-planar limit ($\alpha = 23^\circ$). The Ni–P bonds lengthen with increasing oxidation state (d(Ni–P)$_{avg}$: **1** = 2.1394 Å, $\mathbf{1}^{+}$ = 2.2185 Å, $\mathbf{1}^{2+}$ = 2.2277 Å), and the intra-ligand P–Ni–P angle decreases concomitantly (∠P–Ni–P: **1** = 83.9°, $\mathbf{1}^{+}$ = 81.8°, $\mathbf{1}^{2+}$ = 80.8°). These trends in bond lengths, and bond and dihedral angles were also seen for the Ni(I)/Ni(0) pair of compounds [Ni($P^{tBu}_2N^{Bn}_2$)$_2$][BF_4] and Ni($P^{tBu}_2N^{Bn}_2$)$_2$.[54]

2.3.2. Multi-Frequency EPR Study of 1[BF_4] in Frozen Solution. Figure 2.3 shows EPR spectra of frozen solutions of **1**[BF_4] in butyronitrile at X-band (9-10 GHz), Q-band (34 GHz), and D-band (130 GHz) frequencies. All EPR spectra are depicted as derivative-type spectra, i.e., they are the first derivative of an absorption spectrum. Measurements at different cryogenic temperatures (in the 5–100 K range) revealed no temperature dependence of the EPR spectrum (see Chapter 7, Figure 7.1.3), allowing us to use the optimal temperature for each type of experiment.

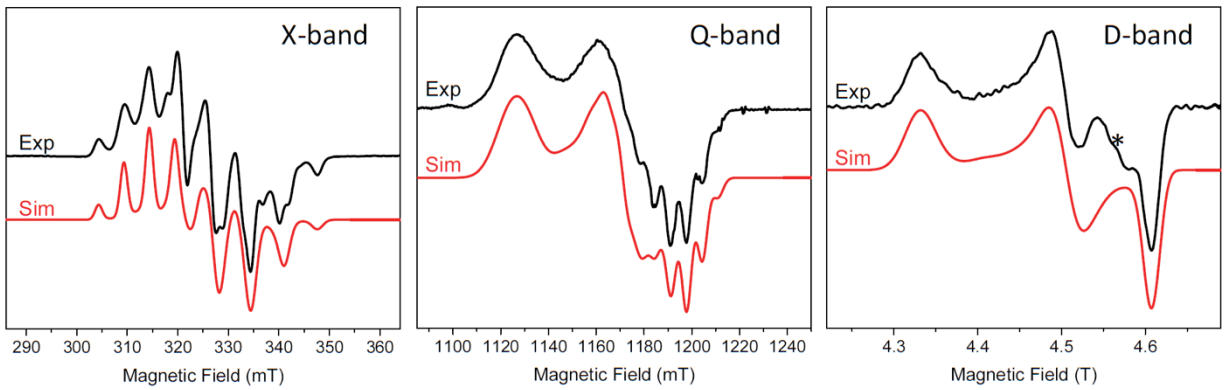

Figure 2.3. Electron paramagnetic resonance spectra (X-, Q-, and D-band) of a 2 mM solution of **1**[BF_4] in butyronitrile at 10 K (black: experimental spectra; red; simulations). Magnetic resonance parameters used for the simulations are provided in Table 2.1. The X-band EPR spectrum was recorded in continuous wave (CW) mode; thus, the spectrum represents the first derivative of an absorption spectrum. The Q-band and D-band measurements generated absorption-type spectra, but were pseudomodulated[34] to yield derivative-type spectra. The asterisk marks the EPR signal of an additional paramagnetic species, probably due to decomposition of $\mathbf{1}^+$; see the Experimental Methods for details.

The comparison of X-band spectra recorded in pulsed mode with those recorded in continuous wave (CW) mode revealed no significant difference (after integration of the CW spectrum or pseudomodulation of the pulsed spectra; see Chapter 7, Figure 7.1.4). This assures that the pulsed experiments probe the same molecules as the CW experiments; thus, conclusions drawn from analyses of the pulsed experiments can be transferred to the CW experiments. The relatively long relaxation times at low temperatures ($T < 20$ K) demonstrate that we were observing individual nickel complexes and not multimers/aggregates (see Chapter 7, Figure 7.1.5).

The X-band EPR spectrum of $\mathbf{1}^+$ exhibits higher resolution than those previously reported for $[Ni(P^R_2N^{R'}_2)_2]^+$ complexes $\mathbf{4}^+$ [24] and $\mathbf{5}^+$,[25] indicating it possesses a well-defined geometry even in frozen solution. The complicated X-band EPR spectrum is caused by the substantial anisotropy of the electronic **g** tensor and the hyperfine interaction with the four ^{31}P nuclei ($I = ½$, 100% natural abundance), which is of comparable magnitude to the **g** tensor anisotropy. The pattern indicates that all four phosphorus nuclei are strongly coupled to the unpaired electron, and that the hyperfine interaction contains both significant isotropic and anisotropic parts. Hyperfine interactions with

other magnetic nuclei (^{1}H, ^{14}N, ^{13}C) are not resolved at any of the three microwave frequencies. No hyperfine splitting is expected (or observed) from the nickel center, because the isotopic distribution of nickel is such that ~99% of nickel centers have no nuclear spin ($I = 0$). The **g** tensor anisotropy is not resolved at X-band, but mostly resolved at Q-band and completely resolved at D-band. Thus, the simulation of the Q-band and D-band spectra allowed the unequivocal determination of the electronic **g** tensor, which was used as a constraint for the simulation of the X-band spectrum; its principal values are 2.146(1), 2.063(1), and 2.017(1). The four ^{31}P hyperfine interaction tensors (**A** tensors) were obtained from simulation of X-band and Q-band spectra. These values are set out in Table 2.1. To limit the number of adjustable parameters for the fit of the spectra, the four ^{31}P **A** tensors were assumed to be identical and their principal to be collinear to the principal axes of the **g** tensor as discussed below in the DFT section, the calculated ^{31}P coupling constants show very good agreement with those obtained by fit of the spectra.

Table 2.1. Electron Paramagnetic Resonance Parameters of $[Ni(P^{R}_{2}N^{R'}_{2})_{2}]^{+}$ Complexes.

Complex	Solvent(s)	*g* values (±0.001)	^{31}P hyperfine coupling constant (MHz)	Ref.
1[BF_4]	butyronitrile	2.146, 2.063, 2.017	150, 160, 185[a]	this work
1[BF_4]	MeCN/CH_2Cl_2 (1:2)	2.146, 2.062, 2.017	150, 160, 185[a]	this work
4[BF_4]	toluene/pyridine	2.104, 2.070, 2.006	210, 220, 220[a]	24
5[BF_4]	MeCN (with pyridine)	2.15, 2.07, 2.00[b]	190, 209, 224, 230[c]	25

[a] Principal components of four equivalent ^{31}P hyperfine coupling tensors. [b] **g** Tensor not spectroscopically resolved but obtained by multi-parameter fit of the X-band EPR spectrum, assuming isotropic ^{31}P hyperfine coupling; values ±0.01. [c] Isotropic hyperfine coupling, four non-equivalent ^{31}P nuclei.

The hyperfine coupling constants measured for $\mathbf{1}^{+}$ are clearly different from those reported previously for $\mathbf{4}^{+}$ [24] and $\mathbf{5}^{+}$ [25] (Table 2.1). The *g* values of $\mathbf{1}^{+}$ are different from those of $\mathbf{4}^{+}$. The *g*

values of complex $\mathbf{5}^+$ are rather uncertain, since the authors did not resolve the **g** tensor in their EPR experiments, but obtained it by a multiparameter fit assuming isotropic ^{31}P hyperfine coupling. A clear comparison with the **g** tensor is thus not possible. Possible reasons for the marked sensitivity of the hyperfine couplings of these $[Ni(P^R{}_2N^{R'}{}_2)_2]^+$ complexes to the nature of the R/R′ substituents will be discussed below. The EPR spectra of **1**[BF_4] samples prepared in two different solvents, butyronitrile and 1:2 acetonitrile/dichloromethane, provided virtually identical magnetic resonance parameters (Table 2.1 and Chapter 7, Figure 7.1.6). These results, in combination with the HYSCORE experiment (described below), lead to the conclusion that the solvent molecules do not coordinate to the nickel ion in the Ni(I) oxidation state, and that the geometry of the $\mathbf{1}^+$ ion is essentially independent of the nature of these solvents. This is also supported by DFT calculations, which could not find a stable structure with acetonitrile ligating the Ni(I) ion while maintaining the four Ni-P bonds.

While the simulations of the X- and Q-band spectra nicely reproduce their ^{31}P hyperfine structure, the intensities are not perfectly fit in several parts of the spectrum (Figure 2.3). One possible reason is that the four ^{31}P hyperfine interaction tensors are not identical, both from principal values and principal axes systems with respect to the electronic **g** tensor axes system. This discrepancy could be caused by small distortions of the phosphorus nuclei from a symmetry-equivalent environment (idealized D_2 symmetry for the NiP_4 core). This possibility has been also noted in previous EPR studies of $\mathbf{4}^+$ and $\mathbf{5}^+$, for which the effects are more pronounced.[24-25] For $\mathbf{5}^+$ the simulation of the EPR spectrum yielded four different ^{31}P hyperfine coupling constants, and the gas-phase molecular structure calculated using DFT exhibited inequivalent Ni–P bond distances (d(Ni–P) = 2.22–2.23 Å).[25] It should be noted that for $\mathbf{5}^+$**,** the multi-parameter fit was restricted to isotropic hyperfine coupling. For $\mathbf{1}^+$, the crystal structure provides Ni–P bond

distances that are equivalent and DFT calculations also provide a near idealized-symmetry structure. Small distortions of the compound under the conditions of the EPR experiment might result from geometric variations among the four 6-membered [$NiP^{Cy}CH_2N^{tBu}CH_2P^{Cy}$] rings present within $\mathbf{1}^+$, which then are trapped in the frozen solvent matrix. Consistent with this possibility, two conformations are observed for the free $P^{Cy}{}_2N^{tBu}{}_2$ ligand in solution at room temperature by NMR spectroscopy.[27] DFT calculations on $\mathbf{1}^+$ and $\mathbf{4}^+$ (see below) also point to marked differences between the symmetries and the energetic accessibility of other conformers for these ions.

To gain further insight into the hyperfine couplings with the ligand magnetic nuclei, which are a fingerprint of spin density distribution within the nearest surroundings, we performed pulsed ENDOR experiments at X-band. The contributions to these spectra from the strongly coupled ^{31}P nuclei are expected to lie in the 50–120 MHz frequency range. Accordingly, the ENDOR spectra exhibit several partially overlapping signals in the frequency region between 60 and 110 MHz. These signals show some dependence on the static magnetic field, confirming that all ^{31}P atoms have a considerable anisotropic contribution to the hyperfine interaction tensor (Chapter 7, Figures 7.1.6 and 7.1.7).

The low frequency region of the ENDOR spectra is dominated by signals from ^1H coupled to the unpaired electron spin (Figure 2.4). The ^1H ENDOR spectra show weak orientation dependence, with the largest ^1H hyperfine coupling around 10 MHz. The larger of those couplings are attributed to ^1H nuclei near to the nickel atom, which carries together with the phosphorus atoms the bulk of the spin density. The nearest ^1H nuclei are those of the eight CH_2 groups connecting the phosphine and amine (at distances of 3.813–4.148 Å, based on the crystal structure), and the four ^1H at the α position of the cyclohexyl groups (3.792, 3.796 Å). The rest of the ENDOR lines (hyperfine coupling < 6 MHz) are assigned to distant ^1H nuclei. Considering the

large number of such protons, no reliable analysis is feasible. To determine how solvent ^{1}H contribute to the ENDOR spectra, Davies ENDOR measurements were also performed for samples in fully deuterated and fully protonated $MeCN/CH_2Cl_2$ (1:2) mixtures (Figure 7.1.9). The comparison clearly shows that solvent ^{1}H contribute only to the matrix part of the ENDOR spectra, *i.e.* the spectral region close to the Larmor frequency. That means that they are only weakly dipolar coupled and distant from the paramagnetic center of compound $\mathbf{1}^{+}$.

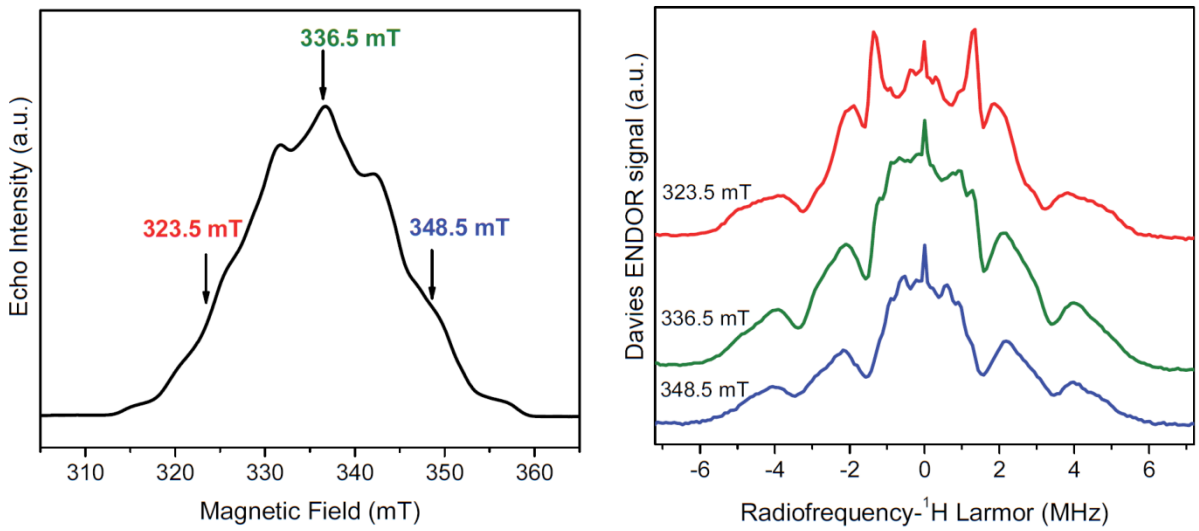

Figure 2.4. Field swept Echo-detected EPR (*left*) and Davies ENDOR spectra (*right*) of **1**[BF_4] in butyronitrile at 15 K. Arrows indicate the positions where ENDOR spectra were detected. For details, see the Experimental Methods.

No clear ENDOR signals attributable to ^{14}N are visible, which is not surprising due to the small hyperfine coupling and quadrupolar nature of this nucleus. To clarify the degree of hyperfine coupling with ^{14}N, we performed a HYSCORE[22, 55] experiment at X-band. An advantage of the HYSCORE experiment compared to ENDOR spectroscopy is its high sensitivity to the nuclei in the (so-called) complete cancelation condition, *i.e.*, when one of the ENDOR transition frequencies is negligibly small. This condition is often fulfilled at X-band for ^{14}N with small hyperfine coupling. The HYSCORE spectrum (Figure 2.5) exhibits typical ^{14}N quadrupole lines in the range 0–5 MHz. Simulation of the HYSCORE spectrum reveals that these lines are due to the relatively

large quadrupole parameter, ($e^2gQ/2h$) ≈ 2.8 MHz, and very small hyperfine coupling, a_{iso} ≈ 0.27 MHz (Chapter 7, Figure 7.1.10). DFT calculations on **1**$^+$ confirm that there is negligible unpaired spin density on the nitrogen nuclei in **1**$^+$ and that the ^{14}N hyperfine couplings are small (A(^{14}N) < 1 MHz; Chapter 7, Table 7.1.8). Signals in the 10–20 MHz range belong to ^{1}H resonances (Larmor frequency of ^{1}H at 350 mT ≈ 14.9 MHz). As for the ENDOR spectra, the HYSCORE spectrum reveals small anisotropy of ^{1}H hyperfine tensors with a maximum hyperfine coupling of about 10 MHz.

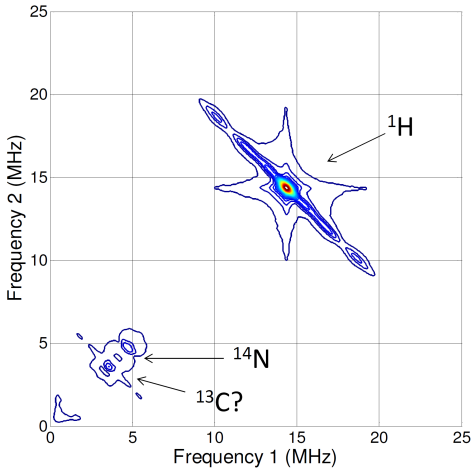

Figure 2.5. X-band HYSCORE spectra of **1**[BF_4] in butyronitrile at 20 K recorded at magnetic field position 336.5 mT. Arrows indicate the group of signals belonging to ^{14}N and ^{1}H nuclei. Signals centered at 3.6 MHz may partially stem from natural abundant ^{13}C (see Chapter 7, Figure 7.1.10).

2.3.3. Density Functional Theory (DFT) Calculations on [Ni($P^R_2N^{R'}_2$)$_2$]$^+$ Complexes.

The EPR spectra of **1**$^+$ and hyperfine coupling constants derived therefrom are distinctly different from those reported previously for the related compounds **4**$^+$ [24] and **5**$^+$.[25] In particular, the spectra for **1**$^+$ are of higher resolution than those of the other compounds, despite the similar conditions employed in their measurement, and the ^{31}P hyperfine coupling constants are considerably smaller (Table 2.1). One possible reason for these differences is that the phosphine R and amine R′ substituents of **4**$^+$ and **5**$^+$ are similar to each other (R = Ph for **4**$^+$ and **5**$^+$, R′ = Ph for **4**$^+$ or substituted

phenyl for $\mathbf{5}^+$; Figure 2.1) but quite different, sterically and electronically, from those of $\mathbf{1}^+$ (R = Cy, R′ = *t*-Bu). In order to probe whether the nature of the ligand substituents could account for the differing experimental observations for these compounds, DFT calculations were performed of the structures and EPR parameters of $\mathbf{1}^+$ and $\mathbf{4}^+$. In addition, we computationally studied compounds $\mathbf{2}^+$ and $\mathbf{3}^+$, in which the R and R′ groups of $\mathbf{1}^+$ and $\mathbf{4}^+$ are permuted (Figure 2.1). Compounds $\mathbf{4}^+$ and $\mathbf{5}^+$ differ only in the nature of the *para* substituent on the amine phenyl group; thus, conclusions regarding the differences between $\mathbf{1}^+$ and $\mathbf{4}^+$ may also apply to differences between $\mathbf{1}^+$ and $\mathbf{5}^+$.

Selected metrical data for the calculated gas-phase structures of $\mathbf{1}^+$, $\mathbf{2}^+$, $\mathbf{3}^+$, and $\mathbf{4}^+$ are set out in Table 2.2; full details are reported in Chapter 7, Tables 7.1.5–13 The conclusion of primary importance from these data is that whereas $\mathbf{1}^+$, $\mathbf{2}^+$, and $\mathbf{3}^+$ are calculated to possess high symmetry structures, the calculations for $\mathbf{4}^+$ provide three structures that are comparatively unsymmetrical. These structures represent discrete minima that lie close within a few kilocalories per mole ($\mathbf{4a}^+$, relative energy = 0 kcal/mol; $\mathbf{4b}^+$, relative energy = +2.7 kcal/mol; $\mathbf{4c}^+$, relative energy = +4.1 kcal/mol). In particular, for $\mathbf{1}^+$, $\mathbf{2}^+$, and $\mathbf{3}^+$, the four Ni–P bonds lengths and two intra-ligand P–Ni–P bond angles are nearly identical for a given compound, yielding structures of approximate D_2 symmetry. For $\mathbf{4}^+$, in contrast, each of the three calculated structures has several different Ni–P bond lengths and P–Ni–P bond angles. The previously reported calculated structure for $\mathbf{5}^+$, which is compositionally similar to $\mathbf{4}^+$, was also noted to have inequivalent Ni–P bond lengths (2.22–2.23 Å).[25] These findings are consistent with the observations, noted in the previous section, that the EPR spectroscopic simulations for $\mathbf{1}^+$ evince a high-symmetry molecular structure about the nickel center, while those for $\mathbf{4}^+$ are consistent with a lower symmetry structure. The EPR spectra of $\mathbf{5}^+$

are qualitatively similar to those of $\mathbf{4}^+$, consistent with it possessing similar structure-controlling R and R′ groups.

Table 2.2. Calculated (DFT) Bond Distances (Å) and Angles (°) for $\mathbf{1}^+$, $\mathbf{2}^+$, $\mathbf{3}^+$, and $\mathbf{4}^+$.[a]

compd	R	R′	*d*(Ni–P)	∠(P–Ni–P)[b]	α[c]	β[d]
$\mathbf{1}^+$	Cy	*t*-Bu	2.225	83.8	69.1	333.7
$\mathbf{2}^+$	Ph	*t*-Bu	2.245	83.1	71.6	334.3
$\mathbf{3}^+$	Cy	Ph	2.229	85.4	60.8	348.7
$\mathbf{4a}^+$[e]	Ph	Ph	2.252, 2.243, 2.243, 2.248	85.0, 84.2	62.4	350.3
$\mathbf{4b}^+$[e]	Ph	Ph	2.275, 2.246, 2.246, 2.275	84.9, 84.9	56.7	354.8
$\mathbf{4c}^+$[e]	Ph	Ph	2.267, 2.240, 2.235, 2.243	85.1, 86.3	59.2	355.0

[a] Only one distance or angle is listed when it applies to all linkages of that type within the compound. [b] Intra-ligand angle. [c] Dihedral angle between inter-ligand P–Ni–P planes. [d] Average sum of three C–N–C angles each for four amine moieties. [e] These structures represent discrete energy minima (kcal/mol): $\mathbf{4a}^+$, 0; $\mathbf{4b}^+$, +2.7; $\mathbf{4c}^+$, +4.1. Energy differences and energetic ordering depending on the functional and basis set.

Pairwise comparisons among the metrical data for these compounds allow the structural consequences of their R and R′ groups to be elucidated. Compounds $\mathbf{1}^+$ and $\mathbf{3}^+$ possess the same phosphine R group (Cy) but differ in their second-coordination sphere amine R′ groups ($\mathbf{1}^+$, *t*-Bu; $\mathbf{3}^+$, Ph). The change in the remote substituent has consequences both for the structure about the amine and for the NiP_4 core. Compared to $\mathbf{1}^+$, the geometries of the amine moieties of $\mathbf{3}^+$ are closer to planar, with the sum of their C–N–C angles *(β)* being larger by 15° ($\mathbf{3}^+$, 348.7˚; $\mathbf{1}^+$, 333.7˚) and the angle within the CH_2–N–CH_2 tether increasing from 111.2˚ ($\mathbf{1}^+$) to 114.8˚ ($\mathbf{3}^+$). These structural differences affect the geometry about the nickel center, as evidenced by the fact that $\mathbf{3}^+$ exhibits a larger P–Ni–P bite angle (85.4˚) than that calculated for $\mathbf{1}^+$ (83.8˚) and, strikingly, by the inter-ligand dihedral angle (α*),* which is notably smaller for $\mathbf{3}^+$ (60.8˚) than for $\mathbf{1}^+$ (69.1˚) despite their

identical phosphine R groups. The Ni–P bond lengths are not significantly impacted by the change in R′. A similar comparison of the calculated structures for $\mathbf{1}^+$ and $\mathbf{2}^+$ reveals the consequences of changing the phosphine R substituent from Cy to Ph while keeping the amine R′ substituent constant (*t*-Bu). Unsurprisingly, this first-coordination sphere substitution affects the calculated Ni–P bond lengths, with those for $\mathbf{2}^+$ (2.245 Å) being slightly longer than those for $\mathbf{1}^+$ (2.225 Å). However, by most other metrics, the overall molecular structure is *less* perturbed by this substitution in R than by the R′ variation between $\mathbf{1}^+$ and $\mathbf{3}^+$. Specifically, $\mathbf{1}^+$ and $\mathbf{2}^+$ exhibit more closely similar P–Ni–P bite angles (83.8˚ and 83.1˚, respectively), inter-ligand dihedral angles α (69.1˚ and 71.6˚) and amine bond-angle sums β (333.7˚ and 334.3˚) than do $\mathbf{1}^+$ and $\mathbf{3}^+$. These group-specific structural perturbations carry over to $\mathbf{4}^+$, which possesses the same phosphine R group as $\mathbf{2}^+$ and amine R′ group as $\mathbf{3}^+$. Compared to $\mathbf{1}^+$, $\mathbf{4a}^+$ exhibits the longer R-controlled Ni–P distances found for $\mathbf{2}^+$, and variations in the R′-controlled P–Ni–P, α, and β angles that are similar to those for $\mathbf{3}^+$. However, the combination in $\mathbf{4}^+$ of these R and R′ structural perturbations results in conformational strains within the $P^R{}_2N^{R'}{}_2$ ligands that cannot be accommodated by a high-symmetry structure of the types observed for $\mathbf{1}^+$, $\mathbf{2}^+$, and $\mathbf{3}^+$, as manifested by the observation of marked inequivalences among its chemically related bond distances and angles and three computed close-lying structural local minima.

In addition to the different molecular symmetries found for $\mathbf{1}^+$ and $\mathbf{4}^+$, the calculated magnetic parameters of these ions also differ significantly from each other. These results are set out in Table 2.3, in which phosphorus hyperfine couplings are given as principal values A_X, A_Y, and A_Z to allow a better comparison to the experimental values. The orientations of the principal axes have been provided in Chapter 7. For $\mathbf{1}^+$, the calculated *g*-values and ^{31}P hyperfine coupling constants are seen to be in good agreement with those observed experimentally. Inasmuch as the

experimental magnetic parameters of $\mathbf{1}^+$ are derived from well-resolved EPR spectra, this level of agreement suggests that the computational methodology is adequate to predict trends in magnetic parameters as a function of ligand substituent and geometry.

Table 2.3. Calculated (DFT) and Experimental EPR Parameters for $[Ni(P^R{}_2N^{R'}{}_2)_2]^+$ Complexes

	g-values		^{31}P hyperfine coupling constant (MHz)	
compd	calcd	exptl	calcd	exptl
$\mathbf{1}^+$	2.1613, 2.0636, 2.0454	2.146, 2.063, 2.017	154, 160, 203	150, 160, 185
$\mathbf{2}^+$	2.1897, 2.0804, 2.0610	n.a.	142, 148, 185	n.a.
$\mathbf{3}^+$	2.1385, 2.0519, 2.0398	n.a.	170, 178, 224	n.a.
$\mathbf{4}^+$	n.a.	2.104, 2.070, 2.006	n.a.	210, 220, 220
$\mathbf{4a}^{+\,a}$	2.1607, 2.0651, 2.0469	n.a.	173, 180, 221 166, 172, 215 161, 168, 209 159, 166, 206	n.a.
$\mathbf{4b}^{+\,b}$	2.1478, 2.0600, 2.0490	n.a.	199, 204, 238 178, 183, 229	n.a.
$\mathbf{4c}^{+\,a}$	2.1443, 2.0596, 2.0470	n.a.	177, 184, 226 192, 198, 242 190, 196, 235 172, 176, 211	n.a.

[a] Four structurally inequivalent phosphorus nuclei; see Table 2.2. [b] Two pairs of structurally inequivalent phosphorus nuclei; see Table 2.2.

The phosphorus hyperfine coupling constants of $\mathbf{1}^+$ are considerably smaller than those for $\mathbf{4}^+$. Because the three calculated structures of $\mathbf{4}^+$ are of low symmetry, multiple hyperfine coupling constants are provided for each chemically distinct phosphorus nucleus. Although this prevents direct comparison to the experimental values, simple averaging indicates that the calculated values for $\mathbf{4}^+$ are larger than those calculated for $\mathbf{1}^+$, in line with experimental observations for the two compounds. It is also striking how different the hyperfine coupling constants are for a given conformer of $\mathbf{4}^+$, and the significant differences of the values of $\mathbf{1}^+$ and $\mathbf{4}^+$ from those of their R/R′-permuted analogues $\mathbf{2}^+$ and $\mathbf{3}^+$. This highlights both the high sensitivity of these values to structural

perturbations and the challenges associated with elucidating them from experiment, especially in frozen solutions in which multiple conformers may be found even for "symmetric" compounds.

The smaller ^{31}P hyperfine coupling constants of $\mathbf{1}^+$ relative to $\mathbf{4}^+$ and $\mathbf{5}^+$ indicate that there are differences in the delocalization onto the ligands of the unpaired spin. The calculated spin densities for $\mathbf{1}^+$ and $\mathbf{4}^+$ are shown in Figure 2.6. It is apparent that, for both, the primary location of electron spin density is on the nickel atom and the four attached phosphorus atoms. Complex $\mathbf{1}^+$ has 75.8% of the Mulliken spin density located on nickel with the four phosphorus atoms having nearly equivalent percentages of 4.6 each for a total of 18.4%. The remaining amount is distributed over the ligand with no single atom having greater than 0.7%. For $\mathbf{4}^+$, the Mulliken spin density is on average 74.4% (**4a**$^+$, 76.2%; **4b**$^+$, 73.9%; **4c**$^+$, 73.2%) on nickel and 19.7% (**4a**$^+$, 19.6%; **4b**$^+$, 19.8%; **4c**$^+$, 19.7%) on the phosphorus. Qualitatively, the increased spin density on the phosphorus atoms for $\mathbf{4}^+$ as compared to $\mathbf{1}^+$ is consistent with the larger hyperfine coupling constant for the former. The increased phosphorus spin density is also qualitatively consistent with the fact that the phosphine R group of $\mathbf{4}^+$ (Ph) is electron withdrawing relative to that of $\mathbf{1}^+$ (Cy), as manifested broadly among metal–phosphine compounds through the stronger π back-bonding to aryl phosphines than to alkyl phosphines.[56] In the present case, however, the precise contribution of the electron-withdrawing nature of the R group on the phosphorus spin densities is difficult to disentangle from geometric factors, which include the pronounced differences in R′-controlled bond and dihedral angles between $\mathbf{1}^+$ and $\mathbf{4}^+$.

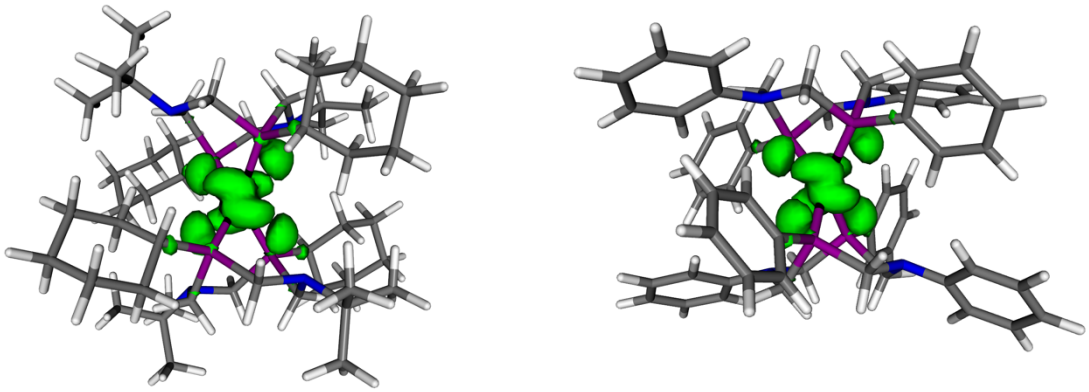

1^{+} **4b**$^{+}$

Figure 2.6. Calculated electron spin densities for complexes **1**$^{+}$ and **4b**$^{+}$ at the 0.002 e/a_0^3 isosurface level. Note that spin density distributions for all **4**$^{+}$ structures look identical. Additional views at smaller isosurface levels are shown in Chapter 7 (Figures 7.1.11–12)

2.4. Conclusions

Crystallographic, DFT computational, and multi-frequency EPR spectroscopic studies of the hydrogen-oxidation catalyst $[Ni(P^{Cy}_2N^{tBu}_2)_2]^+$ (**1**$^{+}$) have provided a number of insights into its intrinsic properties and how these differ from those of previously studied proton-reduction catalysts of the broader $[Ni(P^{R}_2N^{R'}_2)_2]^{n+}$ family. The EPR and ENDOR spectra allowed determination of the electronic **g** tensor and the ^{31}P hyperfine coupling constants, and together with HYSCORE experiments demonstrated that the hyperfine couplings of the ^{1}H and ^{14}N nuclei to the unpaired spin are intermediate and weak, respectively. The EPR spectroscopic data do not exhibit evidence of coordination to the Ni(I) center by the potentially ligating solvents acetonitrile and butyronitrile. The EPR spectra observed for **1**$^{+}$ are of higher resolution and evince a higher symmetry molecular geometry than those reported previously for $Ni(P^{Ph}_2N^{Ph}_2)_2]^+$ (**4**$^{+}$) and $Ni(P^{Ph}_2N^{Ar'}_2)_2]^+$ (**5**$^{+}$). Consistent with this, crystallographic and DFT computational studies of **1**$^{+}$ demonstrate that the NiP_4 core structure is highly symmetric in the solid state and gas phase, respectively. In contrast, the proton-reduction catalyst $[Ni(P^{Ph}_2N^{Ph}_2)_2]^+$ (**4**$^{+}$) is calculated to possess three less symmetrical conformers that are separated in energy by only a few kilocalories per mole.

The distorted structure found for $\mathbf{4}^{+}$ results from a combination of specific R and R′-controlled geometric perturbations, as deduced from the calculated structures of the R/R′-permuted analogues $[Ni(P^{Ph}{}_2N^{tBu}{}_2)_2]^{+}$ ($\mathbf{2}^{+}$) and $[Ni(P^{Cy}{}_2N^{Ph}{}_2)_2]^{+}$ ($\mathbf{3}^{+}$). It is especially noteworthy that, with the exception of the Ni–P bond length, the structural consequences of the remote R′ amine substituent exceed those of the first-coordination-sphere phosphine R substituent, and that both substituents are calculated to have profound effects on the ^{31}P hyperfine coupling constant. The larger ^{31}P hyperfine coupling constants observed for $\mathbf{4}^{+}$ relative to $\mathbf{1}^{+}$ reflect greater spin density delocalization onto the ligands, as supported by DFT calculations.

These results raise the question of whether the molecular and electronic structures of $[Ni(P^{R}{}_2N^{R'}{}_2)_2]^{+}$ complexes are generally as strongly dependent on the nature of the remote amine R′ group as they are upon the first-coordination-sphere R phosphine group, as found here for $\mathbf{1}^{+}$ and $\mathbf{4}^{+}$. The combined experimental approaches described in this report appear suitable to shed light on both on this question and the extent to which these effects influence the catalytic activity of this important class of catalysts.

2.5. Acknowledgements

EPR spectroscopy was performed and analyzed by Dr. Oleg Poluektov and Dr. Jens Niklas at Argonne National Laboratory and DFT calculations were performed by Prof. Kristy Mardis and students Tiara Brown and Anthony Pitts-McCoy of Chicago State University. The crystal structure of $\mathbf{1}^{+}$ was determined by Dr. Ian Steele and Dr. Alex Filatov.

2.6. References

1. Cook, T. R.; Dogutan, D. K.; Reece, S. Y.; Surendranath, Y.; Teets, T. S.; Nocera, D. G. Solar Energy Supply and Storage for the Legacy and Non Legacy Worlds. *Chem. Rev.* **2010**, *110*, 6474-6502.

2. Lewis, N. S.; Nocera, D. G. Powering the Planet: Chemical Challenges in Solar Energy Utilization. *Proc. Natl. Acad. Sci. U. S. A.* **2006**, *103*, 15729-15735.

3. Balzani, V.; Credi, A.; Venturi, M. Photochemical Conversion of Solar Energy. *ChemSusChem* **2008**, *1*, 26-58.

4. Simmons, T. R.; Artero, V. Catalytic Hydrogen Oxidation: Dawn of a New Iron Age. *Angew. Chem., Int. Ed.* **2013**, *52*, 6143-6145.

5. Eckenhoff, W. T.; McNamara, W. R.; Du, P. W.; Eisenberg, R. Cobalt Complexes as Artificial Hydrogenases for the Reductive Side of Water Splitting. *Biochim. Biophys. Acta-Bioenerg.* **2013**, *1827*, 958-973.

6. Eckenhoff, W. T.; Eisenberg, R. Molecular Systems for Light Driven Hydrogen Production. *Dalton Trans.* **2012**, *41*, 13004-13021.

7. Carroll, M. E.; Barton, B. E.; Rauchfuss, T. B.; Carroll, P. J. Synthetic Models for the Active Site of the FeFe -Hydrogenase: Catalytic Proton Reduction and the Structure of the Doubly Protonated Intermediate. *J. Am. Chem. Soc.* **2012**, *134*, 18843-18852.

8. DuBois, D. L. Development of Molecular Electrocatalysts for Energy Storage. *Inorg. Chem.* **2014**, *53*, 3935-3960.

9. Gloaguen, F.; Rauchfuss, T. B. Small Molecule Mimics of Hydrogenases: Hydrides and Redox. *Chem. Soc. Rev.* **2009**, *38*, 100-108.

10. McKone, J. R.; Marinescu, S. C.; Brunschwig, B. S.; Winkler, J. R.; Gray, H. B. Earth-Abundant Hydrogen Evolution Electrocatalysts. *Chem. Sci.* **2014**, *5*, 865-878.

11. Shaw, W. J.; Helm, M. L.; DuBois, D. L. A Modular, Energy-Based Approach to the Development of Nickel Containing Molecular Electrocatalysts for Hydrogen Production and Oxidation. *Biochim. Biophys. Acta-Bioenerg.* **2013**, *1827*, 1123-1139.

12. Bullock, R. M.; Appel, A. M.; Helm, M. L. Production of Hydrogen by Electrocatalysis: Making the H-H Bond by Combining Protons and Hydrides. *Chem. Commun.* **2014**, *50*, 3125-3143.

13. DuBois, D. L.; Bullock, R. M. Molecular Electrocatalysts for the Oxidation of Hydrogen and the Production of Hydrogen - The Role of Pendant Amines as Proton Relays. *Eur. J. Inorg. Chem.* **2011**, 1017-1027.

14. DuBois, M. R.; DuBois, D. L. Development of Molecular Electrocatalysts for CO_2 Reduction and H_2 Production/Oxidation. *Acc. Chem. Res.* **2009**, *42*, 1974-1982.

15. O'Hagan, M.; Ho, M. H.; Yang, J. Y.; Appel, A. M.; DuBois, M. R.; Raugei, S.; Shaw, W. J.; DuBois, D. L.; Bullock, R. M. Proton Delivery and Removal in $[Ni(P^R_2N^{R'}_2)_2]^{2+}$ Hydrogen Production and Oxidation Catalysts. *J. Am. Chem. Soc.* **2012**, *134*, 19409-19424.

16. O'Hagan, M.; Shaw, W. J.; Raugei, S.; Chen, S. T.; Yang, J. Y.; Kilgore, U. J.; DuBois, D. L.; Bullock, R. M. Moving Protons with Pendant Amines: Proton Mobility in a Nickel Catalyst for Oxidation of Hydrogen. *J. Am. Chem. Soc.* **2011**, *133*, 14301-14312.

17. Raugei, S.; Chen, S. T.; Ho, M. H.; Ginovska-Pangovska, B.; Rousseau, R. J.; Dupuis, M.; DuBois, D. L.; Bullock, R. M. The Role of Pendant Amines in the Breaking and Forming of Molecular Hydrogen Catalyzed by Nickel Complexes. *Chem.–Eur. J.* **2012**, *18*, 6493-6506.

18. Yang, J. Y.; Smith, S. E.; Liu, T.; Dougherty, W. G.; Hoffert, W. A.; Kassel, W. S.; DuBois, M. R.; DuBois, D. L.; Bullock, R. M. Two Pathways for Electrocatalytic Oxidation of Hydrogen by a Nickel Bis(diphosphine) Complex with Pendant Amines in the Second Coordination Sphere. *J. Am. Chem. Soc.* **2013**, *135*, 9700-9712.

19. Chen, S. T.; Ho, M. H.; Bullock, R. M.; DuBois, D. L.; Dupuis, M.; Rousseau, R.; Raugei, S. Computing Free Energy Landscapes: Application to Ni-based Electrocatalysts with Pendant Amines for H_2 Production and Oxidation. *ACS Catal.* **2014**, *4*, 229-242.

20. Bencini, A.; Gatteschi, D., *EPR of Exchange Coupled Systems*. Springer-Verlag: Berlin, 1990.

21. Abragam, A.; Bleaney, B., *Electron Paramagnetic Resonance of Transition Ions*. Dover: New York, 1986; p 944.

22. Schweiger, A.; Jeschke, G., *Principles of Pulse Electron Paramagnetic Resonance*. Oxford University Press: New York, 2001.

23. Pilbrow, J. R., *Transition Ion Electron Paramagnetic Resonance*. Clarendon Press: New York, 1991; p 738.

24. Silver, S. C.; Niklas, J.; Du, P. W.; Poluektov, O. G.; Tiede, D. M.; Utschig, L. M. Protein Delivery of a Ni Catalyst to Photosystem I for Light-Driven Hydrogen Production. *J. Am. Chem. Soc.* **2013**, *135*, 13246-13249.

25. Kochem, A.; Neese, F.; van Gastel, M. Spectroscopic and Quantum Chemical Study of the $Ni(P^{Ph}{}_2N^{C6H4CH2P(O)(OEt)2}{}_2)_2$ Electrocatalyst for Hydrogen Production with Emphasis on the Ni-I Oxidation State. *J. Phys. Chem. C* **2014**, *118*, 2350-2360.

26. Kochem, A.; Weyhermüller, T.; Neese, F.; van Gastel, M. EPR and Quantum Chemical Investigation of a Bioinspired Hydrogenase Model with a Redox-Active Ligand in the First Coordination Sphere. *Organometallics* **2015**, *34*, 995-1000.

27. Yang, J. Y.; Chen, S. T.; Dougherty, W. G.; Kassel, W. S.; Bullock, R. M.; DuBois, D. L.; Raugei, S.; Rousseau, R.; Dupuis, M.; DuBois, M. R. Hydrogen Oxidation Catalysis by a Nickel Diphosphine Complex with Pendant tert-Butyl Amines. *Chem. Commun.* **2010**, *46*, 8618-8620.

28. Stolley, R. M.; Darmon, J. M.; Helm, M. L. Solvent and Electrolyte Effects on $Ni(P^R{}_2N^{R'}{}_2)_2$-Catalyzed Electrochemical Oxidation of Hydrogen. *Chem. Commun.* **2014**, *50*, 3681-3684.

29. Pangborn, A. B.; Giardello, M. A.; Grubbs, R. H.; Rosen, R. K.; Timmers, F. J. Safe and Convenient Procedure for Solvent Purification. *Organometallics* **1996**, *15*, 1518-1520.

30. Fulmer, G. R.; Miller, A. J. M.; Sherden, N. H.; Gottlieb, H. E.; Nudelman, A.; Stoltz, B. M.; Bercaw, J. E.; Goldberg, K. I. NMR Chemical Shifts of Trace Impurities: Common Laboratory Solvents, Organics, and Gases in Deuterated Solvents Relevant to the Organometallic Chemist. *Organometallics* **2010**, *29*, 2176-2179.

31. Davies, E. R. A New Pulse ENDOR Technique. *Phys. Lett. A* **1974**, *47*, 1-2.

32. Gemperle, C.; Schweiger, A. Pulsed Electron-Nuclear Double Resonance Methodology. *Chem. Rev.* **1991**, *91*, 1481-1505.

33. Mims, W. B. Pulsed ENDOR Experiments. *Proc. R. Soc. London, A* **1965**, *283*, 452-457.

34. Hyde, J. S.; Pasenkiewicz-Gierula, M.; Jesmanowicz, A.; Antholine, W. E. Pseudo Field Modulation in EPR Spectroscopy. *Appl. Magn. Reson.* **1990**, *1*, 483-496.

35. Poluektov, O. G.; Utschig, L. M.; Schlesselman, S. L.; Lakshmi, K. V.; Brudvig, G. W.; Kothe, G.; Thurnauer, M. C. Electronic Structure of the P-700 Special Pair from High-Frequency Electron Paramagnetic Resonance Spectroscopy. *J. Phys. Chem. B* **2002**, *106*, 8911-8916.

36. Bresgunov, A. Y.; Dubinskii, A. A.; Krimov, V. N.; Petrov, Y. G.; Poluektov, O. G.; Lebedev, Y. S. Pulsed EPR in 2mm Band. *Appl. Magn. Reson.* **1991**, *2*, 715-728.

37. Epel, B.; Gromov, I.; Stoll, S.; Schweiger, A.; Goldfarb, D. Spectrometer manager: A Versatile Control Software for Pulse EPR Spectrometers. *Concepts Magn. Reson. B* **2005**, *26*, 36-45.

38. Niklas, J.; Mardis, K. L.; Rakhimov, R. R.; Mulfort, K. L.; Tiede, D. M.; Poluektov, O. G. The Hydrogen Catalyst Cobaloxime: A Multifrequency EPR and DFT Study of Cobaloxime's Electronic Structure. *J. Phys. Chem. B* **2012**, *116*, 2943-2957.

39. Stoll, S.; Schweiger, A. EasySpin, A Comprehensive Software Package for Spectral Simulation and Analysis in EPR. *J. Magn. Reson.* **2006**, *178*, 42-55.

40. Baker, J.; Wolinski, K.; Malagoli, M.; Kinghorn, D.; Wolinski, P.; Magyarfalvi, G.; Saebo, S.; Janowski, T.; Pulay, P. Software News and Update Quantum Chemistry in Parallel with PQS. *J. Comput. Chem.* **2009**, *30*, 317-335.

41. Neese, F. The ORCA Program System. *WIREs Comput. Mol. Sci.* **2012**, *2*, 73-78.

42. Neese, F. Prediction of Electron Paramagnetic Resonance G Values Using Coupled Perturbed Hartree-Fock and Kohn-Sham Theory. *J. Chem. Phys.* **2001**, *115*, 11080-11096.

43. Stephens, P. J.; Devlin, F. J.; Chabalowski, C. F.; Frisch, M. J. Ab-Initio Calculation of Vibrational Absorption and Circular-Dichroism Spectra Using Density-Functional Force-Fields. *J. Phys. Chem.* **1994**, *98*, 11623-11627.

44. Becke, A. D. Density-Functional Thermochemistry 3. The Role of Exact Exchange. *J. Chem. Phys.* **1993**, *98*, 5648-5652.

45. Lee, C. T.; Yang, W. T.; Parr, R. G. Development of the Colle-Salvetti Correlation-Energy Formula into a Functional of the Electron-Density. *Phys. Rev. B: Condens. Matter* **1988**, *37*, 785-789.

46. Vosko, S. H.; Wilk, L.; Nusair, M. Accurate Spin-Dependent Electron Liquid Correlation Energies for Local Spin-Density Calculations - a Critical Analysis. *Can. J. Phys.* **1980**, *58*, 1200-1211.

47. Rega, N.; Cossi, M.; Barone, V. Development and Validation of Reliable Quantum Mechanical Approaches for the Sudy of Free Radicals in Solution. *J. Chem. Phys.* **1996**, *105*, 11060-11067.

48. Barone, V. In *Recent Advances in Density Functional Methods (Part 1)*, Chong, D. P., Ed. World Scientific: Singapore, 1995; pp 287-334.

49. Kutzelnigg, W.; Fleischer, U.; Schindler, M. In *Deuterium and Shift Calculation*, Diehl, P., Fluck, E., Günther, H., Kosfeld, R., Seelig, J., Eds. Springer-Verlag: Berlin, 1990; Vol. 23.

50. Wachters, A. J. H. Gaussian Basis Set for Molecular Wavefunctions Containing Third-Row Atoms. *J. Chem. Phys.* **1970**, *52*, 1033-1036.

51. Wachters, A. J. H., *IBM Technical Report RJ.* 584; San Jose, CA, 1969.

52. Bauschlicher, C. W.; Langhoff, S. R.; Partridge, H.; Barnes, L. A. Theoretical-Studies of the 1st-Row and 2nd-Row Transition-Metal Methyls and Their Positive-Ions. *J. Chem. Phys.* **1989**, *91*, 2399-2411.

53. Weigend, F.; Ahlrichs, R. Balanced Basis Sets of Split Valence, Triple Zeta Valence and Quadruple Zeta Valence Quality for H to Rn: Design and Assessment of Accuracy. *Phys. Chem. Chem. Phys.* **2005**, *7*, 3297-3305.

54. Wiedner, E. S.; Yang, J. Y.; Chen, S. T.; Raugei, S.; Dougherty, W. G.; Kassel, W. S.; Helm, M. L.; Bullock, R. M.; DuBois, M. R.; DuBois, D. L. Stabilization of Nickel Complexes with Ni-0・・・H-N Bonding Interactions Using Sterically Demanding Cyclic Diphosphine Ligands. *Organometallics* **2012**, *31*, 144-156.

55. Höfer, P.; Grupp, A.; Nebenfuhr, H.; Mehring, M. Hyperfine Sublevel Correlation (Hyscore) Spectroscopy - A 2D Electron-Spin-Resonance Investigation of the Squaric Acid Radical. *Chem. Phys. Lett.* **1986**, *132*, 279-282.

56. Hartwig, J. F., *Organotransition Metal Chemistry*. University Science Books: Mill Valley, California, 2010; p 36-37.

CHAPTER 3: Driving Catalytic Hydrogen Oxidation with Light

3.1. Introduction

The environmental impact of mankind's continued reliance upon fossil fuels compels the enhanced utilization of renewable, carbon-neutral fuels.[1] However, the intermittent nature of the most plentiful renewable energy sources requires subsequent conversion to a form easily stored and transported, such as chemical energy in a fuel.[2] One of the most viable and heavily researched such fuels is hydrogen.[3-4] On demand, the chemical energy contained in hydrogen can be converted to electrical power by oxidation to generate electrons and protons, producing no greenhouse gases.[5-7] However, there are three major impediments to the large-scale implementation of a "hydrogen economy". First, H_2 is currently produced in massive quantities through steam-reformation of natural gas,[8] a process that is both non-renewable and energy-intensive. This hurdle can be overcome through eventual application of our ever-advancing knowledge of solar-driven water splitting, which has the potential to yield an implementable, and carbon-neutral, source of renewable H_2 in the future.[9-11] Second, the most active catalyst known for hydrogen oxidation is platinum,[12] which is limited in its application by its expense and rarity. Because of this, the advancement of an efficient, inexpensive catalyst for this process is a long-standing hurdle to the global-scale utilization of H_2 as a fuel-source. Third, H_2 is a gas at atmospheric temperatures and pressures and as such is both less energy-dense and more difficult to store and transport than liquid fuels.[13]

The difficulty posed by H_2 storage and transportation can be overcome by its utilization in an artificial photosynthetic system for the production of C-based fuels.[14-15] Artificial photosynthesis requires integration of both an oxidative and a reductive catalytic process.[16] Because of the intrinsic difficulties associated with this integration, especially that arising from

the facility of unproductive back-electron transfer between the two catalysts, work has generally focused on using light to drive a single catalytic process, such as CO_2 or proton reduction, with the other catalytic cycle being replaced by stoichiometric sacrificial reagents that suppress back electron transfer by decomposing upon oxidation. Although these are valuable as proof-of-concept experiments, the replacement of the second catalytic cycle with stoichiometrically consumed fine chemicals prevents these systems from being renewable, energy storing, and implementable. If photocatalytic hydrogen oxidation can be demonstrated and incorporated as an oxidative half-reaction, it would enable typical sacrificial electron donors to be replaced and renewable, energy-storing reactions to be driven. Previous work in our group[15] has demonstrated that the dual electron-transfer sensitization of catalysts for the energy-storing reverse-water-gas-shift reaction (RWGS: $CO_2 + H_2 \rightarrow CO + H_2O$) can be driven photochemically, which is a prerequisite for successfully marrying two renewable half-reactions (H_2 oxidation and CO_2 reduction) into one artificial photosynthetic process.[15] With this now demonstrated, the next major obstacle to the development of artificial photosynthetic systems featuring H_2 oxidation is that photocatalytic H_2 oxidation has not been demonstrated with any molecular catalyst. The only prior example of this general approach is heterogeneous, involving photodriven H_2 oxidation on Pt.[17]

In recent years much has been accomplished in the rational development of earth-abundant metal catalysts for the oxidation of H_2. Work by DuBois, Bullock, Shaw and co-workers[18-22] has led to the development of efficient molecular catalysts for hydrogen oxidation and production that feature nickel and iron. Taking cues from the active site structure of hydrogenase enzymes,[23] researchers have incorporated biomimetic motifs into catalyst design.[21] Among the most promising of the catalysts developed are nickel–phosphine complexes of general form $Ni(P^R_2N^{R'}_2)_2^{n+}$, where $P^R_2N^{R'}_2$ (1,5-di(R)-3,7-di(R′)-1,5-diaza-3,7-diphosphacyclooctane) is an heterocyclic diphosphine

ligand featuring two functionalized, non-coordinating pendant amines (Figure 3.1).[18, 24-26] As in hydrogenase, these amines aid catalysis by assisting in the binding and cleaving of hydrogen and in the movement of protons to and from the nickel center. Usefully, the catalytic behavior of these compounds is tunable through varying the substituent groups (R and R′). Altering the amine R′ substituent primarily affects the basicity of the pendant amine and changing the phosphine R group affects the Ni–P bond distance and the redox properties of the Ni center, impacting the hydride acceptor ability of the compound.[27-28] The structural and electronic effects of these variations were described in Chapter 2.

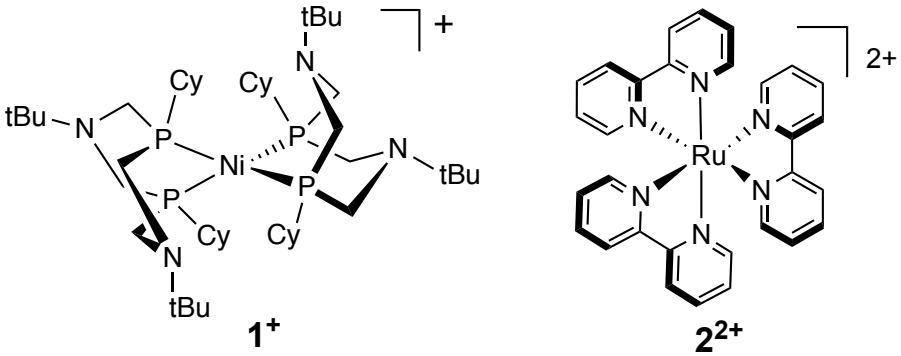

Figure 3.1. (*Left*) The primary $Ni(P^{R}_2N^{R'}_2)_2^{+}$ compound discussed in this chapter (R = cyclohexyl and R′ = *tert*-butyl). (*Right*) The chromophore $Ru(bpy)_3^{2+}$ used for demonstrating photocatalytic H_2 oxidation.

Whereas there have been many recent reports of photocatalytic H_2 production with $Ni(P^{R}_2N^{R'}_2)_2^{n+}$ catalysts, there have been no corresponding reports of light-driven H_2 *oxidation* by these or other molecular catalysts. The aggregated H_2 production findings detail sensitization by homogeneous organometallic chromophores,[29-30] organic dyes,[29, 31] nanoparticles,[32-33] proteins,[34] and in a supramolecular system,[35] among others,[36-39] demonstrating the versatility of $Ni(P^{R}_2N^{R'}_2)_2^{n+}$ compounds for photochemical applications. The compound studied in this chapter, $Ni(P^{Cy}_2N^{tBu}_2)_2^{+}$ (**1**$^{+}$; Figure 3.1), possesses one of the highest rates for molecular H_2 oxidation electrocatalysis and is particularly amenable to use as a photocatalyst because of the large thermodynamic driving force for H_2 binding in the Ni(II) state (ΔG = –33 kJ mol^{-1}).[21, 24] This

increases the probability that the photogenerated Ni(II) will be irreversibly trapped by H_2 binding before back-electron-transfer.

In this chapter we detail the light-driven catalytic oxidation of H_2 by a molecular nickel catalyst. To the best of our knowledge this is the first demonstration of homogenous photocatalytic H_2 oxidation, a fundamental step towards the utilization of hydrogen-sourced reducing equivalents for solar-fuel generation.

3.2. Experimental

For complete information regarding photochemical and characterization methods please refer to Chapter 7.2.

Materials. Acetonitrile, diethyl ether, and pentane were HPLC grade and purified by passage under nitrogen pressure through an anaerobic, stainless-steel system consisting of either two 4.5 in. × 24 in. (1 gal) columns of activated A2 alumina (CH_3CN and Et_2O) or one column of activated A2 alumina and one column of activated BASF R3-11 catalyst (pentane).[40] Benzonitrile (HPLC grade; Sigma-Aldrich) and C_6D_6 (Cambridge Isotope Laboratories) were stored over activated 4A sieves under nitrogen. CD_3CN (Cambridge Isotope Laboratories) was stored over activated 3A sieves under nitrogen. Hydrogen (99.9999%, Airgas) was used without further purification. Pyrrolidine (≥99.5%, Aldrich) was stored under nitrogen and used without further purification. The compounds $[Ni(P^{Cy}_2N^{tBu}_2)_2][BF_4]_2$ (**1**$[BF_4]_2$**)** and $Ni(P^{Cy}_2N^{tBu}_2)_2$ (**1**) were synthesized by standard procedures.[25] $[Ni(P^{Cy}_2N^{tBu}_2)_2][BF_4]$ (**1**$[BF_4]$) was prepared by an alternate route[41] to the original synthesis.[24] $[Ru(bpy)_3][PF_6]_2$ (**2**$[PF_6]_2$; Aldrich, 97%) was recrystallized from hot ethanol and dried under vacuum at 100 °C for at least 24 h. Ferrocene, and $[NBu^n_4][PF_6]$ were recrystallized twice from ethanol and dried for a minimum of 18 h under vacuum at 120 °C

before use. All other reagents and solvents were obtained from commercial sources and used as received.

Preparation of [Ni(H)($P^{Cy}_2N^{tBu}_2$)$_2$][BF_4] (1H[BF_4]). The *in situ* (solution) preparation and $^{31}P\{^1H\}$ NMR spectrum of this compound have been reported,[24] but it has not been previously isolated and characterized. To a stirred, faint-yellow solution of **1** (0.098 g, 0.107 mmol) in Et_2O (10 mL) at room temperature was quickly added HBF_4 (51–57 wt% in Et_2O, Aldrich; 10 μL, 0.077 mmol assuming 57 wt%), which resulted in the immediate precipitation of a bright yellow solid. After 1 h, the yellow powder was collected by filtration, washed with Et_2O, and then dried under vacuum to yield 0.055 g of **1H**[BF_4] (69% yield). The compound is stable in the solid state at −50 °C but thermally degrades in solution at room temperature over several days; other [Ni(H)($P^R_2N^{R'}_2$)$_2$]$^+$ compounds have also been reported to be thermally unstable in solution.[42] ^1H NMR (CD_3CN, 400 MHz, Figures 7.2.2–3): δ 2.99 (d, J_{HH} = 12.3 Hz, 8H, –PC*H*$_2$N–), 2.74 (d, J_{HH} = 12.2 Hz, 8H, –PC*H*$_2$N–), 1.89 (br m, 7H, cyclohexyl), 1.83 (br m, 7H, cyclohexyl), 1.72 (br s, 14H, cyclohexyl), 1.30 (br s, 24H, cyclohexyl), 1.14 (s, 36H, *tert*-butyl), −10.80 (quin, J_{PH} = 22.3 Hz, 1H, Ni–*H*). $^{31}P\{^1H\}$ (CD_3CN, Figure 7.2.4): δ 12.14 (s). $^{31}P\{^1H\}$ (PhCN): δ 12.6 (s) Prior *in situ* literature values: ^1H NMR (PhCN, buffered): δ −13.5 (br s); $^{31}P\{^1H\}$ (PhCN, buffered): δ 13.0 (s).[24]

Electrochemical Methods. Electrochemical experiments were performed at room temperature using a Bioanalytical Systems 100 B/W Electrochemical Workstation and analyzed using BAS 100W version 2.0 software. All potentials are reported relative to the $FeCp_2^{0/+}$ couple. Controlled potential electrolysis (CPE) experiments were performed in a sealed glass "H-cell" consisting of two 30 mL chambers separated by a fine glass frit (Figure 3.8). Each chamber had two 14/20 ground-glass access ports that were sealed with rubber septa. A three-electrode

configuration was used that consisted of a reticulated vitreous carbon foam working electrode (ERG Materials & Aerospace, ca. 15 mm × 10 mm × 5 mm), a platinum wire auxiliary electrode that was separated from the working solution by a medium porosity glass frit, and a Ag/Ag^+ reference electrode (BASi, 0.01 M $AgNO_3$ in CH_3CN containing 0.1 M $[NBu^n_4][PF_6]$) that was separated from the working solution by a Vycor tip. The reference electrode was stored in a solution of 0.1 M $[NBu^n_4][PF_6]$ CH_3CN and a new Vycor plug was used for each experiment The working solution was added to one chamber and consisted of a known amount of $\mathbf{1}^+$, $[Ru(bpy)_3][PF_6]_2$, and pyrrolidine in benzonitrile solution (14 mL) containing 0.1 M $[NBu^n_4][PF_6]$. Depending on the experiment, H_2 or N_2 was delivered via a syringe needle through one of the access ports and vented via a second syringe needle to an oil bubbler. The working solution was sparged with the PhCN-saturated gas (N_2/H_2) in the dark for 30 min prior to measurements and then blanketed with the gas for the remainder of the experiment. For photoelectrochemical experiments, this chamber was positioned above a 447.5 nm LED (Rebel LED, 910 mW, Luxeon Star LEDs) illuminating upwards through the solution and beside a 455 nm LED (455 nm Mounted High Power LED, 900 mW, ThorLabs) that illuminated the solution from the side. The auxiliary chamber always contained the Ag/Ag^+ reference electrode and Pt wire auxiliary electrode, immersed in CH_3CN (20 mL) solution containing $[NBu^n_4][PF_6]$ (0.1 M). Cyclic voltammetry determined that the reference couple lies at –0.20 V relative to the $FeCp_2^{0/+}$ couple in PhCN ($Ag^{0/+}$ (CH_3CN) + 0.20 V = $FeCp_2^{0/+}$ (PhCN)). All potentials are reported relative to $FeCp_2^{0/+}$. Tygon tubing connected the two chambers to equalize the pressure. Control (dark) experiments involved both chambers being wrapped extensively in foil and room lights switched off. After each experiment the measured current was integrated with respect to time, yielding the charge passed.

3.3. Results and Discussion

3.3.1. Mechanistic Considerations of Photocatalytic H_2 Oxidation. The success of the $Ni(P^R_2N^{R'}_2)_2^{n+}$ family of compounds as highly active electrocatalysts for the interconversion of protons and dihydrogen has been accompanied with detailed investigation of the catalytic mechanism.[43-50] The pathways proposed for electrocatalytic H_2 oxidation by $Ni(P^R_2N^{R'}_2)_2^{n+}$ (R = cyclohexyl, R′ = *tert*-butyl) are outlined in Figure 3.2. Oxidation of H_2 requires two oxidation and two deprotonation events.[24] The two oxidation steps, converting $\mathbf{1}^+$ to $\mathbf{1}^{2+}$ and $\mathbf{1H}^+$ to $\mathbf{1H}^{2+}$, have previously been driven via electrolysis. In the present work we will drive them photochemically, using the excited-state of the ubiquitous photoredox chromophore[51-57] $Ru(bpy)_3^{2+}$ ($\mathbf{2}^{2+}$) as the oxidant. Electrocatalytic oxidation of hydrogen has been reported with $\mathbf{1}^{2+}$ at a potential of −0.77 V in CH_3CN and at −0.81 V in benzonitrile,[24] implying that both oxidation steps are accessible from the MLCT-excited state of $\mathbf{2}^{2+}$ (reported $E_{1/2}$ ($\mathbf{2}^{2+*/+}$) = +0.39 V, CH_3CN),[58]

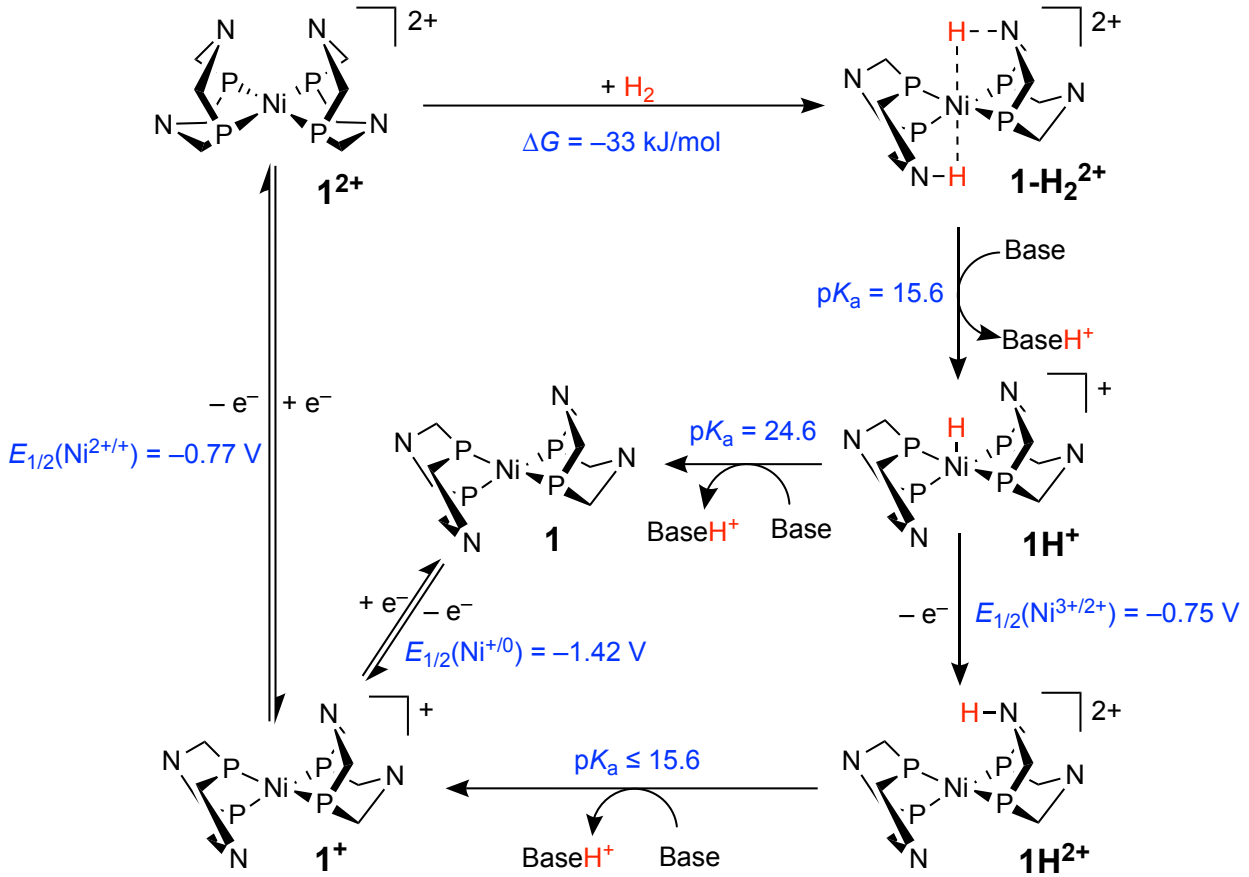

Scheme 3.1. Proposed pathway for the electrocatalytic oxidation of dihydrogen by a $Ni(P^R_2N^{R'}_2)_2^{n+}$ catalyst.[24] Also included is the photochemically-relevant $Ni(P^R_2N^{R'}_2)_2$ (**1**) state. The R (cyclohexyl) and R′ (*tert*-butyl) substituents are not shown for clarity. Key thermodynamic data are depicted in blue (acetonitrile; potentials referenced to $FeCp_2^{0/+}$).[24-25]

To predict how the catalyst will function in a photochemical system it is important to consider what occurs immediately after each oxidation. The system as implemented in this study begins with compound $\mathbf{1}^+$. Upon reductive quenching of the excited chromophore by $\mathbf{1}^+$, the oxidized catalytic species ($\mathbf{1}^{2+}$) needs to be trapped by either an intramolecular or rapid intermolecular process, so as to outcompete back-electron transfer from $\mathbf{2}^+$ that results in regeneration of the ground states. It has been reported that H_2 binding is the rate-limiting step for electrocatalysis, with catalytic turn-over frequency trending with the driving force for hydrogen addition.[21] For compound $\mathbf{1}^{2+}$, the binding of H_2 to form $\mathbf{1\text{-}H_2}^{2+}$ is strongly thermodynamically downhill ($\Delta G = -33$ kJ mol^{-1}). This is the largest driving force for H_2 addition for any compound

in this family and, thus, provides the greatest rate of H_2 binding and the best chance of trapping the photochemically generated oxidized state.[24] Deprotonation of **1-H$_2$$^{2+}$** yields **1H$^+$**. Photochemically driven oxidation of **1H$^+$** by Ru(bpy)$_3^{2+}$* forms **1H^{2+}**, which is followed by a second deprotonation to restore **1$^+$**. When there is a relatively high base concentration ([Base] > 70 mM) it is known from previous work that the concentration of base is not rate-limiting for electrocatalysis;[24] thus, trapping of this second photo-generated oxidized state is faster than for the first. These steps regenerate the initial **1$^+$** state and complete the cycle.

In addition to this cycle there is an additional pathway that proceeds through compound **1** (Scheme 3.1). Although viable under certain electrochemical conditions, this process is off-pathway for photochemical H_2 oxidation because two consecutive photosensitized electron transfer steps are required from **1** to generate the substrate-binding **1^{2+}** species. Photochemically, this is very difficult to achieve because it requires the second photosensitized oxidation to occur faster than the transient products of the first oxidation can undergo back-electron transfer.

Using this mechanistic knowledge, this chapter details a demonstration of light-driven H_2 oxidation with the Ni($P^{Cy}_2N^{tBu}_2$)$_2^{n+}$ catalyst. First, it will be established that each of the two oxidation steps required for complete H_2 oxidation with a photosensitizer can be achieved. It will be shown that **1$^+$** can be oxidized to **1^{2+}** *via* reductive quenching of a photo-excited chromophore, and that transient **1^{2+}** is subsequently trapped by the activation of H_2. A chromophore will again be used to photo-oxidize compound **1H$^+$**, with subsequent rapid deprotonation of the product (**1H^{2+}**) regenerating **1$^+$**. The sum of these two processes provide a demonstration of stepwise photochemical H_2 oxidation. Second, it will be shown that the system can be driven catalytically with an electron sink to remove the reducing equivalents as they are generated. To this end, a photoelectrochemical approach was employed with an electrode serving as an oxidant.

3.3.2. Light-driven Activation and Cleavage of H_2. To determine whether the excited state of $\mathbf{2}^{2+}$ is capable of oxidizing $\mathbf{1}^{+}$, as necessary if it is to be a suitable chromophore for driving photochemical H_2 oxidation, quenching studies were performed in which the emission lifetime of an acetonitrile solution of $\mathbf{2}^{2+}$ (70 μM) was measured with various concentrations of $\mathbf{1}^{+}$ (0.0–2.0 mM). The electronic-absorption spectrum of the solution did not change over the course of these experiments, indicating that no net photochemistry occurred. Though the features of the absorption spectrum principally correspond to $\mathbf{2}^{2+}$, a band due to $\mathbf{1}^{+}$ at > 600 nm is readily observed (Figure 7.2.5). That this band remained unchanged after each measurement indicates that $\mathbf{1}^{+}$ is not consumed. This is expected because the quenching products, $\mathbf{1}^{2+}$ and $\mathbf{2}^{+}$, should undergo back-electron transfer in the absence of H_2 to reform the starting materials. The emission lifetime of $\mathbf{2}^{2+*}$ was found to decrease with increasing $\mathbf{1}^{+}$ concentration in a manner that is in excellent agreement with the Stern–Volmer relationship ($\tau_0/\tau = 1 + k_q\tau_0[Q]$, where τ_0 is the lifetime of the chromophore, τ is the lifetime in the presence of a given concentration of quencher Q, and k_q is the Stern–Volmer quenching rate constant: Figure 3.2). This analysis yielded a quenching rate constant of $k_q = 8.2 \times 10^8$ M^{-1} s^{-1}, which is well below the diffusion-controlled limit. Based on the relevant redox potentials in acetonitrile solution of $\mathbf{1}^{+}$ and $\mathbf{2}^{2+*}$ ($E_{1/2}$: $\mathbf{1}^{+/2+} = -0.77$ V, $\mathbf{2}^{2+*/+} = +0.39$ V), the driving force for the oxidation of **1** by $\mathbf{2}^{2+*}$ is substantial: $\Delta G = -1.16$ V. We postulate that the rate is below the diffusion limit despite the large driving force because of the large inner-sphere reorganization energy associated with the oxidation of $\mathbf{1}^{+}$ to $\mathbf{1}^{2+}$. The solid-state structures of both compounds have been reported previously; the Ni center of $\mathbf{1}^{+}$ has a pseudo-tetrahedral[41] geometry, with the P–Ni–P planes of the two ligands offset by a dihedral angle (α) of 62.1°, whereas d^8 $\mathbf{1}^{2+}$ lies much closer to the square-planar limit (α = 23°)[25].

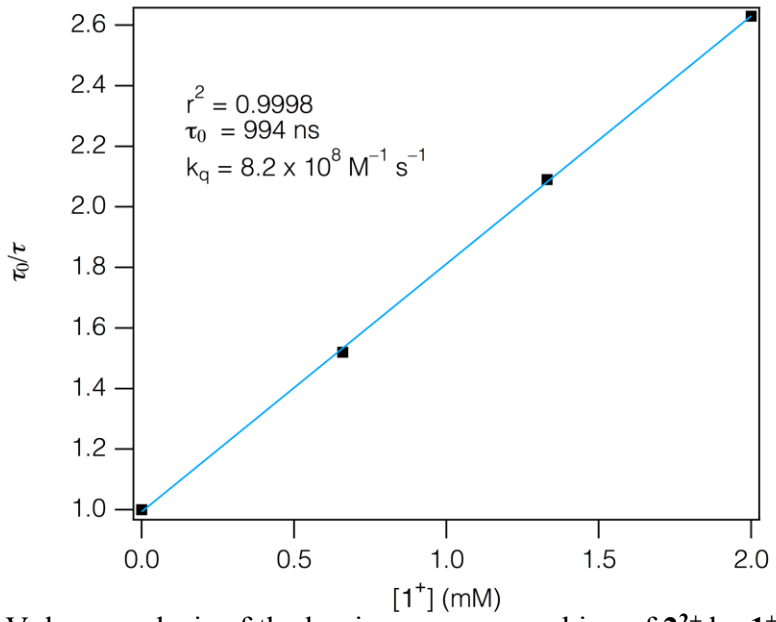

Figure 3.2. Stern-Volmer analysis of the luminescence quenching of $\mathbf{2}^{2+}$ by $\mathbf{1}^+$ in CH_3CN.

To probe whether photogenerated $\mathbf{1}^{2+}$ is sufficiently long-lived to react with H_2 before back-electron transfer from $\mathbf{2}^+$ occurs, a photochemical experiment was conducted in which a benzonitrile solution containing $\mathbf{1}^+$ (1.9 mM), $\mathbf{2}^{2+}$ (67 μM), H_2 (*ca.* 2 atm), and PCy_3O (an inert ^{31}P-NMR internal standard) was photolyzed with 455 nm light. Over the course of 1 hour, the electronic spectrum of the sample in the 400–800 nm region showed complete loss of the absorption band of $\mathbf{1}^+$ and growth of a new feature near 430 nm (Figure 3.3). Monitoring of this sample by $^{31}P\{^1H\}$ NMR spectroscopy showed that, concomitant with the loss of the absorption band of $\mathbf{1}^+$, a resonance at 12.6 ppm appears (Figure 3.4). This resonance is assigned to $\mathbf{1H}^+$ based on comparison with an isolated sample that was independently prepared by the protonation of **1** with HBF_4 ($^{31}P\{^1H\}$ (PhCN): δ 12.6 (s)). Integration of this resonance relative to the internal standard indicates that after 60 minutes of photolysis there is 94% (± 5%) conversion of $\mathbf{1}^+$ to $\mathbf{1H}^+$. Control experiments in which H_2, $\mathbf{1}^+$, and $\mathbf{2}^{2+}$ were individually excluded from otherwise identical samples resulted in an absence of change to either the $^{31}P\{^1H\}$ NMR spectrum or the electronic absorption spectrum. As can be seen in the catalytic cycle (Scheme 3.1), the generation of $\mathbf{1H}^+$

from $\mathbf{1}^{+}$ requires not only oxidation and H_2 binding, but also a base capable of deprotonating $\mathbf{1\text{-}H_2}^{2+}$. The identity of this base in the present reaction will be described later.

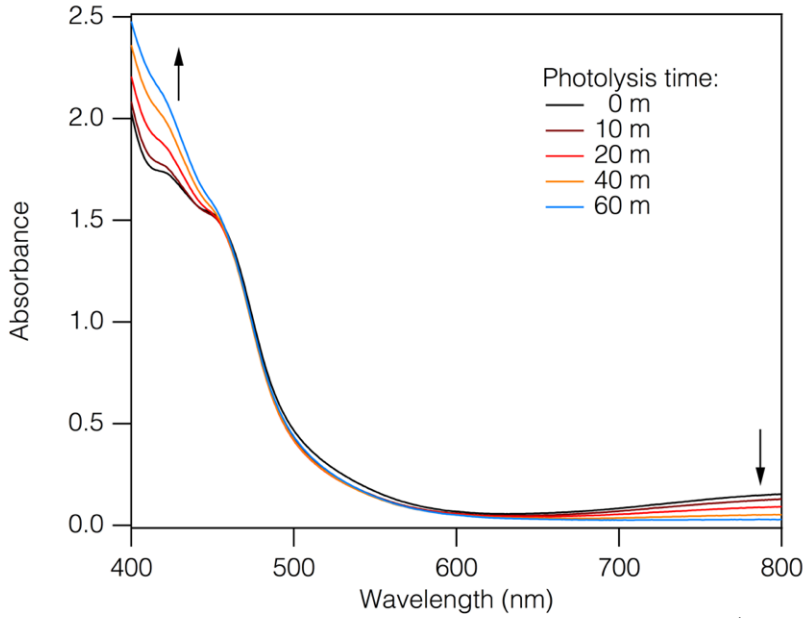

Figure 3.3. Electronic-absorption spectra of a PhCN solution containing $\mathbf{1}^{+}$ (1.9 mM), $\mathbf{2}^{2+}$ (67 μM), and PCy_3O (4.7 mM) in PhCN solution under H_2 (~2 atm) before and during photolysis (λ_{ex} = 455 nm).

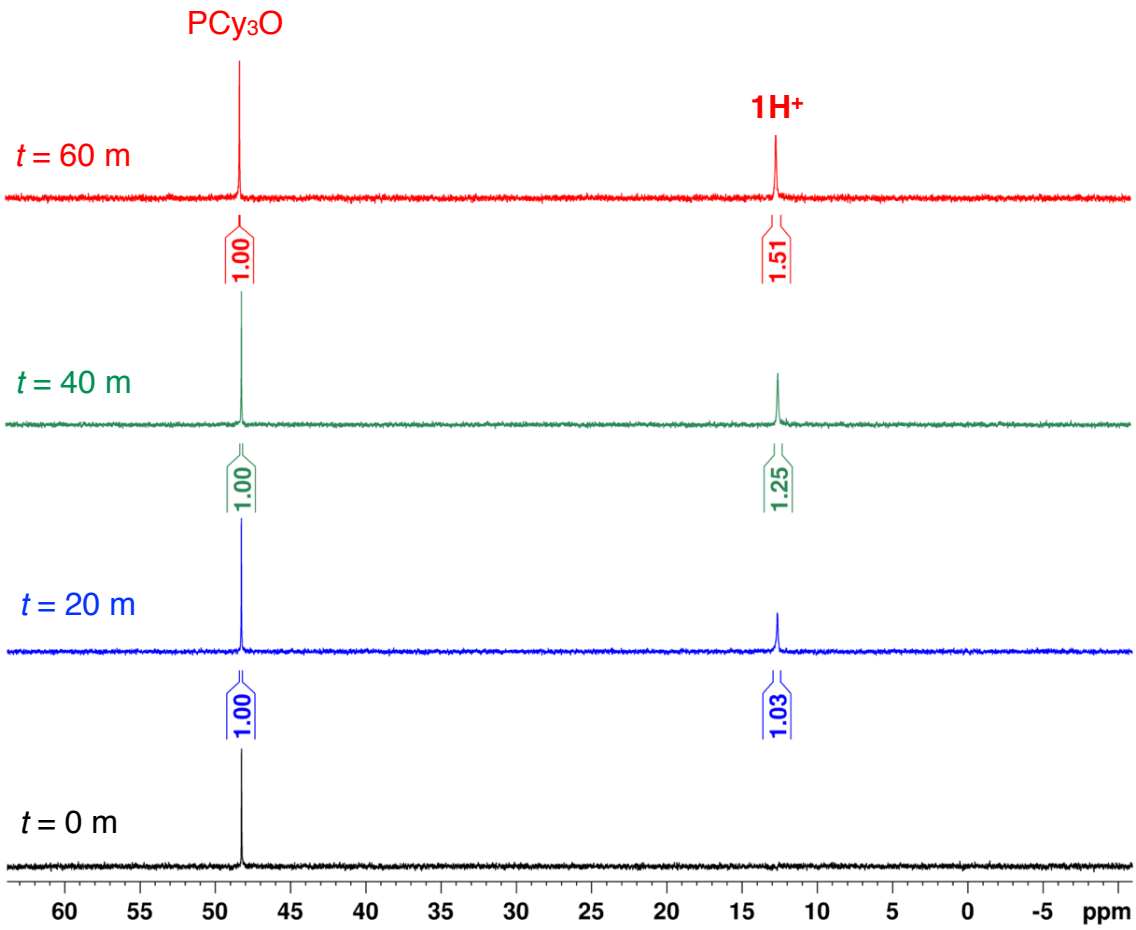

Figure 3.4. $^{31}P\{^{1}H\}$ NMR spectra of a PhCN solution containing $\mathbf{1}^{+}$ (1.9 mM), $\mathbf{2}^{2+}$ (67 μM), and PCy_3O (4.7 mM) during photolysis (λ_{ex} = 455 nm).

To further probe the photochemically sensitized cleavage of H_2 by $\mathbf{1}^{+}$ observed in benzonitrile, and to enable monitoring by ^{1}H NMR, the previously described photolysis experiment was repeated in CD_3CN. Unlike the reaction mixture in benzonitrile, which remained homogeneous throughout the photolysis, one hour of irradiation yielded the precipitation of a white solid (Figure 7.2.10) that was later isolated and shown by NMR to be **1** ($^{31}P\{^{1}H\}$ (C_6D_6): δ 7.4 (s), consistent with the literature[25]), a species that is known to be poorly soluble in acetonitrile. We propose that **1** is formed by the electron-transfer reaction between photogenerated $\mathbf{2}^{+}$ and $\mathbf{1}^{+}$. Monitoring of the solution phase of the reaction mixture by ^{1}H and $^{31}P\{^{1}H\}$ NMR gave resonances corresponding to $\mathbf{1H}^{+}$, as was also observed in benzonitrile solution (Figure 3.4). Systematic

control experiments were performed; no spectroscopic changes were seen when any one component was absent from the solution (Figure 7.2.9). Because base is required to convert **1-H$_2$**$^{2+}$ to **1H**$^+$ and none was added to these samples, we postulate that photogenerated **1** was serving this role. Thermodynamically, **1** is a competent base for this reaction because the pK_a of **1-H$_2$**$^{2+}$ is reported as 15.6 and **1H**$^+$ (the conjugate acid of **1**) is a weaker acid with a pK_a of 24.6.[24] This possibility was investigated by reacting **1-H$_2$**$^{2+}$ in benzonitrile (prepared *in situ* from the reaction between **1**$^{2+}$ and H_2) with 1 equivalent of **1**. Monitoring of the reaction by $^{31}P\{^1H\}$ NMR spectroscopy showed the appearance of a resonance at 12.6 ppm in the ^{31}P spectrum, consistent with the formation of **1H**$^+$ (Figure 3.5). This demonstrates that **1** is competent to deprotonate **1-H$_2$**$^{2+}$.

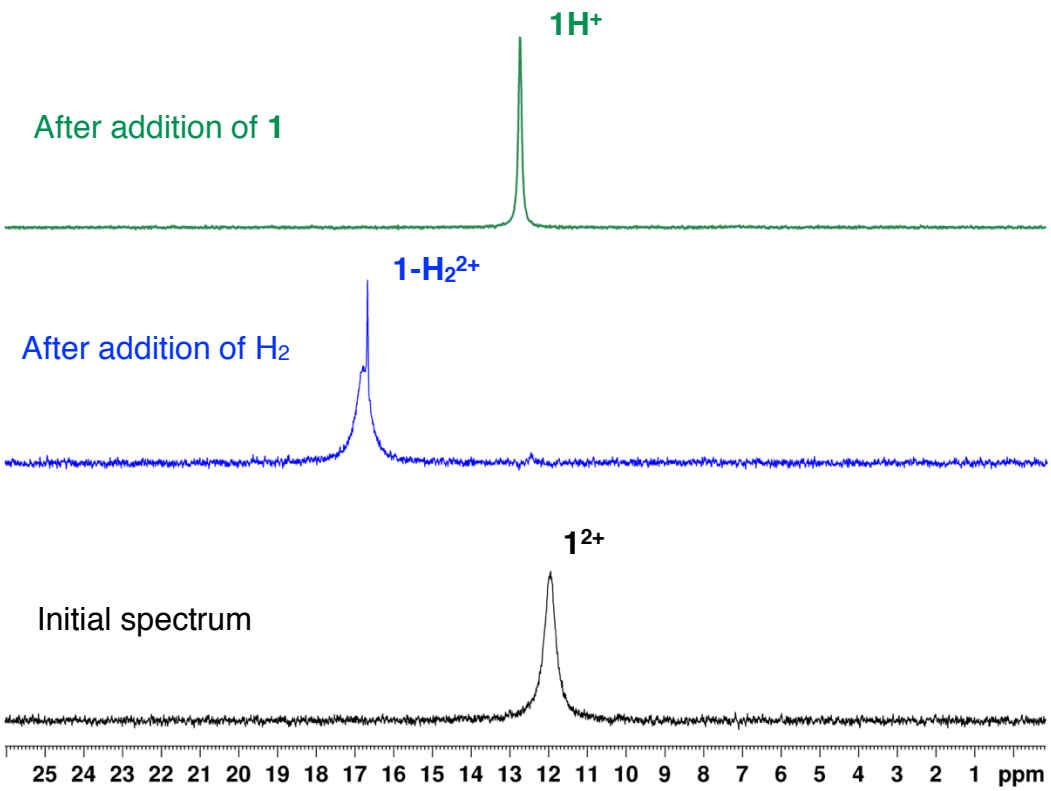

Figure 3.5. $^{31}P\{^1H\}$ NMR spectra showing the deprotonation of **1-H$_2$**$^{2+}$ by **1**. (*Bottom*) The spectrum of **1**$^{2+}$ in PhCN (5% CD_3CN). Addition of H_2 leads to the formation of **1-H$_2$**$^{2+}$ (*middle*), the major component being the endo/endo isomer. Also seen is a minor component of the endo/exo isomer, the presence of which has been previously reported.[24] (*Top*) The addition of one equivalent of **1** yields **1H**$^+$.

The proposed mechanism for the photochemical conversion of $\mathbf{1}^{+}$ to $\mathbf{1H}^{+}$ is outlined in Scheme 3.2. The photo-oxidation of half an equivalent of $\mathbf{1}^{+}$ yields both $\mathbf{1}^{2+}$ and a half equivalent of the reduced chromophore, $\mathbf{2}^{+}$. Subsequently, photogenerated $\mathbf{1}^{2+}$ binds H_2, producing $\mathbf{1\text{-}H_2}^{2+}$. In the absence of an oxidant, $\mathbf{2}^{+}$ thermally reduces another half equivalent of $\mathbf{1}^{+}$, giving **1** and regenerating $\mathbf{2}^{2+}$. Finally, **1** and $\mathbf{1\text{-}H_2}^{2+}$ comproportionate via intramolecular proton transfer to form $\mathbf{1H}^{+}$. These results demonstrate that $\mathbf{1}^{+}$ can be photochemically activated and the $\mathbf{1}^{2+}$ state can be trapped through H_2-binding before back-electron transfer from $\mathbf{2}^{+}$ occurs. The observation of net photochemistry further establishes that H_2 activation by $\mathbf{1}^{2+}$ can outcompete comproportionation of the photogenerated $\mathbf{1}^{2+}$ and **1** states. Catalytic turnover of the chromophore $\mathbf{2}^{2+}$ (TON = 13) has been demonstrated, given the relative concentrations of $\mathbf{1}^{+}$ (1.9 mM) and $\mathbf{2}^{2+}$ (67 μM) employed.

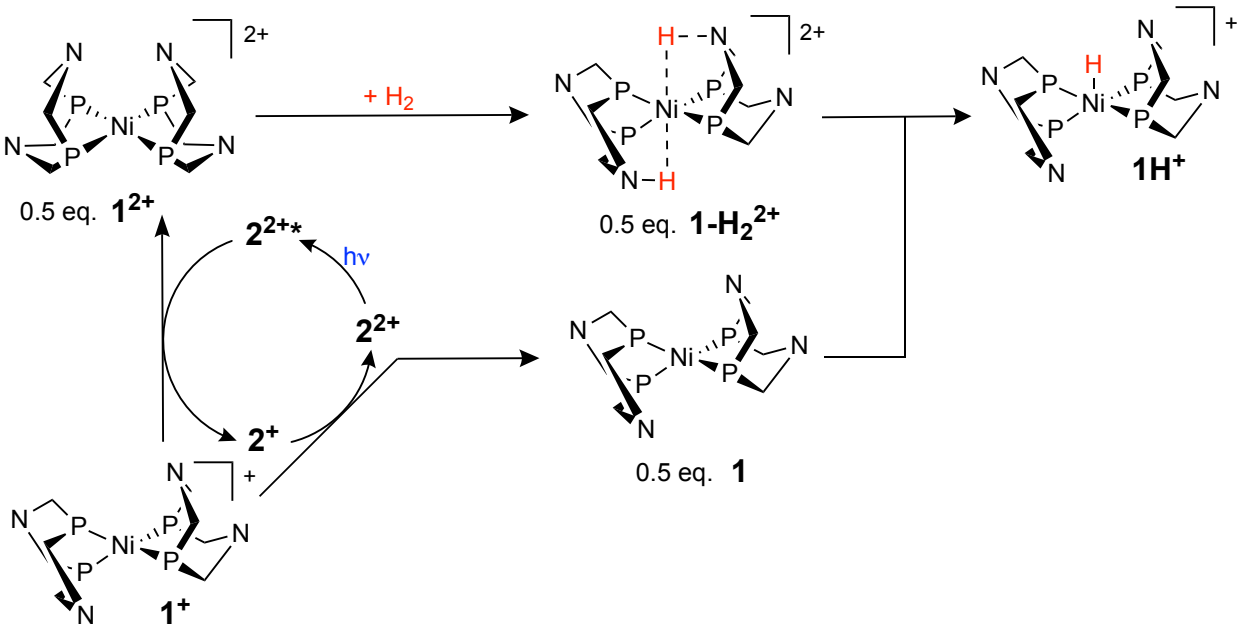

Scheme 3.2. The proposed mechanism by which $\mathbf{1}^{+}$ is converted into $1H^{+}$ photochemically. The R and R′ substituents are not shown for clarity.

3.3.3. Light-Driven Oxidation and Deprotonation of $\mathbf{1H}^{+}$. The vital catalytic intermediate $\mathbf{1H}^{+}$ has been prepared in situ[24] but not previously isolated and independently characterized. For the purpose of photochemically driving hydrogen oxidation with $\mathbf{1}^{+}$, we need to

probe the second oxidative step of the catalytic cycle, namely, oxidation of $\mathbf{1H^+}$; this requires isolation of pure $\mathbf{1H^+}$. The compound was prepared by protonation of **1** using HBF_4 in diethyl ether solution. This yields a yellow precipitate that, upon collection and recrystallization, exhibits a single $^{31}P\{^1H\}$ NMR resonance at 12.1 ppm in CD_3CN (12.6 ppm in benzonitrile). This is distinct from the *in situ* value of 13.0 ppm in benzonitrile reported by DuBois and co-workers for $\mathbf{1H^+}$ as obtained from an equilibrium mixture containing **1**, $\mathbf{1H^+}$, 7-methyl-1,5,7-triazabicyclo[4.4.0]-dec-5-ene (MTBD), and MTBD–H^+.[24] The ^1H NMR spectrum shows a distinctive quintet at −10.8 ppm (J = 22 Hz), consistent with a nickel hydride species coupled to four equivalent ^{31}P nuclei. Similar hydride resonances have been previously reported for other $NiH(P^R_2N^{R'}_2)_2^+$ compounds.[42, 59-60]

To probe whether $\mathbf{1H^+}$ can be oxidized by the excited state of $\mathbf{2^{2+}}$, emission lifetimes for the latter were measured in the presence of various concentrations of $\mathbf{1H^+}$. The emission lifetime of $\mathbf{2^{2+*}}$ is observed to decrease with increasing $\mathbf{1H^+}$ concentrations and a Stern-Volmer analysis (vide supra) yields a quenching rate constant of $k_q = 2.5 \times 10^8$ M^{-1} s^{-1} (Figure 3.6). As noted for $\mathbf{1^+}$ above, this rate constant is much smaller than expected on the basis of the large driving force (ΔG = −1.14 V, based on $E_{1/2}$ ($\mathbf{1H^{+/2+}}$) = –0.75 V and $E_{1/2}$ ($\mathbf{2^{2+*/+}}$) = +0.39 V). It is proposed by DuBois, Bullock *et al.* that the oxidation of $\mathbf{1H^+}$ to form $\mathbf{1H^{2+}}$ results in proton transfer from the Ni center to a pendant base (Scheme 3.1) and a formal change in the oxidation state of Ni from Ni^{2+} to Ni^+. Though the structures of $\mathbf{1H^+}$ and $\mathbf{1H^{2+}}$ are unknown, a crystal structure of the related nickel hydride $[HNi(P^{i\mathrm{Pr}}_2N^{\mathrm{Ph}}_2)_2]^+$ has been reported[59] wherein the geometry around the Ni center is essentially tetrahedral, with a dihedral angle between the two P–Ni–P planes of 88.0°. As discussed previously, the structure of $\mathbf{1^+}$ possesses a dihedral angle (α) of 62.1°. As $\mathbf{1H^{2+}}$ is also a d^9 compound, we postulate that its geometry may be similar to that of $\mathbf{1^+}$. This would mean that

oxidation of $\mathbf{1H}^{+}$ would be associated with both breaking of the Ni–H bond and a change of dihedral angle, resulting in a slow quenching rate.

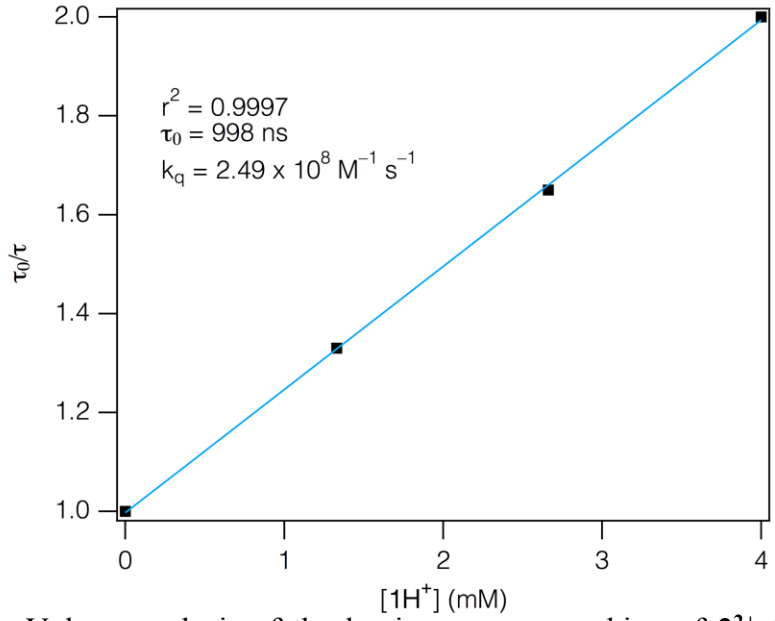

Figure 3.6. Stern-Volmer analysis of the luminescence quenching of $\mathbf{2}^{2+}$ (70 μM) by $\mathbf{1H}^{+}$ in CH_3CN.

In order to drive this portion of the cycle to form $\mathbf{1}^{+}$ prior to back electron transfer from $\mathbf{2}^{+}$ to $\mathbf{1H}^{2+}$, a suitable external base is required in order to deprotonate the latter species. The base generally used by DuBois and co-workers in electrocatalysis with $\mathbf{1}^{+}$ is NEt_3. This base is unsuitable for use in a photocatalytic system with $\mathbf{2}^{2+}$ as a chromophore because NEt_3 is known to act as a sacrificial reductant for quenching $\mathbf{2}^{2+*}$.[61] Instead, pyrrolidine was used as the base. The addition of 0.1 M pyrrolidine to $\mathbf{2}^{2+}$ gives no attenuation of the emission-lifetime, and a concentration of 0.25 M pyrrolidine only results in a 1% decrease in the lifetime (Table 7.2.1). Thus, pyrrolidine either does not quench or negligibly quenches $\mathbf{2}^{2+*}$. Additionally, the pK_a of pyrrolidine is 19.6 in CH_3CN[62] (*cf.* Et_3N has a pK_a of 18.8 in CH_3CN[62]) and so is thermodynamically capable of all necessary deprotonation steps in the H_2 oxidation cycle (Scheme 3.1). This was confirmed by adding H_2 to a solution of $\mathbf{1}^{2+}$ and excess pyrrolidine; $\mathbf{1H}^{+}$ was the only product observed by ^{31}P NMR spectroscopy, indicating that the initially formed $\mathbf{1\text{-}H_2}^{2+}$ (not

observed) was fully deprotonated by pyrrolidine. Importantly, and as demonstrated by this experiment, pyrrolidine is not basic enough to deprotonate **1H**$^+$ (pK_a = 24.6 in PhCN)[24] to give **1**, which is off-pathway for photocatalytic H_2 oxidation (Scheme 3.1).

A 95:5 CH_3CN:CD_3CN solution containing **1H**$^+$, **2**$^{2+}$, PCy_3O (as internal standard), and pyrrolidine was photolyzed in a J. Young NMR tube with 455 nm light. After 45 minutes a white solid was seen and, by $^{31}P\{^1H\}$ NMR, approximately one-half of the **1H**$^+$ had been consumed (Figure 3.7). The solvent was removed under vacuum and C_6D_6 added to solubilize the white solid. The ^{31}P NMR spectrum of the solid in C_6D_6 exhibited a resonance at 7.4 ppm that is assigned to **1**. The amount of **1** was 93% of that of the consumed **1H**$^+$.

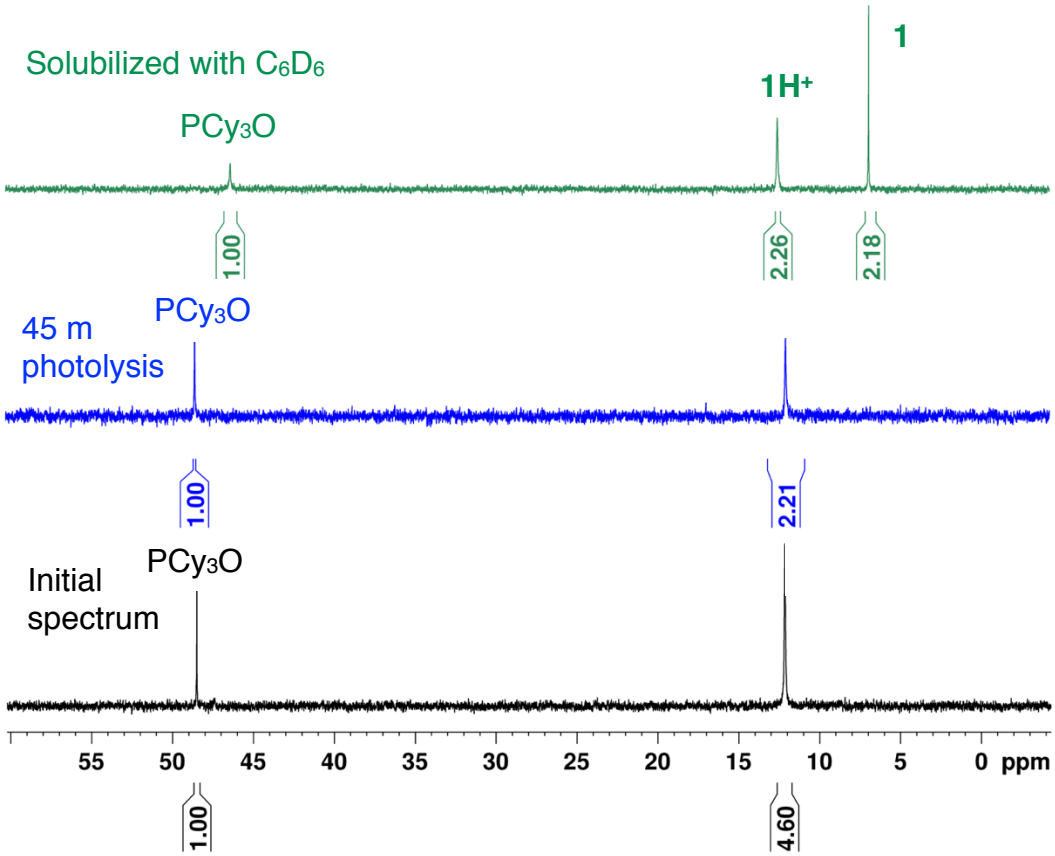

Figure 3.7. $^{31}P\{^1H\}$ NMR spectra of a CD_3CN solution containing **1H**$^+$ (7.5 mM), **2**$^{2+}$ (70 μM) and pyrrolidine (140 mM) during photolysis (λ_{ex} = 455 nm). The top spectrum was taken after drying the end photolysis mixture under vacuum and dissolving the resultant residue in C_6D_6, showing the conversion of **1H**$^+$ to **1**.

The proposed mechanism of $\mathbf{1H^+}$ conversion to **1** is outlined in Scheme 3.3. Upon the oxidation of $\mathbf{1H^+}$ by $\mathbf{2^{2+*}}$, the photogenerated $\mathbf{1H^{2+}}$ state is trapped *via* deprotonation by pyrrolidine, resulting in the formation of $\mathbf{1^+}$. One equivalent of $\mathbf{2^+}$ is also generated, which subsequently reduces $\mathbf{1^+}$ to **1**. **1** is also competent to deprotonate $\mathbf{1H^{2+}}$ but, as this pathway would regenerate $\mathbf{1H^+}$, the accumulation of **1** indicates that deprotonation of $\mathbf{1H^{2+}}$ by pyrrolidine is the primary reaction. This is expected given both the large relative concentration of pyrrolidine used (140 mM) and the insolubility of **1** in acetonitrile. This experiment shows that the second oxidative step necessary for catalytic H_2 oxidation can be achieved photochemically by the chromophore $\mathbf{2^{2+}}$.

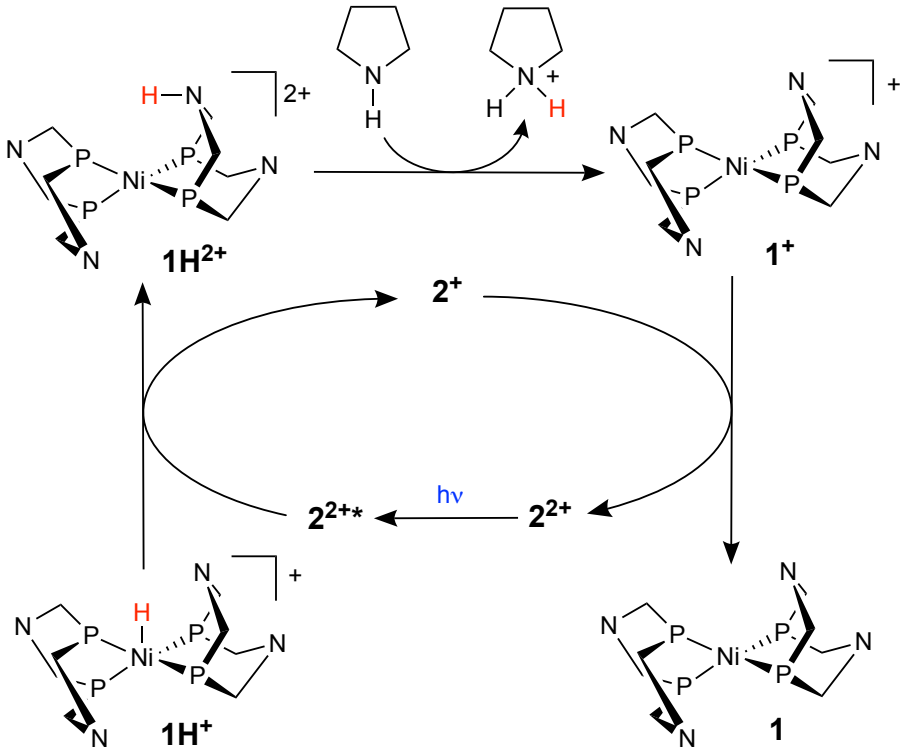

Scheme 3.3. The proposed mechanism for light-driven conversion of $\mathbf{1H^+}$ to **1**. Photochemical oxidation of $\mathbf{1H^+}$ yields $\mathbf{1H^{2+}}$, which is subsequently trapped by deprotonation by pyrrolidine. The reduced chromophore ($\mathbf{2^+}$) then thermally reduces $\mathbf{1^+}$ to **1**. The R and R′ substituents are not shown for clarity.

3.3.4. Photoelectrocatalytic Oxidation of H_2. The above experiments demonstrate that homogeneous photodriven H_2 oxidation can be achieved in a stepwise fashion by photoredox

sensitization of $\mathbf{1}^{+}$. They also show that the necessary electron-transfer steps occur in a manner fully compatible with the electrochemical mechanism proposed by DuBois, Bullock *et al*.[24] Our next objective is to achieve multiple turnovers of the system and establish photocatalytic H_2 oxidation. This requires a sink for the electrons harvested by oxidation of H_2, to avoid unproductive reduction and consumption of catalytic intermediates such as $\mathbf{1}^{+}$. Quantifying the electrons harvested would also enable determination of the number of catalytic turnovers, where each turnover generates two electrons. Inspired by recent work by Miller *et al*,[63] a photoelectrochemical experiment was devised in which an electrode was set at a suitable bias potential to oxidize harvested electrons without directly activating the catalysts. By monitoring the current generated through such an experiment, we can assess the number of turnovers achieved.

In order to demonstrate photocatalysis, controlled potential electrolysis (CPE) was performed. The selection of a suitable potential was dictated by the need to be negative of the $\mathbf{1}^{+/2+}$ couple ($E_{1/2}$ = −0.81 V)[25] so as to prevent direct electrocatalytic H_2 oxidation, and positive of the $\mathbf{1}^{+/0}$ ($E_{1/2}$ = −1.45 V)[25] and $\mathbf{2}^{2+/+}$ ($E_{1/2}$ = −1.73 V)[58] couples to inhibit $\mathbf{1}^{+}$ reduction. Within these bounds, a potential of −1.0 V was used for all CPE experiments. As this potential is positive of the excited-state oxidation potential of $\mathbf{2}^{2+*/3+}$ ($E_{1/2}$ = −1.23 V),[64] there is expected to be oxidation of $\mathbf{2}^{2+*}$ to generate $\mathbf{2}^{3+}$. This will not inhibit photocatalytic H_2 oxidation because the $\mathbf{2}^{3+}$ state ($E_{1/2}(\mathbf{2}^{2+/3+})$ = + 0.87 V)[54] could either be reduced back to $\mathbf{2}^{2+}$ by the electrode, resulting in no net current being passed, or it can thermally oxidize $\mathbf{1}^{+}$ to $\mathbf{1}^{2+}$, enabling H_2 oxidation to occur and net current to be generated. In the second case we are still witnessing photocatalysis because oxidation of an excited-state is required for the generation of the catalytically capable species, and there will be no catalysis (and no net current produced) in the absence of light.

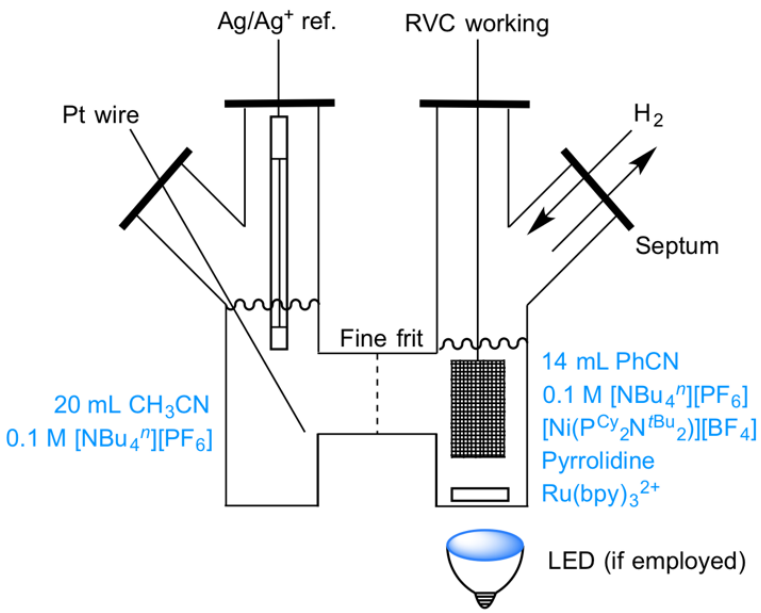

Figure 3.8. Schematic of the H-cell used for controlled-potential electrolysis experiments.

All CPE experiments were carried out in an H-cell as outlined in Figure 3.8. Electrolysis of a PhCN solution of $\mathbf{2}^{2+}$ (70 μM), $\mathbf{1}^{+}$ (0.4 mM), H_2 (1 atm) and pyrrolidine (190 nm) in the dark gives a small, persistent current of between −20 and −13 μA and a total charge of −1.2 C is passed over 22 hours (Figure 3.9). Contrastingly, when an identical solution is electrolyzed under irradiation with a 455 nm LED there is drastic current enhancement, with the current initially increasing to a peak value of −180 μA before dropping in a linear fashion over the course of the experiment, ending at −40 μA after 22 hours. A total charge of −8.1 C was passed which, after correction for dark current, corresponds to a total of 18 e^{-} Ni^{-1} and thus a TON of 9 with respect to the catalyst. Repetition of this experiment while toggling the light source (Figure 3.9) shows that the current is highly responsive to irradiation, indicating that the response is not just photoinitiated, but is the result of a photodriven process as sustained current enhancement is dependent upon sustained illumination.

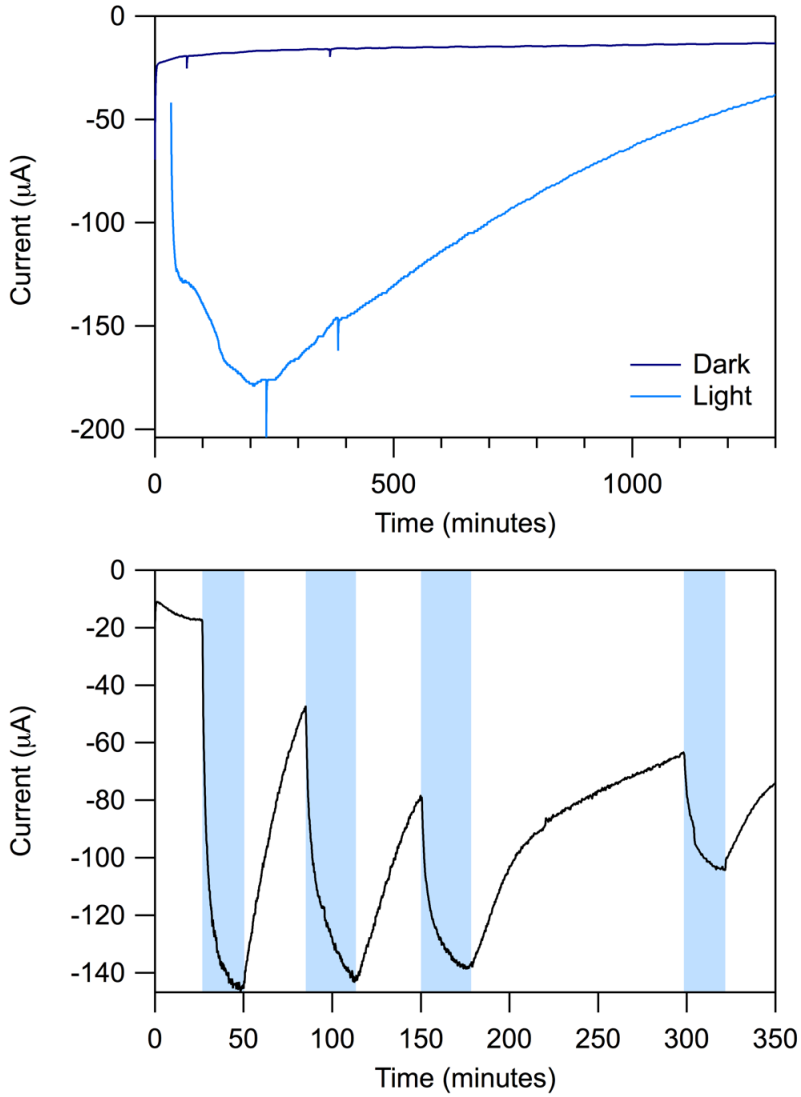

Figure 3.9. Traces of current *vs.* time for CPE (E = –1.0 V) of a benzonitrile solution containing [^{n}Bu$_4$N][PF$_6$] (0.1 M), 1^+ (0.4 mM), 2^{2+} (70 μM), and pyrrolidine (190 mM) under a H_2 atmosphere. (*Top*) Traces for electrolysis under both dark and light (λ_{ex} = 455 nm) conditions. (*Bottom*) A trace for an experiment under toggling between light (455 nm irradiation, blue background) and dark (white background) conditions.

When an identical reaction mixture is electrolyzed in the absence of H_2, a similar dark current is observed of about −15 μA (Figure 7.2.14). Upon illumination of this mixture, however, the current increases to −55 μA before decreasing in magnitude, and then going positive. This corresponds to a light-induced oxidative process, likely corresponding to the oxidation of $\mathbf{2}^{2+*}$ to $\mathbf{2}^{3+}$, the later reduction of which results in the positive current seen at long reaction time. A PhCN

solution of [^{n}Bu$_4$N][PF$_6$] was electrolyzed in both the dark and light at the same potential and, as expected, gave a very small current response (+5 μA) in both cases (Figure 7.2.13).

Photoelectrocatalytic H_2 oxidation has been demonstrated by these CPE experiments. The presence of light leads to significant and sustained current enhancement, consistent with an oxidative process. Repetition of the experiment in the absence of H_2 leads to a much smaller oxidative current enhancement that decays (comparatively) quickly, leading to the subsequent detection of a reductive process. This corresponds to the lack of net charge generation, implying that the charge carriers that give the sustained current under H_2 are dihydrogen-sourced.

3.4. Conclusions

We have demonstrated photocatalytic hydrogen oxidation with a molecular nickel catalyst. This has proved to be possible by using a catalyst that has a large driving force for substrate binding, so upon photochemical oxidation it is capable to out-compete back electron transfer. By taking a stepwise approach, we were able to determine that every process necessary for the catalytic cycle was achievable with chromophoric activation. Catalysis was demonstrated in a photoelectrocatalytic system, with an electrode acting as an electron acceptor. The findings reported here are vitally important for the development of new photocatalytic systems that are not reliant on sacrificial electron donors; an important step towards the renewable production of solar fuels.

3.5. References

1. Appel, A. M.; Bercaw, J. E.; Bocarsly, A. B.; Dobbek, H.; DuBois, D. L.; Dupuis, M.; Ferry, J. G.; Fujita, E.; Hille, R.; Kenis, P. J. A.; Kerfeld, C. A.; Morris, R. H.; Peden, C. H. F.; Portis, A. R.; Ragsdale, S. W.; Rauchfuss, T. B.; Reek, J. N. H.; Seefeldt, L. C.; Thauer, R. K.; Waldrop, G. L. Frontiers, Opportunities, and Challenges in Biochemical and Chemical Catalysis of CO_2 Fixation. *Chem. Rev.* **2013**, *113*, 6621–6658.

2. Mikkelsen, M.; Jørgensen, M.; Krebs, F. C. The Teraton Challenge. A Review of Fixation and Transformation of Carbon Dioxide. *Energy Environ. Sci.* **2010**, *3*, 43–81.

3. Esswein, A. J.; Nocera, D. G. Hydrogen Production by Molecular Photocatalysis. *Chem. Rev.* **2007**, *107*, 4022–4047.

4. Kudo, A.; Miseki, Y. Heterogeneous Photocatalyst Materials for Water Splitting. *Chem. Soc. Rev.* **2009**, *38*, 253–278.

5. Armstrong, F. A.; Belsey, N. A.; Cracknell, J. A.; Goldet, G.; Parkin, A.; Reisner, E.; Vincent, K. A.; Wait, A. F. Dynamic Electrochemical Investigations of Hydrogen Oxidation and Production by Enzymes and Implications for Future Technology. *Chem. Soc. Rev.* **2008**, *38*, 36–51.

6. Turner, J. A. Sustainable Hydrogen Production. *Science* **2004**, *305*, 972–974.

7. Ogo, S. H_2 and O_2 Activation–A Remarkable Insight into Hydrogenase. *Chem. Rec.* **2014**, *14*, 397–409.

8. Palo, D. R.; Dagle, R. A.; Holladay, J. D. Methanol Steam Reforming for Hydrogen Production. *Chem. Rev.* **2007**, *107*, 3992–4021.

9. Kärkäs, M. D.; Verho, O.; Johnston, E. V.; Åkermark, B. Artificial Photosynthesis: Molecular Systems for Catalytic Water Oxidation. *Chem. Rev.* **2014**, *24*, 11863–12001.

10. Walter, M. G.; Warren, E. L.; McKone, J. R.; Boettcher, S. W.; Mi, Q.; Santori, E. A.; Lewis, N. S. Solar Water Splitting Cells. *Chem. Rev.* **2010**, *110*, 6446–6473.

11. Kim, D.; Sakimoto, K. K.; Hong, D.; Yang, P. Artificial Photosynthesis for Sustainable Fuel and Chemical Production. *Angew. Chem., Int. Ed.* **2015**, *54*, 3259–3266.

12. Sheng, W.; Gasteiger, H. A.; Shao-Horn, Y. Hydrogen Oxidation and Evolution Reaction Kinetics on Platinum: Acid vs Alkaline Electrolytes. *J. Electrochem. Soc.* **2010**, *157*, B1529–B1536.

13. Sakintuna, B.; Lamaridarkrim, F.; Hirscher, M. Metal Hydride Materials for Solid Hydrogen Storage: A Review. *Int. J. Hydrogen Energy* **2007**, *32*, 1121–1140.

14. Concepcion, J. J.; House, R. L.; Papanikolas, J. M.; Meyer, T. J. Chemical Approaches to Artificial Photosynthesis. *Proc. Natl. Acad. Sci. U. S. A.* **2012**, *109*, 15560–15564.

15. La Porte, N. T.; Moravec, D. B.; Hopkins, M. D. Electron-Transfer Sensitization of H_2 Oxidation and CO_2 Reduction Catalysts Using a Single Chromophore. *Proc. Natl. Acad. Sci. U. S. A.* **2014**, *111*, 9745–9750.

16. Frischmann, P. D.; Mahata, K.; Würthner, F. Powering the Future of Molecular Artificial Photosynthesis with Light-Harvesting Metallosupramolecular Dye Assemblies. *Chem. Soc. Rev.* **2013**, *42*, 1847–1870.

17. Ettedgui, J.; Diskin-Posner, Y.; Weiner, L.; Neumann, R. Photoreduction of Carbon Dioxide to Carbon Monoxide with Hydrogen Catalyzed by a Rhenium(I)

Phenanthroline−Polyoxometalate Hybrid Complex. *J. Am. Chem. Soc.* **2011**, *133*, 188–190.

18. Bullock, R. M.; Helm, M. L. Molecular Electrocatalysts for Oxidation of Hydrogen Using Earth-Abundant Metals: Shoving Protons Around with Proton Relays. *Acc. Chem. Res.* **2015**, *48*, 2017–2026.

19. Helm, M. L.; Stewart, M. P.; Bullock, R. M.; DuBois, M. R.; DuBois, D. L. A Synthetic Nickel Electrocatalyst with a Turnover Frequency Above 100,000 s^{-1} for H_2 Production. *Science* **2011**, *333*, 863–866.

20. DuBois, D. L. Development of Molecular Electrocatalysts for Energy Storage. *Inorg. Chem.* **2014**, *53*, 3935–3960.

21. Shaw, W. J.; Helm, M. L.; DuBois, D. L. A Modular, Energy-Based Approach to the Development of Nickel Containing Molecular Electrocatalysts for Hydrogen Production and Oxidation. *Biochim. Biophys. Acta* **2013**, *1827*, 1123–1139.

22. Priyadarshani, N.; Dutta, A.; Ginovska, B.; Buchko, G. W.; O'Hagan, M.; Raugei, S.; Shaw, W. J. Achieving Reversible H_2/H^+ Interconversion at Room Temperature with Enzyme-Inspired Molecular Complexes: A Mechanistic Study. *ACS Catal.* **2016**, *6*, 6037–6049.

23. Gloaguen, F.; Rauchfuss, T. B. Small Molecule Mimics of Hydrogenases: Hydrides and Redox. *Chem. Soc. Rev.* **2009**, *38*, 100–108.

24. Yang, J. Y.; Smith, S. E.; Liu, T.; Dougherty, W. G.; Hoffert, W. A.; Kassel, W. S.; DuBois, M. R.; DuBois, D. L.; Bullock, R. M. Two Pathways for Electrocatalytic Oxidation of Hydrogen by a Nickel Bis(diphosphine) Complex with Pendant Amines in the Second Coordination Sphere. *J. Am. Chem. Soc.* **2013**, *135*, 9700–9712.

25. Yang, J. Y.; Chen, S.; Dougherty, W. G.; Kassel, W. S.; Bullock, R. M.; DuBois, D. L.; Raugei, S.; Rousseau, R.; Dupuis, M.; DuBois, M. R. Hydrogen Oxidation Catalysis by a Nickel Diphosphine Complex with Pendant *Tert*-Butyl Amines. *Chem. Commun.* **2010**, *46*, 8618–8620.

26. Boralugodage, N. P.; Arachchige, R. J.; Dutta, A.; Buchko, G. W.; Shaw, W. J. Evaluating the Role of Acidic, Basic, and Polar Amino Acids and Dipeptides on a Molecular Electrocatalyst for H_2 Oxidation. *Catal. Sci. Technol.* **2017**, *7*, 1108–1121.

27. DuBois, M. R.; DuBois, D. L. The Roles of the First and Second Coordination Spheres in the Design of Molecular Catalysts for H_2 Production and Oxidation. *Chem. Soc. Rev.* **2009**, *38*, 62–72.

28. Raugei, S.; DuBois, D. L.; Rousseau, R.; Chen, S.; Ho, M.-H.; Bullock, R. M.; Dupuis, M. Toward Molecular Catalysts by Computer. *Acc. Chem. Res.* **2015**, *48*, 248–255.

29. McLaughlin, M. P.; McCormick, T. M.; Eisenberg, R.; Holland, P. L. A Stable Molecular Nickel Catalyst for the Homogeneous Photogeneration of Hydrogen in Aqueous Solution. *Chem. Commun.* **2011**, *47*, 7989–7991.

30. Gross, M. A.; Reynal, A.; Durrant, J. R.; Reisner, E. Versatile Photocatalytic Systems for H_2 Generation in Water Based on an Efficient DuBois-Type Nickel Catalyst. *J. Am. Chem. Soc.* **2014**, *136*, 356–366.

31. Kamire, R. J.; Majewski, M. B.; Hoffeditz, W. L.; Phelan, B. T.; Farha, O. K.; Hupp, J. T.; Wasielewski, M. R. Photodriven Hydrogen Evolution by Molecular Catalysts Using Al_2O_3-Protected Perylene-3,4-Dicarboximide on NiO Electrodes. *Chem. Sci.* **2017**, *8*, 541–549.

32. Martindale, B. C. M.; Hutton, G. A. M.; Caputo, C. A.; Reisner, E. Solar Hydrogen Production Using Carbon Quantum Dots and a Molecular Nickel Catalyst. *J. Am. Chem. Soc.* **2015**, *137*, 6018–6025.

33. Martindale, B. C.; Joliat, E.; Bachmann, C.; Alberto, R.; Reisner, E. Clean Donor Oxidation Enhances the H_2 Evolution Activity of a Carbon Quantum Dot-Molecular Catalyst Photosystem. *Angew. Chem., Int. Ed.* **2016**, *55*, 9402–9406.

34. Silver, S. C.; Niklas, J.; Du, P.; Poluektov, O. G.; Tiede, D. M.; Utschig, L. M. Protein Delivery of a Ni Catalyst to Photosystem I for Light-Driven Hydrogen Production. *J. Am. Chem. Soc.* **2013**, *135*, 13246–13249.

35. Weingarten, A. S.; Kazantsev, R. V.; Palmer, L. C.; McClendon, M.; Koltonow, A. R.; Samuel, A. P. S.; Kiebala, D. J.; Wasielewski, M. R.; Stupp, S. I. Self-Assembling Hydrogel Scaffolds for Photocatalytic Hydrogen Production. *Nat. Chem.* **2014**, *6*, 964–970.

36. Caputo, C. A.; Gross, M. A.; Lau, V. W.; Cavazza, C.; Lotsch, B. V.; Reisner, E. Photocatalytic Hydrogen Production using Polymeric Carbon Nitride with a Hydrogenase and a Bioinspired Synthetic Ni Catalyst. *Angew. Chem., Int. Ed.* **2014**, *53*, 11538–11542.

37. Moore, G. F.; Sharp, I. D. A Noble-Metal-Free Hydrogen Evolution Catalyst Grafted to Visible Light-Absorbing Semiconductors. *J. Phys. Chem. Lett.* **2013**, *4*, 568–572.

38. Rosser, T. E.; Gross, M. A.; Lai, Y.-H.; Reisner, E. Precious-Metal Free Photoelectrochemical Water Splitting with Immobilised Molecular Ni and Fe Redox Catalysts. *Chem. Sci.* **2016**, *7*, 4024–4035.

39. Kasap, H.; Caputo, C. A.; Martindale, B. C.; Godin, R.; Lau, V. W.; Lotsch, B. V.; Durrant, J. R.; Reisner, E. Solar-Driven Reduction of Aqueous Protons Coupled to Selective Alcohol Oxidation with a Carbon Nitride-Molecular Ni Catalyst System. *J. Am. Chem. Soc.* **2016**, *138*, 9183–9192.

40. Pangborn, A. B.; Giardello, M. A.; Grubbs, R. H.; Rosen, R. K.; Timmers, F. J. Safe and convenient procedure for solvent purification. *Organometallics* **1996**, *15*, 1518-1520.

41. Niklas, J.; Westwood, M.; Mardis, K. L.; Brown, T. L.; Pitts-McCoy, A. M.; Hopkins, M. D.; Poluektov, O. G. X-ray Crystallographic, Multifrequency Electron Paramagnetic Resonance, and Density Functional Theory Characterization of the $Ni(P^{Cy}_2N^{tBu}_2)_2^{n+}$ Hydrogen Oxidation Catalyst in the Ni(I) Oxidation State. *Inorg. Chem.* **2015**, *54*, 6226–6234.

42. Wiedner, E. S.; Yang, J. Y.; Chen, S.; Raugei, S.; Dougherty, W. G.; Kassel, W. S.; Helm, M. L.; Bullock, R. M.; Rakowski DuBois, M.; DuBois, D. L. Stabilization of Nickel Complexes with $Ni^0\cdots H–N$ Bonding Interactions Using Sterically Demanding Cyclic Diphosphine Ligands. *Organometallics* **2012**, *31*, 144–156.

43. Klug, C. M.; O'Hagan, M.; Bullock, R. M.; Appel, A. M.; Wiedner, E. S. Impact of Weak Agostic Interactions in Nickel Electrocatalysts for Hydrogen Oxidation. *Organometallics* **2017**, *36*, 2275–2284.

44. Stolley, R. M.; Darmon, J. M.; Das, P.; Helm, M. L. Nickel Bis-Diphosphine Complexes: Controlling the Binding and Heterolysis of H_2. *Organometallics* **2016**, *35*, 2965–2974.

45. Stolley, R. M.; Darmon, J. M.; Helm, M. L. Solvent and Electrolyte Effects on $Ni(P^R_2N^{R'}_2)_2$-Catalyzed Electrochemical Oxidation of Hydrogen. *Chem. Commun.* **2014**, *50*, 3681–3684.

46. Das, P.; Ho, M.-H.; O'Hagan, M.; Shaw, W. J.; Morris Bullock, R.; Raugei, S.; Helm, M. L. Controlling Proton Movement: Electrocatalytic Oxidation of Hydrogen by a Nickel(II) Complex Containing Proton Relays in the Second and Outer Coordination Spheres. *Dalton Trans.* **2014**, *43*, 2744–2754.

47. Chen, S.; Ho, M.-H.; Bullock, R. M.; DuBois, D. L.; Dupuis, M.; Rousseau, R.; Raugei, S. Computing Free Energy Landscapes: Application to Ni-based Electrocatalysts with Pendant Amines for H_2 Production and Oxidation. *ACS Catal.* **2014**, *4*, 229–242.

48. Franz, J. A.; O'Hagan, M.; Ho, M.-H.; Liu, T.; Helm, M. L.; Lense, S.; DuBois, D. L.; Shaw, W. J.; Appel, A. M.; Raugei, S.; Bullock, R. M. Conformational Dynamics and Proton Relay Positioning in Nickel Catalysts for Hydrogen Production and Oxidation. *Organometallics* **2013**, *32*, 7034–7042.

49. O'Hagan, M.; Ho, M.-H.; Yang, J. Y.; Appel, A. M.; DuBois, M. R.; Raugei, S.; Shaw, W. J.; DuBois, D. L.; Bullock, R. M. Proton Delivery and Removal in $[Ni(P^R_2N^{R'}_2)_2]^{2+}$ Hydrogen Production and Oxidation Catalysts. *J. Am. Chem. Soc.* **2012**, *134*, 19409–19424.

50. O'Hagan, M.; Shaw, W. J.; Raugei, S.; Chen, S.; Yang, J. Y.; Kilgore, U. J.; DuBois, D. L.; Bullock, R. M. Moving Protons with Pendant Amines: Proton Mobility in a Nickel Catalyst for Oxidation of Hydrogen. *J. Am. Chem. Soc.* **2011**, *133*, 14301–14312.

51. Thompson, D. W.; Ito, A.; Meyer, T. J. $[Ru(bpy)_3]^{2+}$* and Other Remarkable Metal-to-Ligand Charge Transfer (MLCT) Excited States. *Pure Appl. Chem.* **2013**, *85*, 1257–1305.

52. Morris, A. J.; Meyer, G. J.; Fujita, E. Molecular Approaches to the Photocatalytic Reduction of Carbon Dioxide for Solar Fuels. *Acc. Chem. Res.* **2009**, *42*, 1983–1994.

53. Meyer, T. J. Photochemistry of Metal Coordination Complexes: Metal to Ligand Charge Transfer Excited States. *Pure Appl. Chem.* **1986**, *58*, 1193–1206.

54. Rillema, D. P.; Allen, G.; Meyer, T. J.; Conrad, D. Redox Properties of Ruthenium (II) Trischelate Complexes Containing the Ligands 2,2'-bipyrazine, 2,2'-bipyridine, and 2,2'-bipyrimidine. *Inorg. Chem.* **1983**, *22*, 1617–1622.

55. Caspar, J. V.; Meyer, T. J. Photochemistry of $Ru(bpy)_3^{2+}$: Solvent Effects. *J. Am. Chem. Soc.* **1983**, *105*, 5583–5590.

56. Durham, B.; Caspar, J. V.; Nagle, J. K.; Meyer, T. J. Photochemistry of $Ru(bpy)_3^{2+}$. *J. Am. Chem. Soc.* **1982**, *104*, 4803–4810.

57. Hammarström, L. Accumulative Charge Separation for Solar Fuels Production: Coupling Light-Induced Single Electron Transfer to Multielectron Catalysis. *Acc. Chem. Res.* **2015**, *48*, 840–850.

58. Prier, C. K.; Rankic, D. A.; MacMillan, D. W. C. Visible Light Photoredox Catalysis with Transition Metal Complexes: Applications in Organic Synthesis. *Chem. Rev.* **2013**, *113*, 5322–5363.

59. Das, P.; Stolley, R. M.; van der Eide, E. F. A Ni(II)–Bis(diphosphine)–Hydride Complex Containing Proton Relays –Structural Characterization and Electrocatalytic Studies. *Eur. J. Inorg. Chem.* **2014**, 4611–4618.

60. Galan, B. R.; Schöffel, J.; Linehan, J. C.; Seu, C.; Appel, A. M.; Roberts, J. A. S.; Helm, M. L.; Kilgore, U. J.; Yang, J. Y.; DuBois, D. L.; Kubiak, C. P. Electrocatalytic Oxidation of Formate by $[Ni(P^R_2N^{R'}_2)_2(CH_3CN)]^{2+}$ Complexes. *J. Am. Chem. Soc.* **2011**, *133*, 12767–12779.

61. Yamazaki, Y.; Takeda, H.; Ishitani, O. Photocatalytic Reduction of CO_2 Using Metal Complexes. *J. Photochem. Photobiol., C* **2015**, *25*, 106–137.

62. Kaljurand, I.; Kütt, A.; Sooväli, L.; Rodima, T.; Mäemets, V.; Leito, I.; Koppel, I. A. Extension of the Self-Consistent Spectrophotometric Basicity Scale in Acetonitrile to a Full Span of 28 pK_a Units: Unification of Different Basicity Scales. *J. Org. Chem.* **2005**, *70*, 1019–1028.

63. Pitman, C. L.; Miller, A. Molecular Photoelectrocatalysts for Visible Light-Driven Hydrogen Evolution from Neutral Water. *ACS Catal.* **2014**, *4*, 2727–2733.

64. Sattler, W.; Ener, M. E.; Blakemore, J. D.; Rachford, A. A.; LaBeaume, P. J.; Thackeray, J. W.; Cameron, J. F.; Winkler, J. R.; Gray, H. B. Generation of Powerful Tungsten Reductants by Visible Light Excitation. *J. Am. Chem. Soc.* **2013**, *135*, 10614–10617.

CHAPTER 4: Electrochemical Development of a System Competent for the Light-Driven Reverse Water-Gas-Shift Reaction

4.1. Introduction

The successful replacement of fossil fuels with renewable energy requires technology to efficiently convert the energy obtained from intermittent renewable sources (wind, tidal, solar) to a form that is easily stored and distributed, such as chemical energy.[1-7] As discussed in Chapter 1, the light-driven reverse water-gas shift reaction (RWGS: $CO_2 + H_2 \rightarrow CO + H_2O$) is an energy-storing reaction involving renewable reactants that has the potential to be driven through an artificial photosynthetic scheme.[8-9] It utilizes H_2 oxidation as a source of reducing equivalents in order to convert CO_2 to CO, while the protons produced balance the reaction by generating H_2O. Unlike the vast majority of photochemical reactions[10-13] this does not consume sacrificial donors, and is an energy-storing system ($\Delta H_f = 41.2$ kJ mol^{-1})[14].

Neumann and co-workers[15] reported a mixed molecular–heterogeneous system that performs this reaction, wherein reducing equivalents are derived from the oxidation of H_2 by colloidal platinum, and CO_2 is catalytically reduced by a $[Re^{I}(phen)(CO)_3L]^+$ (phen = 1,10-phenanthroline) chromophore/CO_2 reduction catalyst that is linked with a polyoxometalate cluster. This is the only report of light-driven, molecular-catalyst-containing CO_2 reduction that does not employ a conventional sacrificial electron donor. The finding proved the concept that two catalytic cycles could be integrated to yield an energy-storing photodriven reaction, and raised the possibility that an all-molecular system containing earth-abundant metals might be developed.

Relevant to developing a molecular artificial-photosynthetic RWGS system, research in our group[9] demonstrated that a H_2 oxidation catalyst ($Cp^RCr(CO)_3^-$) and a CO_2 reduction catalyst ($Re(bpy^R)(CO)_3Cl$) could be co-activated by chromophore-sensitized inter-catalyst electron

transfer in high yield following the single-photon excitation of the zinc–tetraphenylporphyrin (ZnTPP) photoredox chromophore. The doubly sensitized state was found to have a lifetime of greater than 10 μs. This lifetime should be sufficient for active catalysts to initiate substrate binding prior to unproductive back electron transfer, although these particular catalysts do not fall into this category. This research was furthered through a subsequent study by our group[8] that employed the more catalytically active[16-17] H_2 oxidation catalyst $Ni(P^{Cy}_2N^{tBu}_2)_2^+$ (**1**$^+$, discussed in Chapters 2 and 3; Figure 4.1) and a cobalt–diimine CO_2 reduction catalyst that rapidly binds CO_2 upon redox sensitization. It was demonstrated using transient-absorption spectroscopy that, under a mixed CO_2/H_2 atmosphere, excitation of ZnTPP resulted in inter-catalyst electron transfer and in trapping of the reduced Co catalyst by CO_2. However, only trace CO production was observed.

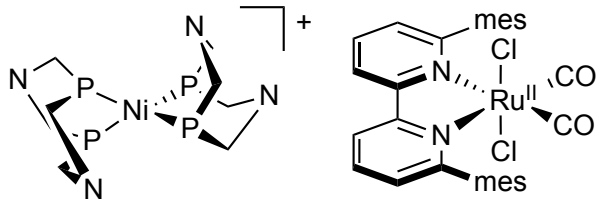

1$^+$ **2**

Figure 4.1. The catalysts discussed in this chapter. The phosphine (cyclohexyl) and amine (*tert*-butyl) substituents of **1**$^+$ are not shown for clarity.

In order to develop a functional photo-driven system for the RWGS reaction, it is evident that these proof-of-concept experiments must be extended to further explore the compositional and reaction-condition criteria necessary for each component: chromophore, H_2 oxidation catalyst, and CO_2 reduction catalyst. In this chapter we detail experiments employing ZnTPP as the chromophore, **1**$^+$ as H_2 oxidation catalyst, and the ruthenium CO_2 reduction catalyst *trans(Cl)*-$Ru(bpy^{mes})(CO)_2Cl_2$ (**2**, bpy^{mes} = 6,6′-dimesityl-2,2′-bipyridine; Figure 4.1). These components meet the thermodynamic criteria for achieving the photocatalytic RWGS reaction. Although key individual steps of the overall photocatalytic RWGS reaction were demonstrated, the overall reaction was not.

4.2. Experimental

Detailed experimental procedures and additional figures can be found in Chapter 7.3. The compounds $[Ni(P^{Cy}_2N^{tBu}_2)_2][BF_4]$ (**1**$^+$),[18] $[Ni(P^{Cy}_2N^{tBu}_2)_2][BF_4]_2$ (**1**$^{2+}$),[17] *trans(Cl)*-Ru(6,6′-dimesityl-2,2′-bipyridine)$(CO)_2Cl_2$ (**2**),[19] and *N*-(*t*-butyl)pyrrolidine (**4**),[20] were synthesized according to standard procedures. The compound pyrrolidinium tetrafluoroborate was prepared by an adapted literature method.[21] *N*-(*o*-tolyl)pyrrolidine (**3**) was synthesized by an analogous route to that reported for **4**. Zinc–tetraphenylporphyrin (ZnTPP) was prepared by a group member, Nathan T. La Porte, using standard methods.[8]

Electrochemical experiments were performed at room temperature under a N_2, CO_2, H_2, or H_2/CO_2 (28:72 v/v) atmosphere with a BAS 100B/W electrochemical workstation. All samples were in CH_3CN solution with 0.1 M $[NBu^n_4][PF_6]$ electrolyte. Potentials are referenced to the $FeCp_2^{0/+}$ couple. CV measurements were performed in a single-compartment cell with a three-electrode configuration consisting of a glassy carbon working electrode (A = 0.07 cm^2), a platinum auxiliary electrode (A = 0.02 cm^2), and a silver wire quasi-reference electrode. Controlled potential electrolysis (CPE) experiments used a three-electrode configuration, featuring a reticulated vitreous carbon foam working electrode, a platinum wire auxiliary electrode separated from the working solution by a medium porosity glass frit, and a Ag/Ag^+ reference electrode.

4.3. Results and Discussion

4.3.1. Design Criteria. A general scheme is shown in Scheme 4.1 for accomplishing the reverse water-gas-shift (RWGS) reaction *via* the photochemical electron-transfer sensitization of H_2 oxidation (Cat_{H2}, **A**) and CO_2 reduction (Cat_{CO2}, **B**) catalysts by a chromophore (Chr, **C**).[8-9] To enable catalysis, protons need to be shuttled from **A** to **B** *via* an acid-base pair **D**. This scheme imposes a variety of design criteria on the components of the system, which are described herein

to explain the selection of the particular catalysts, chromophore, and acid-base pairs chosen for the present study. In general, the requirements are as follows:

1. The excited-state reduction potential of Chr must be sufficient to oxidize Cat_{H2} at all mechanistic steps in the H_2 oxidation cycle that require removal of electrons, and its excited-state oxidation potential should be insufficient to reduce Cat_{CO2}.
2. The oxidation potential of the reduced chromophore Chr^- must be sufficient to thermally reduce Cat_{CO2} at all relevant steps in the CO_2 reduction cycle.
3. The catalysts should operate by single-electron steps rather than multielecton steps, to be compatible with the one-photon/one-electron mechanism of photoredox chromophores.
4. The sensitized catalysts should undergo an irreversible process (e.g., substrate binding or transformation) that either is fast on the time scale of unproductive back-electron transfer or otherwise inhibits it.
5. The pK_as of protonated forms of Cat_{H2} during H_2 activation should be smaller than those of the protonated forms of Cat_{CO2} during CO_2 reduction; that is, there must be a thermodynamic driving force for transferring protons from the H_2 to the CO_2 catalyst cycle.
6. The base should not inhibit either catalyst by coordinating to it or binding to CO_2.
7. The chromophore should possess a lower-energy photoactive excited state than the catalysts to avoid energy transfer.

In the remainder of this section these criteria will be used to explain the rationale for selecting the H_2 oxidation catalyst (**A**), CO_2 reduction catalyst (**B**), and chromophore (**C**) used in this study, backed by experimental data as appropriate. In the next section (4.3.2), experimental data will be presented that support the selection of the conjugate acid/base pair (**D**).

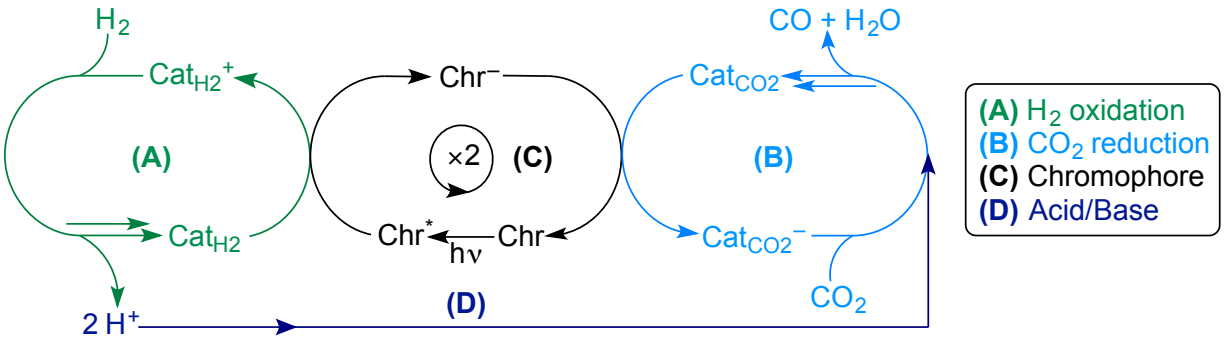

Scheme 4.1. Schematic Representation of the Light-Driven Reverse Water-Gas-Shift Reaction.

4.3.1.1. H_2 Oxidation Catalyst. The H_2-oxidation catalyst $Ni(P^{Cy}_2N^{tBu}_2)_2^+$ ($\mathbf{1}^+$) is the only known light-driven H_2 oxidation catalyst, as described in Chapter 3. Thus, all other components of the RWGS system were selected in order to be compatible with $\mathbf{1}^+$. The proposed mechanism for catalytic H_2 oxidation with $\mathbf{1}^+$ is shown in Scheme 4.2 and was thoroughly discussed in Chapter 3. A key point is the strongly favorable binding of H_2 to $\mathbf{1}^{2+}$ ($\Delta G = -33$ kJ mol^{-1}), enabling back-electron transfer to be outcompeted upon photochemical oxidation. The use of other H_2 oxidation catalysts with potentially preferable properties would introduce severe limitations on **B**, **C**, and **D**. For example, catalysts of the type $FeCp^R(P^{R'}_2N^{R''})$[34-37] are more active than $\mathbf{1}^+$ but are incompatible with use of coordinating bases and solvents such as acetonitrile, a common medium for photochemical CO_2 reduction.[38-39] Similarly, catalysts with metalloradical active states, such as $[Cp^RCr(CO)_3]^-$, have the advantage of being mechanistically simple because they cycle through only two oxidation states, as was valuable in initial proof-of-concept experiments[9] demonstrating light-driven inter-catalyst electron transfer in a RWGS system, but generally have rates of H_2 binding too slow to outcompete unproductive back-electron transfer.[9]

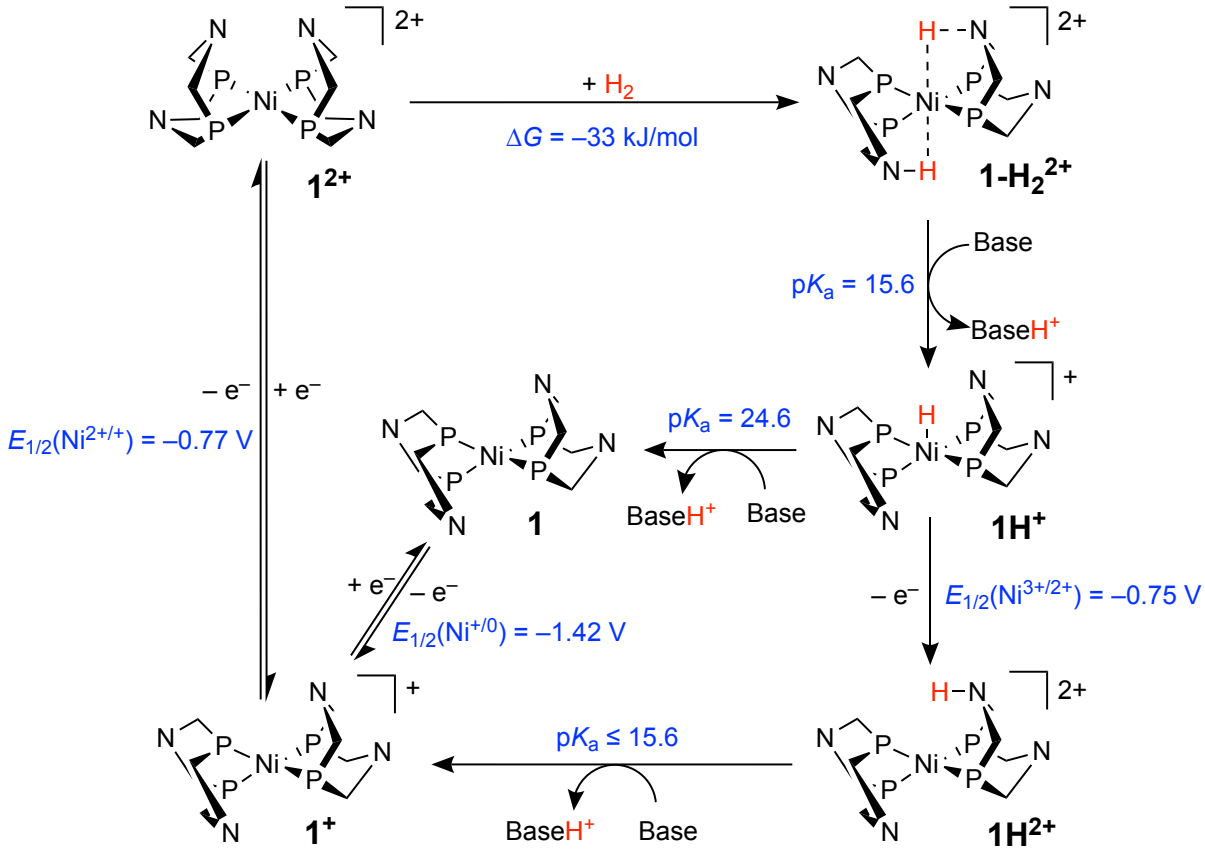

Scheme 4.2. The mechanism of H_2 oxidation by $\mathbf{1}^+$.[16-17] Thermodynamic data for the catalytic intermediates are shown in blue (acetonitrile solution; potentials referenced to $FeCp_2^{0/+}$). The R (cyclohexyl) and R′ (*tert*-butyl) substituents are not shown for clarity.

4.3.1.2. CO_2 Reduction Catalyst. The selection of CO_2 reduction catalyst (**B**) benefits from the fact that homogeneous photocatalytic reduction of CO_2 has been heavily investigated.[10-13, 39-45] One catalyst that stands out as satisfying the criteria necessary for the light-driven RWGS reaction, and which will be examined in this chapter, is *trans(Cl)*-Ru(bpy^{mes})(CO)$_2$Cl$_2$ (**2**, Figure 4.1, bpy^{mes} = 6,6′-dimesityl-2,2′-bipyridine). The photocatalytic reduction of CO_2 by **2** has been reported by Ishida *et al.*[19] using $Ru(bpy)_3^{2+}$ as chromophore and BNAH as sacrificial electron donor; in *N,N*-dimethylacetamide/H_2O, CO was produced selectively (>90%) with >200 turnovers. This demonstrates that **2** can function in a light-driven system, albeit one that uses a sacrificial reductant. Subsequent detailed mechanistic study of the electrocatalytic reduction of CO_2 by **2** (Scheme 4.3) by Kubiak *et al.*[53] showed that, following each one-electron reduction, **2** undergoes

rapid, irreversible processes that could limit back-electron transfer and enable net photochemistry to occur. Specifically, CV experiments in the presence of protons and of CO_2 indicated that the first reduction of **2** is coupled to protonation and that the second reduction is coupled with coordination of CO_2. Catalyst **2** operates at chromophore-accessible potentials, with electrolysis in 0.5 M PhOH/CH_3CN at −1.7 V providing CO production with Faradaic efficiency of 63% (with formate as a side product), and at −2.2 V gave CO with a Faradaic efficiency of 95%.

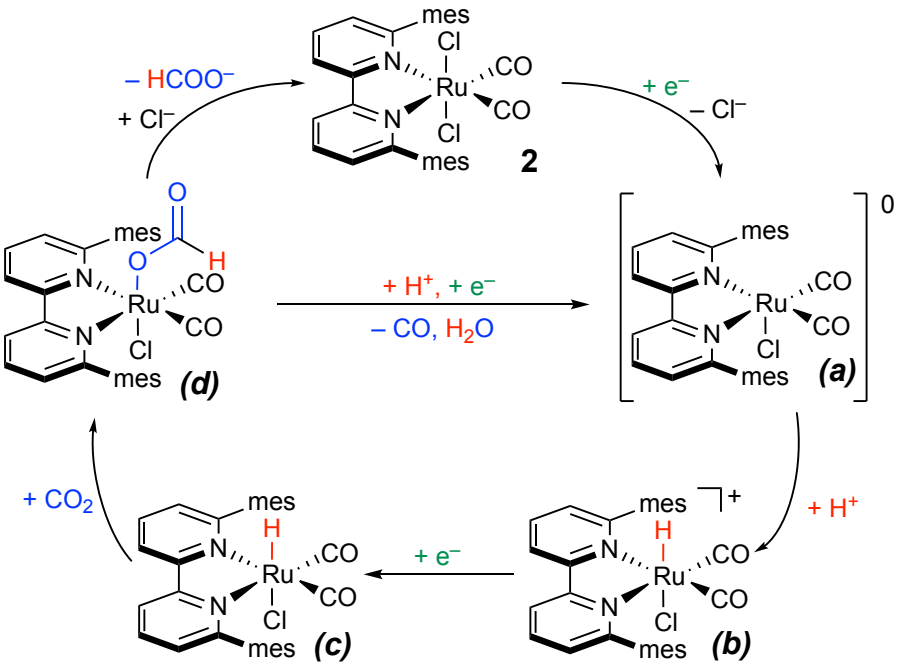

Scheme 4.3. The mechanism of electrocatalytic CO_2 reduction by **2**.[53]

Several potentially desirable classes of CO_2 reduction catalysts with higher activity than **2** have properties that render them incompatible with the criteria set out above for accomplishing the light-driven RWGS reaction. For example, iron(0)–tetraphenylporphyrins are among the most efficient and active electrocatalysts for the reduction of CO_2 to CO,[46] and have been employed in a light-driven system that produces methane and CO from CO_2 using $Ir(ppy)_3$ as chromophore and triethylamine (TEA) as a sacrificial electron donor.[47] However, the chloro Fe(III) precursor requires three $1e^-$ reductions to generate an Fe^0 state capable of binding CO_2;[12] this is only feasible

photochemically when using an irreversible sacrificial donor such as TEA. Further, iron porphyrins possess intense visible absorption bands[47] that overlap with the absorption bands of common chromophores such as $Ru(bpy)_3^{2+}$.[48] Indeed, their behavior as photocatalysts has been demonstrated by the production of multiple equivalents of CO in the absence of an external chromophore. A second major class of active CO_2 reduction catalysts not suitable for use in the RWGS system are of the form $M(bpy^R)(CO)_3X^{n+}$,[10, 39-40, 49-50] where M = Re or Mn, bpy^R is a 2,2′-bipyridine derivative, and L is a neutral (n = 1) or anionic (n = 0) ligand. Prior work in our group developed a proof-of-concept system for the light-driven RWGS reaction that utilized catalysts of the type $Re(bpy^R)(CO)_3Cl$ (R = H, *t*-Bu, OMe, CO_2Me).[9] However, there was no evidence that these compounds could undergo the necessary loss of the X ligand following $1e^-$ reduction to allow coordination of CO_2 on the time scale necessary to outcompete back-electron transfer. Further, there is evidence from prior photocatalytic studies involving sacrificial donors (such as triethanolamine) that these donors—absent from the system in Scheme 4.1—play a significant role in photocatalysis.[52]

4.3.1.3. Chromophore. The chromophore (**C** in Scheme 4.1) for the light-driven RWGS reaction must redox-sensitize both **A** and **B**: the excited chromophore oxidizes **A**, giving a reduced Chr^- species that then reduces **B**. This is the preferred order of electron-transfer reactions because it is consistent with the mechanism of photocatalytic H_2 oxidation developed in Chapter 3, and because reduced chromophores (Chr^-) tend to be stronger reductants than their excited states, thus providing a stronger driving force for subsequent reduction of **B**. At the same time, the chromophore should not directly reduce **B** from the excited state. The common chromophores ZnTPP and $Ru(bpy)_3^{2+}$ (Table 4.1) are both thermodynamically capable of driving H_2 oxidation by $\mathbf{1}^+$ (E_{cat} = –0.8 V) and CO_2 reduction by **2** (E_{cat} = –1.7 V).

Table 4.1. Photophysical Data for the Chromophores Discussed in this Chapter.[a]

Compound	$E_{1/2}$ (ox)	$E_{1/2}$ (red)	$E_{1/2}$ (*/ox)	$E_{1/2}$ (*/red)	λ_{abs} (nm)	τ (μs)	Ref
ZnTPP (T_1)	+0.39 V	–1.74 V	–1.20 V	–0.15 V	565; 602	1200	54
$Ru(bpy)_3^{2+}$	+0.89 V	–1.73 V	–1.23 V	+0.39 V	452	0.86	55

[a] All values are in CH_3CN solution and potentials are reported relative to the $FeCp_2^{0/+}$ couple.

In addition to sensitizing inter-catalyst electron transfer, the chromophore should possess lower-energy photoactive excited states than those of the catalysts to prevent chromophore → catalyst energy transfer. It was demonstrated in Chapter 3 that H_2 oxidation by $\mathbf{1}^+$ was photoredox sensitized using $Ru(bpy)_3^{2+}$ (λ_{max} = 452 nm, Table 4.1).[55] As described in Chapter 6, however, **2** was found to be highly photosensitive in acetonitrile solution upon exposure to both ambient laboratory lighting (standard overhead fluorescent lamps) and blue light (λ_{ex} = 455 nm). Thus, $Ru(bpy)_3^{2+}$ is unsuitable for use with **2** because of the possibility that incomplete chromophore filtering of light with these wavelengths will degrade **2**. Relative to $Ru(bpy)_3^{2+}$, ZnTPP has lower energy absorption bands (Q(1,0) = 565 nm and Q(0,0) = 602 nm, Table 4.1).[54] Despite **2** not exhibiting any absorbance at wavelengths longer than 500 nm, photolysis of an acetonitrile solution of **2** with a 565 nm LED (suitable for exciting Q(1,0) of ZnTPP) slowly resulted in changes to the electronic absorption spectrum (Figure 4.2). This is likely the result of the LED emission tailing to 500 nm. In contrast, photolysis of **2** with a 590 nm LED (suitable for exciting Q(0,0) of ZnTPP) resulted in the electronic-absorption spectrum of **2** remaining unchanged. Thus, ZnTPP is a suitable chromophore for use with **2**.

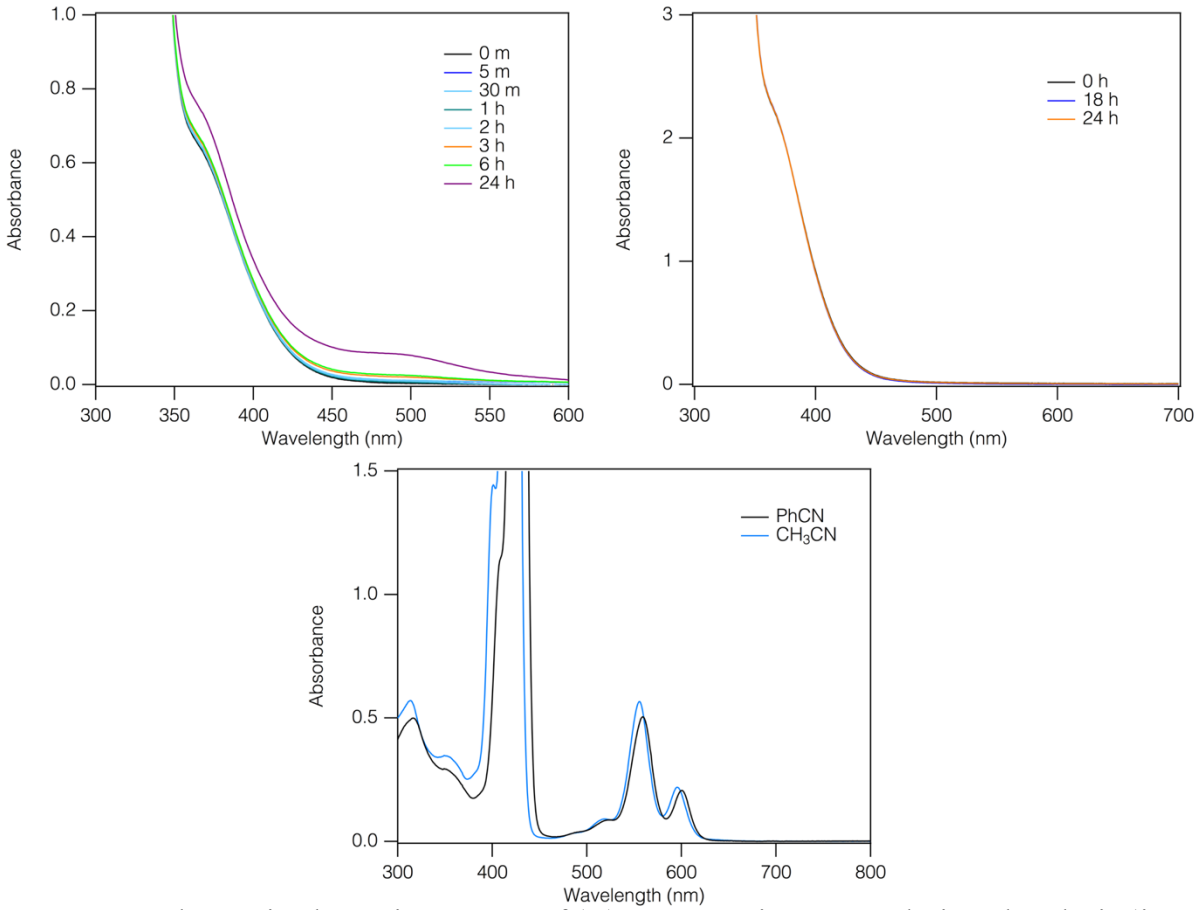

Figure 4.2. Electronic-absorption spectra of (A) 0.7 mM **2** in CH_3CN during photolysis (λ_{ex} = 565 nm), (B) 2.3 mM **2** in CH_3CN during photolysis (λ_{ex} = 590 nm), and (C) ZnTPP in PhCN and CH_3CN.

4.3.1.4. Solvent. In addition to components **A–D**, the choice of solvent needs to be considered. Polar aprotic solvents are frequently used in molecular catalytic processes due to their ability to stabilize charged intermediates. It is reported[16-17] that $\mathbf{1}^+$ is an active electrocatalyst in both acetonitrile and benzonitrile and, in Chapter 3, we demonstrated that it functions as a photocatalyst in both solvents. ZnTPP is soluble in both, with only a small effect seen upon its absorption maxima (Figure 4.2). Electrocatalytic CO_2 reduction has been demonstrated for **2** in acetonitrile solution[53] but there are no reports of its activity in benzonitrile. Because of this, and the relative scarcity of pK_a data in benzonitrile, acetonitrile is used as the solvent for this study.

4.3.2. Electrochemical Studies of the Acid/Base Pair for Inter-Catalyst Proton Transfer. A conjugate acid/base pair (**D** in Scheme 4.1) is necessary to transfer the protons generated from the hydrogen oxidation catalyst to the CO_2 reduction catalyst. The minimum pK_a required for catalytic hydrogen oxidation by $\mathbf{1}^+$ is 15.6 (Scheme 4.2). Examples of bases that are known to be compatible with $\mathbf{1}^+$ are NEt_3, *t*$BuNH_2$, *n*$BuNH_2$, and pyrrolidine.[16-17] Of these, pyrrolidine (pK_a(pyrrolidinium) = 19.56) is the best candidate base for the light-driven RWGS reaction. Primary amines are unsuitable because they react with CO_2, and NEt_3 is known to act as a sacrificial electron donor to $Ru(bpy)_3^{2+}$ whereas pyrrolidine does not quench the excited state of $Ru(bpy)_3^{2+}$ (Chapter 3). Less is known about the requirements of the proton source for CO_2 reduction by **2**. Phenol was used in the one detailed study of **2**. Because phenol (pK_a = 29.14) is a poorer acid than pyrrolidinium,[56] phenoxide is suitable (thermodynamically) to serve as the base for H_2 oxidation and pyrrolidinium is suitable (thermodynamically) to serve as the acid for CO_2 reduction. Given this wide pK_a range, it is expected that a suitable acid/base pair can be found to activate both $\mathbf{1}^+$ and **2**. Electrochemical studies were conducted to identify this base, as described below.

4.3.2.1. Electrochemical Investigation of Simple Acids Suitable for 2. Several proton sources that are potentially compatible with $\mathbf{1}^+$ were investigated for application in a light-driven RWGS system with **2**. *C*oulometric electrochemical techniques were used to simulate "ideal" RWGS photochemical conditions, wherein the application of a potential corresponding to the oxidation of $ZnTPP^-$ ($E_{1/2}(ZnTPP^{0/-})$ = –1.74 V) approximates the photochemical condition where $ZnTPP^-$ is present with infinite lifetime in a very large concentration. This enables the suitability of potential acid/base pairs to be determined more quickly, and with fewer variables, than is possible with photochemical experiments. Three proton sources were studied: phenol (the acid

used in the study of the CO_2 reduction catalysis by **2**), pyrrolidinium (the conjugate acid of the base suitable for photocatalytic H_2 oxidation using $\mathbf{1}^+$), and 2,2,2-trifluoroethanol (TFE, pK_a = 33,[56] to determine if the pK_a space can be expanded to include weaker acids than phenol). Controlled potential electrolysis (CPE) experiments (Table 4.2) were performed in which **2** in acetonitrile solution containing these acids was reduced under a CO_2 atmosphere. After each experiment, the gas within the headspace was analyzed by gas chromatography and the presence of formate in the solution was assayed by ^{1}H NMR spectroscopy.[53] With phenol, the results are indistinguishable from literature results under similar conditions,[53] whereby CO is selectively generated and formate and H_2 are minor products. With pyrrolidinium (0.05 M), CO_2 reduction was not observed but H_2 was produced very selectively (85.7% Faradaic efficiency). The weaker acid TFE gave some CO production, but the process is less efficient overall than with phenol, even with a far higher acid concentration (1.9 M *vs.* 0.5 M).

Table 4.2. CPE Experiments of CO_2 Reduction by **2** and Different Acids.[a]

Acid	[Acid] (M)	[2] (mM)	Faradaic Efficiency (%)		Formate Detected	Turnovers[b]
			CO	H_2		
Phenol	0.5	0.7	48.6	2.1	Yes	7.2
Pyrrolidinium	0.05	1.0	Trace	85.7	No	4.2
TFE	1.9	0.6	21.1	Trace	No	3.7

[a] All experiments were carried out at −1.74 V under 1 atm (0.28 M) CO_2 in 0.1 M $[NBu_4^n][PF_6]$ CH_3CN. For experimental details see the Electrochemical Methods section. [b] A turnover is defined as two electrons being passed per catalyst molecule. Where multiple runs provided different numbers of turnovers, the mean is given.

These results show that the amount of H_2 produced increases with the acidity of the proton source, and that although phenol and TFE are competent for CO_2 reduction from **2**, pyrrolidinium

is unsuitable. The behavior of TFE relative to phenol is as expected for a weaker acid, with a greater quantity of the substrate required to generate comparable catalytic efficiencies.

4.3.2.2. Electrochemical Investigation of Bases Suitable for 2 and 1^+. Building on the results above, several bases were surveyed for their compatibility with the catalysts $\mathbf{1}^+$ and **2**, ZnTPP as chromophore, and phenol as proton source. First, phenoxide was examined as a potential base. Phenoxide is not an ideal base because it is basic enough ($pK_a = 29.14$)[56] to deprotonate $\mathbf{1H}^+$ ($pK_a = 24.6$)[16] to give **1** (Scheme 4.2). This is undesirable because **1** requires two sequential photo-oxidation steps to generate $\mathbf{1}^{2+}$ and bind H_2, which is unlikely because there are not irreversible trapping steps that would outcompete back-electron transfer. Nevertheless, phenoxide was studied as a base because generation of **1** would be proof-of-concept that reducing equivalents provided by H_2 could be used in the catalytic reduction of CO_2 (Scheme 4.4), that is, it would be a step further than any previously studied homogeneous photocatalytic RWGS system.[8-9] Addition of excess sodium phenoxide (40 mM) to a CD_3CN solution of $\mathbf{1}^{2+}$ (1 mM) resulted in a color change from red to orange. The $^{31}P\{^1H\}$ NMR spectrum (Figure 4.3) showed that the initial single resonance of $\mathbf{1}^{2+}$ ($\delta = 12.0$ ppm) disappeared and was replaced by two intense singlets at 49.9 ppm and −23.6 ppm, together with a weak signal at 11.4 ppm. The resulting compound does not appear to react with H_2, as evidenced by a lack of further change to the ^{31}P NMR spectrum. This finding precludes the use of phenoxide as a base for H_2-oxidation with $\mathbf{1}^+$. We hypothesize that phenoxide coordinates to $\mathbf{1}^{2+}$ to give a five-coordinate species. Other catalysts of the type $Ni(P_2N_2)_2^{2+}$ are observed to react with Lewis bases. For example, $Ni(P^{Ph}_2N^{Ph}_2)_2^{2+}$ reacts irreversibly with Cl^- to give $Ni(Cl)(P^{Ph}_2N^{Ph}_2)_2^+$.[58] The coordination of a fifth ligand (such as Cl^- or CH_3CN) is reported[58-59] to inhibit the binding of H_2 to the metal center.

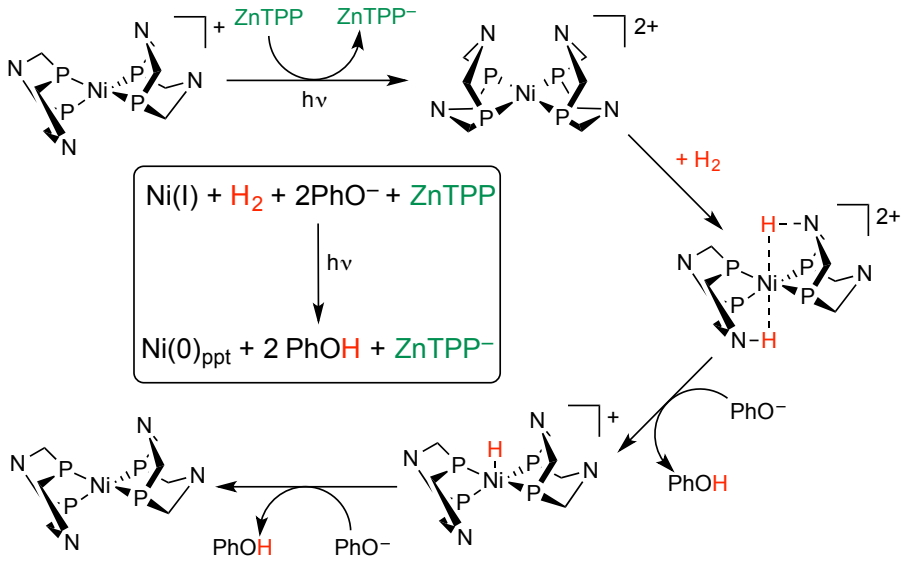

Scheme 4.4. Proof-of-concept stoichiometric system that prepares $ZnTPP^-$ from H_2-sourced reducing equivalents to drive photocatalytic CO_2 reduction.

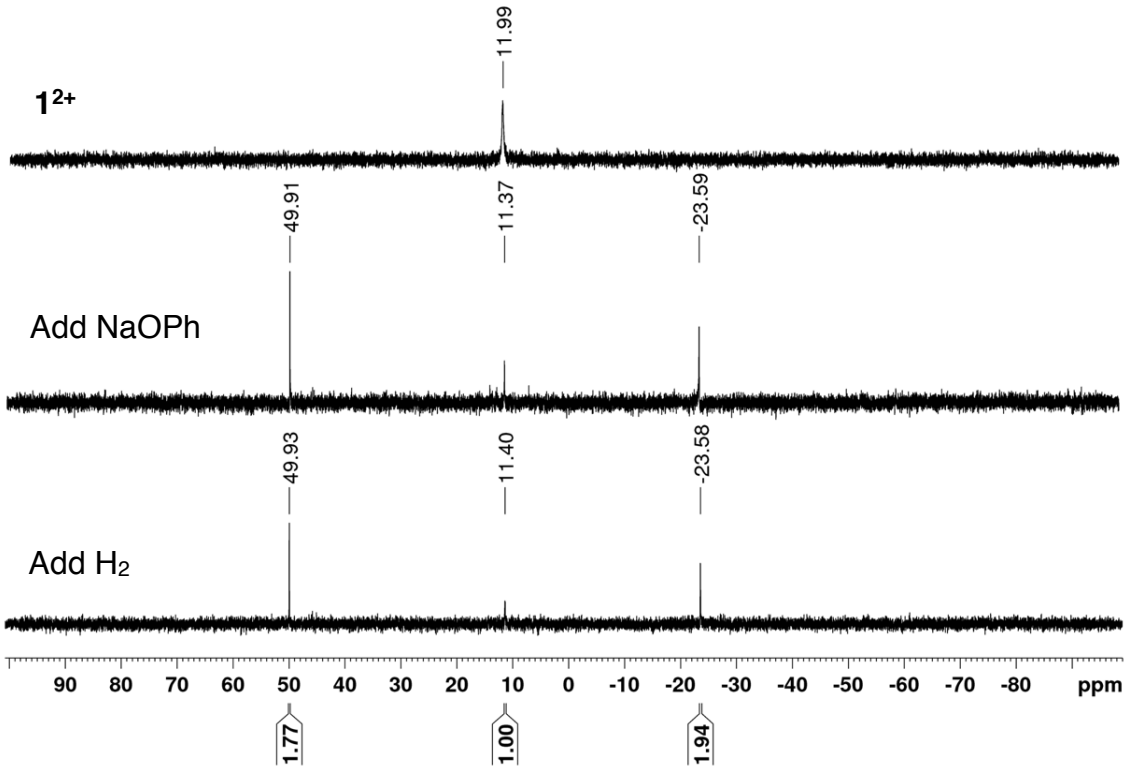

Figure 4.3. $^{31}P\{^1H\}$ NMR spectra in CD_3CN of (*Top*) $\mathbf{1}^{2+}$ (1 mM) in CD_3CN, (*Middle*) after addition of NaOPh (40 mM), and (*Bottom*) after subsequent addition of H_2.

The second base examined was pyrrolidine, which was shown in Chapter 3 to be suitable for use in photocatalytic H_2 oxidation with $\mathbf{1}^+$, but was shown above to be unsuitable, as

pyrrolidinium, as a proton source for catalytic CO_2 by **2**. To understand this latter behavior, CVs of **2** under CO_2 were measured in the presence of PhOH and increasing amounts of pyrrolidine (Figure 4.4). In the absence of pyrrolidine, the CV exhibits a peaked waveform ($E(i_{max}) \approx 2.3$ V) under CO_2, consistent with a report of electrocatalytic CO_2 reduction under identical conditions.[53] The addition of pyrrolidine alters the shape of this catalytic response and decreases the peak current by approximately 30%. CPE experiments at −1.74 V and subsequent GC analysis of the headspace showed only a trace (unquantifiable) amount of CO is produced together with a large amount of H_2 (corresponding to a Faradaic efficiency of 67.9%, Table 4.3), indicating that CO_2 reduction by **2** is inhibited by pyrrolidine even in the presence of phenol.

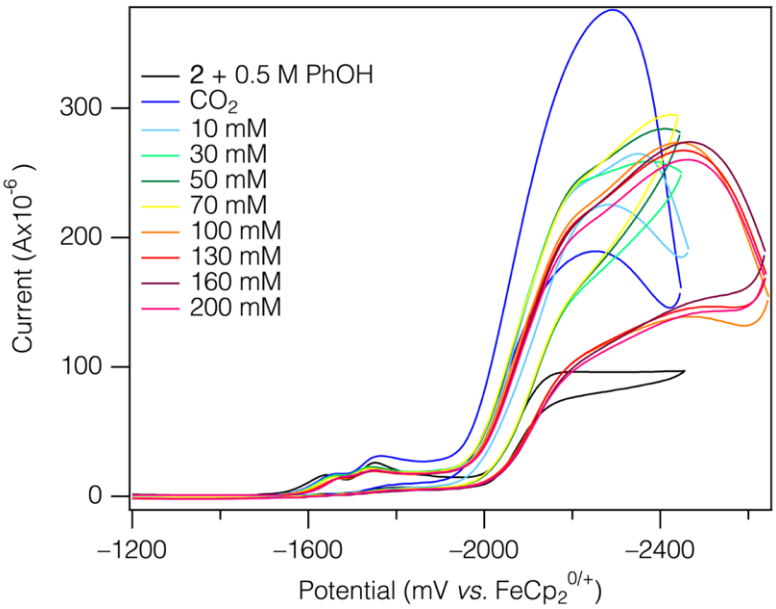

Figure 4.4. CV of **2** (0.5 mM) in 0.1 M $[NBu^n_4][PF_6]$ CH_3CN with PhOH (0.5 M) at a scan rate of 0.1 V/s under N_2 (black), CO_2 (blue) and with titration of pyrrolidine under CO_2.

Two routes by which pyrrolidine could inhibit electrocatalytic CO_2 reduction by **2** include binding of pyrrolidine to coordinatively unsaturated catalytic intermediates (Scheme 4.3) and reversible coordination to CO_2. Primary and some secondary amines bind to CO_2 to give carbamates;[60] although such reactivity has not been reported for pyrrolidine, even the occurrence of weak coordination could inhibit its activation by **2**. In either hypothesis, the addition of a

sterically hindering moiety to pyrrolidine would inhibit coordination and enable CO_2 reduction to occur. Thus, two sterically hindered *N*-*R*-pyrrolidines (*R* = *ortho*-tolyl (**3**) and *tert*-butyl (**4**); Figure 4.5) were employed in electrochemical studies of CO_2 reduction by **2** and of catalytic H_2 oxidation with $\mathbf{1}^+$.

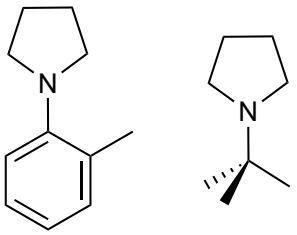

3 **4**

Figure 4.5. The sterically-hindered pyrrolidines examined in this chapter.

Base **3** was found to be suitable for use with **2** but not with $\mathbf{1}^+$. CVs of **2** in the presence of CO_2, 0.5 M phenol and varying amounts of **3** (0–160 mM) are depicted in Figure 4.6. The addition of **3** decreases the catalytic current observed but, unlike pyrrolidine, does not change the shape of the current response. This is consistent with **3** partially inhibiting CO_2 reduction by **2**, but not altering the mechanism of the catalytic process. Bulk electrolysis of a CH_3CN solution containing **2**, 0.5 M phenol, and 50 mM **3** at −1.74 V, followed by GC analysis of the headspace, indicates that CO is produced with a Faradaic efficiency of 11.0% and H_2 is generated only in small amounts (< 2% Faradaic efficiency). Thus, **3** is more suitable than pyrrolidine for use in a catalytic system containing **2** because it is less inhibiting of CO_2 reduction and greatly increases selectivity against unwanted H_2 production. The suitability of **3** as a base for driving H_2 oxidation by $\mathbf{1}^+$ was probed by $^{31}P\{^1H\}$ NMR spectroscopy. Addition of excess **3** to a $^{31}P\{^1H\}$ NMR spectroscopic sample containing $\mathbf{1\text{-}H_2}^{2+}$ (δ = 17.4, 17.1 ppm, prepared in situ in CD_3CN from $\mathbf{1}^{2+}$ (δ = 12.0 ppm) and H_2) did not result in a change to the pale-yellow color of the solution, nor to the resonances observed in the $^{31}P\{^1H\}$ NMR spectrum (Figure 4.7). This indicates that $\mathbf{1H}^+$ was not formed and that **3** is not a competent base for driving catalytic H_2 oxidation by $\mathbf{1}^+$.

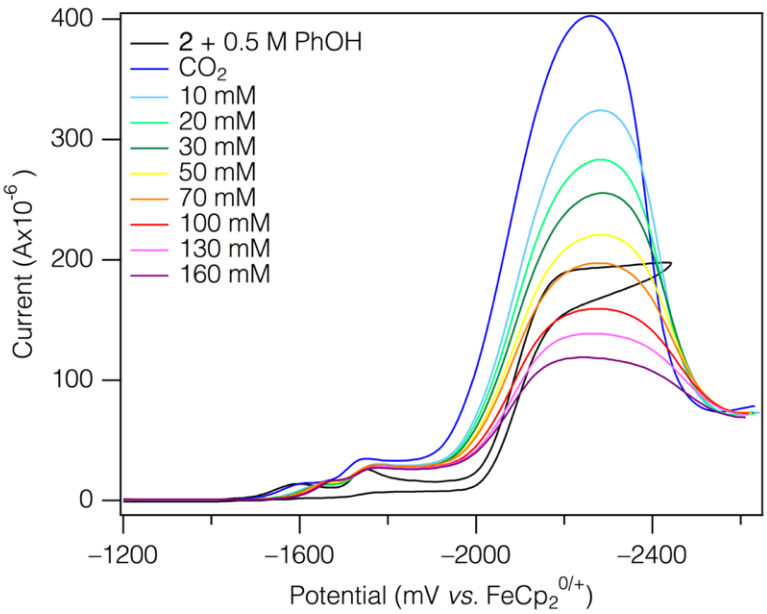

Figure 4.6. CV of **2** (0.5 mM) with PhOH (0.5 M) in 0.1 M [NBu$^n_4$][PF_6] CH_3CN at 0.1 V/s under N_2 (black) and CO_2 (blue) with titration of *N*-(*o*-tolyl)pyrrolidine (**3**). For clarity, only forward traces are shown for scans with added **3**.

Table 4.3. Efficiency and Product Selectivity of Electrocatalytic CO_2 Reduction by **2** Using Various Bases.[a]

Base	[Base] (M)	[2] (mM)	Faradaic Efficiency (%)		Formate Detected	Turnovers[b]
			CO	H_2		
None	—	0.7	48.6	2.1	Yes	7.2
Pyrrolidine	0.05	0.4	Trace	67.9	No	5.6
3	0.05	0.4	11.0	1.9	No	2.9
	0.05	0.6	7.5	Trace	No	2.7
4	0.01	0.4	16.6	2.3	No	2.9
	0.005	0.5	38.0	4.5	No	3.2

[a] All experiments were carried out at −1.74 V under 1 atm (0.28 M) CO_2 in 0.1 M [NBu_4^n][PF_6] CH_3CN and with PhOH (0.5 M). For experimental details see Section 7.3.3. [b] A turnover is defined as two electrons being passed per catalyst molecule. Where multiple runs provided different numbers of turnovers, the mean is given.

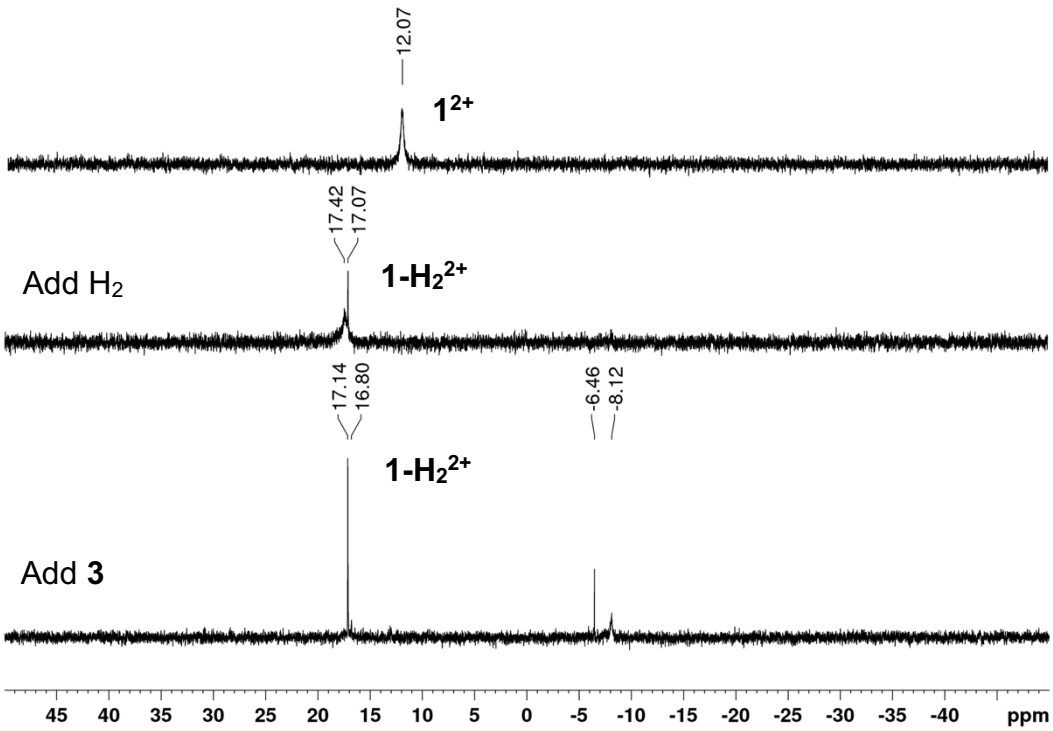

Figure 4.7. $^{31}P\{^{1}H\}$ NMR spectra in CD_3CN of (*Top*) 1 mM $\mathbf{1}^{2+}$ in CD_3CN, (*Middle*) after addition of H_2, and (*Bottom*) after subsequent addition of 70 mM **3**. The appearance of resonances at –6.46 and –8.12 is consistent with the isomerization of $\mathbf{1\text{-}H_2}^{2+}$.[16]

Unlike base **3**, base **4** was found to be compatible with both electrocatalytic CO_2 reduction by **2** and oxidation of H_2 by $\mathbf{1}^{+}$. CV measurements of **2** in acetonitrile in the presence of CO_2, 0.5 M phenol and increasing amounts of **4** (0–190 mM, Figure 4.8) show that, like for **3**, the magnitude of the observed current decreases but the shape of the waveform is not altered. Bulk electrolysis of a solution containing **2**, 0.5 M phenol, and 50 mM **4** at −1.74 V, and subsequent GC analysis of the headspace, shows that CO is produced (with a Faradaic efficiency of 7.5%) while H_2 is only generated in a trace amount (Table 4.3). Similar experiments at lower concentrations of **4** demonstrated that CO production is more efficient when a lower concentration of **4** used (Table 4.3); this is consistent with the observation by CV of a decrease in catalytic current with increasing **4** concentration.

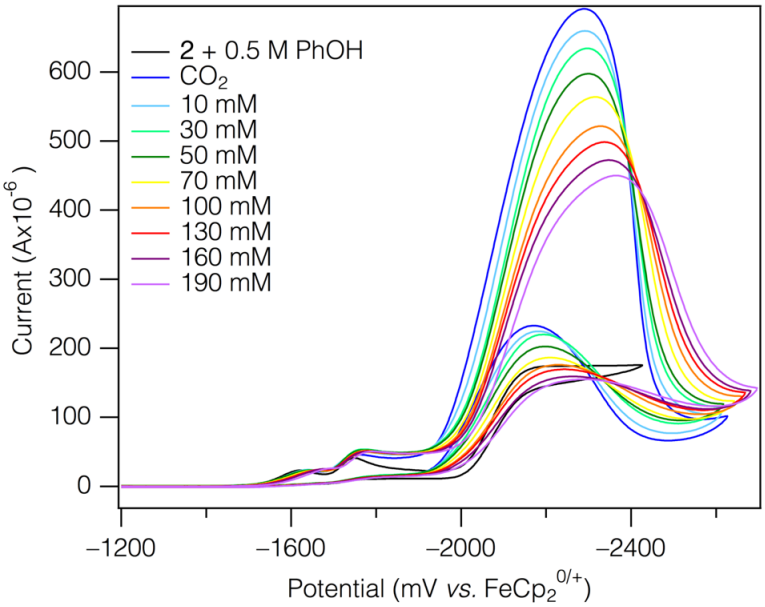

Figure 4.8. Cyclic voltammograms of **2** (0.7 mM) with PhOH (0.5 M) in 0.1 M $[NBu^n_4][PF_6]$ CH_3CN at 0.1 V/s under N_2 (black) and CO_2 (blue) with titration of **4**.

The use of **4** as a base in the catalytic H_2 oxidation with $\mathbf{1}^+$ was studied via an NMR-scale reaction and using electrochemical methods. Addition of excess **4** (70 mM) to a solution of $\mathbf{1\text{-}H_2}^{2+}$ (prepared in situ via the reaction between $\mathbf{1}^{2+}$ (1 mM) and H_2 in CD_3CN solution) led to a color change from pale yellow to dark yellow. Analysis of this reaction mixture via ^{31}P-NMR spectroscopy demonstrated that $\mathbf{1\text{-}H_2}^{2+}$ was consumed and $\mathbf{1H}^+$ (δ = 12.8 ppm) was formed (Figure 4.9). This result suggests that **4** is a competent base for use in catalytic H_2 oxidation by $\mathbf{1}^+$. This was confirmed *via* cyclic voltammetry studies of $\mathbf{1}^+$ under H_2 in the presence and absence of **4** as a base (Figure 4.10). Under an atmosphere of H_2 and in the absence of base, $\mathbf{1}^+$ is found to exhibit two oxidations with properties consistent with those reported previously by DuBois and coworkers.[16-17] The first, at E_p = −0.74 V is irreversible and corresponds to the $\mathbf{1}^+/\mathbf{1}^{2+}$ couple, with the irreversibility arising because $\mathbf{1}^{2+}$ rapidly reacts with H_2 to yield $\mathbf{1\text{-}H_2}^{2+}$. The second oxidation at $E_{1/2}$ = −0.36 V is reversible and assigned to $\mathbf{1\text{-}H_2}^{2+/3+}$. A catalytic wave is not observed because no base is present. Upon the addition of **4** (1–100 mM; 2–200-fold excess) a current enhancement is observed at the potential of the $\mathbf{1}^{+/2+}$ couple. The magnitude of the enhancement increases with

base concentration up to 50 mM, consistent with electrocatalytic H_2 oxidation.[16-17] (Simultaneously, current enhancement is also observed at the potential of the **1-H$_2$**$^{2+/3+}$ couple due to an alternative catalytic pathway not discussed in this work.[16]) Importantly, electrocatalysis is observed in the presence of very low concentrations of **4** (1 mM). This is relevant because, as noted above, CO_2 reduction by **2** in the presence of **4** is most efficient when the concentration of **4** is as low as possible (Table 4.3).

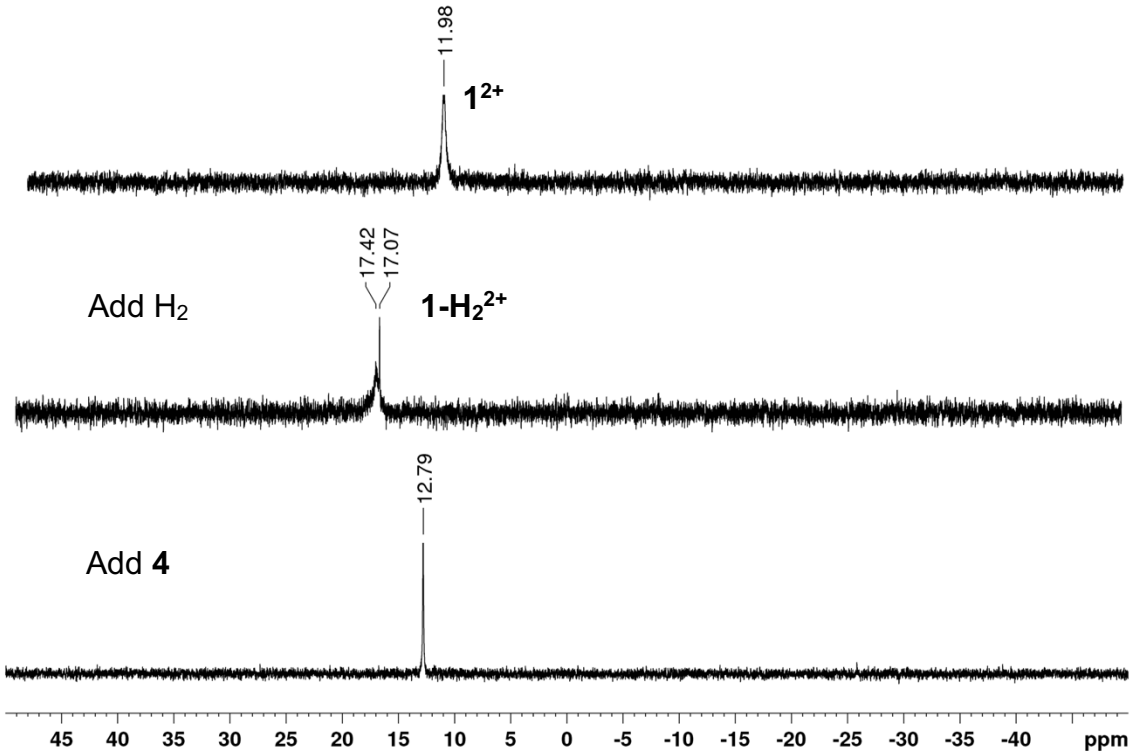

Figure 4.9. $^{31}P\{^1H\}$ NMR spectra in CD_3CN of (*Top*) 1 mM **1**$^{2+}$ in CD_3CN, (*Middle*) after addition of H_2, and (*Bottom*) after subsequent addition of 70 mM **4**.

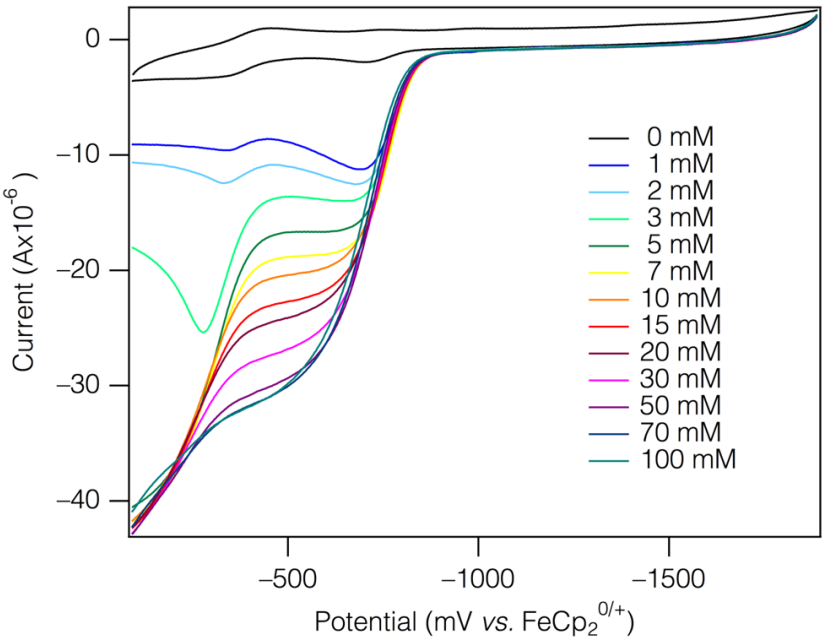

Figure 4.10. Cyclic voltammograms of $\mathbf{1}^+$ (0.5 mM) in $[NBu^n_4][PF_6]$ (0.1 M) CH_3CN at 0.1 V/s under H_2 with titration of **4**. Only forward scans are shown for traces with added base for clarity.

The experiments detailed in this section demonstrate that **4** is both a competent base to drive electrocatalytic H_2 oxidation by $\mathbf{1}^+$ and, under similar conditions, minimally inhibits electrocatalytic CO_2 reduction by **2**. Therefore, **4** is a suitable base for use in a light-driven RWGS system.

4.3.3. Studies of the Photochemical RWGS Reaction

Detailed in this section are attempts to utilize ZnTPP, $\mathbf{1}^+$, **2**, phenol, and **4** in a functional photocatalytic system for accomplishing the light-driven RWGS reaction. The first set of experiments set out to establish that photocatalytic H_2 oxidation by $\mathbf{1}^+$ and ZnTPP would occur in the presence of PhOH and **4**, as will be necessary for the full RWGS system. Compound **2** was not present; thus, these experiments were similar to those described in Chapter 3 in which the reaction mixtures did not contain an acceptor for the electrons produced by H_2 oxidation. Photolysis using a 590 nm LED of a CH_3CN solution containing $\mathbf{1}^+$ (0.8 mM), PhOH (0.5 M), **4** (10 mM), and ZnTPP under a H_2/CO_2 (28:72) atmosphere resulted in

significant changes to the electronic absorption and ^{31}P NMR spectrum of the sample. In the electronic-absorption spectrum (Figure 4.11) the 800-nm band attributable to $\mathbf{1}^+$ decreases in intensity, consistent with the consumption of $\mathbf{1}^+$, and the absorbance increases slightly at wavelengths < 525 nm, which is the region of a rising absorption exhibited by $\mathbf{1H}^+$ (Figure 7.2.8). The ZnTPP Q(0,0) and Q(1,0) bands do not appreciably change in intensity, indicating that ZnTPP is not being consumed. The $^{31}P\{^1H\}$ NMR spectrum of the sample (Figure 4.11B) confirms the production of $\mathbf{1H}^+$ upon photolysis. These experiments demonstrate that with all components of a potential RWGS system present, excepting **2**, the light-induced activation of H_2 by $\mathbf{1}^+$ is still achievable—even under only a partial H_2 atmosphere.

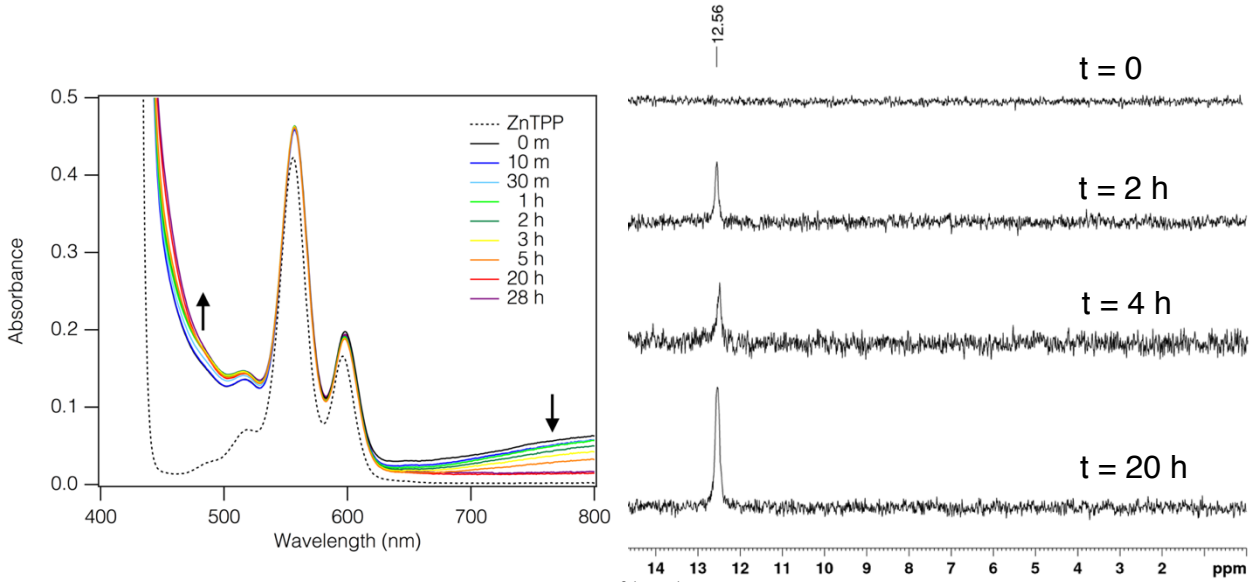

Figure 4.11. (A) Electronic-absorption and (B) $^{31}P\{^1H\}$ NMR spectra of a solution containing $\mathbf{1}^+$ (0.8 mM), PhOH (0.5 M), **4** (10 mM), and ZnTPP (50 μM) in CH_3CN under H_2/CO_2 (28:72) during photolysis (λ_{ex} = 590 nm).

The second set of photochemical experiments were designed to demonstrate the light-driven RWGS reaction using all components. A wide array of conditions were explored, involving variation of the relative and absolute concentrations of ZnTPP, $\mathbf{1}^+$, **2**, and **4**, with the aim of using these variables to control the relative rates of productive and unproductive electron transfer reactions. The results are compiled in Table 4.4.

Table 4.4. Conditions and Results from Photochemical RWGS Experiments with ZnTPP, $\mathbf{1}^+$, **2**, and **4**, under CO_2/H_2.

Time	[$\mathbf{1}^+$] (mM)	[2] (mM)	[4] (mM)	CO Production
48 h	0.1	1.0	10	Trace
48 h	7.0	1.2	10	0
48 h[a]	1.0[a]	1.0[a]	10[b]	0[a]
72 h	0.7	1.4	10	Trace
24 h	0.5	1.0	10	Trace
96 h	1.3	1.3	10	0
48 h	0.8	1.0	5	Trace
96 h	1.1	0.1	5	0
96 h	1.1	0.1	10	0
96 h	1.1	2.0	5	0
24 h	3.0	0.5	5	0
120 h	0.6	0.5	10	Trace
48 h	0.7	1.0	10	0.1

[a] All experiments were carried out under 1 atm (0.28 M) CO_2 in 0.1 M [NBu_4^n][PF_6] CH_3CN with 0.5 M PhOH, 80 μM ZnTPP, and irradiation from a 590 nm LED. For experimental details see Section 7.3.3. All potentials are referenced to the $FeCp_2^{0/+}$ couple. [b]With 0.1 M [NBu^n_4][PF_6].

Unfortunately, no experiment yielded more than trace production of CO, despite incorporating a wide array of catalyst concentrations (0.1–7 mM $\mathbf{1}^+$; 0.1–2 mM **2**) and the amounts of acid and base shown to photogenerate $\mathbf{1H}^+$ (vide infra). Thus, the light-driven RWGS reaction was not successfully demonstrated. The precise reason for the system's failure to produce CO is unknown, though it is likely due to limited reduction of **2** and/or its rapid deactivation by back-electron transfer. One possible process that could prevent the reduction of **2** by $ZnTPP^-$ is the reduction of $\mathbf{1}^+$ to **1**, which has a larger thermodynamic driving force from $ZnTPP^-$ ($E_{1/2}(\mathbf{1}^{+/0})$ = −1.42 V, ΔG = −0.32 V, CH_3CN)[54] than does the reduction of **2** ($\Delta G \cong$ −0.05 V, CH_3CN).[53] Alternatively, sensitized $\mathbf{2}^-$ might reduce $\mathbf{1}^+$ to **1** more rapidly than it can be trapped via Cl^- loss and subsequent coordination of CO_2. Due to the relatively low reduction potential of $\mathbf{1}^+$, there are

no CO_2 reduction catalysts that can be driven at potentials positive of the $\mathbf{1}^{+/0}$ couple. To circumvent the unproductive reduction of $\mathbf{1}^+$, a system could be developed with a different H_2 oxidation catalyst, such as $FeCp^R(P_2N)$,[37] which cannot be reduced from its resting state. However other issues would arise, particularly regarding the selection of a compatible acid/base pair.

4.4. Conclusions

The efforts to demonstrate the photochemically driven RWGS reaction detailed herein were unsuccessful. The key design criteria for a system capable of accomplishing the light-driven RWGS reaction have been elucidated, with it being found that $\mathbf{1}^+$ and **2** are promising catalysts for such an application. It was also demonstrated that electrochemical techniques can be utilized to efficiently screen the prospective components of artificial photosynthetic systems. CO_2 reduction by **2** has been further probed, with it being established that (1) catalysis is inhibited by sterically unencumbered amines and that (2) weak proton sources, like phenol and TFE, are needed to disfavor catalytic proton reduction. Phenol and **4** were found to be a competent acid-base pair to be used with $\mathbf{1}^+$ and **2** in a system for accomplishing the light-driven RWGS reaction. It was subsequently demonstrated that hydrogen can be activated through the photochemical sensitization of $\mathbf{1}^+$ by ZnTPP (T_1) in the presence of phenol and **4**, generating $ZnTPP^-$. Unfortunately, the photochemical experiments intended to demonstrate the light-driven RWGS reaction yielded no more than trace production of CO. We postulate that the failure to accomplish the RWGS reaction is due to limited sensitization of **2** and/or its rapid deactivation by back-electron transfer. This work details some key issues in the development of artificial photosynthetic systems, particularly regarding the necessity of avoiding kinetically-favored unproductive pathways.

4.5. References

1. Concepcion, J. J.; House, R. L.; Papanikolas, J. M.; Meyer, T. J. Chemical Approaches to Artificial Photosynthesis. *Proc. Natl. Acad. Sci. U. S. A.* **2012**, *109*, 15560–15564.

2. Cook, T. R.; Dogutan, D. K.; Reece, S. Y.; Surendranath, Y.; Teets, T. S.; Nocera, D. G. Solar Energy Supply and Storage for the Legacy and Nonlegacy Worlds. *Chem. Rev.* **2010**, *110*, 6474–6502.

3. Lewis, N. S.; Nocera, D. G. Powering the Planet: Chemical Challenges in Solar Energy Uilization. *Proc. Natl. Acad. Sci. U. S. A.* **2006**, *103*, 15729–15735.

4. Kim, D.; Sakimoto, K. K.; Hong, D.; Yang, P. Artificial Photosynthesis for Sustainable Fuel and Chemical Production. *Angew. Chem., Int. Ed.* **2015**, *54*, 3259–3266.

5. Kärkäs, M. D.; Verho, O.; Johnston, E. V.; Åkermark, B. Artificial Photosynthesis: Molecular Systems for Catalytic Water Oxidation. *Chem. Rev.* **2014**, *24*, 11863–12001.

6. Frischmann, P. D.; Mahata, K.; Würthner, F. Powering the Future of Molecular Artificial Photosynthesis with Light-Harvesting Metallosupramolecular Dye Assemblies. *Chem. Soc. Rev.* **2013**, *42*, 1847–1870.

7. Sekizawa, K.; Maeda, K.; Domen, K.; Koike, K.; Ishitani, O. Artificial Z-scheme Constructed with a Supramolecular Metal Complex and Semiconductor for the Photocatalytic Reduction of CO_2. *J. Am. Chem. Soc.* **2013**, *135*, 4596–4599.

8. La Porte, N. T. Photosensitizing the Reverse Water-Gas Shift Reaction. Ph.D. Thesis, The University of Chicago, 2015.

9. La Porte, N. T.; Moravec, D. B.; Hopkins, M. D. Electron-Transfer Sensitization of H_2 Oxidation and CO_2 Reduction Catalysts Using a Single Chromophore. *Proc. Natl. Acad. Sci. U. S. A.* **2014**, *111*, 9745–9750.

10. Yamazaki, Y.; Takeda, H.; Ishitani, O. Photocatalytic Reduction of CO_2 Using Metal Complexes. *J. Photochem. Photobiol., C* **2015**, *25*, 106–137.

11. Tamaki, Y.; Ishitani, O. Supramolecular Photocatalysts for the Reduction of CO_2. *ACS Catal.* **2017**, *7*, 3394–3409.

12. Bonin, J.; Maurin, A.; Robert, M. Molecular Catalysis of the Electrochemical and Photochemical Reduction of CO_2 with Fe and Co Metal Based Complexes. Recent Advances. *Coord. Chem. Rev.* **2017**, *334*, 184–198.

13. Morris, A. J.; Meyer, G. J.; Fujita, E. Molecular Approaches to the Photocatalytic Reduction of Carbon Dioxide for Solar Fuels. *Acc. Chem. Res.* **2009**, *42*, 1983–1994.

14. Jacobs, G.; Davis, B. H. In *Catalysis*, The Royal Society of Chemistry: Cambridge, UK, 2007; pp 122–285.

15. Ettedgui, J.; Diskin-Posner, Y.; Weiner, L.; Neumann, R. Photoreduction of Carbon Dioxide to Carbon Monoxide with Hydrogen Catalyzed by a Rhenium(I) Phenanthroline−Polyoxometalate Hybrid Complex. *J. Am. Chem. Soc.* **2011**, *133*, 188–190.

16. Yang, J. Y.; Smith, S. E.; Liu, T.; Dougherty, W. G.; Hoffert, W. A.; Kassel, W. S.; DuBois, M. R.; DuBois, D. L.; Bullock, R. M. Two Pathways for Electrocatalytic Oxidation of Hydrogen by a Nickel Bis(diphosphine) Complex with Pendant Amines in the Second Coordination Sphere. *J. Am. Chem. Soc.* **2013**, *135*, 9700–9712.

17. Yang, J. Y.; Chen, S.; Dougherty, W. G.; Kassel, W. S.; Bullock, R. M.; DuBois, D. L.; Raugei, S.; Rousseau, R.; Dupuis, M.; DuBois, M. R. Hydrogen Oxidation Catalysis by a Nickel Diphosphine Complex with Pendant *Tert*-Butyl Amines. *Chem. Commun.* **2010**, *46*, 8618–8620.

18. Niklas, J.; Westwood, M.; Mardis, K. L.; Brown, T. L.; Pitts-McCoy, A. M.; Hopkins, M. D.; Poluektov, O. G. X-ray Crystallographic, Multifrequency Electron Paramagnetic Resonance, and Density Functional Theory Characterization of the $Ni(P^{Cy}_2N^{tBu}_2)_2^{n+}$ Hydrogen Oxidation Catalyst in the Ni(I) Oxidation State. *Inorg. Chem.* **2015**, *54*, 6226–6234.

19. Kuramochi, Y.; Itabashi, J.; Fukaya, K.; Enomoto, A.; Yoshida, M.; Ishida, H. Unexpected Effect of Catalyst Concentration on Photochemical CO_2 Reduction by *trans(Cl)*-$Ru(bpy)(CO)_2Cl_2$: New Mechanistic Insight into the $CO/HCOO^-$ Selectivity. *Chem. Sci.* **2015**, *6*, 3063–3074.

20. Bertrand, S.; Hoffman, N.; Pete, J.-P. Highly Efficient and Stereoselective Radical Addition of Tertiary Amines to Electron-Deficient Alkenes—Application to the Enantioselective Synthesis of Necine Bases. *Eur. J. Org. Chem.* **2000**, 2227–2238.

21. Biaggi, C.; Benaglia, M.; Raimondi, L.; Cozzi, F. Organocatalytic Synthesis of Dipyrromethanes by the Addition of N-methylpyrrole to Aldehydes. *Tetrahedron* **2006**, *62*, 12375–12379.

22. Capps, K. B.; Bauer, A.; Kiss, G.; Hoff, C. D. The Rate and Mechanism of Oxidative Addition of H_2 to the $Cr(CO)_3C_5Me_5$ Radical—Generation of a Model for Reaction of H_2 with the $Co(CO)_4$ Radical. *J. Organomet. Chem.* **1999**, *586*, 23–30.

23. Raugei, S.; Helm, M. L.; Hammes-Schiffer, S.; Appel, A. M.; O'Hagan, M.; Wiedner, E. S.; Bullock, R. M. Experimental and Computational Mechanistic Studies Guiding the Rational Design of Molecular Electrocatalysts for Production and Oxidation of Hydrogen. *Inorg. Chem.* **2016**, *55*, 445–460.

24. Bullock, R. M.; Helm, M. L. Molecular Electrocatalysts for Oxidation of Hydrogen Using Earth-Abundant Metals: Shoving Protons Around with Proton Relays. *Acc. Chem. Res.* **2015**, *48*, 2017–2026.

25. DuBois, D. L. Development of Molecular Electrocatalysts for Energy Storage. *Inorg. Chem.* **2014**, *53*, 3935–3960.

26. Shaw, W. J.; Helm, M. L.; DuBois, D. L. A Modular, Energy-Based Approach to the Development of Nickel Containing Molecular Electrocatalysts for Hydrogen Production and Oxidation. *Biochim. Biophys. Acta* **2013**, *1827*, 1123–1139.

27. DuBois, M. R.; DuBois, D. L. The Roles of the First and Second Coordination Spheres in the Design of Molecular Catalysts for H_2 Production and Oxidation. *Chem. Soc. Rev.* **2009**, *38*, 62–72.

28. Rakowski DuBois, M.; DuBois, D. L. Development of Molecular Electrocatalysts for CO_2 Reduction and H_2 Production/Oxidation. *Acc. Chem. Res.* **2009**, *42*, 1974–1982.

29. Ogo, S. H_2 and O_2 activation by [NiFe] Hydrogenases – Insights from Model Complexes. *Coord. Chem. Rev.* **2017**, *334*, 43–53.

30. Simmons, T. R.; Artero, V. Catalytic Hydrogen Oxidation: Dawn of a New Iron Age. *Angew. Chem., Int. Ed.* **2013**, *52*, 6143–6145.

31. Gloaguen, F.; Rauchfuss, T. B. Small Molecule Mimics of Hydrogenases: Hydrides and Redox. *Chem. Soc. Rev.* **2009**, *38*, 100–108.

32. Tard, C.; Pickett, C. J. Structural and Functional Analogues of the Active Site of the [Fe]-, [NiFe]-, and [FeFe]-Hydrogenases. *Chem. Rev.* **2009**, *109*, 2245–2274.

33. Stolley, R. M.; Darmon, J. M.; Das, P.; Helm, M. L. Nickel Bis-Diphosphine Complexes: Controlling the Binding and Heterolysis of H_2. *Organometallics* **2016**, *35*, 2965–2974.

34. Liu, T.; Liao, Q.; O'Hagan, M.; Hulley, E. B.; DuBois, D. L.; Bullock, R. M. Iron Complexes Bearing Diphosphine Ligands with Positioned Pendant Amines as Electrocatalysts for the Oxidation of H_2. *Organometallics* **2015**, *34*, 2747–2764.

35. Darmon, J. M.; Raugei, S.; Liu, T.; Hulley, E. B.; Weiss, C. J.; Bullock, R. M.; Helm, M. L. Iron Complexes for the Electrocatalytic Oxidation of Hydrogen: Tuning Primary and Secondary Coordination Spheres. *ACS Catal.* **2014**, *4*, 1246–1260.

36. Liu, T.; Dubois, D. L.; Bullock, R. M. An Iron Complex with Pendent Amines as a Molecular Electrocatalyst for Oxidation of Hydrogen. *Nat. Chem.* **2013**, *5*, 228–233.

37. Darmon, J. M.; Kumar, N.; Hulley, E. B.; Weiss, C. J.; Raugei, S.; Bullock, R. M.; Helm, M. L. Increasing the Rate of Hydrogen Oxidation Without Increasing the Overpotential: A Bio-Inspired Iron Molecular Electrocatalyst with an Outer Coordination Sphere Proton Relay. *Chem. Sci.* **2015**, *6*, 2737–2745.

38. Francke, R.; Schille, B.; Roemelt, M. Homogeneously Catalyzed Electroreduction of Carbon Dioxide-Methods, Mechanisms, and Catalysts. *Chem. Rev.* **2018**.

39. Elgrishi, N.; Chambers, M. B.; Wang, X.; Fontecave, M. Molecular Polypyridine-Based Metal Complexes as Catalysts for the Reduction of CO_2. *Chem. Soc. Rev.* **2017**, *46*, 761–796.

40. Stanbury, M.; Compain, J.-D.; Chardon-Noblat, S. Electro and Photoreduction of CO_2 Driven by Manganese-Carbonyl Molecular Catalysts. *Coord. Chem. Rev.* **2018**, *361*, 120–137.

41. Takeda, H.; Cometto, C.; Ishitani, O.; Robert, M. Electrons, Photons, Protons and Earth-Abundant Metal Complexes for Molecular Catalysis of CO_2 Reduction. *ACS Catal.* **2016**, *7*, 70–88.

42. Kumar, B.; Llorente, M.; Froehlich, J.; Dang, T.; Sathrum, A.; Kubiak, C. P. Photochemical and Photoelectrochemical Reduction of CO_2. *Annu. Rev. Phys. Chem.* **2012**, *63*, 541–569.

43. Manbeck, G. F.; Fujita, E. A Review of Iron and Cobalt Porphyrins, Phthalocyanines and Related Complexes for Electrochemical and Photochemical Reduction of Carbon Dioxide. *J. Porphyrins Phthalocyanines* **2015**, *19*, 45–64.

44. Liu, X.; Inagaki, S.; Gong, J. Heterogeneous Molecular Systems for Photocatalytic CO_2 Reduction with Water Oxidation. *Angew. Chem., Int. Ed.* **2016**, *55*, 14924–14950.

45. Reithmeier, R.; Bruckmeier, C.; Rieger, B. Conversion of CO_2 via Visible-Light Promoted Homogeneous Redox Catalysis. *Catalysts* **2012**, *2*, 544–571.

46. Costentin, C.; Drouet, S.; Robert, M.; Saveant, J. M. A Local Proton Source Enhances CO_2 Electroreduction to CO by a Molecular Fe Catalyst. *Science* **2012**, *338*, 90–94.

47. Rao, H.; Schmidt, L. C.; Bonin, J.; Robert, M. Visible-Light-Driven Methane Formation From CO_2 with a Molecular Iron Catalyst. *Nature* **2017**, *548*, 74–77.

48. Thompson, D. W.; Ito, A.; Meyer, T. J. $[Ru(bpy)_3]^{2+}$* and Other rRmarkable Metal-to-Ligand Charge Transfer (MLCT) Excited States. *Pure Appl. Chem.* **2013**, *85*, 1257–1305.

49. Grice, K. A. Carbon Dioxide Reduction with Homogenous Early Transition Metal Complexes: Opportunities and Challenges for Developing CO_2 Catalysis. *Coord. Chem. Rev.* **2017**, *336*, 78–95.

50. Grice, K. A.; Kubiak, C. P. In *Adv. Inorg. Chem.*, Aresta, M., van Eldik, R., Eds. Academic Press: Waltham, MA, 2014; Vol. 66, pp 163–188.

51. Riplinger, C.; Sampson, M. D.; Ritzmann, A. M.; Kubiak, C. P.; Carter, E. A. Mechanistic Contrasts Between Manganese and Rhenium Bipyridine Electrocatalysts for the Reduction of Carbon Dioxide. *J. Am. Chem. Soc.* **2014**, *136*, 16285–16298.

52. Morimoto, T.; Nakajima, T.; Sawa, S.; Nakanishi, R.; Imori, D.; Ishitani, O. CO_2 Capture by a Rhenium(I) Complex with the Aid of Triethanolamine. *J. Am. Chem. Soc.* **2013**, *135*, 16825–16828.

53. Machan, C. W.; Sampson, M. D.; Kubiak, C. P. A Molecular Ruthenium Electrocatalyst for the Reduction of Carbon Dioxide to CO and Formate. *J. Am. Chem. Soc.* **2015**, *137*, 8564–8571.

54. Darwent, J. R.; Douglas, P.; Harriman, A.; Porter, G.; Richoux, M.-C. Metal Phthalocyanines and Porphyrins as Photosensitizers for Reduction of Water to Hydrogen. *Coord. Chem. Rev.* **1982**, *44*, 83–126.

55. Prier, C. K.; Rankic, D. A.; MacMillan, D. W. C. Visible Light Photoredox Catalysis with Transition Metal Complexes: Applications in Organic Synthesis. *Chem. Rev.* **2013**, *113*, 5322–5363.

56. Kaljurand, I.; Kütt, A.; Sooväli, L.; Rodima, T.; Mäemets, V.; Leito, I.; Koppel, I. A. Extension of the Self-Consistent Spectrophotometric Basicity Scale in Acetonitrile to a Full Span of 28 pK_a Units: Unification of Different Basicity Scales. *J. Org. Chem.* **2005**, *70*, 1019–1028.

57. Ho, M. H.; O'Hagan, M.; Dupuis, M.; DuBois, D. L.; Bullock, R. M.; Shaw, W. J.; Raugei, S. Water-Assisted Proton Delivery and Removal in Bio-Inspired Hydrogen Production Catalysts. *Dalton Trans.* **2015**, *44*, 10969–10979.

58. Franz, J. A.; O'Hagan, M.; Ho, M.-H.; Liu, T.; Helm, M. L.; Lense, S.; DuBois, D. L.; Shaw, W. J.; Appel, A. M.; Raugei, S.; Bullock, R. M. Conformational Dynamics and Proton Relay Positioning in Nickel Catalysts for Hydrogen Production and Oxidation. *Organometallics* **2013**, *32*, 7034–7042.

59. Stolley, R. M.; Darmon, J. M.; Helm, M. L. Solvent and Electrolyte Effects on $Ni(P^R_2N^{R'}_2)_2$-Catalyzed Electrochemical Oxidation of Hydrogen. *Chem. Commun.* **2014**, *50*, 3681–3684.

60. Maeda, C.; Miyazaki, Y.; Ema, T. Recent Progress in Catalytic Conversions of Carbon Dioxide. *Catal. Sci. Technol.* **2014**, *4*, 1482–1497.

CHAPTER 5: Ligand Effects on Electrocatalytic CO_2 Reduction by Ruthenium–Bipyridyl Complexes. Characterization of a Photostable, non-CO-Bearing Catalyst

5.1. Introduction

The environmental consequences of rising atmospheric CO_2 levels have stimulated significant research into the development of catalytic approaches to converting CO_2 to fuels and other useful chemicals. Progress in this field has been detailed by many recent review articles.[1-48] The conversion of CO_2 to energy-rich compounds via electrochemical methods typically proceeds through multiple proton-coupled electron-transfer reactions. For an excellent discussion of this topic please see, among others,[36-43] a recent review by Francke *et al*.[45] For example, the reduction of CO_2 to CO requires coordinated delivery of two electrons and two protons, and that to methanol requires six such reducing equivalents. A common design approach for coordinating the electron-transfer and proton-transfer reactions of molecular transition-metal electrocatalysts is to employ π-unsaturated redox-active ligands, such as polypyridines, that undergo a ligand-centered reduction at a potential comparable to those of the metal-centered substrate-transformation processes.[42-44, 46, 48] In such catalysts, the presence of the reduced ligand facilitates rapid intramolecular electron transfer to the metal in sequence with protonation steps.[46]

Metal-polypyridyl electrocatalysts for CO_2 reduction have been extensively investigated, with a recent review describing the properties of over 70 different complexes.[46] The most common architecture among these catalysts are complexes of the form $M(bpy^R)(CO)_nX_{4-n}$, where bpy^R is 2,2′-bipyridine or a derivative in which R substituents are employed to modify its electronic or steric properties, and X typically is an anionic ligand. Intuitively, the preponderance of CO as a ligand within metal-polypyridyl catalysts is logical because of its ability to stabilize the low metal oxidation states that are produced during CO_2 reduction reactions. Indeed, many highly active

catalysts bear multiple CO ligands, as illustrated by the extensively studied $Re(bpy^R)(CO)_3Cl$, $Mn(bpy^R)(CO)_3Cl$, and $Ru(bpy^R)(CO)_2Cl_2$ catalyst families.[45-48] Efforts to improve the catalytic properties of these compounds have largely focused on understanding the effects of varying the bpy^R substituents.[8-10, 33, 42, 44-48] In contrast, the question of whether neutral ligands other than CO will support comparable catalytic activity has been much less explored.[45-46] In addition to the potential opportunities for steric and electronic control that such derivatives present, CO-free catalysts are also of interest because metal–carbonyl compounds are often light sensitive, making photoinduced CO loss a potential catalyst degradation pathway.[49]

One complex that exemplifies these points is *trans(Cl)*-$Ru(bpy)(CO)_2Cl_2$ (**1**, Figure 5.1), which is an active electrocatalyst for the reduction of CO_2 to CO and formate under a variety of reaction conditions.[50-52] Compound **1** has also been employed in artificial-photosynthetic systems for CO_2 reduction, wherein the electrons are supplied from a photoredox chromophore and sacrificial reductant.[53-55] The derivative $Ru(bpy^{mesityl})(CO)_2Cl_2$ (**1′**, Figure 5.1) has recently been found to possess improved stability and properties owing to its sterically hindering mesityl groups,[56] and has also been employed in light-driven systems.[54] The question of how the catalytic function of these $Ru(bpy^R)(CO)_2Cl_2$ compounds, with respect to CO_2 reduction, is affected by replacement of CO with other neutral ligands has only been investigated computationally thus far.[57] Ramakrishnan *et al.* probed the reactivity of single-reduced **1** (as $[Ru(bpy)(CO)_2(CH_3CN)Cl]^+$) and compared its reactivity towards CO_2 to the analogue $[Ru(bpy)(PMe_3)_2(CH_3CN)Cl]^+$. The substitution of CO for more electron-donating PMe_3 groups increases the nucleophilicity of the Ru center and enables CO_2 binding at the first reduction. Beyond its fundamental interest, this question is relevant because **1** is photosensitive.[58-69] Photolysis of **1** with near-UV light in acetonitrile (a common solvent for electrocatalytic CO_2

reduction reactions) is reported to produce, in sequence, the photosensitive compounds *cis(Cl)*-Ru(bpy)(CO)(CH_3CN)Cl_2 (**2*c***) and *trans(CH₃CN)*-Ru(bpy)(CH_3CN)$_2Cl_2$ (**3**), and ultimately yielding *mer*-[Ru(bpy)(CH_3CN)$_3$Cl]$^+$ (**4**$^+$) as the final product of photolysis (Figure 5.1).[67-68] If **1** is also photosensitive to visible light, this would have potential implications for its use in artificial-photosynthetic systems that employ common transition-metal photoredox chromophores,[53-55] and raise the question of whether photoproducts of **1** formed by adventitious photolysis in room light are active in and contribute to electrocatalytic CO_2 reduction in studies of this compound.

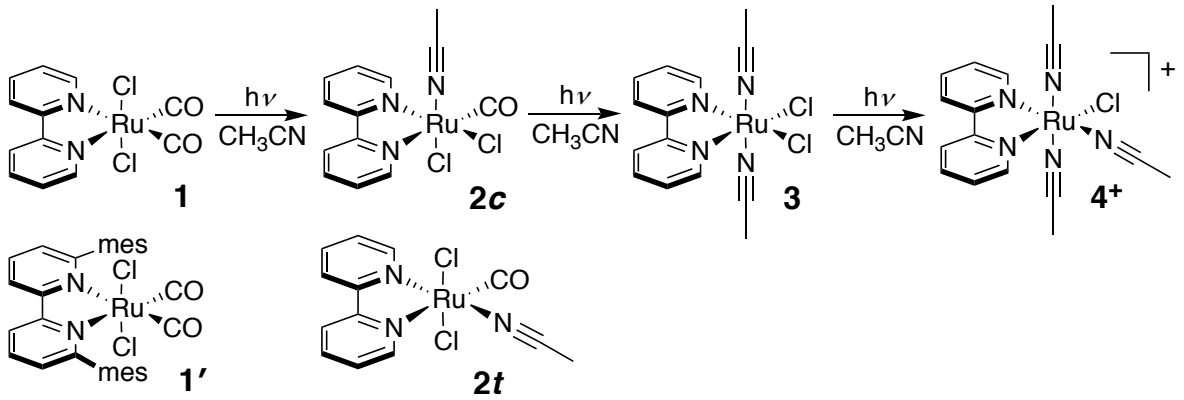

Figure 5.1. The reported photochemical reactivity of **1** under 366 nm irradiation in CH_3CN,[67-68] and depictions of related compounds (mes = 2,4,6-trimethylphenyl).

The electrochemistry of **1** under CO_2 in homogenous acetonitrile-H_2O solutions has been explored by cyclic voltammetry.[52] A catalytic current enhancement is observed, and with titration of H_2O (0–10%) the amount of current increases concurrently with a positive shift of the onset potential of the catalytic wave. This behavior is ascribed to **1** as a molecular electrocatalyst; although **1** electropolymerizes upon reduction under N_2, forming [Ru(bpy)(CO)$_2$]$_n$, the anodic feature assigned to dissolution of [Ru(bpy)(CO)$_2$]$_n$ is suppressed under CO_2—indicating that polymerization is not readily occurring upon reduction.[52] Bulk electrolyses with **1** under CO_2 have been carried out under a variety of conditions,[51-52] with CO and formate being detected as primary products in all cases. Product selectivity is greatly influenced by the solvent and proton source used.

These considerations motivated an investigation of the comparative electrocatalytic properties of **1**, *trans(Cl)*-Ru(bpy)(CO)(CH_3CN)Cl_2 (**2*t***), **3**, and $\mathbf{4}^+$ (Figure 5.1) for the reduction of CO_2. We report that **1** is highly photosensitive to visible light, producing **2*c***, **3**, and $\mathbf{4}^+$; **2*t*** may be present as a minor product. Compounds **1**, **2*t***, **3**, and $\mathbf{4}^+$ are found to be electrocatalysts for the reduction of CO_2 to CO and formate, and for H^+ to H_2, in mixed acetonitrile–phenol solutions. Among these catalysts, the photostable, non-CO bearing compound $\mathbf{4}^+$ exhibits the highest Faradaic efficiency for CO_2 reduction. This indicates that use of CO ligands is not a prerequisite for optimizing catalytic function within this class of ruthenium polypyridyl complexes, and suggests that further variation of the neutral ligands within the $[Ru(bpy)L_3Cl]^+$ motif may provide opportunities for developing improved catalysts. The photostability of $\mathbf{4}^+$ also confers the advantage that it can be studied under routine laboratory lighting conditions, unlike the photosensitive catalysts, and will be more robust in artificial-photosynthetic systems for CO_2 reduction.

5.2. Experimental Section

Materials. Acetonitrile used for syntheses, electrochemistry, photochemistry, and electronic-absorption spectroscopy was HPLC grade and purified by passage under nitrogen pressure through two 4.5 in. × 24 in. (1 gal) columns of activated A2 alumina.[70] Acetonitrile (for recrystallizations), ethyl acetate, methanol, hexane, chloroform, and toluene (all HPLC grade); diethyl ether and ethanol (anhydrous); trimethylamine *N*-oxide dihydrate (98%, stored under N_2); and CD_3CN were used as received. Compounds **1**,[50] **3**,[71] and **1′**[56] were synthesized according to standard procedures; **2*t*** was prepared following an outline reported for its synthesis[72] (see Supporting Information). Ferrocene and $[NBu^n_4][PF_6]$ were recrystallized twice from ethanol and

dried for a minimum of 18 h under vacuum at 120 °C. CO_2 (research grade, 99.9999%) and phenol (≥99%, unstabilized, stored under N_2 in the dark) were used as received.

Spectroscopy. ^{1}H NMR spectra were recorded using a Bruker DRX 400 NMR spectrometer. Chemical shifts were measured relative to the isotopic impurity in the CD_3CN solvent (δ 1.94).[73] Electronic-absorption spectra were obtained with a Cary 300 UV-Vis spectrophotometer of samples contained in quartz cuvettes. Infrared spectra were recorded with a Thermo Scientific Nicolet NEXUS 670 FT-IR spectrometer.

Synthesis of *mer*-[Ru(bpy)(CH_3CN)$_3$Cl]Cl (4Cl). A vigorously stirred, pale yellow solution of **1** (0.070 g, 0.18 mmol) in acetonitrile (250 mL) under N_2 was irradiated for 24 h by an array of white LEDs, resulting in an orange solution. (The photolysis can also be conducted using a 26 W compact-fluorescent lightbulb with an irradiation time of one week.) The solvent was removed under vacuum to give a dark red residue. In air, the residue was washed with toluene (3 × 50 mL) and ethyl acetate (3 × 50 mL). The remaining red solid was dissolved in *ca*. 10 mL acetonitrile and the resulting solution filtered through a fine-porosity sintered-glass filter. Slow addition of diethyl ether (*ca*. 100 mL) resulted in precipitation of red-orange microcrystals, which were collected by filtration and dried under vacuum (yield 0.043 g, 53%). A second crop of product was obtained by removing the solvent from the filtrate under reduced pressure, dissolving the red-orange residue in a minimal volume of acetonitrile, and layering the resulting solution with diethyl ether. After standing at room temperature for 2 days, crystals of the product had formed that were suitable for X-ray diffraction experiments (total yield 0.059 g, 73%). ^{1}H NMR (CD_3CN, 400 MHz, 295 K; Figures 7.4.4 and 7.4.5): δ 9.79 (d, 1H, J_{HH} = 5.6 Hz, bpy), 9.12 (d, 1H, J_{HH} = 5.6 Hz, bpy), 8.36 (d, 2H, J_{HH} = 8.0 Hz, bpy), 8.03 (m, 2H, bpy), 7.61 (m, 2H, bpy), 2.66 (s, 3H, CH_3CN), 2.19

(s, 6H, CH_3CN). UV-Vis (CH_3CN, Figure 7.4.7): λ_{max} = 437 nm. X-ray crystal structure: see Chapter 7.4.

Electrochemistry. See Chapter 7.4 for full details of electrochemical procedures. Experiments were performed at room temperature under either a N_2 or CO_2 atmosphere in CH_3CN solution containing 0.1 M [NBu^n_4][PF_6] as electrolyte. Potentials were determined relative to $FeCp_2$ or $FeCp^*_2$ internal standards and are reported relative to $FeCp_2^{0/+}$. Cyclic voltammetry experiments were performed in a single-compartment cell with a three-electrode configuration consisting of a glassy carbon working electrode (A = 0.07 cm^2), a platinum auxiliary electrode (A = 0.02 cm^2), and a silver wire quasi-reference electrode. Controlled potential electrolysis experiments were performed in a sealed four-neck cell (total volume = 100 mL). A three-electrode configuration was used that consisted of a reticulated vitreous carbon foam working electrode (ERG Materials & Aerospace, ca. 15 mm × 10 mm × 5 mm), a platinum wire auxiliary electrode that was separated from the working solution by a medium porosity glass frit, and a Ag/Ag^+ reference electrode (BASi, 0.01 M $AgNO_3$ in CH_3CN containing 0.1 M [NBu^n_4][PF_6]) that was separated from the working solution by a CoralPor tip. The working solution (40 mL) contained a known amount of catalyst, 0.5 M PhOH, and a stir bar. The auxiliary compartment contained 5 mL of a CH_3CN solution containing 0.1 M ferrocene (as a sacrificial reductant) and 0.1 M [NBu^n_4][PF_6]. Controlled-potential electrolysis products were analyzed by gas chromatography (CO, H_2) and ^{1}H-NMR spectroscopy (formate).

5.3. Results and Discussion

5.3.1. Photochemistry of 1 with Visible Light. It has previously been reported that exhaustive UV photolysis (λ_{ex} = 366 nm) of **1** in CH_3CN provides **4Cl** as the terminal product, with ***2c*** and **3** as photosensitive intermediates (vide supra).[67-68] It is found here that **1** also

undergoes rapid photosubstitution with visible light, even though this pale-yellow compound absorbs very weakly in the visible-wavelength region (Figure 5.2). Irradiation of an acetonitrile solution of **1** at 455 nm (blue LED) results in the appearance, within minutes, of an electronic-absorption band centered at 450 nm. This band is at the same position and has the same shape as that reported for **2*c*** during the UV photolysis of **1**.[68] The ^{1}H-NMR spectrum previously reported for a sample of **2*c*** prepared in situ by UV photolysis of **1** contained several unassigned resonances of moderate intensity;[67] one at 9.34 ppm is identical in chemical shift and multiplicity to a resonance reported here for **2*t*** (Table 7.4.1), suggesting that **2*t*** is a minor product of the photolysis of **1** at 366 nm. Further 455-nm photolysis of the sample results in the appearance of shoulders near 377 and 550 nm (Figure 5.2.), which are coincident with the positions of bands reported for an independently synthesized sample of **3**[71] and similar to those observed in samples prepared under UV photolysis.[68] Extended photolysis eventually results in the full depletion of the bands for **1**, **2*c***, and **3** and formation of a strong band at 437 nm (Figure 5.2.), identical to that found for $\mathbf{4}^{+}$.[68] These results demonstrate that **1**, **2*c***, and **3** are all photosensitive to visible light, and that $\mathbf{4}^{+}$ is photostable (or photostationary) in acetonitrile solution.

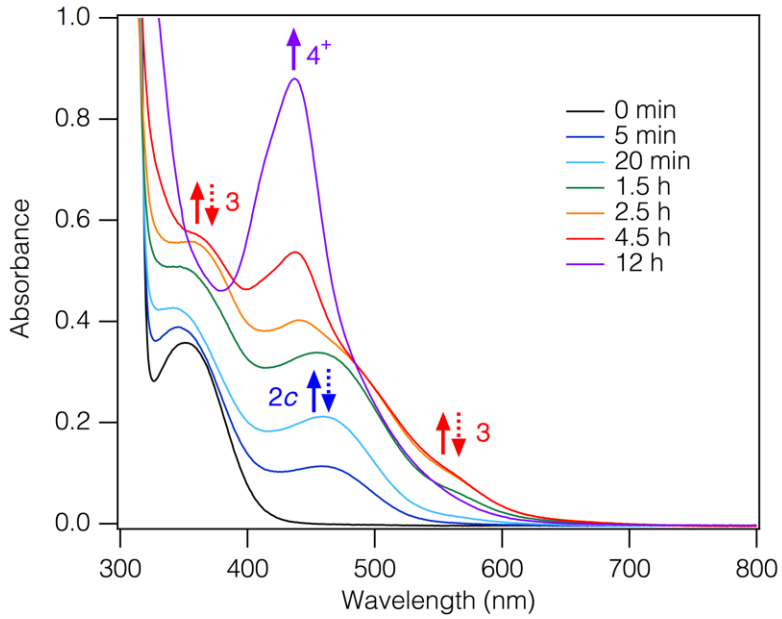

Figure 5.2. Electronic-absorption spectra during the photolysis of **1** in CH_3CN (λex = 455 nm). Solid and dashed arrows indicate the growth and disappearance, respectively, of bands associated with the indicated compounds.

Preparative-scale photolysis of **1** using either a white LED or compact fluorescent bulb in CH_3CN solution provided, following workup, a pure sample of **4Cl** whose ^{1}H-NMR spectrum is largely similar to that reported for a previously reported sample that was prepared in-situ by UV photolysis. The chemical shift of one CH_3CN ligand for the purified sample prepared here differs substantially from that reported for the in-situ sample (2.66 ppm; in situ,[67] 2.12 ppm; Table 7.4.1); the cause for this discrepancy is unknown. The identity of the product as **4Cl** was confirmed via an X-ray crystal structure (Figure 7.4.8), metrical data for which are in close agreement with those for a previously reported (nonisomorphous) crystal structure of the salt (Table 7.4.4).[67]

5.3.2. Electrochemistry of 1, 2*t*, 3, and 4^+. The isolated compounds **1**, **2*t***, **3**, and $\mathbf{4}^+$ were investigated by cyclic voltammetry (CV) to establish baseline properties relevant to their electrocatalytic activity. Prior detailed studies of **1**[52, 74-75] and **3**[71] by CV and coulometric methods found that they possess a reversible one-electron metal-centered oxidation and an irreversible two-electron reduction; the reported CV of **4Cl** exhibits similar features,[68] suggesting the same

assignments. The redox potentials determined under the conditions of the present study for **1**, **3**, and **4Cl** (Table 5.1, Figures 7.4.8–10) are in good agreement with earlier values when corrected for the difference in reference standard (ΔE < 0.1 V, Table 7.4.5). The CV of ***2t*** (Figure 5.3.), which has not previously been studied, also shows a reversible 1e$^-$ oxidation and irreversible reduction, with the latter inferred to be a two-electron process based on its peak current relative to the oxidation. The potentials observed for ***2t*** are within 20–40 mV of those reported for ***2c***[68] (Table 7.4.5), as is reasonable for two compounds with identical ligand sets. Among these four compounds, the CV of **1** (Figure 7.4.9) is distinctive due to the appearance of a sharp anodic feature at −0.8 V that is present only following a sweep of the potential through that of the 2e$^-$ reduction. This feature has been assigned to an electroprecipitation-redissolution process for a film identified as $[Ru(bpy)(CO)_2]_n$;[50, 52, 74, 76] this is noted here because the polymer is an active electrocatalyst for CO_2 reduction,[52, 77-78] but is absent in the CVs of samples of **1** under electrocatalysis conditions of this study (vide infra).[79]

Table 5.1. Redox Potentials (V *vs*. $FeCp_2^{0/+}$) of **1**, ***2t***, **3**, and $\mathbf{4}^+$ from Cyclic Voltammetry.[a]

Compound	$E_{1/2}$ (Ox)	E_p[b] (Red)
1	+1.35	−1.61
2t	+0.70	−1.82
3	−0.01	−2.12
$\mathbf{4}^+$	+0.69	−1.88

[a] Measured in CH_3CN solution with 0.1 M $[NBu^n_4][PF_6]$. [b] E_p at a 0.1 V/s scan rate.

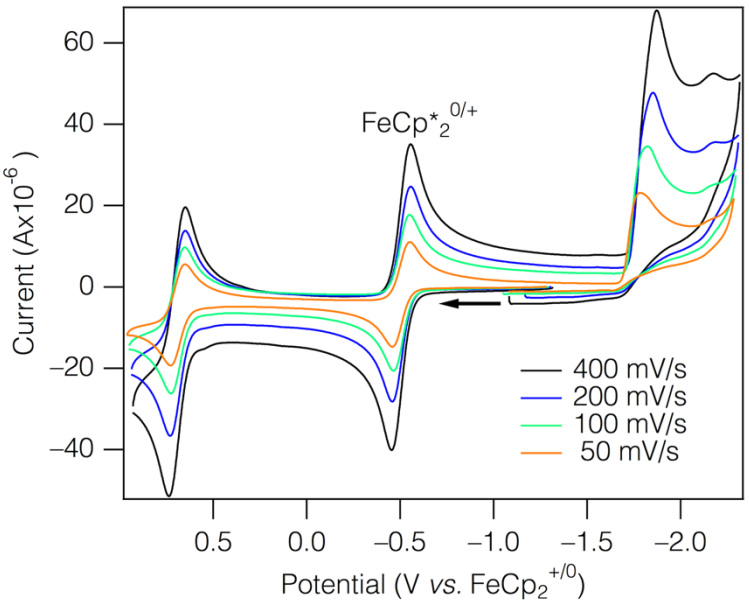

Figure 5.3. Cyclic voltammograms of **2*t*** (1.0 mM) in CH_3CN containing 0.1 M $[NBu^n_4][PF_6]$. The arrow indicates the direction of the scans. The reversibility of the $Ru^{II/III}$ couple was established via a Randles-Sevcik analysis (Figure 7.4.12).

The redox potentials of **1**, **2*t***, and **3** differ from each other in a manner consistent with the different electron-withdrawing abilities of the CO and CH_3CN supporting ligands. Successive replacement of CO by CH_3CN from **1** to **2*t*** to **3** results in a decrease in oxidation potential of *ca.* 0.7 V per substitution and in a shift of the reduction to more negative potentials by approximately 0.2–0.3 V per substitution, with the smaller shifts for the reduction potential reflecting the fact this process is ligand centered rather than metal centered.

5.3.3. Electrocatalytic CO_2 and proton reduction by 1, 2*t*, 3, and 4^+. The electrocatalytic reduction of CO_2 by **1, 2*t***, **3**, and $\mathbf{4}^+$ was studied in CH_3CN solution containing phenol as a proton source. Phenol was employed in order to allow direct comparison with results from a previous detailed study of electrocatalytic CO_2 reduction by **1′** using identical conditions.[56] The cyclic voltammograms of **1, 2*t***, **3**, and $\mathbf{4}^+$ in CH_3CN containing 0.5 M phenol under an atmosphere of either N_2 or CO_2 are shown in Figure 5.4. Under N_2, the CVs of all compounds exhibit a substantial increase in current at potentials negative of that of the first reduction, compared to those observed

in the absence of phenol. The onset potential for the current enhancement depends on the nature of the ligands, falling in the order *ca.* −1.7 V (**1**), −1.8 V (***2t***, $\mathbf{4}^+$), and −2.0 V *vs.* $FeCp_2^{0/+}$ (**3**). Under identical conditions, the CV of phenol in the absence of these compounds shows a steeply rising current beginning at *ca*. −2.0 V (Figure 7.4.13) that arises from proton reduction.[80] The fact that the onset potentials of current enhancement for **1**, ***2t***, and $\mathbf{4}^+$ are shifted to more positive potentials than that of phenol indicates that these complexes catalyze proton reduction. Consistent with this interpretation, the CVs of **1**, ***2t***, and $\mathbf{4}^+$ as a function of the concentration of phenol (Figures 7.4.13–15) show that the catalytic current rises steadily with added phenol. Gas-chromatographic (GC) analysis of the gas present in the headspace following extended reductive electrolysis confirms that H_2 is produced. In the case of **3**, it is not possible to distinguish between metal-catalyzed proton reduction and proton reduction at the electrode due to the overlap between their current responses (Figure 7.4.13). For **1**, it is noteworthy that the anodic feature observed at −0.8 V in the absence of phenol (Figure 7.4.9) that is associated with electrogenerated $[Ru(bpy)(CO)_2]_n$[50, 52, 74, 76] is absent in the presence of phenol (Figure 7.4.14). That a heterogeneous catalyst is not responsible for the observed catalytic activity for **1** was confirmed by an electrode rinse test (Figure 7.4.17).[81]

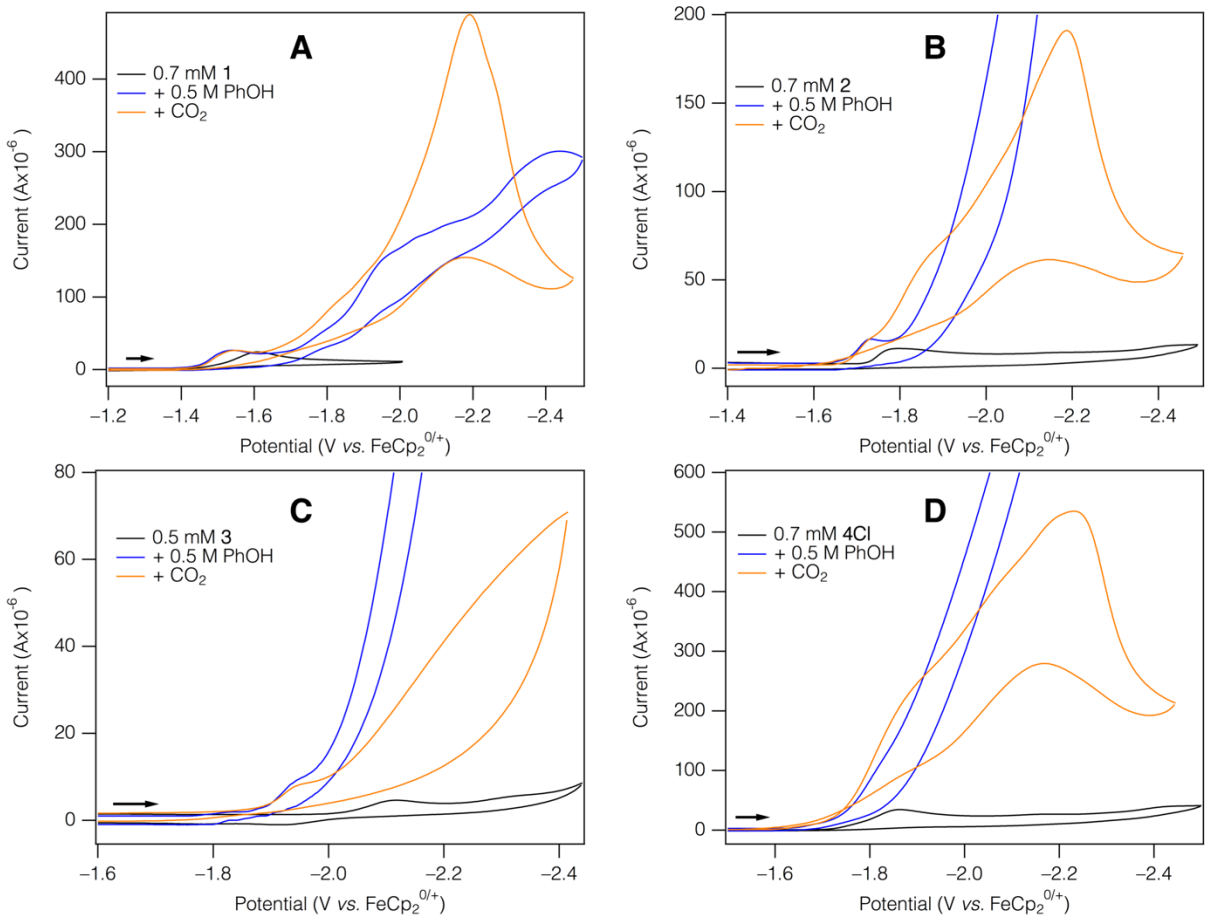

Figure 5.4. Cyclic voltammograms (ν = 0.1 V/s) of **1** (A), **2*t*** (B), **3** (C), and $\mathbf{4}^{+}$ (D) in CH_3CN containing 0.1 M $[NBu^n_4][PF_6]$ in the absence and presence of substrates. The black traces are for the compounds without substrate. The other traces are for samples that contain 0.5 M PhOH under N_2 atmosphere (blue) and CO_2 atmosphere (orange).

Addition of CO_2 (1 atm) to solutions of **1**, **2*t***, **3**, and $\mathbf{4}^{+}$ in acetonitrile containing 0.5 M phenol results in substantial changes to their cyclic voltammograms (Figure 5.4), consistent with the occurrence of electrocatalytic CO_2 reduction. The CVs of compounds **1**, **2*t***, and $\mathbf{4}^{+}$ exhibit peaked catalytic waves ($E_p \cong -2.2$ V), indicating both that CO_2 is depleted within the electrode double layer under these experimental conditions[82] and that the Faradaic efficiency of CO_2 reduction is much greater than for H_2 production (vide infra). The reduction potentials of the compounds do not change under CO_2 when compared to those in acetonitrile/phenol solution in the absence of CO_2.

The products formed *via* electrocatalyzed reduction of CO_2 and phenol by **1**, **2*t***, **3**, and **4** were identified as CO, H_2, and (except for **3**) formate, via GC and ^{1}H-NMR spectroscopic analyses of bulk-electrolyzed samples. These experiments also allowed determination of the Faradaic efficiencies for CO and H_2 production. The results are set out in Table 5.2. For **1**, **2*t***, and **4**, bulk electrolyses were carried out at two potentials (−1.80 and −2.20 V). These potentials were selected because the peak catalytic current is centered at *ca.* −2.2 V for **1**, **2*t***, and $\mathbf{4}^+$ and all three compounds exhibit an inflection in the current profile at *ca.* −1.8 V (Figure 5.4). Compound **3** was examined only at −2.2 V because it does not exhibit catalytic current at −1.8 V.

Table 5.2. Faradaic Efficiency and Product Selectivity of Ruthenium Electrocatalysts.[a]

Cat.	*E* (V vs $FeCp_2$)	[Cat] (mM)	Faradaic Efficiency[b] (%)		Formate Detected	Turnovers[c]
			CO	H_2		
1	−1.80	0.5	16.1 ± 0.9	5.7 ± 0.2	Yes	13.7
	−2.20	0.7	17.2 ± 3.6	4.3 ± 0.9	Yes	6.4
2*t*	−1.80	0.6	14.8 ± 5.1	3.3 ± 1.3	Yes	3.2
	−2.20	0.7	9.3 ± 1.2	5.5 ± 0.9	Yes	3.7
3	−2.20	0.5	16.7 ± 1.2	57.9 ± 3.0	No	6.0
$\mathbf{4}^+$	−1.80	0.6	30.4 ± 4.8	7.9 ± 1.3	Yes	3.5
	−2.20	0.6	34.1 ± 0.3	7.8 ± 0.2	Yes	3.6
1′	−1.7[d]	1.0[d]	63 ± 16[d]	1.8 ± 0.8[d]	Yes[d]	5.2[d]
	−1.80	0.5	65 ± 19	1.4 ± 0.7	Yes	2.8
	−2.2[d]	1.0[d]	95[d]	1[d]		5.2[d]

[a] Experiments were carried out under 1 atm CO_2 in CH_3CN solution containing 0.1 M $[NBu^n_4][PF_6]$ and 0.5 M PhOH. [b] Standard deviations were calculated from 3 measurements. [c] One turnover is defined as two electrons being passed per catalyst molecule. [d] Ref. [56].

The results of the bulk electrolysis experiments show that product selectivity and Faradaic efficiency are dependent on the nature of the supporting ligands of the ruthenium catalysts. In terms of selectivity, compounds **1**, **2*t***, and $\mathbf{4}^+$ possess Faradaic efficiencies that are greater for CO_2 reduction than for proton reduction by ratios ranging from *ca.* 2–5, with $\mathbf{4}^+$ exhibiting the highest

overall ratio across the two potentials. Compound **3**, in contrast, exhibits a much larger Faradaic efficiency for proton reduction than CO_2 reduction, commensurate with the catalytic current for this compound in the absence of CO_2 being indistinguishable from that for the direct reduction of phenol at the electrode. With regards to trends in the efficiency of CO production, $\mathbf{4}^+$ exhibits Faradaic efficiencies at the two potentials (30.4 and 34.1%) that are approximately double those of **1**, **2*t***, and **3** (9.3–17.2%), with the latter three compounds showing only a small variation as a function of supporting ligand.

The metrics for electrocatalytic reduction of CO_2 by **1**, **2*t***, **3**, and $\mathbf{4}^+$ may be compared to those previously reported for related **1′** (Figure 5.1), which was found to produce CO, formate, and H_2 under comparable conditions to those utilized in the present chapter (1 atm CO_2, 0.5 M PhOH, CH_3CN solution) at potentials of −1.7 V and −2.2 V.[56] To allow a direct comparison to the results obtained for **1**, **2*t***, and $\mathbf{4}^+$ at −1.8 V, the products and Faradaic efficiencies of **1′** were measured under our conditions at this potential; the results for **1′** at −1.8 V are the same, within experimental error, to those reported at −1.7 V (Table 5.2). The Faradaic efficiency of **1′** for CO production at −1.8 V is twice that of $\mathbf{4}^+$, the best of the present catalysts, and it exhibits much higher selectivity against coproduction of H_2. In addition, the Faradaic efficiency of **1′** is substantially larger at −2.2 V than at −1.8 V, whereas those for **1**, **2*t***, and $\mathbf{4}^+$ are the same (within experimental error) at the two potentials. A critical difference between **1′** and **1**, **2*t***, **3**, and $\mathbf{4}^+$ that appears to account for their different catalytic properties is that **1′** possesses two one-electron reductions (separated by 0.17 V) rather than the single two-electron reduction observed for **1**, **2*t***, **3**, and $\mathbf{4}^+$. The different behavior of the two types of compounds results from the fact that the bulky mesityl substituents of **1′** prevent dimerization or polymer formation upon reduction, unlike the behavior reported for bpy derivatives.[50, 74, 76, 83]

5.4. Conclusions

It has been found that **1** is photosensitive to visible light in acetonitrile solution, producing as primary and downstream photochemical products **2*c***, **3**, and $\mathbf{4}^{+}$. As previously reported for **1**,[50-52] compounds **2*t***, **3**, and $\mathbf{4}^{+}$ are active electrocatalysts for the reduction of CO_2. In acetonitrile solution in the presence of phenol, the products produced are CO, formate, and H_2. Among these catalysts the photostable, non-CO-bearing complex $\mathbf{4}^{+}$ exhibits the highest Faradaic efficiency for CO production (by a factor of two). Although the Faradaic efficiencies and selectivities for CO_2 reduction are lower for **1**, **2*t***, **3**, and $\mathbf{4}^{+}$ than for **1′**, the present results are noteworthy in two broad respects. First, the observations that the catalytic metrics for **2*t*** are comparable to **1** and that those for $\mathbf{4}^{+}$ are better than both demonstrates that CO is not an essential ligand for catalytic function within the $Ru^{II}(bpy)L_n$ class of compounds. This suggests, additionally, that further variation of the monodentate ligands within $Ru^{II}(bpy)L_n$ complexes (for which $\mathbf{4}^{+}$ provides a starting material) is a route to improving catalyst performance. Second, $\mathbf{4}^{+}$ is photostable in acetonitrile solution, whereas CO-containing catalysts **1**, **2*t***, and **3** are highly photosensitive to visible light.[84] Thus, unlike these other catalysts, $\mathbf{4}^{+}$ can be studied and employed under normal ambient-lighting laboratory conditions without concern that adventitious photolysis is decomposing the catalyst or that its photoproducts are also contributing to the catalytic response. This robustness may be particularly valuable for applications of $\mathbf{4}^{+}$ in artificial photosynthesis, such have been reported for **1** and **1′**.[53-54]

5.5. References

1. Appel, A. M.; Bercaw, J. E.; Bocarsly, A. B.; Dobbek, H.; DuBois, D. L.; Dupuis, M.; Ferry, J. G.; Fujita, E.; Hille, R.; Kenis, P. J.; Kerfeld, C. A.; Morris, R. H.; Peden, C. H.; Portis, A. R.; Ragsdale, S. W.; Rauchfuss, T. B.; Reek, J. N.; Seefeldt, L. C.; Thauer, R. K.; Waldrop, G. L. Frontiers, Opportunities, and Challenges in Biochemical and Chemical Catalysis of CO_2 Fixation. *Chem. Rev.* **2013**, *113*, 6621–6658.

2. Bonin, J.; Maurin, A.; Robert, M. Molecular Catalysis of the Electrochemical and Photochemical Reduction of CO_2 with Fe and Co Metal Based Complexes. Recent Advances. *Coord. Chem. Rev.* **2017**, *334*, 184–198.

3. Costentin, C.; Robert, M.; Saveant, J. M. Catalysis of the Electrochemical Reduction of Carbon Dioxide. *Chem. Soc. Rev.* **2013**, *42*, 2423–2436.

4. DuBois, D. L. Development of Molecular Electrocatalysts for Energy Storage. *Inorg. Chem.* **2014**, *53*, 3935–3960.

5. Jones, J.-P.; Prakash, G. K. S.; Olah, G. A. Electrochemical CO_2 Reduction: Recent Advances and Current Trends. *Isr. J. Chem.* **2014**, *54*, 1451–1466.

6. Kortlever, R.; Shen, J.; Schouten, K. J.; Calle-Vallejo, F.; Koper, M. T. Catalysts and Reaction Pathways for the Electrochemical Reduction of Carbon Dioxide. *J. Phys. Chem. Lett.* **2015**, *6*, 4073–4082.

7. Rakowski DuBois, M.; DuBois, D. L. Development of Molecular Electrocatalysts for CO_2 Reduction and H_2 Production/Oxidation. *Acc. Chem. Res.* **2009**, *42*, 1974–1982.

8. Finn, C.; Schnittger, S.; Yellowlees, L. J.; Love, J. B. Molecular Approaches to the Electrochemical Reduction of Carbon Dioxide. *Chem. Commun.* **2012**, *48*, 1392–1399.

9. Takeda, H.; Cometto, C.; Ishitani, O.; Robert, M. Electrons, Photons, Protons and Earth-Abundant Metal Complexes for Molecular Catalysis of CO2 Reduction. *ACS Catal.* **2016**, *7*, 70–88.

10. Saveant, J. M. Molecular Catalysis of Electrochemical Reactions. Mechanistic Aspects. *Chem. Rev.* **2008**, *108*, 2348–2378.

11. Goeppert, A.; Czaun, M.; Jones, J. P.; Surya Prakash, G. K.; Olah, G. A. Recycling of Carbon Dioxide to Methanol and Derived Products—Closing the Loop. *Chem. Soc. Rev.* **2014**, *43*, 7995–8048.

12. Voiry, D.; Shin, H. S.; Loh, K. P.; Chhowalla, M. Low-Dimensional Catalysts for Hydrogen Evolution and CO_2 Reduction. *Nat. Rev. Chem.* **2018**, *2*, 0105.

13. Artz, J.; Muller, T. E.; Thenert, K.; Kleinekorte, J.; Meys, R.; Sternberg, A.; Bardow, A.; Leitner, W. Sustainable Conversion of Carbon Dioxide: An Integrated Review of Catalysis and Life Cycle Assessment. *Chem. Rev.* **2018**, *118*, 434–504.

14. Tamaki, Y.; Ishitani, O. Supramolecular Photocatalysts for the Reduction of CO_2. *ACS Catal.* **2017**, *7*, 3394–3409.

15. Song, Q.-W.; Zhou, Z.-H.; He, L.-N. Efficient, Selective and Sustainable Catalysis of Carbon Dioxide. *Green Chem.* **2017**, *19*, 3707–3728.

16. Hernández, S.; Amin Farkhondehfal, M.; Sastre, F.; Makkee, M.; Saracco, G.; Russo, N. Syngas Production from Electrochemical Reduction of CO_2: Current Status and Prospective Implementation. *Green Chem.* **2017**, *19*, 2326–2346.

17. Zhu, D. D.; Liu, J. L.; Qiao, S. Z. Recent Advances in Inorganic Heterogeneous Electrocatalysts for Reduction of Carbon Dioxide. *Adv. Mater.* **2016**, *28*, 3423–3452.

18. Liu, X.; Inagaki, S.; Gong, J. Heterogeneous Molecular Systems for Photocatalytic CO_2 Reduction with Water Oxidation. *Angew. Chem., Int. Ed.* **2016**, *55*, 14924–14950.

19. Daza, Y. A.; Kuhn, J. N. CO2 Conversion by Reverse Water Gas Shift Catalysis: Comparison of Catalysts, Mechanisms and their Consequences For CO_2 Conversion to Liquid Fuels. *RSC Adv.* **2016**, *6*, 49675–49691.

20. Yamazaki, Y.; Takeda, H.; Ishitani, O. Photocatalytic Reduction of CO_2 Using Metal Complexes. *J. Photochem. Photobiol., C* **2015**, *25*, 106–137.

21. White, J. L.; Baruch, M. F.; Pander Iii, J. E.; Hu, Y.; Fortmeyer, I. C.; Park, J. E.; Zhang, T.; Liao, K.; Gu, J.; Yan, Y.; Shaw, T. W.; Abelev, E.; Bocarsly, A. B. Light-Driven Heterogeneous Reduction of Carbon Dioxide: Photocatalysts and Photoelectrodes. *Chem. Rev.* **2015**, *115*, 12888–12935.

22. Costentin, C.; Robert, M.; Saveant, J. M. Current Issues in Molecular Catalysis Illustrated by Iron Porphyrins as Catalysts of the CO_2-to-CO Electrochemical Conversion. *Acc. Chem. Res.* **2015**, *48*, 2996–3006.

23. Maeda, C.; Miyazaki, Y.; Ema, T. Recent Progress in Catalytic Conversions of Carbon Dioxide. *Catal. Sci. Technol.* **2014**, *4*, 1482–1497.

24. Lanzafame, P.; Centi, G.; Perathoner, S. Catalysis for Biomass and CO_2 Use Through Solar Energy: Opening New Scenarios for A Sustainable and Low-Carbon Chemical Production. *Chem. Soc. Rev.* **2014**, *43*, 7562–7580.

25. Kondratenko, E. V.; Mul, G.; Baltrusaitis, J.; Larrazábal, G. O.; Pérez-Ramírez, J. Status and Perspectives of CO_2 Conversion Into Fuels and Chemicals by Catalytic, Photocatalytic and Electrocatalytic Processes. *Energy Environ. Sci.* **2013**, *6*, 3112–3135.

26. Reithmeier, R.; Bruckmeier, C.; Rieger, B. Conversion of CO_2 via Visible-Light Promoted Homogeneous Redox Catalysis. *Catalysts* **2012**, *2*, 544–571.

27. Mori, K.; Yamashita, H.; Anpo, M. Photocatalytic Reduction of CO_2 with H_2O on Various Titanium Oxide Photocatalysts. *RSC Adv.* **2012**, *2*, 3165–3172.

28. Kumar, B.; Llorente, M.; Froehlich, J.; Dang, T.; Sathrum, A.; Kubiak, C. P. Photochemical and Photoelectrochemical Reduction of CO_2. *Annu. Rev. Phys. Chem.* **2012**, *63*, 541–569.

29. Whipple, D. T.; Kenis, P. J. A. Prospects of CO_2 Utilization via Direct Heterogeneous Electrochemical Reduction. *J. Phys. Chem. Lett.* **2010**, *1*, 3451–3458.

30. Takeda, H.; Ishitani, O. Development of Efficient Photocatalytic Systems for CO_2 Reduction Using Mononuclear and Multinuclear Metal Complexes Based on Mechanistic Studies. *Coord. Chem. Rev.* **2010**, *254*, 346–354.

31. Roy, S. C.; Varghese, O. K.; Paulose, M.; Grimes, C. A. Toward Solar Fuels: Photocatalytic Conversion of Carbon Dioxide to Hydrocarbons. *ACS Nano* **2010**, *4*, 1259–1278.

32. Morris, A. J.; Meyer, G. J.; Fujita, E. Molecular Approaches to the Photocatalytic Reduction of Carbon Dioxide for Solar Fuels. *Acc. Chem. Res.* **2009**, *42*, 1983–1994.

33. Stanbury, M.; Compain, J.-D.; Chardon-Noblat, S. Electro and Photoreduction of CO_2 Driven by Manganese-Carbonyl Molecular Catalysts. *Coord. Chem. Rev.* **2018**, *361*, 120–137.

34. Omae, I. Recent Developments in Carbon Dioxide Utilization for the Production of Organic Chemicals. *Coord. Chem. Rev.* **2012**, *256*, 1384–1405.

35. Grice, K. A. Carbon Dioxide Reduction with Homogenous Early Transition Metal Complexes: Opportunities and Challenges for Developing CO_2 Catalysis. *Coord. Chem. Rev.* **2017**, *336*, 78–95.

36. Benson, E. E.; Kubiak, C. P.; Sathrum, A. J.; Smieja, J. M. Electrocatalytic and Homogeneous Approaches to Conversion of CO_2 to Liquid Fuels. *Chem. Soc. Rev.* **2009**, *38*, 89–99.

37. Lim, R. J.; Xie, M.; Sk, M. A.; Lee, J.-M.; Fisher, A.; Wang, X.; Lim, K. H. A Review on the Electrochemical Reduction of CO_2 in Fuel Cells, Metal Electrodes and Molecular Catalysts. *Catal. Today* **2014**, *233*, 169–180.

38. Manbeck, G. F.; Fujita, E. A Review of Iron and Cobalt Porphyrins, Phthalocyanines and Related Complexes for Electrochemical and Photochemical Reduction of Carbon Dioxide. *J. Porphyrins Phthalocyanines* **2015**, *19*, 45–64.

39. Mikkelsen, M.; Jørgensen, M.; Krebs, F. C. The Teraton Challenge. A Review of Fixation and Transformation of Carbon Dioxide. *Energy Environ. Sci.* **2010**, *3*, 43–81.

40. Taheri, A.; Berben, L. A. Making C–H Bonds with CO_2: Production of Formate by Molecular Electrocatalysts. *Chem. Commun.* **2016**, *52*, 1768–1777.

41. Schneider, J.; Jia, H.; Muckerman, J. T.; Fujita, E. Thermodynamics and Kinetics of CO_2, CO, and H^+ Binding to the Metal Centre of CO_2 Reduction Catalysts. *Chem. Soc. Rev.* **2012**, *41*, 2036–2051.

42. Grice, K. A.; Kubiak, C. P. In *Advances in Inorganic Chemistry*, Aresta, M., van Eldik, R., Eds. Academic Press: Waltham, MA, 2014; Vol. 66, pp 163–188.

43. Inglis, J. L.; MacLean, B. J.; Pryce, M. T.; Vos, J. G. Electrocatalytic Pathways Towards Sustainable Fuel Production from Water and CO_2. *Coord. Chem. Rev.* **2012**, *256*, 2571–2600.

44. Apaydin, D. H.; Schlager, S.; Portenkirchner, E.; Sariciftci, N. S. Organic, Organometallic and Bioorganic Catalysts for Electrochemical Reduction of CO_2. *ChemPhysChem* **2017**, *18*, 3094–3116.

45. Francke, R.; Schille, B.; Roemelt, M. Homogeneously Catalyzed Electroreduction of Carbon Dioxide-Methods, Mechanisms, and Catalysts. *Chem. Rev.* **2018**.

46. Elgrishi, N.; Chambers, M. B.; Wang, X.; Fontecave, M. Molecular Polypyridine-Based Metal Complexes as Catalysts for the Reduction of CO_2. *Chem. Soc. Rev.* **2017**, *46*, 761–796.

47. Qiao, J.; Liu, Y.; Hong, F.; Zhang, J. A Review of Catalysts for the Electroreduction of Carbon Dioxide to Produce Low-Carbon Fuels. *Chem. Soc. Rev.* **2014**, *43*, 631–675.

48. Windle, C. D.; Perutz, R. N. Advances in Molecular Photocatalytic and Electrocatalytic CO_2 Reduction. *Coord. Chem. Rev.* **2012**, *256*, 2562–2570.

49. Wrighton, M. Photochemistry of Metal Carbonyls. *Chem. Rev.* **1974**, *74*, 401–430.

50. Chardon-Noblat, S.; Deronzier, A.; Ziessel, R.; Zsoldos, D. Selective Synthesis and Electrochemical Behavior of *trans(Cl)*- and *cis(Cl)*- [$Ru(bpy)(CO)_2Cl_2$] Complexes (bpy = 2,2'-Bipyridine). Comparative Studies of Their Electrocatalytic Activity Toward the Reduction of Carbon Dioxide. *Inorg. Chem.* **1997**, *36*, 5384–5389.

51. Ishida, H.; Fujiki, K.; Ohba, T.; Ohkubo, K.; Tanaka, K.; Terada, T.; Tanaka, T. Ligand Effects of Ruthenium 2,2′-Bipyridine and 1,10-Phenanthroline Complexes on the Electrochemical Reduction of CO_2. *J. Chem. Soc., Dalton Trans.* **1990**, 2155–2160.

52. Collomb-Dunand-Sauthier, M.-N.; Deronzier, A.; Ziessel, R. Electrocatalytic Reduction of Carbon Dioxide with Mono(bipyridine)carbonylruthenium Complexes in Solution or as Polymeric Thin Films. *Inorg. Chem.* **1994**, *33*, 2961–2967.

53. Lehn, J.-M.; Ziessel, R. Photochemical Reduction of Carbon Dioxide to Formate Catalyzed by 2,2'-Bipyridine- or 1,10-Phenanthroline-Ruthenium(II) Complexes. *J. Organomet. Chem.* **1990**, *382*, 157–173.

54. Kuramochi, Y.; Itabashi, J.; Fukaya, K.; Enomoto, A.; Yoshida, M.; Ishida, H. Unexpected Effect of Catalyst Concentration on Photochemical CO_2 Reduction by *trans(Cl)*-$Ru(bpy)(CO)_2Cl_2$: New Mechanistic Insight into the $CO/HCOO^-$ Selectivity. *Chem. Sci.* **2015**, *6*, 3063–3074.

55. Sekizawa, K.; Maeda, K.; Domen, K.; Koike, K.; Ishitani, O. Artificial Z-scheme Constructed with a Supramolecular Metal Complex and Semiconductor for the Photocatalytic Reduction of CO_2. *J. Am. Chem. Soc.* **2013**, *135*, 4596–4599.

56. Machan, C. W.; Sampson, M. D.; Kubiak, C. P. A Molecular Ruthenium Electrocatalyst for the Reduction of Carbon Dioxide to CO and Formate. *J. Am. Chem. Soc.* **2015**, *137*, 8564–8571.

57. Ramakrishnan, S.; Chidsey, C. E. D. Initiation of the Electrochemical Reduction of CO_2 by a Singly Reduced Ruthenium(II) Bipyridine Complex. *Inorg. Chem.* **2017**, *56*, 8326–8333.

58. Eskelinen, E.; Kinnunen, T.-J. J.; Haukka, M.; Pakkanen, Tapani A. Photochemical Studies of *cis(CO),trans(Cl)*-[Ru(bpy)$(CO)_2Cl_2$] (bpy = 2,2′-Bipyridine): Ligand Exchange Reactions in Methanol. *Eur. J. Inorg. Chem.* **2002**, *2002*, 1169–1173.

59. Gabrielsson, A.; Zalis, S.; Matousek, P.; Towrie, M.; Vlcek, A., Jr. Ultrafast Photochemical Dissociation of an Equatorial CO Ligand From *trans(X,X)*-[Ru$(X)_2(CO)_2$(bpy)] (X = Cl, Br, I): A Picosecond Time-Resolved Infrared Spectroscopic and DFT Computational Study. *Inorg. Chem.* **2004**, *43*, 7380–7388.

60. Bokach, N. A.; Haukka, M.; Hirva, P.; Guedes Da Silva, M. F. C.; Kukushkin, V. Y.; Pombeiro, A. J. L. Photoinduced Synthesis and Electrochemical Properties of New Ruthenium(Mono)Bipyridine Dialkylcyanamide and Propiononitrile Complexes. *J. Organomet. Chem.* **2006**, *691*, 2368–2377.

61. Deacon, G. B.; Kepert, C. M.; Sahely, N.; Skelton, B. W.; Spiccia, L.; Thomas, N. C.; White, A. H. Synthesis and Structures of Photodecarbonylated Ruthenium(II) Complexes—Potential Intermediates for Mixed Ligand Complexes. *J. Chem. Soc., Dalton Trans.* **1999**, 275–277.

62. Mulhern, D.; Brooker, S.; Gorls, H.; Rau, S.; Vos, J. G. Synthesis of Mononuclear and Dinuclear Ruthenium(II) Tris(heteroleptic) Complexes via Photosubstitution in Bis(carbonyl) Precursors. *Dalton Trans.* **2006**, 51–57.

63. Kubeil, M.; Vernooij, R. R.; Kubeil, C.; Wood, B. R.; Graham, B.; Stephan, H.; Spiccia, L. Studies of Carbon Monoxide Release from Ruthenium(II) Bipyridine Carbonyl Complexes Upon UV-Light Exposure. *Inorg. Chem.* **2017**, *56*, 5941–5952.

64. Kepert, C. M.; Deacon, G. B.; Sahely, N.; Spiccia, L.; Fallon, G. D.; Skelton, B. W.; White, A. H. Synthesis of Heteroleptic Bis(diimine)carbonylchlororuthenium(II) Complexes from Photodecarbonylated Precursors. *Inorg. Chem.* **2004**, *43*, 2818–2827.

65. Spiccia, L.; Deacon, G. B.; Kepert, C. M. Synthetic Routes to Homoleptic and Heteroleptic Ruthenium(II) Complexes Incorporating Bidentate Imine Ligands. *Coord. Chem. Rev.* **2004**, *248*, 1329–1341.

66. This concern may also apply to closely-related **1′**, the synthesis of which was described as being conducted in the dark.

67. Eskelinen, E.; Haukka, M.; Venäläinen, T.; Pakkanen, T. A.; Wasberg, M.; Chardon-Noblat, S.; Deronzier, A. Light-Induced Decarbonylation, Solvolysis, and Isomerization of $Ru(L)(CO)_2Cl_2$ (L = 2,2'-Bipyridine and 4,4'-Dimethyl-2,2'-bipyridine) in Acetonitrile. *Organometallics* **2000**, *19*, 163–169.

68. Collomb-Dunand-Sauthier, M.-N.; Deronzier, A. Photochemical Reactivity of $[Ru^{II}(L)(CO)_2Cl_2]$ and $[Me_4N]$ $[Ru^{III}(L)(CO)Cl_3]$ (L = 2,2'-Bipyridine or 4,4'-Di(isopropoxycarbonyl)-2,2'-Bipyridine) in CH_3CN and the Redox Properties of the Resulting New Complexes. *J. Organomet. Chem.* **1993**, *444*, 191–198.

69. Hartl, F.; Aarnts, M. P.; Nieuwenhuis, H. A.; van Slageren, J. Electrochemistry of Different Types of Photoreactive Ruthenium(II) Dicarbonyl α-Diimine Complexes. *Coord. Chem. Rev.* **2002**, *230*, 107–125.

70. Pangborn, A. B.; Giardello, M. A.; Grubbs, R. H.; Rosen, R. K.; Timmers, F. J. Safe and Convenient Procedure for Solvent Purification. *Organometallics* **1996**, *15*, 1518–1520.

71. Chardon-Noblat, S.; Renfrew, A.; Lafolet, F.; Deronzier, A.; Jakonen, M.; Laurila, E.; Haukka, M. An Easy Electrochemical and Chemical Synthesis of $[Ru(bpy)(CH_3CN)_2Cl_2]$: A Synthon for Heteroleptic Tris(diimine) Ru(II) Complexes. *Dalton. Trans.* **2008**, 5891–5896.

72. Thomas, N. C. Reactions of Ruthenium(II) Carbonyl Complexes. *Inorg. Chim. Acta* **1986**, *120*, L7–L8.

73. Fulmer, G. R.; Miller, A. J. M.; Sherden, N. H.; Gottlieb, H. E.; Nudelman, A.; Stoltz, B. M.; Bercaw, J. E.; Goldberg, K. I. NMR Chemical Shifts of Trace Impurities: Common Laboratory Solvents, Organics, and Gases in Deuterated Solvents Relevant to the Organometallic Chemist. *Organometallics* **2010**, *29*, 2176–2179.

74. Collomb-Dunand-Sauthier, M.-N.; Deronzier, A.; Ziessel, R. Electrochemical Behaviour of $[Ru^{II}(L)(CO)_2Cl_2]$ $[Ru^{II}(L)(CO)Cl_3][Me_4N]$ and $[Ru^{II}(L)(CO)_2(CH_3CN)_2][CF_3SO_3]_2$ Complexes (L = 2,2'-Bipyridine or 4,4'-Isopropoxycarbonyl-2,2'-bipyridine). *J. Electroanal. Chem* **1993**, *350*, 43–55.

75. Collomb-Dunand-Sauthier, M.-N.; Deronzier, A.; Ziessel, R. Electrochemical Characterization of $[Ru^{II}(bpy)(CO)_2Cl_2]$ (bpy = 2,2'-bipyridine). *J. Electroanal. Chem* **1991**, *319*, 347–353.

76. Chardon-Noblat, S.; Deronzier, A.; Zsoldos, D.; Ziessel, R.; Haukka, M.; Pakkanen, T.; Venäläinen, T. Mode of Formation of Polymeric $[\{Ru(bipy)(CO)_2\}_n]$ (bipy = 2,2′-Bipyridine) Films. *J. Chem. Soc., Dalton Trans.* **1996**, 2581–2583.

77. Chardon-Noblat, S.; Deronzier, A.; Ziessel, R.; Zsoldos, D. Electroreduction of CO_2 Catalyzed by Polymeric $[Ru(bpy)(CO)_2]_n$ Films in Aqueous Media: Parameters Influencing the Reaction Selectivity. *J. Electroanal. Chem* **1998**, *444*, 253–260.

78. Collomb-Dunand-Sauthier, M.-N.; Deronzier, A.; Ziessel, R. Electrocatalytic Reduction of CO_2 in Water on a Polymeric $[\{Ru^0(bpy)(CO)_2\}_n]$ (bpy = 2,2′-Bipyridine) Complex Immobilized on Carbon Electrodes. *J. Chem. Soc., Chem. Commun.* **1994**, 189–191.

79. Bulk reduction of the compound **2*c*** in acetonitrile is reported to produce an oligomer of the form $[Ru(bpy)(CO)(CH_3CN)]_n$ that, unlike $[Ru(bpy)(CO)_2]_n$, remains soluble (Hartl, F.; Renfrew, A. K.; Lafolet, F.; Mahabiersing, T.; Calhorda, M. J.; Chardon-Noblat, S; Haukka, M.; Deronzier, A. *Inorg. Chem.* **2009**, 48, 8233–8244). It is possible that similar processes may occur for the compounds **2*t*** and **4Cl** discussed in this work.

80. McCarthy, B. D.; Martin, D. J.; Rountree, E. S.; Ullman, A. C.; Dempsey, J. L. Electrochemical Reduction of Brønsted Acids by Glassy Carbon in Acetonitrile—Implications for Electrocatalytic Hydrogen Evolution. *Inorg. Chem.* **2014**, *53*, 8350–8361.

81. Artero, V.; Fontecave, M. Solar Fuels Generation and Molecular Systems: Is It Homogeneous or Heterogeneous Catalysis? *Chem. Soc. Rev.* **2013**, *42*, 2338–2356.

82. Martin, D. J.; McCarthy, B. D.; Rountree, E. S.; Dempsey, J. L. Qualitative Extension of the EC' Zone Diagram to a Molecular Catalyst for a Multi-Electron, Multi-Substrate Electrochemical Reaction. *Dalton Trans.* **2016**, *45*, 9970–9976.

83. Hartl, F.; Renfrew, A. K.; Lafolet, F.; Mahabiersing, T.; Calhorda, M. J.; Chardon-Noblat, S.; Haukka, M.; Deronzier, A. Soluble Redox-Active Polymetallic Chains $[\{Ru^0(CO)(L)(bpy)\}_m]_n$ (bpy = 2,2'-Bipyridine, L = PrCN, Cl^-; $m = 0, -1$): Electrosynthesis and Characterization. *Inorg. Chem.* **2009**, *48*, 8233–8244.

84. One may surmise that **1′** is also photosensitive, given that its synthesis is described as being conducted with shielding from light (Machan, C. W.; Sampson, M. D.; Kubiak, C. P. *J. Am. Chem. Soc.* **2015**, *137*, 8564-8571).

CHAPTER 6: A Photostable, Selective Ruthenium–Bipyridyl Electrocatalyst for CO_2 Reduction

6.1. Introduction

As discussed in Chapter 1, the catalytic conversion of CO_2 to fuels and other useful chemicals is of significant interest because of the steadily increasing atmospheric concentration of this greenhouse gas.[1-48] The electrochemical reduction of CO_2 to energy-rich species, such as CO and methanol, typically requires multiple proton-coupled electron-transfer reactions,[45] and the incorporation of π-unsaturated redox-active ligands, such as polypyridines, is one common method of enabling transition metal compounds to achieve coordinated electron-transfer and proton-transfer reactions.[42-44, 46, 48] A ligand-centered reduction enables subsequent rapid intramolecular electron transfer to the metal in sequence with protonation steps.[46]

Metal-polypyridyl electrocatalysts for CO_2 reduction have been extensively investigated, with the most common architecture of such catalysts being the general form $M(bpy^R)(CO)_nX_{4-n}$, where bpy^R is 2,2′-bipyridine, or a functionalized variant, in which R substituents are incorporated to modify electronic or steric properties, and X typically is an anionic ligand. The electron-withdrawing ability of CO allows it to stabilize the low-oxidation state species generally produced during CO_2 reduction and rationalizes its utilization in such catalysts. Indeed, many highly active catalysts bear multiple CO ligands, such as the extensively studied $Re(bpy^R)(CO)_3Cl$, $Mn(bpy^R)(CO)_3Cl$, and $Ru(bpy^R)(CO)_2Cl_2$ catalyst families.[45-48] While the effects of varying bpy^R substituents has been heavily investigated as a means of improving catalytic function,[8-10, 33, 42, 44-48] the substitution of CO for other neutral ligands has been much less explored.[45-46] A key advantage to the development of such derivatives is that metal–carbonyl compounds are often light sensitive, with photoinduced CO loss a potential catalyst degradation pathway.[49]

The compound *trans(Cl)*-Ru(bpy)$(CO)_2Cl_2$ (Figure 6.1), which is an active electrocatalyst for the reduction of CO_2 to CO and formate under a variety of reaction conditions, typifies many of these traits. Although it has been employed in artificial-photosynthetic systems for CO_2 reduction, wherein the electrons are supplied from a photoredox chromophore and sacrificial reductant,[50-52] prior studies of Ru(bpy)$(CO)_2Cl_2$ demonstrate that it undergoes stepwise photo-induced ligand substitution in acetonitrile solution upon irradiation with UV or visible light.[53-54] Upon photolysis, monodecarbonylation yields Ru(bpy)$(CO)(CH_3CN)Cl_2$ as the initial product. Further irradiation generates Ru(bpy)$(CH_3CN)_2Cl_2$ and, finally, *mer*-[Ru(bpy)$(CH_3CN)_3Cl$]Cl. In Chapter 5 we explored ligand variation of Ru(bpy)$(CO)_2Cl_2$ and its influence upon catalytic function. Each of the compounds *trans(Cl)*-Ru(bpy)$(CO)(CH_3CN)Cl_2$, Ru(bpy)$(CH_3CN)_2Cl_2$, and Ru(bpy)$(CH_3CN)_3Cl^+$ were prepared and all were found to be active electrocatalysts for the reduction of CO_2. The most selective catalyst for the production of CO, under the conditions of the study, was observed to be [Ru(bpy)$(CH_3CN)_3Cl^+$; a compound that, unlike its congeners, has the advantage of being photostable in acetonitrile solution.

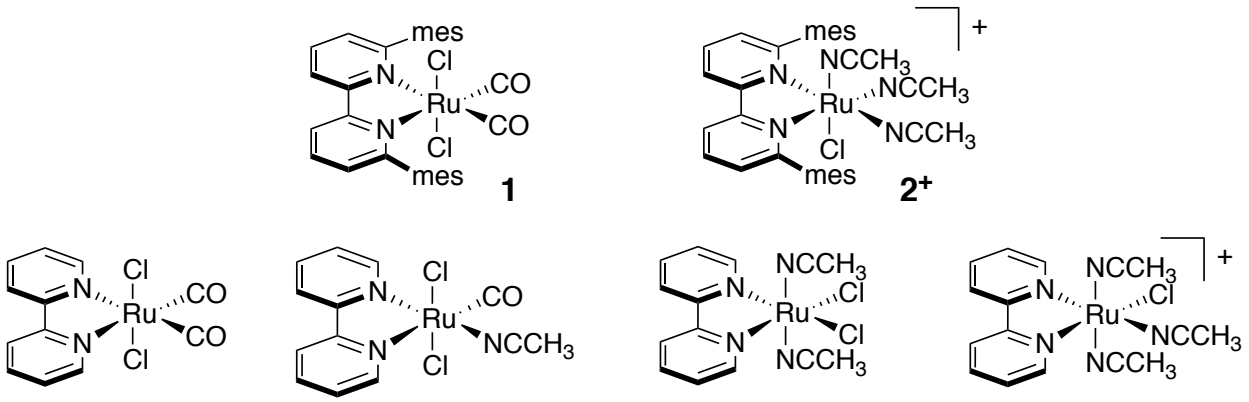

Figure 6.1. Compounds discussed in this study.

Recently, it has been reported that the incorporation of sterically hindering mesityl groups enhances the catalytic activity of *trans(Cl)*-Ru(bpy^{mes})$(CO)_2Cl_2$ (**1**, Figure 6.1; bpy^{mes} = 6,6′-dimesityl-2,2′-bipyridine), as compared to unfunctionalized *trans(Cl)*-Ru(bpy)$(CO)_2Cl_2$. A recent

report by Kuramochi *et. al*.[51] detailed the photocatalytic reduction of CO_2 with both $Ru(bpy)(CO)_2Cl_2$ and **1**. It was found that the bulky mesityl moieties of **1** enabled enhanced selectivity for CO production by limiting dimerization. This work was furthered by Kubiak and coworkers[55] who reported the detailed electrocatalytic behavior of **1** and investigated the mechanism of catalysis. It was found that, unlike $Ru(bpy)(CO)_2Cl_2$,[56-59] **1** was found to have no propensity for metal-metal bond formation—illustrating the importance of the sterically hindering mesityl groups. Additionally, it was found that **1** is a highly selective catalyst for the reduction of CO_2 to CO, with a Faradaic efficiency of 95% at –2.2 V *vs.* $FeCp_2^{0/+}$, in phenol-acetonitrile solution. The mechanism by which **1** achieves the selective electrocatalytic reduction CO_2 to CO was probed and described.[55]

Stability is a key issue in the development of catalysts for CO_2 reduction.[47] The photoreactivity of $Ru(bpy)(CO)_2Cl_2$ limits its application in photocatalytic systems and raises the question of whether **1** is photosensitive, which is relevant both with regard to the potential contribution of photoproducts to measurements of its electrocatalytic properties and its use in photoredox-sensitized catalytic systems. A literature procedure for the synthesis of **1** specifies that it should be carried out in the dark,[55] suggesting that photoinstability was a potential concern. We find that, indeed, **1** is unstable to even ambient laboratory light. We have synthesized the new ion *fac*-$[Ru(bpy^{mes})(CH_3CN)_3Cl]^+$ (**2**$^+$, Figure 6.1), which was isolated as two salts (**2Cl** and **2[PF$_6$]**). In contrast to **1**, we find **2**$^+$ to be photostable. To examine what effect ligand substitution has on electrocatalytic ability, we have investigated the electrochemical behavior of **2**$^+$ under experimental conditions both similar to and different from those used in detailed study of **1**. The suitability of **2**$^+$ as a proton and CO_2 reduction catalyst was probed in acetonitrile, and it was found that **2**$^+$ is an active electrocatalyst that, under certain conditions, exhibits higher efficiency for CO

production than does **1**. The difference in electrochemical and electrocatalytic behavior between $\mathbf{2}^{+}$ and **1** is discussed and related to ligand identity.

6.2. Experimental Section

Materials. Solvents used for syntheses, electrochemistry, photochemistry, and electronic-absorption spectroscopy were HPLC grade, and were further purified by passage under nitrogen pressure through an anaerobic, stainless steel system consisting of either two 4.5 in. × 24 in. (1 gal) columns of activated A2 alumina (acetonitrile) or one column of A2 alumina and one column of BASF R3-11 catalyst (toluene).[60] Acetonitrile used for recrystallizations, hexane (HPLC grade), chloroform (HPLC grade), diethyl ether (anhydrous), and CD_2Cl_2 were used as received. **1** was synthesized according to a published procedure.[51] The synthesis of **2[PF$_6$]** is described in Supporting Information. Ferrocene and $[NBu^n_4][PF_6]$ were recrystallized twice from ethanol and dried for a minimum of 18 h under vacuum at 120 °C. The electrocatalysis substrates CO_2 (research grade, 99.9999%) and phenol (≥99%, unstabilized, stored under N_2 in the dark) were used as received.

Spectroscopy and Photochemistry. ^{1}H and ^{13}C NMR spectra were recorded at room temperature using a Bruker DRX 400 NMR spectrometer. Chemical shifts were measured relative to solvent resonances.[61] Electrospray ionization (ESI) mass spectra were measured in acetonitrile solution with an Agilent 6224 spectrometer. Electronic-absorption spectra were measured with a Cary 300 spectrophotometer of samples contained in quartz cuvettes. Non-preparative photolysis experiments were conducted with samples contained in quartz cuvettes in a sample chamber that was sealed from ambient light and contained a 455 nm LED (900 mW, ThorLabs model M455L2).

Synthesis of *fac*-[Ru(6,6′-dimesityl-2,2′-bipyridyl)(CH$_3$CN)$_3$Cl]Cl (2Cl). A vigorously stirred, pale-yellow solution of **1** (0.048 g, 0.08 mmol) in CH_3CN (250 mL) under N_2 was

photolyzed for 15 h with light from an array of white LEDs (Super Bright LEDs, part no. 4NFLS-CWH24-24V-CL, 6000 K), resulting in formation of an orange solution. (The photolysis can also be conducted using a 26 W compact fluorescent light bulb over a period of one week.) The solvent was removed under vacuum, yielding a dark red residue; this was washed with toluene (3 × 40 mL). The red solid was extracted into CH_3CN (4 mL) and the resulting solution filtered through a fine-porosity sintered glass frit. Dropwise addition of diethyl ether yielded a red crystalline material that was collected by filtration and dried under vacuum overnight (yield 0.041 g, 77%). ^{1}H NMR (CD_3CN, 400 MHz, 295 K, Figures 7.5.2 and 7.5.3): δ 8.27 (d, 2H, J_{HH} = 8.0 Hz, bpy), 7.99 (t, 2H, J_{HH} = 8.0 Hz, bpy), 7.21 (d, 2H, J_{HH} = 8.0 Hz, bpy), 6.98 (s, 2H, mesityl-C_6H_2), 6.95 (s, 2H, mesityl-C_6H_2), 2.45 (s, 3H, CH_3CN), 2.35 (s, 6H, mesityl-CH_3), 2.20 (s, 6H, CH_3CN), 2.10 (s, 6H, mesityl-CH_3), 1.96 (s, 6H, mesityl-CH_3). $^{13}C\{^1H\}$ NMR (CD_2Cl_2, 400 MHz, 295 K, Figure 7.5.4): δ 167.70 (bpy or mesityl Ar), 161.16 (bpy or mesityl Ar), 139.17 (bpy or mesityl Ar), 138.44 (bpy or mesityl Ar), 138.07 (bpy or mesityl Ar), 137.37 (bpy or mesityl Ar), 136.16 (bpy or mesityl Ar), 128.68 (bpy or mesityl Ar), 128.49 (bpy or mesityl Ar), 128.18 (bpy or mesityl Ar), 122.18 ($CH_3\underline{C}N$), 121.77 ($CH_3\underline{C}N$), 21.49 (mesityl-$\underline{C}H_3$), 21.38 (mesityl-$\underline{C}H_3$), 20.60 (mesityl-$\underline{C}H_3$), 5.78 ($\underline{C}H_3CN$), 5.60 ($\underline{C}H_3CN$). ESI-MS (*m*/*z*, Figure 7.5.5): [M^+] = 652.17, predicted = 652.18. UV-Vis (CH_3CN, Figure 7.5.6): λ_{max} = 447 nm.

Electrochemistry. Full details of electrochemical procedures are provided in the Supporting Information. Experiments were performed at room temperature under either a N_2 or CO_2 atmosphere in CH_3CN solution containing 0.1 M [NBu^n_4][PF_6] as electrolyte. Redox potentials were measured relative to $FeCp_2$ or $FeCp^*_2$ internal standards and are reported relative to $FeCp_2^{0/+}$. Cyclic voltammetry experiments were performed in a single-compartment cell with a three-electrode configuration consisting of a glassy carbon working electrode (A = 0.07 cm^2), a

platinum auxiliary electrode (A = 0.02 cm^2), and a silver wire quasi-reference electrode. Controlled potential electrolysis experiments were performed in a sealed four-neck cell (total volume = 100 mL). A three-electrode configuration was used that consisted of a reticulated vitreous carbon foam working electrode (ERG Materials & Aerospace, ca. 15 mm × 10 mm × 5 mm), a platinum wire auxiliary electrode that was separated from the working solution by a medium porosity glass frit, and a Ag/Ag^+ reference electrode (BASi, 0.01 M $AgNO_3$ in CH_3CN containing 0.1 M $[NBu^n_4][PF_6]$) that was separated from the working solution by a CoralPor tip. The working solution (40 mL) contained a known amount of catalyst, 0.5 M PhOH, and a stir bar. The auxiliary compartment contained 5 mL of a CH_3CN solution containing 0.1 M ferrocene (as a sacrificial reductant) and 0.1 M $[NBu^n_4][PF_6]$. Controlled-potential electrolysis products were analyzed by gas chromatography (CO, H_2) and ^{1}H-NMR spectroscopy (formate).

6.3. Results and Discussion

6.3.1. Photochemistry of 1 and Synthesis and Characterization of 2^+. Compound **1** was found to be highly photosensitive to visible light in acetonitrile solution. A solution of **1** in a sealed cuvette exhibited evidence of decomposition within minutes when allowed to stand under ambient laboratory lighting (overhead fluorescent lamps), as indicated by the appearance in the electronic-absorption spectrum of a new band at 485 nm and absorption tail extending to ~600 nm (Figure 6.2A). Photolysis of a sample of **1** in acetonitrile solution with a blue LED (λ_{max} = 455 nm) accelerates these changes, with strong bands at 380 nm, 485 nm and 565 nm appearing within 5 minutes (Figure 6.2B). These bands are at similar positions to those seen during the visible-light (Chapter 5) and UV-light[53] photolysis of the related compound $Ru(bpy)(CO)_2Cl_2$ in acetonitrile, suggesting they arise from an analogous set of CO-loss photoproducts. Specifically, the band at 485 nm is attributed to $Ru(bpy^{mes})(CO)(CH_3CN)Cl_2$ (*cf.* $Ru(bpy)(CO)(CH_3CN)Cl_2$, λ_{max} = 456 nm;

Chapter 5), which is the initial photoproduct of $Ru(bpy)(CO)_2Cl_2$, and the bands at 380 nm and 565 nm are assigned to the secondary photolysis product $Ru(bpy^{mes})(CH_3CN)_2Cl_2$ (*cf.* $Ru(bpy)(CH_3CN)_2Cl_2$, λ_{max} = 377 nm and 550 nm; Chapter 5).[62] Consistent with this attribution of the bands to primary and secondary photolysis products, during the first hour of photolysis the intensities of the bands at 380 nm and 565 nm overtake that of the initially observed 485-nm band. With continued irradiation the bands at 380 nm, 485 nm, and 565 nm diminish in intensity and a single strong band appears at 447 nm (Figure 6.2C). This band is assigned to the terminal photoproduct $\mathbf{2}^+$, based on full characterization of an isolated sample (described below). Exhaustive UV photolysis of $Ru(bpy)(CO)_2Cl_2$ and $Ru(bpy^{Me})(CO)_2Cl_2$ also produce compounds of composition $Ru(bpy^R)(CH_3CN)_3Cl^+$ (Chapter 5).[53-54]

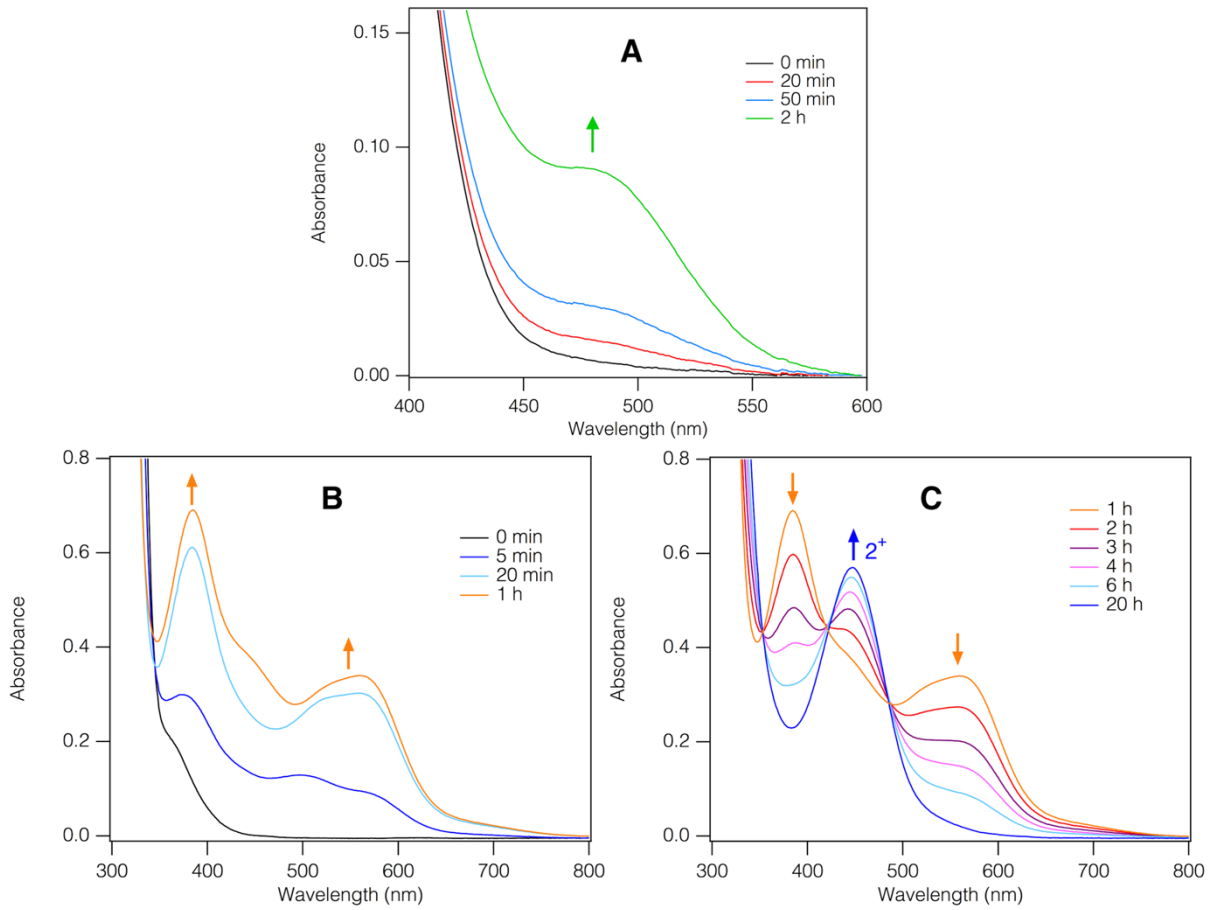

Figure 6.2. Electronic-absorption spectra of **1** and its photolysis products in CH_3CN: (A) *via* exposure to ambient laboratory light (from overhead fluorescent lighting); (B) and (C) using a 455-nm LED. The sample concentrations are: (A) 1.0 mM; (B) and (C) 0.3 mM.

Preparative-scale photolysis of **1** in CH_3CN using either a blue LED or compact fluorescent bulb provided **2Cl** in 77% isolated yield, following purification. The related compound **2[PF$_6$]** is prepared by salt metathesis between **2Cl** and KPF_6 (see Chapter 7.5.2). The compounds were characterized by ^{1}H-NMR, ^{13}C-NMR, and UV-visible spectroscopy, high-resolution mass spectrometry, and X-ray crystallography. The ^{1}H and ^{13}C NMR spectra of **2**$^+$ are consistent with a *fac* geometry, based on the number of resonances observed for the bipyridyl unit. This stereochemical assignment is supported by the crystal structure of **2[PF$_6$]** (Figure 6.3). The nature of the Ru(bpy^R)$(CO)_2Cl_2$ R groups clearly play an important role in determining the geometry of the terminal Ru(bpy^R)$(CH_3CN)_3Cl^+$ photoproduct, as evidenced by the observed *fac* geometries of

$\mathbf{2}^+$ and related *fac*-Ru(4,4′-dimethylbpy)$(CH_3CN)_3Cl^+$ and the *mer* geometry found for *mer*-Ru(bpy)$(CH_3CN)_3Cl^+$, but the origin that of this effect has not been investigated.[54-55]

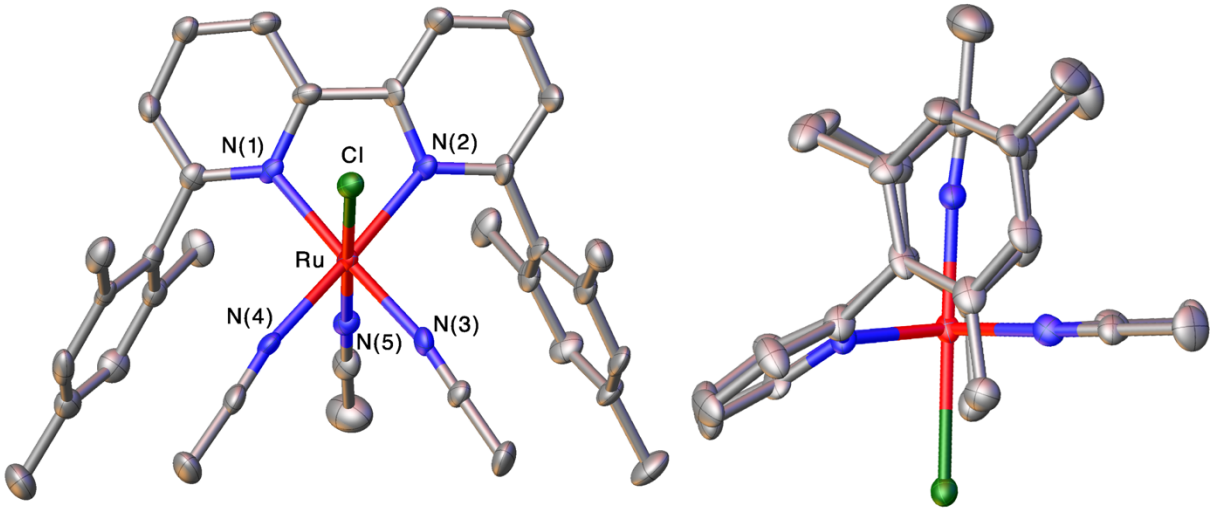

Figure 6.3. Thermal-ellipsoid representation of the $\mathbf{2}^+$ core of **2**$[PF_6]$ (40% probability ellipsoids). Carbon (grey), nitrogen (blue), chlorine (green), and ruthenium (red) atoms are shown; hydrogen atoms, PF_6^-, and interstitial $CHCl_3$ are omitted for clarity. Selected bond lengths (Å) and angles (deg): Ru–Cl = 2.5220(19), Ru–N(1) = 2.070(6), Ru–N(2) = 2.029(6), Ru–N(3) = 2.037(7), Ru–N(4) = 1.980(6), Ru–N(5) = 2.058(6), N(1)–Ru–N(2) = 76.4(2)°, N(3)–Ru–N(4) = 78.9(2)°, Cl–Ru–N(5) = 178.75(18)°.

The structure of $\mathbf{2}^+$ can be compared to that previously reported for **1**.[55] For both compounds, the steric hindrance provided by the mesityl moieties leads to distortion of the equatorial ligands. For $\mathbf{2}^+$, we find the Ru–N–C angles of the equatorial CH_3CN ligands to be distorted from the ideal 180°, instead being 170.0° and 171.6°. In the case of **1** the Ru–C–O bond angles deviate to similar values (*ca.* 171.0°). The identity, and steric requirements, of the equatorial ligands seems to have a great impact on the orientation of the bpy^{mes} ligand. Interestingly, in $\mathbf{2}^+$, the bpy^{mes} ligand is canted backwards out of the equatorial plane of the compound (C–C–N–$Ru_{average}$ = 22.4°). This may be to limit steric clash between the CH_3– groups of the equatorial acetonitrile ligands with the mesityl groups of the bpy ligand. For $\mathbf{2}^+$, the two aromatic rings of the bipyridyl plane are coplanar with a N–C–C–N torsion angle of 2.04°; this differs greatly from the structure of **1** which has a much more distorted bipyridyl plane (N–C–C–N = 16.9°).

6.3.2. Photochemistry of 2^+. As is expected from its method of synthesis, $\mathbf{2}^+$ is observed as being photostable in acetonitrile solution. It is, however, not straightforward to differentiate between $\mathbf{2}^+$ being photostable in acetonitrile or merely photo*stationary*, with the compound undergoing degenerate CH_3CN-for-CH_3CN ligand substitution. In order to investigate the photostability of $\mathbf{2}^+$ under conditions relevant for electrocatalytic reduction of CO_2, photochemical studies were carried out in 4% H_2O-acetonitrile (v/v). It has been reported that the compound $[Ru(bpy)(CH_3CN)_4]^{2+}$ undergoes facile photo-induced ligand substitution when under 390 nm irradiation in acetone-d_6 solution containing trace water,[63] providing $[Ru(bpy)(CH_3CN)_2(H_2O)_2]^{2+}$ in 90% yield in 4 h. Studying the photochemistry of $\mathbf{2}^+$ in mixed H_2O-acetonitrile solution enables us to have a potential photoproduct that (1) should be favorably formed if $\mathbf{2}^+$ is photoreactive and (2) we can easily monitor by spectrophotometry.

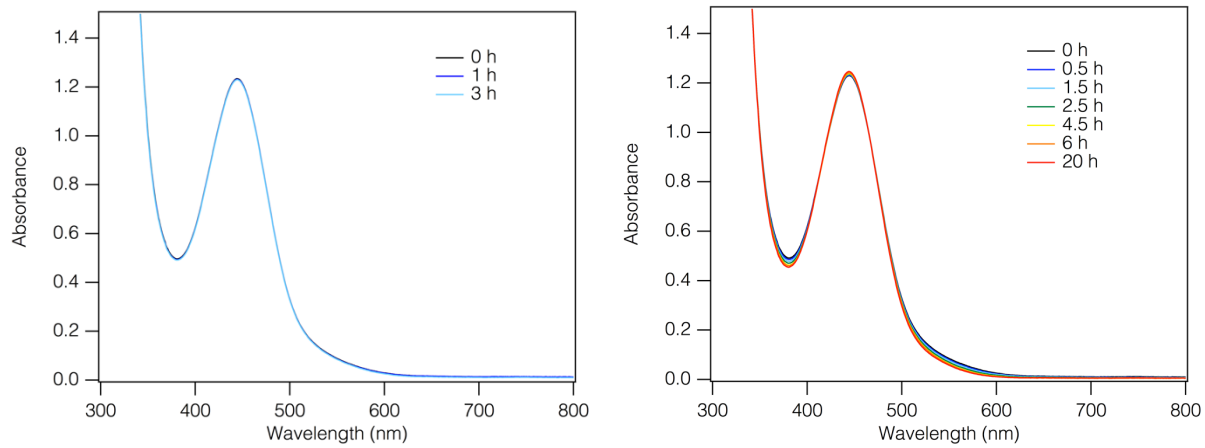

Figure 6.4. Electronic-absorption spectra of **2Cl** (0.6 mM) in 4% H_2O-CH_3CN (v/v) (*Left*) in the dark, and (*Right*) under ambient laboratory lighting.

The electronic absorption spectrum of **2Cl** in 4% H_2O-acetonitrile (v/v) is very similar to that in pure acetonitrile, exhibiting a slight shift in λ_{max} from 447 nm to 444 nm. The compound is thermally stable in this solvent mixture over 3 h when the solution is protected from light (Figure 6.4). When exposed to ambient laboratory light under conditions similar to those employed for the study of **1** (Figure 6.4), $\mathbf{2}^+$ undergoes very slight changes over 4.5 h ($\Delta A = 0.008$ at λ_{max}; 0.7%

change), indicating that, unlike **1**, it can be handled for the duration of typical electrocatalysis experiments with minimal precautions. Even after 20 h of exposure to ambient light, $\Delta A = 0.017$ at λ_{max}, or a 1.4% change. These experiments demonstrate the photostability of $\mathbf{2}^+$.

6.3.3. Electrochemistry of $\mathbf{2}^+$. The electrochemical properties of $\mathbf{2}^+$ in acetonitrile solution were determined by cyclic voltammetry (CV) and differential pulse voltammetry (DPV). The CV of $\mathbf{2}^+$ (Figure 6.5) exhibits features arising from one oxidative and two reductive processes. The redox potentials for these processes are set out in Table 6.1. For **2[PF$_6$]**, the oxidation is reversible (Figure 6.5B) and assigned to the $Ru^{II/III}$ couple ($E_{1/2}$ = 0.63 V *vs.* $FeCp_2^{0/+}$). This potential is similar to that recently reported for the related compound *mer*-$Ru(bpy)(CH_3CN)_3Cl^+$ ($E_{1/2}$ = 0.69 V; Chapter 5).The oxidative wave observed for **2Cl**, in contrast, is quasi-reversible (Figure 7.5.9) due to overlap with the oxidation of Cl^- at *ca.* +0.7 V; DPV of **2Cl** (Figure 7.5.10) demonstrates it possesses the same oxidation potential as that of **2[PF$_6$]**.[63-64] The two reductions of $\mathbf{2}^+$ are observed at −2.01 and −2.33 V. The first reduction is irreversible and exhibits an associated oxidative process at −1.76 V that is present both when the scan is reversed after the first and after the second reduction. As the scan rate is increased a small anodic feature begins to grow at −1.95 V (ΔE_p = 60 mV relative to the cathodic peak at E_p = −2.01 V, the same as measured for the $FeCp_2^{0/+}$ internal reference); this suggests that the first reduction may be quasi-reversible at fast scan rates. The second reduction of $\mathbf{2}^+$ (E_p = −2.33 V) is irreversible.

Table 6.1. Redox Potentials (V *vs.* $FeCp_2^{0/+}$) of **1** and $\mathbf{2}^+$.[a]

Catalyst	$E_{1/2}$ (Ox)	E_p (1st Red)[b]	E_p (2nd Red)[b]
1	+1.22	−1.69[c]	−1.89[c]
$\mathbf{2}^+$	+0.63	−2.01	−2.33

[a] All measurements are by CV in CH_3CN solution with 0.1 M $[NBu^n_4][PF_6]$. [b] Measured at v = 0.1 V/s. [c] From ref. 55.

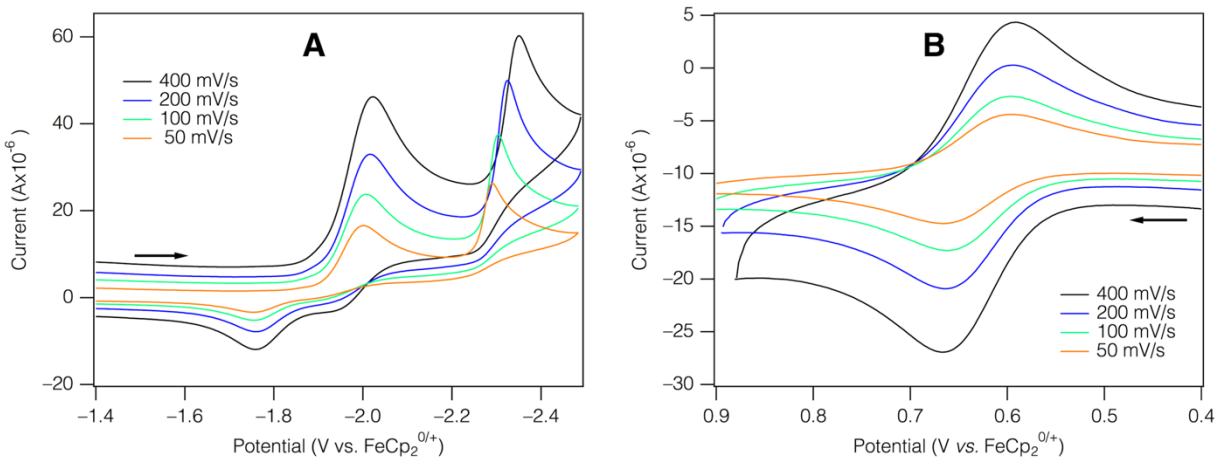

Figure 6.5. Cyclic voltammograms of $\mathbf{2}^+$-containing compounds in CH_3CN solution containing 0.1 M $[NBu^n_4][PF_6]$: (A) **2Cl** (2 mM); (B) **2[PF$_6$]** (0.7 mM).

The electrochemistry of the related compound **1** in acetonitrile was previously described in detail by Kubiak and coworkers,[55] which provides a basis for assigning the reduction processes of $\mathbf{2}^+$. Compound **1** also exhibits two one-electron reductions (Table 6.1), which were assigned as bpy-centered processes. The first reduction (E_p = −1.69 V) is irreversible and produces $[Ru^{II}(bpy^{mes\bullet})(CO)_2Cl_2]^-$, which undergoes rapid ligand-to-metal electron transfer and loss of Cl^- to give $Ru^{I}(bpy^{mes})(CO)_2Cl$. The second reduction, which is associated with this latter product, is quasi-reversible ($E_{1/2}$ = −1.86 V) and generates $[Ru^{I}(bpy^{mes\bullet})(CO)_2Cl]^-$. The reduction potentials of $\mathbf{2}^+$ are negative of those of **1** by 0.3–0.4 V ($\Delta E_{red1}(\mathbf{2}^+–\mathbf{1})$ = −0.32 V, $\Delta E_{red2}(\mathbf{2}^+–\mathbf{1})$ = −0.44 V). The approximately constant shift of the reduction potentials between **1** and $\mathbf{2}^+$ suggests that the natures of these processes are similar in the two compounds, namely, that the first reduction of $\mathbf{2}^+$ results in formation of $Ru^{II}(bpy^{mes\bullet})(CH_3CN)_3Cl$ and the second reduction in formation of $Ru^{I}(bpy^{mes\bullet})(CH_3CN)_3$. The negative shifts of the reduction potentials for $\mathbf{2}^+$ relative to **1** arise from the substantially poorer electron-withdrawing ability of the acetonitrile ligands of $\mathbf{2}^+$ compared with the CO ligands of **1**. This difference also plays a role in determining the stability of the electrogenerated transients for **1** and $\mathbf{2}^+$, as indicated by the different degrees of reversibility of their electrochemical processes. The first reduction for **1** is irreversible at CV scan rates up to

3.2 V/s, whereas that for $\mathbf{2}^+$ begins to show an anodic wave as the scan rate is increased to 0.4 V/s. This suggests that chloride loss from the first reduction product to form of $Ru(bpy^{mes})(CO)_2Cl$ is faster than that to form $[Ru(bpy^{mes})(CH_3CN)_3]^+$. Conversely, the second reduction of **1** is quasi-reversible (v = 0.1–3.0 V/s) while that for $\mathbf{2}^+$ is irreversible at all scan rates studied (0.05–0.4 V/s), consistent with the greater ability of CO ligands compared with acetonitrile ligands to stabilize highly reduced compounds.

Although not of importance for electrocatalytic CO_2 reduction, the oxidation potentials of **1** and $\mathbf{2}^+$ are found to differ by a similar amount as are their reductions. The oxidation of **1** (Figure 7.5.11) is found to be a reversible, one-electron process with $E_{1/2}$ = 1.22 V (Table 6.1). This is assigned to the $Ru^{II/III}$ couple, based on its similarity to this couple for the related compound $Ru(bpy)(CO)_2Cl_2$ ($E_{1/2}$ = 1.35 V).[59] The oxidation potential of $\mathbf{2}^+$ is shifted from that of **1** by –0.59 V, with the slightly larger shift as compared to that found for the reductions (–0.32, –0.44 V) arising from the fact that the metal-centered oxidation will be more sensitive to the nature of the ligands than the bipyridyl-centered reductions.

6.3.4. Electrocatalytic Reduction of CO_2 by $\mathbf{2}^+$. The electrochemical reduction of $\mathbf{2}^+$ in the presence of CO_2 is found to result in the catalytic production of CO. These experiments were conducted in acetonitrile solution with phenol as the proton source, to provide consistency with the detailed study by Kubiak and coworkers of electrocatalytic CO_2 reduction by **1**.[55] Compound **1** and the compounds $Ru(bpy)(CO)_2Cl_2$ and *mer*-$[Ru(bpy)(CH_3CN)_3Cl]^+$, which are analogues of **1** and $\mathbf{2}^+$, respectively, are also known to be electrocatalysts for the reduction of protons from phenol to H_2 (Chapter 5);[55] thus, the electrochemistry of $\mathbf{2}^+$ in the presence of phenol was also studied in the absence of CO_2 in order to understand possible background proton-reduction processes. Under N_2, the CV of $\mathbf{2}^+$ in acetonitrile solution containing 0.5 M phenol (the

concentration employed in the prior study of **1**)[55] shows an increase in current at potentials negative of *ca*. −1.85 V relative to that observed without phenol (Figure 6.6A). This current response is shifted slightly positive (by 50–75 mV) of that observed for 0.5 M phenol in the absence of $\mathbf{2}^{+}$, suggesting but not clearly establishing that $\mathbf{2}^{+}$ is serving as a proton-reduction catalyst. To probe this further, controlled-potential electrolysis experiments were conducted at −1.90 V, which is within the first reduction wave of $\mathbf{2}^{+}$ but positive of the potential at which current steeply rises from direct reduction of phenol at the electrode. Gas-chromatographic analysis of the headspace of a bulk electrolyzed sample confirmed the presence of H_2, which is produced with a Faradaic efficiency of 57.5% (Table 6.2). CVs of $\mathbf{2}^{+}$ with lower concentrations of phenol show that the potential of the first reduction does not appear to change (Figure 7.5.12), suggesting that the process is not coupled with protonation of the metal center under these conditions, but this is difficult to establish at higher phenol concentrations owing to the substantial background current.

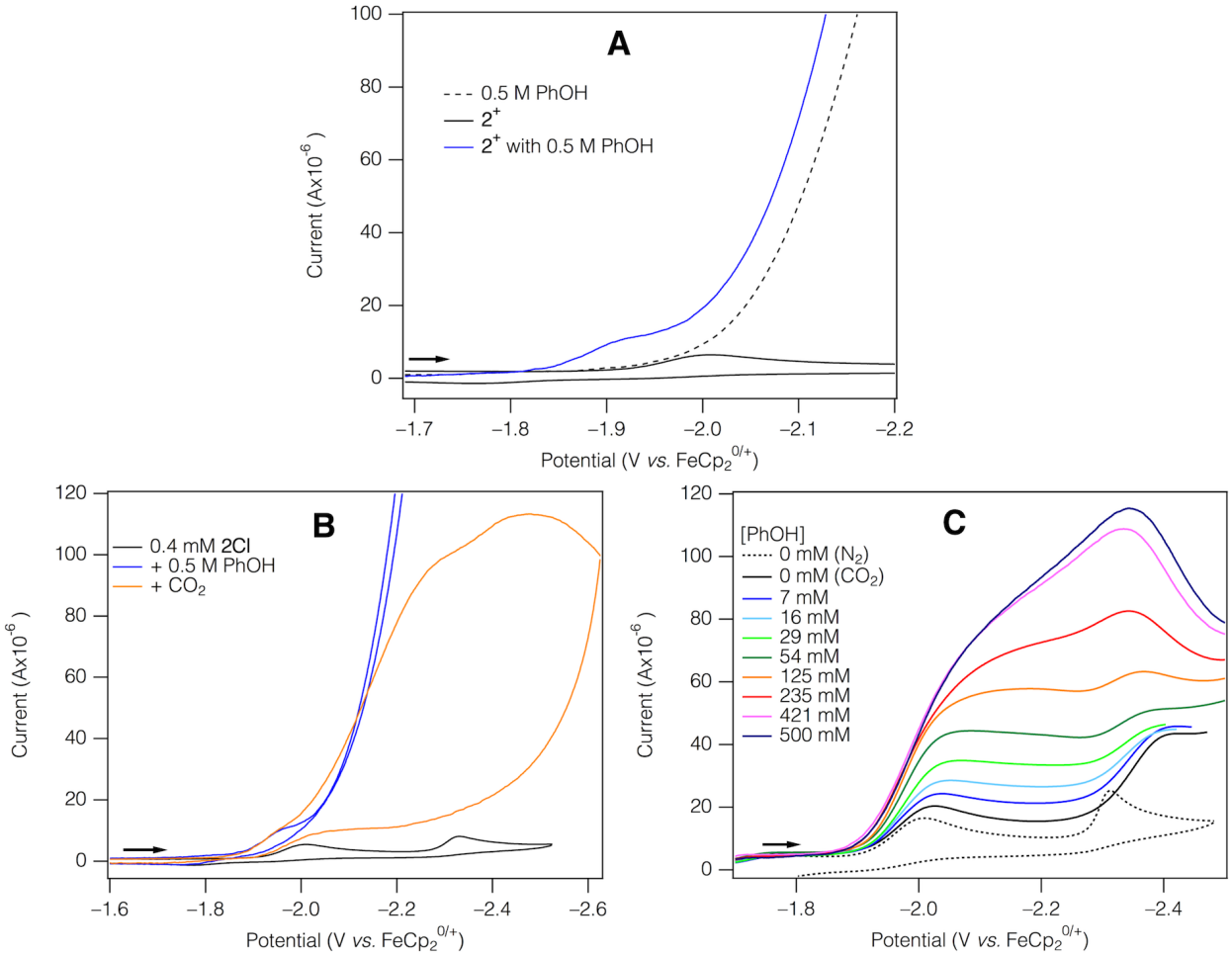

Figure 6.6. Cyclic voltammograms (v = 0.1 V/s) of **2Cl** in CH_3CN containing 0.1 M $[NBu^n_4][PF_6]$ with different combinations of substrates: (A) Under an N_2 atmosphere, **2Cl** (0.4 mM) in the absence of substrate (black) and with PhOH (0.5 M), and a PhOH (0.5 M) blank (dashed); (B) **2Cl** (0.4 mM) under an N_2 atmosphere (black) with PhOH (0.5 M; blue), and upon subsequent addition of CO_2 (orange), (C) **2Cl** (0.6 mM) in the absence of substrate (dotted), and under a CO_2 atmosphere (solid) with increasing amounts of PhOH.

The CV of $\mathbf{2}^+$ under 1 atm of CO_2 in acetonitrile containing phenol differs substantially in appearance from those under identical conditions in the absence of CO_2 (Figure 6.6B), in that the steeply rising waveform associated with H_2 production is replaced by a structured waveform with lower current response at potentials below –2.0 V. The nature of the waveform under CO_2 is dependent on phenol concentration, as shown in Figure 6.6C. In the absence of phenol, the current response in the region of the first reduction is similar to that observed under N_2 but there is a small increase in current enhancement near the second reduction of the compound. Qualitatively similar

behavior was noted for the related compound **1** under CO_2 without phenol, and attributed to the presence of trace H_2O introduced with CO_2.[55] With increasing phenol concentration (7–54 mM, Figure 6.6C) there is a steady increase in current at −2.05 V, close to the first reduction of 2^+, followed by a plateau in the wave at potentials up to *ca*. –2.3 V. This indicates that a catalytic process is occurring at a rate which is independent of potential. The observation that the presence of CO_2 does not result in a change in the first reduction potential of $\mathbf{2}^+$ (Figure 6.6B) indicates that the first reduction is not coupled to CO_2 binding or coordination. A similar observation was also made for **1**.[55] At potentials more negative than −2.3 V the current response is very similar to that observed in the absence of phenol. At higher concentrations of phenol (125–500 mM) the enhancement of the current in this potential range is greater, leading to the waveform exhibiting a peak at *ca*. −2.35 V; this indicates that substrate is depleted within the double layer under these experimental conditions.[65]

The nature and efficiencies of the catalytic reduction processes of $\mathbf{2}^+$ in the presence of CO_2 and phenol were established through controlled-potential electrolysis experiments and corresponding gas-chromatographic and NMR-spectroscopic analyses. The results are set out in Table 6.2, alongside those for **1**. At an electrolysis potential of −2.05 V, which is near the first reduction of $\mathbf{2}^+$, and with 0.1 M phenol, which corresponds to the highest phenol concentration at which the current plateau is observed (Figure 6.6C), it is found that CO was generated with a Faradaic efficiency of 69.0%, formate is not produced, and H_2 is a trace product. The second catalytic process observed near −2.20 V, which appears at higher concentrations of phenol, was probed by controlled potential electrolysis in the presence of 0.5 M phenol. The major product is again CO (with a Faradaic efficiency of 44.1%), but H_2 is also produced with substantial efficiency

(34.7%). Thus, the more cathodic feature observed by CV corresponds to electrocatalytic proton reduction.

Table 6.2. Electrocatalytic Faradaic Efficiency for CO_2 and Proton Reduction by **1** and $\mathbf{2}^+$.[a]

Cat	*E* (V)	[Cat] (mM)	[PhOH] (M)	Faradaic Efficiency (%)		Formate Detected	Turnovers[c]
				CO	H_2		
1	−1.7[d]	1.0[d]	0.5	63 ± 16[d]	1.8 ± 0.8[d]	Yes[d]	5.2[d]
	−2.05	0.6	0.1	48.6 ± 1.2	Trace	No	5.6
	−2.2[d]	1.0[d]	0.5	95[d]	1[d]	—	5.2[d]
	−2.2[d e]	1.0[d e]	0.5	0[d,e]	52[d,e]	—	5.2[d,e]
$\mathbf{2}^+$	−1.90[e]	0.5[e]	0.5	0[e]	57.5 ± 6.4[e]	—	6.9[e]
	−2.05	0.5	0.1	69.0 ± 3.9	Trace	No	4.2
	−2.20	0.5	0.5	44.1 ± 2.5	34.7 ± 1.5	No	7.3

[a] Experiments were carried out under 1 atm (0.28 M) CO_2 in CH_3CN containing 0.1 M $[NBu_4^n][PF_6]$. [b] Uncertainties are calculated sample standard deviations from 3 measurements. [c] One turnover is defined as two electrons being passed per catalyst molecule; where multiple runs provided different numbers of turnovers, the mean is given. [d] From ref. 55. [e] Under N_2 or Ar atmosphere.

These electrocatalysis results for $\mathbf{2}^+$ may be compared with those for related compound 1. Under the controlled-potential electrolysis conditions at which $\mathbf{2}^+$ is most selective (*E* = –2.05 V, 0.1 M phenol), **1** is found to also produce CO with high selectivity (i.e., no formate and trace H_2 are detected) but lower Faradaic efficiency (48.6% vs. 69.0%). The earlier study of **1** by Kubiak and coworkers[55] employed a higher phenol concentration (0.5 M). At this concentration, the Faradaic efficiency for CO production by **1** is increased substantially at more negative potentials (95% at *E* = −2.20 V) with minimal production of H_2,[66] whereas for $\mathbf{2}^+$ CO production under these conditions is less efficient and selective. The origin of this difference appears to be that $\mathbf{2}^+$ is a more efficient catalyst than **1** for proton reduction from phenol, as indicated by the fact that it exhibits a Faradaic efficiency for H_2 production at –1.90 V (57.5%, Table 6.2) that is experimentally indistinguishable from that for **1** at the more negative potential of –2.2 V (52%).[55]

Interestingly, these trends contrast with those recently reported for the related bpy derivatives of **1** and $\mathbf{2}^{+}$, namely, $Ru(bpy)(CO)_2Cl_2$ and *fac*-$[Ru(bpy)(CH_3CN)_3Cl]^{+}$ (Chapter 5). The Faradaic efficiency for CO production at –2.20 V in the presence of 0.5 M phenol by *fac*-$[Ru(bpy)(CH_3CN)_3Cl]^{+}$ was found to be roughly double that for $Ru(bpy)(CO)_2Cl_2$, with the two compounds exhibiting similar efficiencies for H_2 production at this potential. Critical to these differences is the steric protection toward catalyst oligomerization imparted by the mesityl groups of **1** and $\mathbf{2}^{+}$, which results in these compounds possessing two one-electron reductions instead of the single two-electron reductions observed by the bpy derivatives.

6.4. Conclusions

The electrochemical and photochemical properties of the $Ru(bpy^{mes})$-containing complexes $\mathbf{2}^{+}$ and **1** depend significantly upon the nature of their supporting ligands. Both complexes electrocatalyze the reduction of CO_2 to CO in acetonitrile solution containing phenol. At –2.2 V with 0.5 M phenol, **1** is a highly selective and efficient catalyst for CO production compared with $\mathbf{2}^{+}$, which coproduces H_2. In contrast, at lower proton concentrations (0.1 M phenol) and potentials (–2.05 V) $\mathbf{2}^{+}$ is a more efficient catalyst than **1** for the reduction of CO_2 to CO. Relevant to its potential stability as a catalyst, $\mathbf{2}^{+}$ is photolytically stable in acetonitrile solution whereas **1** decomposes under ambient lighting conditions; this property provides greater utility for application of $\mathbf{2}^{+}$ in artificial photosynthetic schemes. Perhaps of more general importance is that these useful properties are found for a complex that does not possess CO ligands, which are the most commonly found supporting ligands for metal-polypyridyl electrocatalysts.[46] This suggests derivatives prepared from $\mathbf{2}^{+}$ containing other neutral ligands in place of CH_3CN could provide rich opportunities to further modulate and optimize these properties.

6.5. References

1. Appel, A. M.; Bercaw, J. E.; Bocarsly, A. B.; Dobbek, H.; DuBois, D. L.; Dupuis, M.; Ferry, J. G.; Fujita, E.; Hille, R.; Kenis, P. J.; Kerfeld, C. A.; Morris, R. H.; Peden, C. H.; Portis, A. R.; Ragsdale, S. W.; Rauchfuss, T. B.; Reek, J. N.; Seefeldt, L. C.; Thauer, R. K.; Waldrop, G. L. Frontiers, Opportunities, and Challenges in Biochemical and Chemical Catalysis of CO_2 Fixation. *Chem. Rev.* **2013**, *113*, 6621–6658.

2. Bonin, J.; Maurin, A.; Robert, M. Molecular Catalysis of the Electrochemical and Photochemical Reduction of CO_2 with Fe and Co Metal Based Complexes. Recent Advances. *Coord. Chem. Rev.* **2017**, *334*, 184–198.

3. Costentin, C.; Robert, M.; Saveant, J. M. Catalysis of the Electrochemical Reduction of Carbon Dioxide. *Chem. Soc. Rev.* **2013**, *42*, 2423–2436.

4. DuBois, D. L. Development of Molecular Electrocatalysts for Energy Storage. *Inorg. Chem.* **2014**, *53*, 3935–3960.

5. Jones, J.-P.; Prakash, G. K. S.; Olah, G. A. Electrochemical CO_2 Reduction: Recent Advances and Current Trends. *Isr. J. Chem.* **2014**, *54*, 1451–1466.

6. Kortlever, R.; Shen, J.; Schouten, K. J.; Calle-Vallejo, F.; Koper, M. T. Catalysts and Reaction Pathways for the Electrochemical Reduction of Carbon Dioxide. *J. Phys. Chem. Lett.* **2015**, *6*, 4073–4082.

7. Rakowski DuBois, M.; DuBois, D. L. Development of Molecular Electrocatalysts for CO_2 Reduction and H_2 Production/Oxidation. *Acc. Chem. Res.* **2009**, *42*, 1974–1982.

8. Finn, C.; Schnittger, S.; Yellowlees, L. J.; Love, J. B. Molecular Approaches to the Electrochemical Reduction of Carbon Dioxide. *Chem. Commun.* **2012**, *48*, 1392–1399.

9. Takeda, H.; Cometto, C.; Ishitani, O.; Robert, M. Electrons, Photons, Protons and Earth-Abundant Metal Complexes for Molecular Catalysis of CO_2 Reduction. *ACS Catal.* **2016**, *7*, 70–88.

10. Saveant, J. M. Molecular Catalysis of Electrochemical Reactions. Mechanistic Aspects. *Chem. Rev.* **2008**, *108*, 2348–2378.

11. Goeppert, A.; Czaun, M.; Jones, J. P.; Surya Prakash, G. K.; Olah, G. A. Recycling of Carbon Dioxide to Methanol and Derived Products—Closing the Loop. *Chem. Soc. Rev.* **2014**, *43*, 7995–8048.

12. Voiry, D.; Shin, H. S.; Loh, K. P.; Chhowalla, M. Low-Dimensional Catalysts for Hydrogen Evolution and CO_2 Reduction. *Nat. Rev. Chem.* **2018**, *2*, 0105.

13. Artz, J.; Muller, T. E.; Thenert, K.; Kleinekorte, J.; Meys, R.; Sternberg, A.; Bardow, A.; Leitner, W. Sustainable Conversion of Carbon Dioxide: An Integrated Review of Catalysis and Life Cycle Assessment. *Chem. Rev.* **2018**, *118*, 434–504.

14. Tamaki, Y.; Ishitani, O. Supramolecular Photocatalysts for the Reduction of CO_2. *ACS Catal.* **2017**, *7*, 3394–3409.

15. Song, Q.-W.; Zhou, Z.-H.; He, L.-N. Efficient, Selective and Sustainable Catalysis of Carbon Dioxide. *Green Chem.* **2017**, *19*, 3707–3728.

16. Hernández, S.; Amin Farkhondehfal, M.; Sastre, F.; Makkee, M.; Saracco, G.; Russo, N. Syngas Production from Electrochemical Reduction of CO_2: Current Status and Prospective Implementation. *Green Chem.* **2017**, *19*, 2326–2346.

17. Zhu, D. D.; Liu, J. L.; Qiao, S. Z. Recent Advances in Inorganic Heterogeneous Electrocatalysts for Reduction of Carbon Dioxide. *Adv. Mater.* **2016**, *28*, 3423–3452.

18. Liu, X.; Inagaki, S.; Gong, J. Heterogeneous Molecular Systems for Photocatalytic CO_2 Reduction with Water Oxidation. *Angew. Chem., Int. Ed.* **2016**, *55*, 14924–14950.

19. Daza, Y. A.; Kuhn, J. N. CO2 Conversion by Reverse Water Gas Shift Catalysis: Comparison of Catalysts, Mechanisms and their Consequences For CO_2 Conversion to Liquid Fuels. *RSC Adv.* **2016**, *6*, 49675–49691.

20. Yamazaki, Y.; Takeda, H.; Ishitani, O. Photocatalytic Reduction of CO_2 Using Metal Complexes. *J. Photochem. Photobiol., C* **2015**, *25*, 106–137.

21. White, J. L.; Baruch, M. F.; Pander Iii, J. E.; Hu, Y.; Fortmeyer, I. C.; Park, J. E.; Zhang, T.; Liao, K.; Gu, J.; Yan, Y.; Shaw, T. W.; Abelev, E.; Bocarsly, A. B. Light-Driven Heterogeneous Reduction of Carbon Dioxide: Photocatalysts and Photoelectrodes. *Chem. Rev.* **2015**, *115*, 12888–12935.

22. Costentin, C.; Robert, M.; Saveant, J. M. Current Issues in Molecular Catalysis Illustrated by Iron Porphyrins as Catalysts of the CO_2-to-CO Electrochemical Conversion. *Acc. Chem. Res.* **2015**, *48*, 2996–3006.

23. Maeda, C.; Miyazaki, Y.; Ema, T. Recent Progress in Catalytic Conversions of Carbon Dioxide. *Catal. Sci. Technol.* **2014**, *4*, 1482–1497.

24. Lanzafame, P.; Centi, G.; Perathoner, S. Catalysis for Biomass and CO_2 Use Through Solar Energy: Opening New Scenarios for A Sustainable and Low-Carbon Chemical Production. *Chem. Soc. Rev.* **2014**, *43*, 7562–7580.

25. Kondratenko, E. V.; Mul, G.; Baltrusaitis, J.; Larrazábal, G. O.; Pérez-Ramírez, J. Status and Perspectives of CO_2 Conversion Into Fuels and Chemicals by Catalytic, Photocatalytic and Electrocatalytic Processes. *Energy Environ. Sci.* **2013**, *6*, 3112–3135.

26. Reithmeier, R.; Bruckmeier, C.; Rieger, B. Conversion of CO_2 via Visible-Light Promoted Homogeneous Redox Catalysis. *Catalysts* **2012**, *2*, 544–571.

27. Mori, K.; Yamashita, H.; Anpo, M. Photocatalytic Reduction of CO_2 with H_2O on Various Titanium Oxide Photocatalysts. *RSC Adv.* **2012**, *2*, 3165–3172.

28. Kumar, B.; Llorente, M.; Froehlich, J.; Dang, T.; Sathrum, A.; Kubiak, C. P. Photochemical and Photoelectrochemical Reduction of CO_2. *Annu. Rev. Phys. Chem.* **2012**, *63*, 541–569.

29. Whipple, D. T.; Kenis, P. J. A. Prospects of CO_2 Utilization via Direct Heterogeneous Electrochemical Reduction. *J. Phys. Chem. Lett.* **2010**, *1*, 3451–3458.

30. Takeda, H.; Ishitani, O. Development of Efficient Photocatalytic Systems for CO_2 Reduction Using Mononuclear and Multinuclear Metal Complexes Based on Mechanistic Studies. *Coord. Chem. Rev.* **2010**, *254*, 346–354.

31. Roy, S. C.; Varghese, O. K.; Paulose, M.; Grimes, C. A. Toward Solar Fuels: Photocatalytic Conversion of Carbon Dioxide to Hydrocarbons. *ACS Nano* **2010**, *4*, 1259–1278.

32. Morris, A. J.; Meyer, G. J.; Fujita, E. Molecular Approaches to the Photocatalytic Reduction of Carbon Dioxide for Solar Fuels. *Acc. Chem. Res.* **2009**, *42*, 1983–1994.

33. Stanbury, M.; Compain, J.-D.; Chardon-Noblat, S. Electro and Photoreduction of CO_2 Driven by Manganese-Carbonyl Molecular Catalysts. *Coord. Chem. Rev.* **2018**, *361*, 120–137.

34. Omae, I. Recent Developments in Carbon Dioxide Utilization for the Production of Organic Chemicals. *Coord. Chem. Rev.* **2012**, *256*, 1384–1405.

35. Grice, K. A. Carbon Dioxide Reduction with Homogenous Early Transition Metal Complexes: Opportunities and Challenges for Developing CO_2 Catalysis. *Coord. Chem. Rev.* **2017**, *336*, 78–95.

36. Benson, E. E.; Kubiak, C. P.; Sathrum, A. J.; Smieja, J. M. Electrocatalytic and Homogeneous Approaches to Conversion of CO_2 to Liquid Fuels. *Chem. Soc. Rev.* **2009**, *38*, 89–99.

37. Lim, R. J.; Xie, M.; Sk, M. A.; Lee, J.-M.; Fisher, A.; Wang, X.; Lim, K. H. A Review on the Electrochemical Reduction of CO_2 in Fuel Cells, Metal Electrodes and Molecular Catalysts. *Catal. Today* **2014**, *233*, 169–180.

38. Manbeck, G. F.; Fujita, E. A Review of Iron and Cobalt Porphyrins, Phthalocyanines and Related Complexes for Electrochemical and Photochemical Reduction of Carbon Dioxide. *J. Porphyrins Phthalocyanines* **2015**, *19*, 45–64.

39. Mikkelsen, M.; Jørgensen, M.; Krebs, F. C. The Teraton Challenge. A Review of Fixation and Transformation of Carbon Dioxide. *Energy Environ. Sci.* **2010**, *3*, 43–81.

40. Taheri, A.; Berben, L. A. Making C–H Bonds with CO_2: Production of Formate by Molecular Electrocatalysts. *Chem. Commun.* **2016**, *52*, 1768–1777.

41. Schneider, J.; Jia, H.; Muckerman, J. T.; Fujita, E. Thermodynamics and Kinetics of CO_2, CO, and H^+ Binding to the Metal Centre of CO_2 Reduction Catalysts. *Chem. Soc. Rev.* **2012**, *41*, 2036–2051.

42. Grice, K. A.; Kubiak, C. P. In *Advances in Inorganic Chemistry*, Aresta, M., van Eldik, R., Eds. Academic Press: Waltham, MA, 2014; Vol. 66, pp 163–188.

43. Inglis, J. L.; MacLean, B. J.; Pryce, M. T.; Vos, J. G. Electrocatalytic Pathways Towards Sustainable Fuel Production from Water and CO_2. *Coord. Chem. Rev.* **2012**, *256*, 2571–2600.

44. Apaydin, D. H.; Schlager, S.; Portenkirchner, E.; Sariciftci, N. S. Organic, Organometallic and Bioorganic Catalysts for Electrochemical Reduction of CO_2. *ChemPhysChem* **2017**, *18*, 3094–3116.

45. Francke, R.; Schille, B.; Roemelt, M. Homogeneously Catalyzed Electroreduction of Carbon Dioxide-Methods, Mechanisms, and Catalysts. *Chem. Rev.* **2018**.

46. Elgrishi, N.; Chambers, M. B.; Wang, X.; Fontecave, M. Molecular Polypyridine-Based Metal Complexes as Catalysts for the Reduction of CO_2. *Chem. Soc. Rev.* **2017**, *46*, 761–796.

47. Qiao, J.; Liu, Y.; Hong, F.; Zhang, J. A Review of Catalysts for the Electroreduction of Carbon Dioxide to Produce Low-Carbon Fuels. *Chem. Soc. Rev.* **2014**, *43*, 631–675.

48. Windle, C. D.; Perutz, R. N. Advances in Molecular Photocatalytic and Electrocatalytic CO_2 Reduction. *Coord. Chem. Rev.* **2012**, *256*, 2562–2570.

49. Wrighton, M. Photochemistry of Metal Carbonyls. *Chem. Rev.* **1974**, *74*, 401–430.

50. Lehn, J.-M.; Ziessel, R. Photochemical Reduction of Carbon Dioxide to Formate Catalyzed by 2,2'-Bipyridine- or 1,10-Phenanthroline-Ruthenium(II) Complexes. *J. Organomet. Chem.* **1990**, *382*, 157–173.

51. Kuramochi, Y.; Itabashi, J.; Fukaya, K.; Enomoto, A.; Yoshida, M.; Ishida, H. Unexpected Effect of Catalyst Concentration on Photochemical CO_2 Reduction by *trans(Cl)*-$Ru(bpy)(CO)_2Cl_2$: New Mechanistic Insight into the $CO/HCOO^-$ Selectivity. *Chem. Sci.* **2015**, *6*, 3063–3074.

52. Sekizawa, K.; Maeda, K.; Domen, K.; Koike, K.; Ishitani, O. Artificial Z-scheme Constructed with a Supramolecular Metal Complex and Semiconductor for the Photocatalytic Reduction of CO_2. *J. Am. Chem. Soc.* **2013**, *135*, 4596–4599.

53. Collomb-Dunand-Sauthier, M.-N.; Deronzier, A. Photochemical Reactivity of $[Ru^{II}(L)(CO)_2Cl_2]$ and $[Me_4N]$ $[Ru^{III}(L)(CO)Cl_3]$ (L = 2,2'-Bipyridine or 4,4'-Di(isopropoxycarbonyl)-2,2'-Bipyridine) in CH_3CN and the Redox Properties of the Resulting New Complexes. *J. Organomet. Chem.* **1993**, *444*, 191–198.

54. Eskelinen, E.; Haukka, M.; Venäläinen, T.; Pakkanen, T. A.; Wasberg, M.; Chardon-Noblat, S.; Deronzier, A. Light-Induced Decarbonylation, Solvolysis, and Isomerization of $Ru(L)(CO)_2Cl_2$ (L = 2,2'-Bipyridine and 4,4'-Dimethyl-2,2'-bipyridine) in Acetonitrile. *Organometallics* **2000**, *19*, 163–169.

55. Machan, C. W.; Sampson, M. D.; Kubiak, C. P. A Molecular Ruthenium Electrocatalyst for the Reduction of Carbon Dioxide to CO and Formate. *J. Am. Chem. Soc.* **2015**, *137*, 8564–8571.

56. Chardon-Noblat, S.; Deronzier, A.; Ziessel, R.; Zsoldos, D. Selective Synthesis and Electrochemical Behavior of *trans(Cl)*- and *cis(Cl)*- $[Ru(bpy)(CO)_2Cl_2]$ Complexes (bpy = 2,2'-Bipyridine). Comparative Studies of Their Electrocatalytic Activity Toward the Reduction of Carbon Dioxide. *Inorg. Chem.* **1997**, *36*, 5384–5389.

57. Chardon-Noblat, S.; Deronzier, A.; Zsoldos, D.; Ziessel, R.; Haukka, M.; Pakkanen, T.; Venäläinen, T. Mode of Formation of Polymeric $[\{Ru(bipy)(CO)_2\}_n]$ (bipy = 2,2′ -Bipyridine) Films. *J. Chem. Soc., Dalton Trans.* **1996**, 2581‑2583.

58. Collomb-Dunand-Sauthier, M.-N.; Deronzier, A.; Ziessel, R. Electrocatalytic Reduction of Carbon Dioxide with Mono(bipyridine)carbonylruthenium Complexes in Solution or as Polymeric Thin Films. *Inorg. Chem.* **1994**, *33*, 2961–2967.

59. Collomb-Dunand-Sauthier, M.-N.; Deronzier, A.; Ziessel, R. Electrochemical Behaviour of $[Ru^{II}(L)(CO)_2Cl_2]$ $[Ru^{II}(L)(CO)Cl_3][Me_4N]$ and $[Ru^{II}(L)(CO)_2(CH_3CN)_2][CF_3SO_3]_2$ Complexes (L = 2,2'-Bipyridine or 4,4'-Isopropoxycarbonyl-2,2'-bipyridine). *J. Electroanal. Chem* **1993**, *350*, 43–55.

60. Pangborn, A. B.; Giardello, M. A.; Grubbs, R. H.; Rosen, R. K.; Timmers, F. J. Safe and Convenient Procedure for Solvent Purification. *Organometallics* **1996**, *15*, 1518–1520.

61. Fulmer, G. R.; Miller, A. J. M.; Sherden, N. H.; Gottlieb, H. E.; Nudelman, A.; Stoltz, B. M.; Bercaw, J. E.; Goldberg, K. I. NMR Chemical Shifts of Trace Impurities: Common Laboratory Solvents, Organics, and Gases in Deuterated Solvents Relevant to the Organometallic Chemist. *Organometallics* **2010**, *29*, 2176–2179.

62. Chardon-Noblat, S.; Renfrew, A.; Lafolet, F.; Deronzier, A.; Jakonen, M.; Laurila, E.; Haukka, M. An Easy Electrochemical and Chemical Synthesis of $[Ru(bpy)(CH_3CN)_2Cl_2]$: A Synthon for Heteroleptic Tris(diimine) Ru(II) Complexes. *Dalton. Trans.* **2008**, 5891–5896.

63. Petroni, A.; Slep, L. D.; Etchenique, R. Ruthenium(II) 2,2'-Bipyridyl Tetrakis Acetonitrile Undergoes Selective Axial Photocleavage. *Inorg. Chem.* **2008**, *47*, 951–956.

64. Cauqis, G.; Deronzier, A.; Sillion, B.; Damin, B.; Garapon, J. Electrochemical Behaviour of N-Chloroparatoluene-Sulphonamidate, *N,N*-Dichloroparatoluenesulphonamide and Paratoluenesulphonamide in Acetonitrile. *J. Electroanal. Chem* **1981**, *117*, 139–146.

65. Martin, D. J.; McCarthy, B. D.; Rountree, E. S.; Dempsey, J. L. Qualitative Extension of the EC' Zone Diagram to a Molecular Catalyst for a Multi-Electron, Multi-Substrate Electrochemical Reaction. *Dalton Trans.* **2016**, *45*, 9970–9976.

66. These results were reproduced under the experimental protocol employed in this study: E = –2.2 V, 0.5 mM **1**, CO = 97.8 ± 3.2%, H_2 = 1.5 ± 0.1%.

CHAPTER 7: Supplementary Information

7.1. Chapter 2 Supplementary Information

7.1.1. Definitions

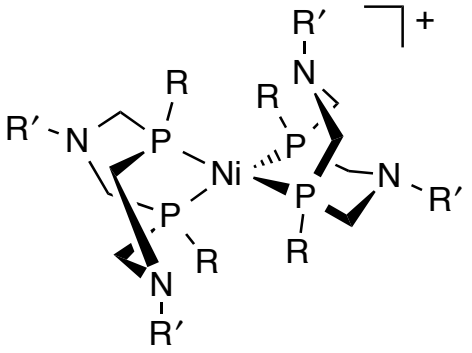

Compound	R	R′
1$^+$	Cy	*t*-Bu
2$^+$	Ph	*t*-Bu
3$^+$	Cy	Ph
4$^+$	Ph	Ph
5$^+$	Ph	$C_6H_4CH_2P(O)(OEt)_2$

Figure 7.1.1. The compounds discussed in Section 7.1.

7.1.2. Single-Crystal X-ray Diffraction Study of 1[BF$_4$]. A rod-shaped crystal fragment ($0.23 \times 0.23 \times 0.92$ mm) was selected under a stereo-microscope while immersed in fluorolube oil to avoid possible reaction with air. The crystal was removed from the oil using a tapered glass fiber that also served to hold the crystal for data collection. The crystal was mounted and centered on a Bruker D8 Venture system with CMOS detector and Mo microsource radiation; the crystal was cooled to 100 K. Frames separated in reciprocal space were obtained and provided an orientation matrix and initial cell parameters. Final cell parameters were obtained from the full data set, with the exception outlined below. A "full sphere" data set was obtained using a combination of omega and phi scans, which sample approximately all of reciprocal space to a resolution of 0.75 Å, with an integration time of 7.5 sec/frame. Data reduction was made using APEX2 software[1] including SAINT for integration. One of the data collection runs contained

several frames showing abrupt changes in average correlation coefficient and average spot intensity. These frames were removed from further data processing. Eliminating these data was not detrimental to the completeness of the structural data used for structure solution and refinement. Absorption corrections were applied using SADABS[2] based on redundant diffractions.

The structure was solved by SHELXT[3] and refined by a full-matrix least-squares procedure using the Bruker SHELXTL software package (version 6.14, XL refinement program version 2014/7).[4-5] Repeated difference Fourier maps allowed recognition of all expected C and N atoms. Following anisotropic refinement of all non-H atoms, ideal H atom positions were calculated. Final refinement was anisotropic for non-H atoms and isotropic-riding for H atoms. Further information about the structure is presented in Tables 7.1–2 and Figure 7.1.2.

Table 7.1.1. Crystallographic Data for $[Ni(P^{Cy}_2N^{tBu}_2)_2][BF_4]$ (**1**$[BF_4]$).

parameter	**1**$[BF_4]$	
formula	$C_{48}H_{96}N_4NiP_4BF_4$	
formula wt	998.68	
space group	*C*2/*c*	
unit cell dimensions	*a* = 22.729(6)	α = 90.0˚
	b = 11.661(3)	β = 104.225(7)˚
	c = 20.503(6)	γ = 90.0˚
V (Å^3)	5268(2)	
Z	4	
density (calcd) (Mg/m^3)	1.259	
μ (mm^{-1})	0.540	
T (K)	100(2)	
wavelength (Å)	0.71073	
GOF on F^2	1.076	
final R indices [$I > 2\sigma$(I)][a]	R1 = 0.0335, *w*R2 = 0.0698	
final R indices (all data)[a]	R1 = 0.0532, *w*R2 = 0.0774	

[a] $R1 = \sum\left||F_o| - |F_c|\right| / \sum|F_C|$, $wR2 = [\sum w(F_o^2 - F_c^2)^2 / \sum[w(F_o^2)^2]]^{1/2}$

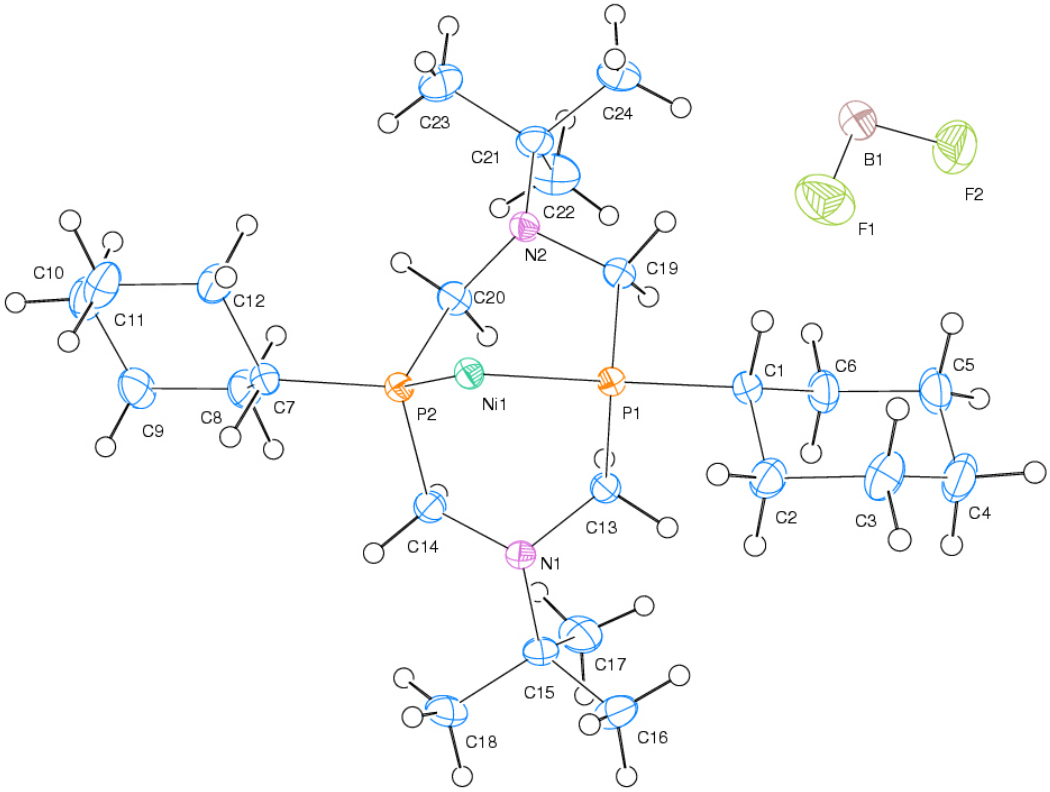

Figure 7.1.2. Thermal-ellipsoid representation (40% probability ellipsoids) of one crystallographically unique $P^{Cy}{}_2N^{tBu}{}_2$ ligand about the Ni center of **1**[BF_4], showing the full numbering scheme.

Table 7.1.2. Selected Bond Lengths (Å) and Angles (°) for **1**[BF_4] as Determined by X-ray Crystallography.

Ni(1)-P(1)#1	2.2175(7)	C(19)-P(1)-Ni(1)	111.47(7)
Ni(1)-P(1)	2.2175(7)	C(13)-P(1)-Ni(1)	111.87(7)
Ni(1)-P(2)#1	2.2195(7)	C(14)-P(2)-C(7)	100.10(9)
Ni(1)-P(2)	2.2195(7)	C(14)-P(2)-C(20)	102.02(10)
P(1)-C(1)	1.848(2)	C(7)-P(2)-C(20)	102.12(9)
P(1)-C(19)	1.851(2)	C(14)-P(2)-Ni(1)	111.55(7)
P(1)-C(13)	1.8676(19)	C(7)-P(2)-Ni(1)	126.11(7)
P(2)-C(14)	1.8491(19)	C(20)-P(2)-Ni(1)	111.91(7)
P(2)-C(7)	1.849(2)	C(13)-N(1)-C(14)	111.51(15)
P(2)-C(20)	1.869(2)	C(13)-N(1)-C(15)	111.67(15)
N(1)-C(13)	1.458(2)	C(14)-N(1)-C(15)	113.32(15)
N(1)-C(14)	1.463(2)	C(20)-N(2)-C(19)	111.60(15)
N(1)-C(15)	1.510(2)	C(20)-N(2)-C(21)	111.83(16)
N(2)-C(20)	1.458(3)	C(19)-N(2)-C(21)	113.36(15)
N(2)-C(19)	1.458(2)	C(2)-C(1)-C(6)	110.32(17)
N(2)-C(21)	1.507(3)	C(2)-C(1)-P(1)	111.72(14)
C(1)-C(2)	1.523(3)	C(6)-C(1)-P(1)	115.11(14)
C(1)-C(6)	1.531(3)	C(1)-C(2)-C(3)	110.45(18)
C(2)-C(3)	1.525(3)	C(4)-C(3)-C(2)	111.62(19)
C(3)-C(4)	1.515(3)	C(5)-C(4)-C(3)	111.11(19)
C(4)-C(5)	1.507(3)	C(12)-C(7)-C(8)	110.42(17)
C(5)-C(6)	1.528(3)	C(12)-C(7)-P(2)	111.51(14)
C(7)-C(12)	1.524(3)	C(8)-C(7)-P(2)	115.42(14)
C(7)-C(8)	1.530(3)	C(9)-C(8)-C(7)	111.33(18)
C(8)-C(9)	1.527(3)	C(10)-C(9)-C(8)	111.38(19)
C(9)-C(10)	1.514(3)	C(9)-C(10)-C(11)	110.82(19)
C(10)-C(11)	1.519(3)	C(10)-C(11)-C(12)	111.86(19)
C(11)-C(12)	1.526(3)	C(7)-C(12)-C(11)	110.18(18)
C(15)-C(18)	1.525(3)	N(1)-C(13)-P(1)	115.67(13)
C(15)-C(17)	1.528(3)	N(1)-C(14)-P(2)	114.10(13)
C(15)-C(16)	1.530(3)	N(1)-C(15)-C(18)	109.96(17)
C(21)-C(22)	1.524(3)	N(1)-C(15)-C(17)	112.68(17)
C(21)-C(24)	1.528(3)	C(18)-C(15)-C(17)	108.52(19)
C(21)-C(23)	1.528(3)	N(1)-C(15)-C(16)	107.64(17)
P(1)#1-Ni(1)-P(1)	111.36(4)	C(18)-C(15)-C(16)	108.07(19)
P(1)#1-Ni(1)-P(2)#1	81.83(3)	C(17)-C(15)-C(16)	109.87(19)
P(1)-Ni(1)-P(2)#1	140.49(2)	N(2)-C(19)-P(1)	114.26(13)
P(1)#1-Ni(1)-P(2)	140.49(2)	N(2)-C(20)-P(2)	115.57(14)
P(1)-Ni(1)-P(2)	81.83(3)	N(2)-C(21)-C(22)	112.90(17)
P(2)#1-Ni(1)-P(2)	112.13(3)	N(2)-C(21)-C(24)	109.85(18)
C(1)-P(1)-C(19)	99.85(9)	C(22)-C(21)-C(24)	108.28(19)
C(1)-P(1)-C(13)	102.07(9)	N(2)-C(21)-C(23)	107.74(17)
C(19)-P(1)-C(13)	102.08(9)	C(22)-C(21)-C(23)	109.9(2)
C(1)-P(1)-Ni(1)	126.41(7)	C(24)-C(21)-C(23)	108.06(19)

7.1.3. Electron Paramagnetic Spectroscopy

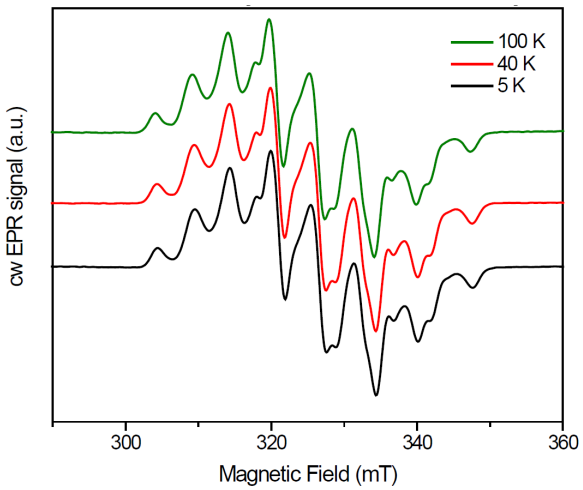

Figure 7.1.3. Comparison of CW X-band EPR spectra of **1**[BF_4] in butyronitrile at 5 K (black), 40 K (red), and 100 K (green). The CW X-band EPR spectra show no temperature dependence in the temperature range investigated (5-100 K). The same paramagnetic species is thus monitored in this temperature range. This allows us to use the respective optimal temperature for experiments at different microwave frequencies (X-, Q-, D-band).

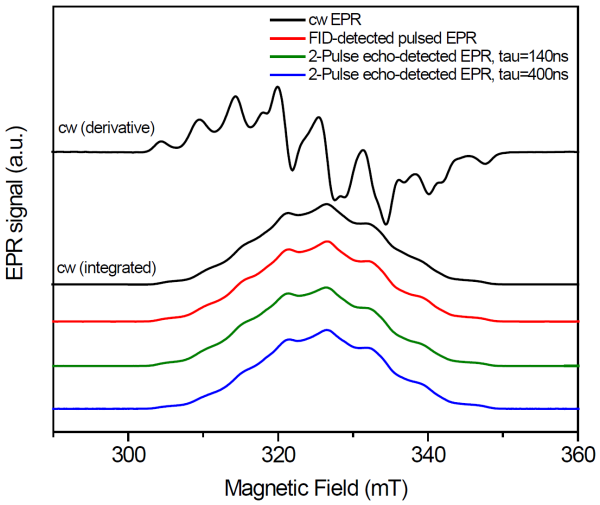

Figure 7.1.4. Comparison of CW and pulsed X-band EPR spectra of **1**[BF_4] in butyronitrile at 5–15 K. Note that the magnetic field has been adjusted to compensate for differences in mw frequencies. The integrated CW EPR spectrum is very similar to spectra recorded with various pulse sequences. This ensures that same paramagnetic species is monitored in CW and pulsed EPR experiments.

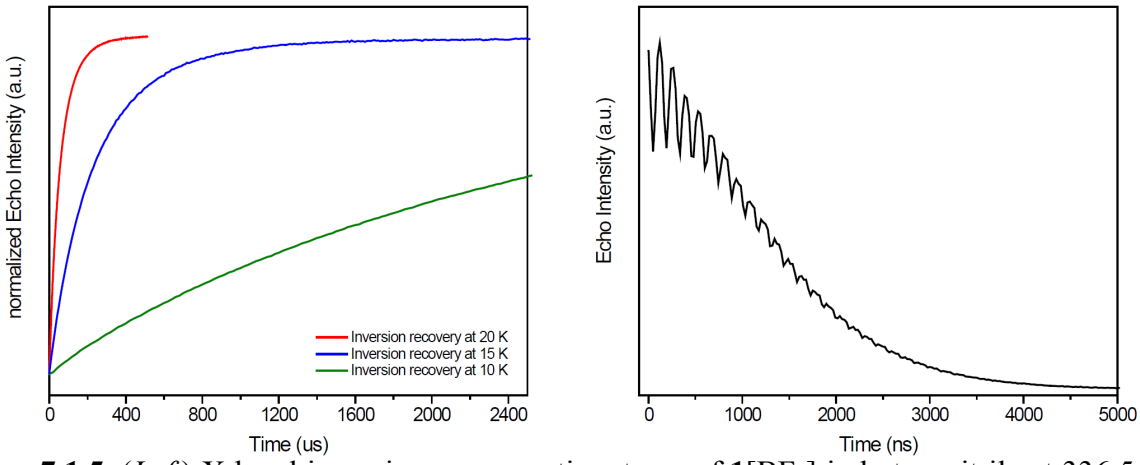

Figure 7.1.5. (*Left*) X-band inversion recovery time trace of **1**[BF_4] in butyronitrile at 336.5 mT (maximum echo intensity; see Figures 7.1.7 and 7.1.8). (*Right*) X-band 2-Pulse ESEEM time trace of **1**[BF_4] in butyronitrile at 336.5 mT (maximum echo intensity; see Figures 7.1.7 and 7.1.8) at 15 K. A strong effect of temperature on spin-lattice relaxation time (T_{1e}) was observed; 15 K was chosen for most pulsed X-band experiments. The relatively long spin-spin relaxation time (T_{2e}) confirms that we observed isolated paramagnetic complexes and not aggregates/multimers.

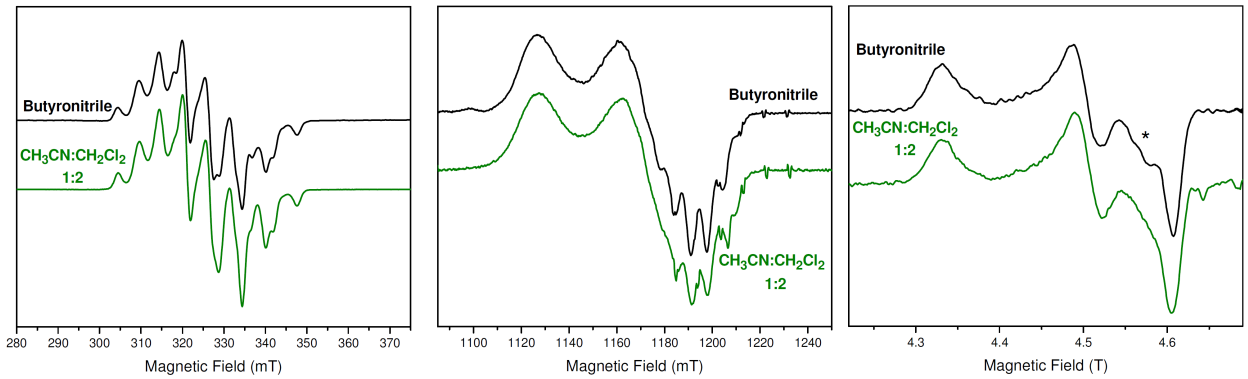

Figure 7.1.6. Comparison of EPR spectra of **1**[BF_4] in butyronitrile (black) and 1:2 CH_3CN:CH_2Cl_2 (green) at 5–15 K. The X-band EPR spectrum has been recorded in continuous wave (CW) mode; thus, the spectrum represents the first derivative of an absorption spectrum. The Q-band and D-band measurements generated absorption-type spectra, but were pseudomodulated[6] to yield derivative-type spectra. The asterisk marks the EPR signal of an additional paramagnetic substance, probably due to decomposition of $\mathbf{1}^+$; see Chapter 2 for details. The EPR spectra of **1**[BF_4] observed at the three different microwave frequencies are virtually identical in the two solvents. For magnetic resonance parameters, see main text.

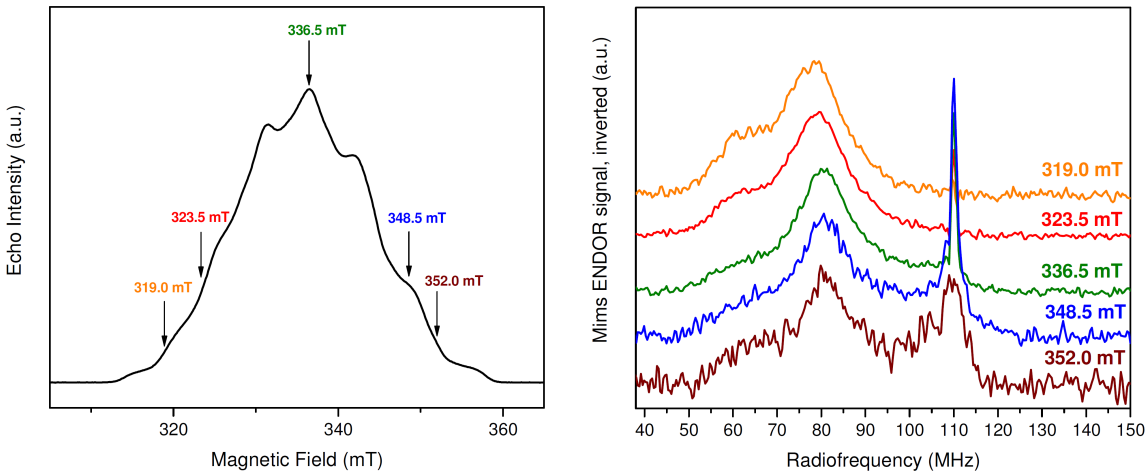

Figure 7.1.7. (*Left*) Field-swept echo-detected X-band EPR spectrum of 1[BF_4] in butyronitrile at 15 K. Arrows indicate the magnetic field positions where the ENDOR spectra were recorded. (*Right*) ^{31}P X-band Mims ENDOR spectra (inverted) of **1**[BF_4] in butyronitrile at 15 K. The ^{31}P nuclei are strongly coupled to the unpaired electron of **1**[BF_4]; the ENDOR signals of each ^{31}P nucleus are centered around A/2. The ENDOR frequencies and intensities are dependent on the static magnetic field selected. Hyperfine interaction extracted from analysis of the ENDOR spectra agrees with the information extracted from simulation of the EPR spectra. The sharp signal around 110 MHz is an artifact of our setup.

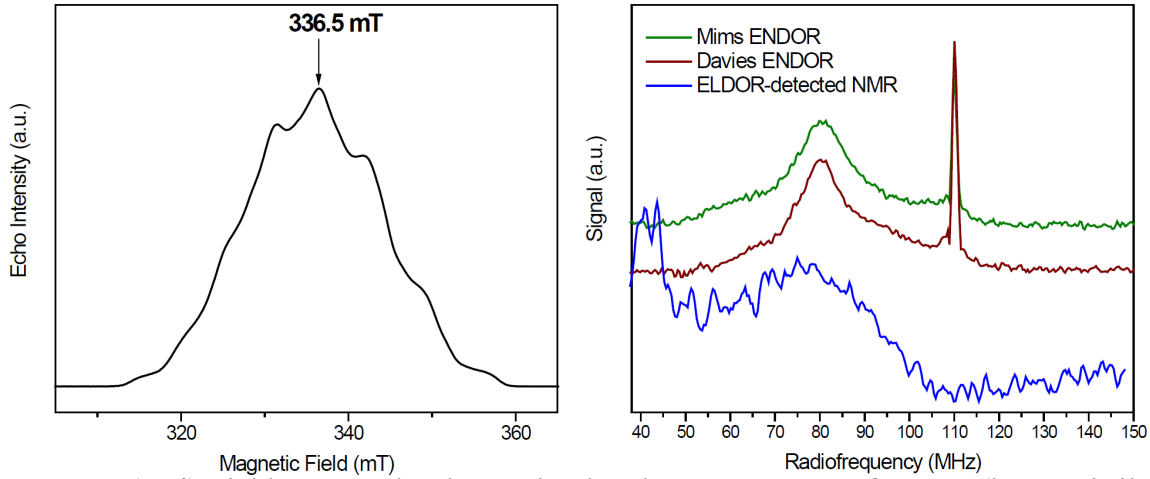

Figure 7.1.8. (*Left*) Field-swept echo-detected X-band EPR spectrum of **1**[BF_4] (butyronitrile, 15 K). (*Right*) ^{31}P X-band Mims ENDOR spectrum (green; inverted), ^{31}P X-band Davies ENDOR spectrum (brown), and ELDOR-detected NMR spectrum (blue) of **1**[BF_4] (butyronitrile, 15 K). Davies ENDOR delivered essentially the same information as Mims ENDOR. ELDOR-detected NMR (no RF irradiation) shows resonance at the same frequencies, confirming that these signals are not an artifact of the intense RF irradiation.

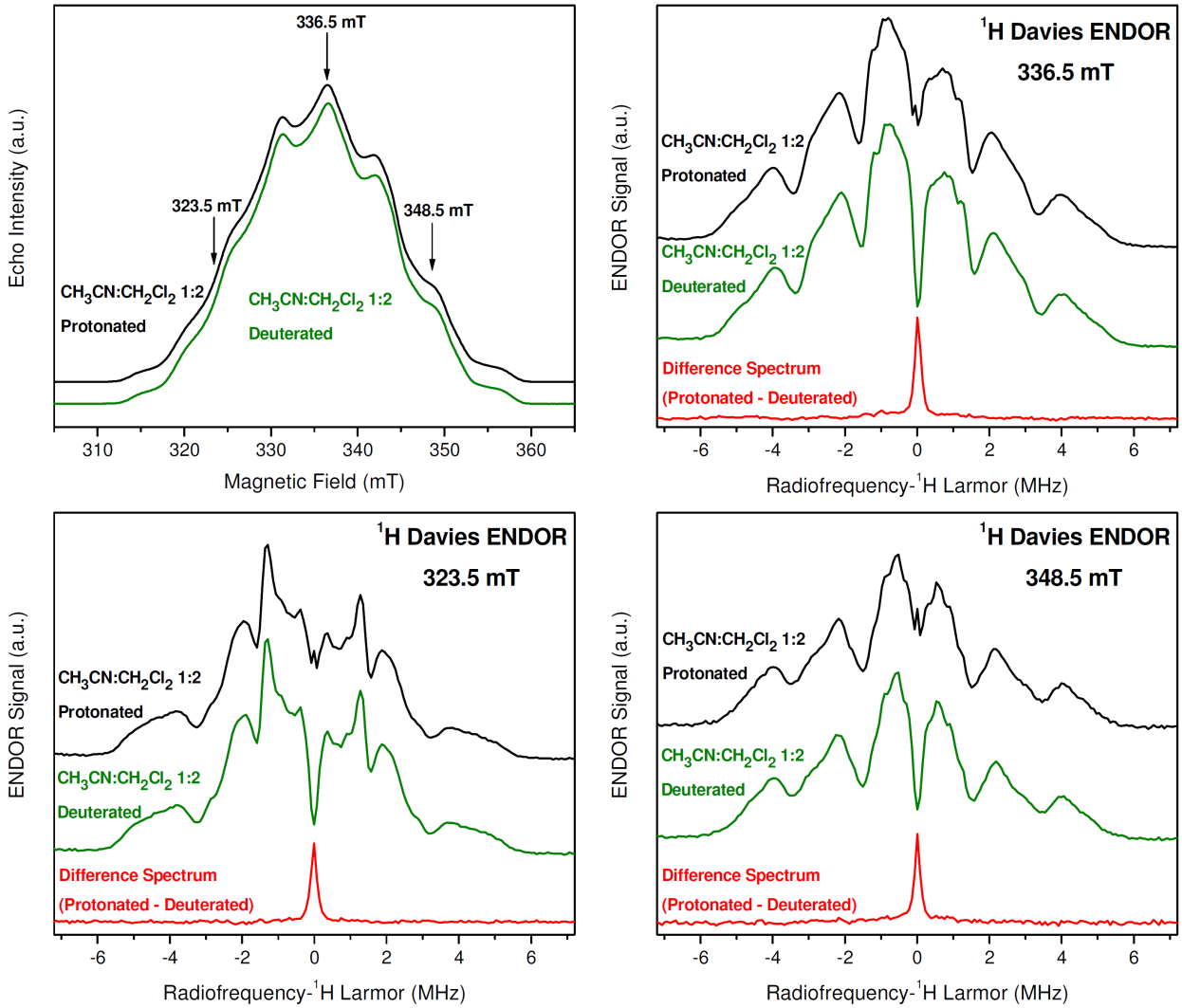

Figure 7.1.9. Pulsed X-band EPR and Davies ENDOR spectra of **1**[BF_4] in fully protonated (black) and fully deuterated (green) 1:2 CH_3CN:CH_2Cl_2 mixtures at 15 K. (*Upper left*) Field-swept echo-detected X-band EPR spectra; arrows indicate the magnetic field positions where the ENDOR spectra were recorded. (*Upper right*) ^{1}H X-band Davies ENDOR spectra; the red trace is the difference spectrum. (*Lower left*) ^{1}H X-band Davies ENDOR spectra, recorded at 323.5 mT; the red trace is the difference spectrum. (*Lower right*) ^{1}H X-band Davies ENDOR spectra, recorded at 348.5 mT; the red trace is the difference spectrum. The comparison of ^{1}H Davies ENDOR measurements of **1**[BF_4] in fully deuterated and fully protonated 1:2 CH_3CN:CH_2Cl_2 mixtures clearly shows that solvent ^{1}H contribute only to the matrix part of the ENDOR spectra, i.e., the spectral region close to the Larmor frequency. This means that they are only weakly dipolar coupled and distant from the paramagnetic center of compound **1**$^+$.

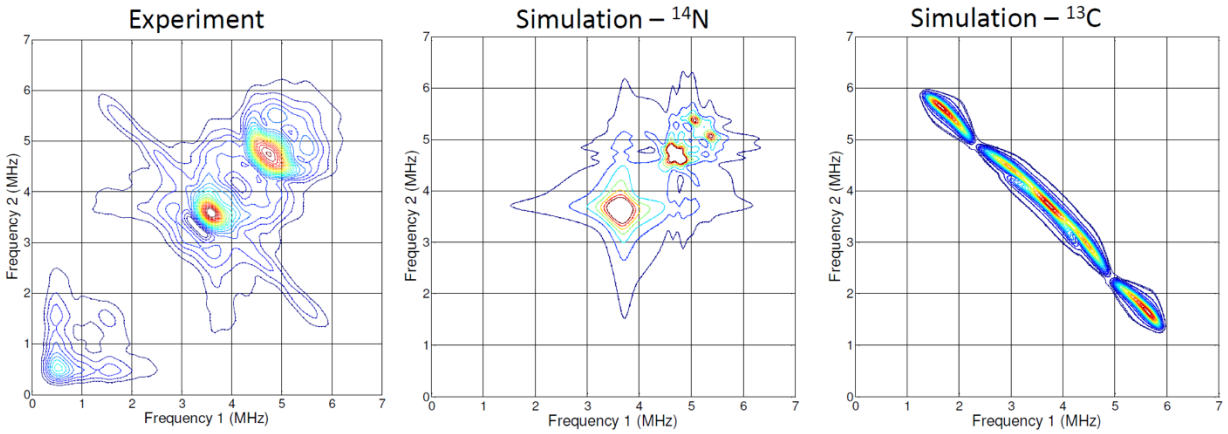

Figure 7.1.10. (*Left*) HYSCORE spectrum of **1**[BF_4] recorded at magnetic field position 336.5 mT (butyronitrile, 20 K). (*Middle*) Simulation of HYSCORE spectrum with one ^{14}N nucleus; A-tensor (+0.3, +0.2, +0.3 MHz), Q-tensor (+1.38, +1.46, –2.84 MHz). (*Right*) Simulation of HYSCORE spectrum with two ^{13}C nuclei; A-tensors (+2.7, +4.6, +2.7 MHz) and (–1.4, +2.6, –1.4 MHz). Note that the levels of contour plot intensities are not adjusted. The signals of weakly coupled ^{14}N nuclei (four nitrogen nuclei almost equidistant from the Ni-center) dominate the depicted part of the HYSCORE spectrum. Signals from intermediate and weakly coupled ^{13}C nuclei may contribute to the HYSCORE spectrum.

7.1.4. Density Function Theory Calculations

Table 7.1.3. Effect of Functional and Basis Set on Calculated EPR Parameters for $\mathbf{1}^+$.[a]

Functional	Basis Set	g-values	^{31}P A-tensors (MHz)[b]
B3LYP	def2-TZVP[7]	2.1664, 2.0702, 2.0541	155, 161, 203
B3LYP	EPRII for C, N, H[10,11] IGLOII for P[8] Wachters for Ni[9-11]	2.1613, 2.0636, 2.0454	154, 160, 203

[a] EPR parameters were calculated using Orca 2.9.1[12] and the B3LYP functional.[13-16] The initial structure was optimized with BP86|3-21G and used a slightly different starting structure than that of the main text resulting in g-values that differ by less than 1/10,000th. [b] The hyperfine coupling constants of the four ^{31}P nuclei were found to be identical within 1 MHz in both calculations, respectively.

Table 7.1.4. Effect of Functional and Basis Set used for Geometry Optimization on the Calculated EPR Parameters for 1^+.[a]

Functional	Basis Set	g-values	Isotropic Hyperfine Couplings of the four ^{31}P nuclei (MHz)	Average Ni–P distance (Å)[b]
BP86	3-21G	2.1614, 2.0636, 2.0454	172, 172, 172, 172	2.225 (0.0002)
BP86	6-31G	2.1668, 2.0698, 2.0535	203, 204, 203, 204	2.297 (0.0002)
B3LYP	3-21G	2.2217, 2.1066, 2.0830	136, 139, 136, 139	2.280 (0.0006)
B3LYP	6-31G	2.2444, 2.1229, 2.0974	151, 151, 151, 151	2.382 (0.0003)
PBE	3-21G	2.1538, 2.0596, 2.0422	177, 177, 177, 177	2.220 (0.0001)
PBE	6-31G	2.1609, 2.0664, 2.0506	206, 207, 206, 207	2.291(0.0001)
— [c]	— [c]	2.146, 2.063, 2.017	165, 165, 165, 165	2.2185 (0.0014)

[a] EPR parameters were calculated using Orca 2.9.1,[12] the B3LYP functional,[13-16] the EPRII basis set[17-18] for C, N, and H, the IGLOII basis set[8] for P, and Wachters basis set[9-11] for Ni. [b] Ni–P distance averaged over the four bonds is given with the standard deviation in parentheses. [c] Experimentally determined EPR parameters, Ni–P distance determined from crystal structure.

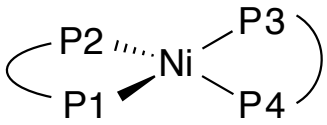

Figure 7.1.11. Numbering system for phosphorus nuclei of $\mathbf{1}^+$.

Table 7.1.5. Calculated (BP86|3-21G) Ni–P Bond Lengths of $Ni(P^R_2N^{R'}_2)_2^+$ Complexes. Atom Numbers are Defined in Figure 7.1.11.

Compound	R	R′	*d*(Ni–P) (Å)				d_{av}(Ni–P) (Å)
			Ni–P1	Ni–P2	Ni–P3	Ni–P4	
$\mathbf{1}^+$	Cy	*t*Bu	2.225	2.225	2.224	2.225	2.225
$\mathbf{2}^+$	Ph	*t*Bu	2.244	2.245	2.245	2.245	2.245
$\mathbf{3}^+$	Cy	Ph	2.229	2.229	2.229	2.229	2.229
$\mathbf{4a}^+$	Ph	Ph	2.252	2.243	2.243	2.248	2.247
$\mathbf{4b}^+$	Ph	Ph	2.275	2.246	2.246	2.275	2.261
$\mathbf{4c}^+$	Ph	Ph	2.267	2.240	2.235	2.243	2.246

Table 7.1.6. Calculated (BP86|3-21G) NiP_4 Bond Angles of $Ni(P^R{}_2N^{R'}{}_2)_2{}^+$ Complexes. Atom Numbers are Defined in Figure 7.1.11. For definition of R/R′, see Table 7.1.5.

Compound	∠(P–Ni–P) intra-ligand (˚)		∠(P–Ni–P) inter-ligand (˚)				α (˚)
	P1–Ni–P2	P3–Ni–P4	P1–Ni–P3	P1–Ni–P4	P2–Ni–P3	P2–Ni–P4	
1$^+$	83.78	83.77	135.50	113.31	113.23	135.51	69.09
2$^+$	83.09	83.09	134.33	114.96	114.89	134.34	71.62
3$^+$	85.44	85.44	139.81	108.42	108.36	139.82	60.85
4a$^+$	84.96	84.15	138.52	109.80	109.64	139.94	62.37
4b$^+$	84.86	84.85	142.40	110.99	103.64	142.41	56.66
4c$^+$	85.06	86.25	143.21	109.70	105.17	138.26	59.18

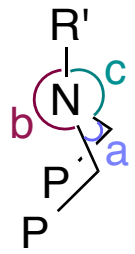

Figure 7.1.12. Labeling system for bond angles about nitrogen nuclei.

Table 7.1.7. Calculated (BP86|3-21G) Bond Angles about the Pendant Amines of $Ni(P^{R}_2N^{R'}_2)_2^+$ Complexes. Angles *a*, *b*, and *c* are Defined in Figure 7.1.12.

Compound	∠a (˚)				∠$_{av}$ a (˚)
	CH_2–**1**N(R′)–CH_2	CH_2–**2**N(R′)–CH_2	CH_2–**3**N(R′)–CH_2	CH_2–**4**N(R′)–CH_2	
1$^+$	111.18	111.18	111.18	111.18	111.18
2$^+$	111.66	111.66	111.66	111.66	111.66
3$^+$	114.77	114.81	114.77	114.80	114.79
4a$^+$	115.10	115.13	115.83	116.00	115.52
4b$^+$	116.96	115.66	115.68	116.94	116.31
4c$^+$	117.52	116.87	115.15	115.62	116.29
Compound	∠b (˚)				∠$_{av}$ b (˚)
	CH_2–**1**N(R′)–CH_2	CH_2–**2**N(R′)–CH_2	CH_2–**3**N(R′)–CH_2	CH_2–**4**N(R′)–CH_2	
1$^+$	111.22	111.22	111.22	111.22	111.22
2$^+$	111.82	111.81	111.81	111.81	111.81
3$^+$	117.18	117.14	117.13	117.19	117.16
4a$^+$	112.57	119.33	118.83	118.95	117.42
4b$^+$	121.63	118.43	118.46	121.60	120.03
4c$^+$	121.01	122.11	116.90	120.70	120.18
Compound	∠c (˚)				∠$_{av}$ c (˚)
	CH_2–**1**N(R′)–CH_2	CH_2–**2**N(R′)–CH_2	CH_2–**3**N(R′)–CH_2	CH_2–**4**N(R′)–CH_2	
1$^+$	111.25	111.27	111.27	111.25	111.26
2$^+$	110.85	110.86	110.85	110.86	110.86
3$^+$	116.75	116.68	116.68	116.75	116.72
4a$^+$	115.47	118.22	117.67	117.94	117.33
4b$^+$	119.78	117.22	117.23	119.78	118.51
4c$^+$	119.01	119.52	116.36	119.27	118.54

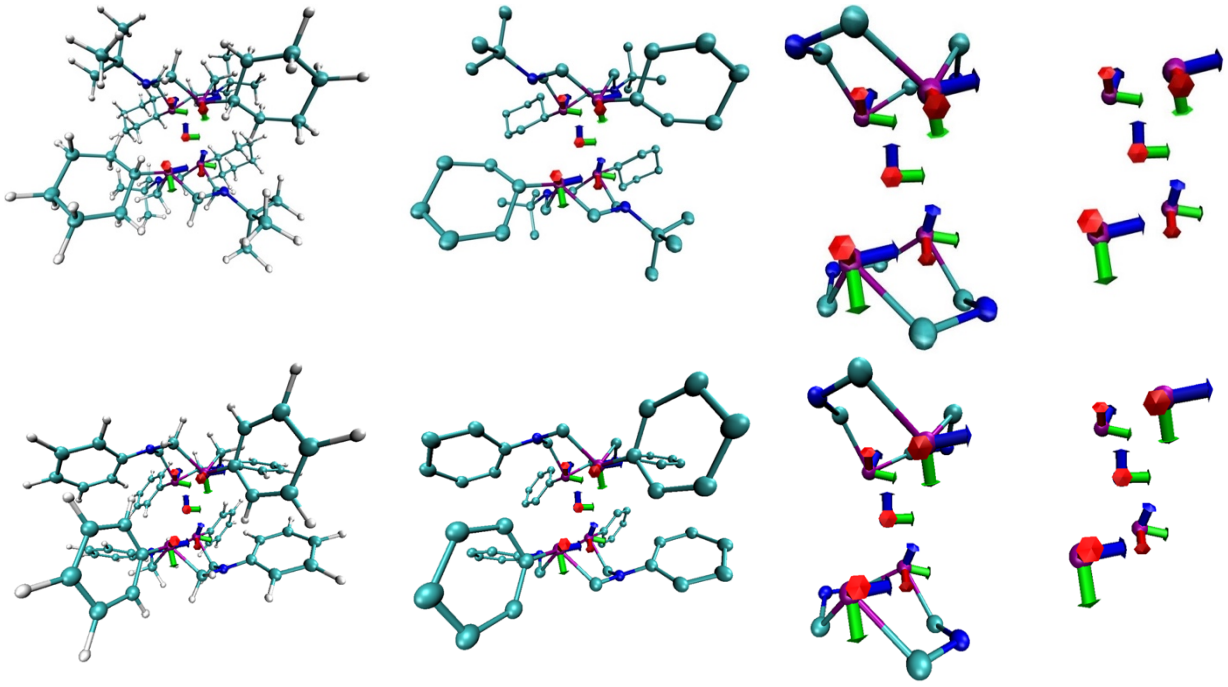

a **b** **c** **d**

Figure 7.1.13. Calculated structures of complexes $\mathbf{1}^+$ (*top*) and $\mathbf{4b}^+$ (*bottom*) with orientation of g-tensor on central nickel atom (blue = g_Z, red = g_Y, green = g_X; $g_X > g_Y > g_Z$) and orientation of ^{31}P A-tensors (blue=A_Z, red=A_Y, green=A_X; $A_X > A_Y > A_Z$): (a) all-atom; (b), no hydrogens; (c) only the central scaffold; (d) only the central nickel atom and the four surrounding phosphorus atoms. See Tables 7.1.8 and 7.1.12 for ^{31}P A-tensors of complexes $\mathbf{1}^+$ and $\mathbf{4b}^+$.

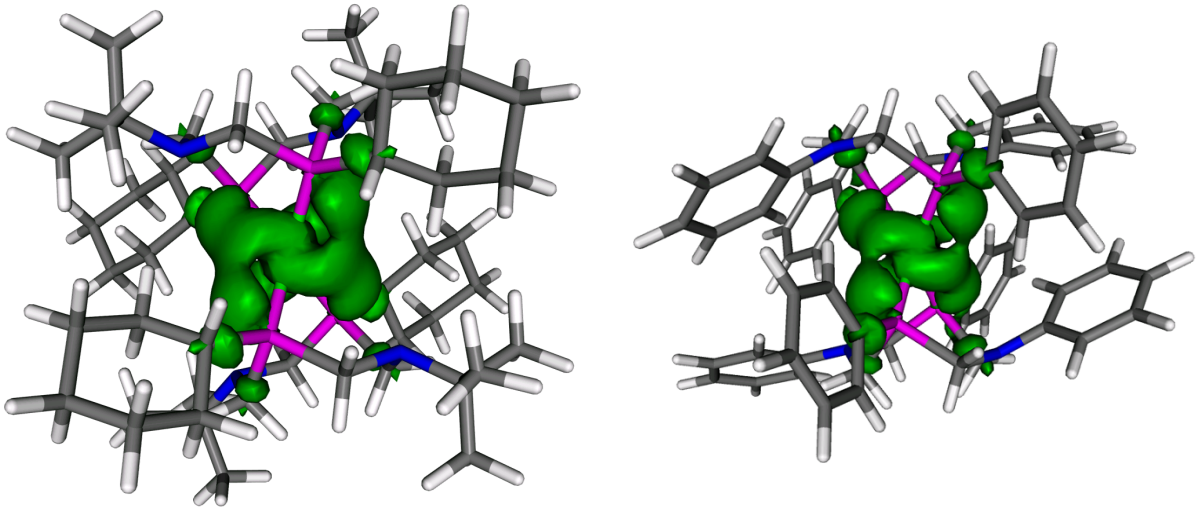

1$^+$ **4b**$^+$

Figure 7.1.14. Calculated electron spin densities for 1^+ and a representative 4^+ structure ($4b^+$) at the 0.001 e/a_0^3 isosurface level.

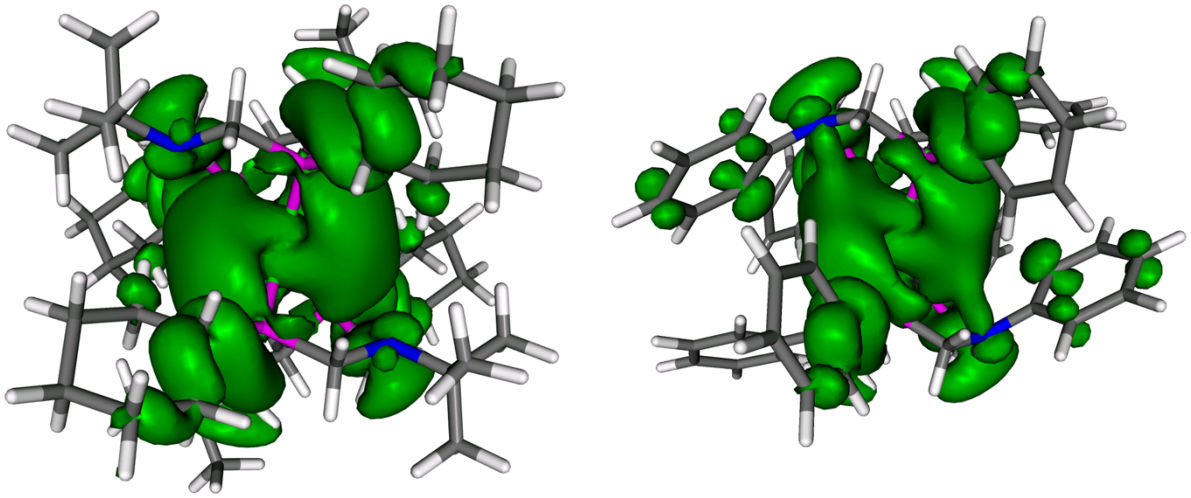

1$^+$ **4b**$^+$

Figure 7.1.15. Calculated electron spin densities for **1**$^+$ and a representative **4**$^+$ structure (**4b**$^+$) at the 0.0001 e/a_0^3 isosurface level.

7.2. Chapter 3 Supplementary Information

7.2.1. Definitions

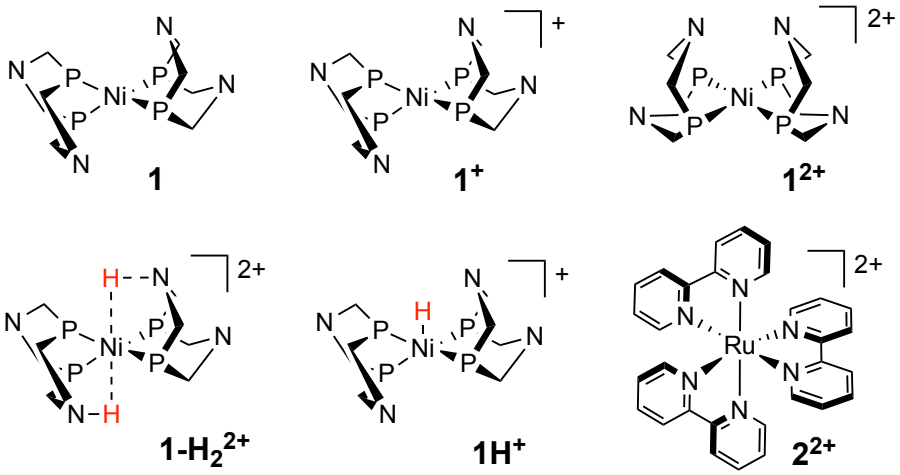

Figure 7.2.1. The compounds discussed in Section 7.2. For clarity, the phosphine (cyclohexyl) and amine (*tert*-butyl) substituents of the nickel compounds are not shown.

7.2.2. Synthesis and Characterization of Compounds

Methods. All manipulations were performed under a nitrogen atmosphere using standard glovebox and Schlenk techniques, unless otherwise noted. ^{1}H and $^{31}P\{^{1}H\}$ NMR spectra were recorded at room temperature with Bruker DRX 400 or AF500 spectrometers. Chemical shifts were measured relative to the isotopic impurity in the NMR solvent (^{1}H)[19] or an external standard of 85% H_3PO_4 in D_2O (^{31}P). J. Young NMR tubes were employed for some experiments; these tubes are topped with Teflon valves that provide an air-tight seal and enable connection to a vacuum line. Electronic-absorption spectra were obtained with a Cary 300 UV-visible spectrophotometer of samples contained in quartz cuvettes.

Preparation of $1H^+$ by the reaction between $1\text{-}H_2^{2+}$ and 1. A solution sample of $\mathbf{1\text{-}H_2^{2+}}$ was prepared *in situ* by adaptation of a reported procedure.[20] A J. Young NMR tube was charged with 1 mL of a 3.2 mM solution of $\mathbf{1}[BF_4]_2$ (3.2 μmol) in PhCN that contained 5% v/v CD_3CN. The sample was degassed *via* 3 freeze–pump–thaw cycles on a high vacuum line, back-filled with

H_2 during the final thaw process (~2 atm), and sealed. The sample immediately changed color from red to pale yellow and the formation of **1-H_2**$^{2+}$ was shown by $^{31}P\{^1H\}$ NMR (δ = 16.8 Figure 3.5). The NMR tube was reopened under N_2 and **1** (3.0 mg (± 0.2 mg); 3.28 μmol) was added. The color of the solution turned to a darker yellow. The $^{31}P\{^1H\}$ NMR spectrum showed the presence of only **1H**$^+$ (δ = 12.6, Figure 3.5).

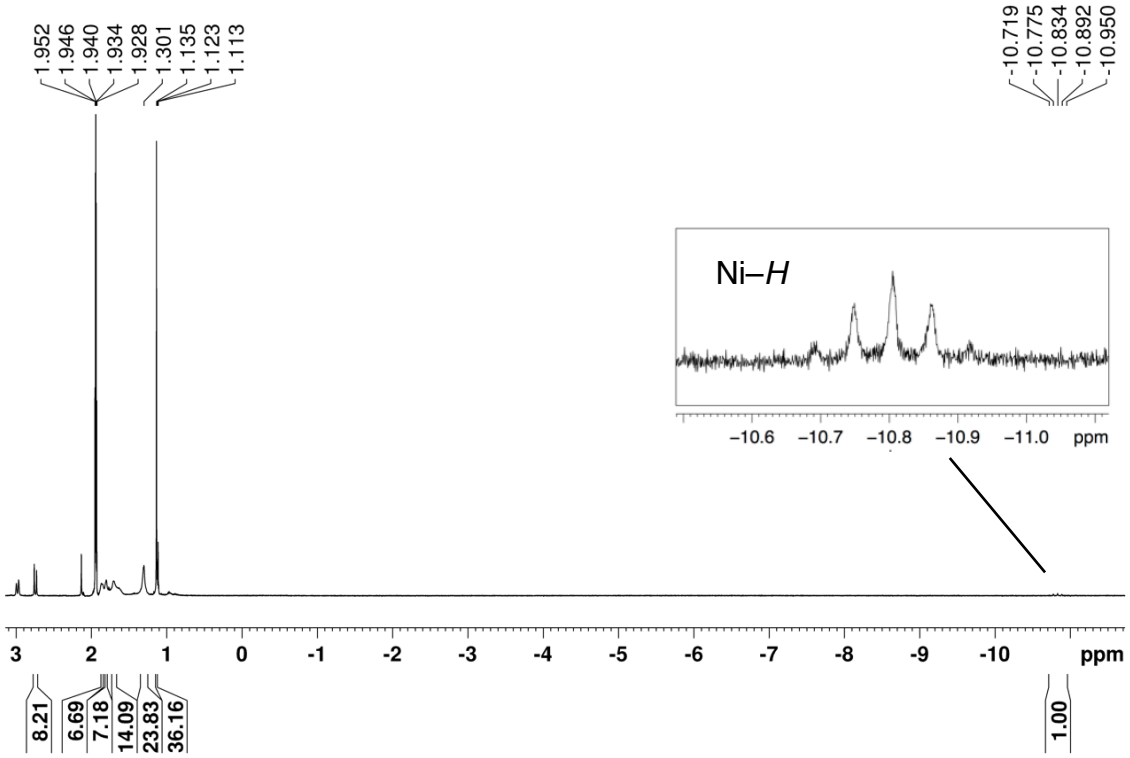

Figure 7.2.2. ^1H NMR spectrum of **1H**[BF_4] (CD_3CN, 400 MHz). The Ni–H resonance is shown in the inset.

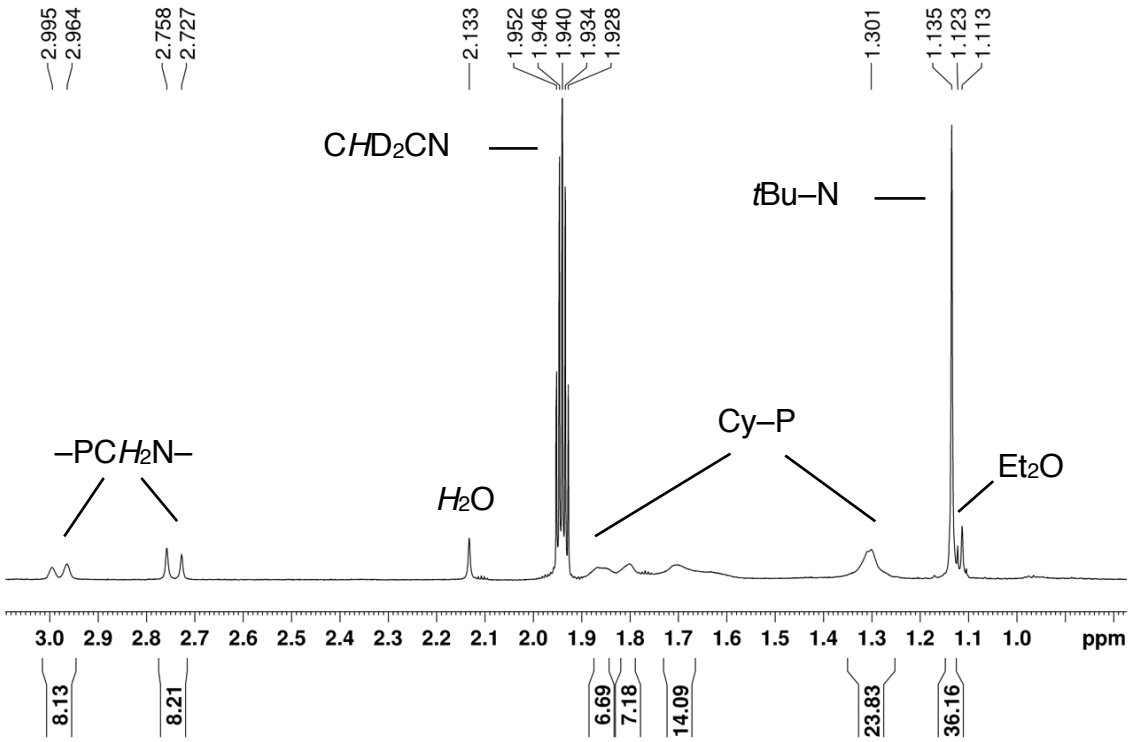

Figure 7.2.3. Expansion of Figure 7.2.2 (^{1}H NMR spectrum of **1H**[BF_4]; CD_3CN, 400 MHz).

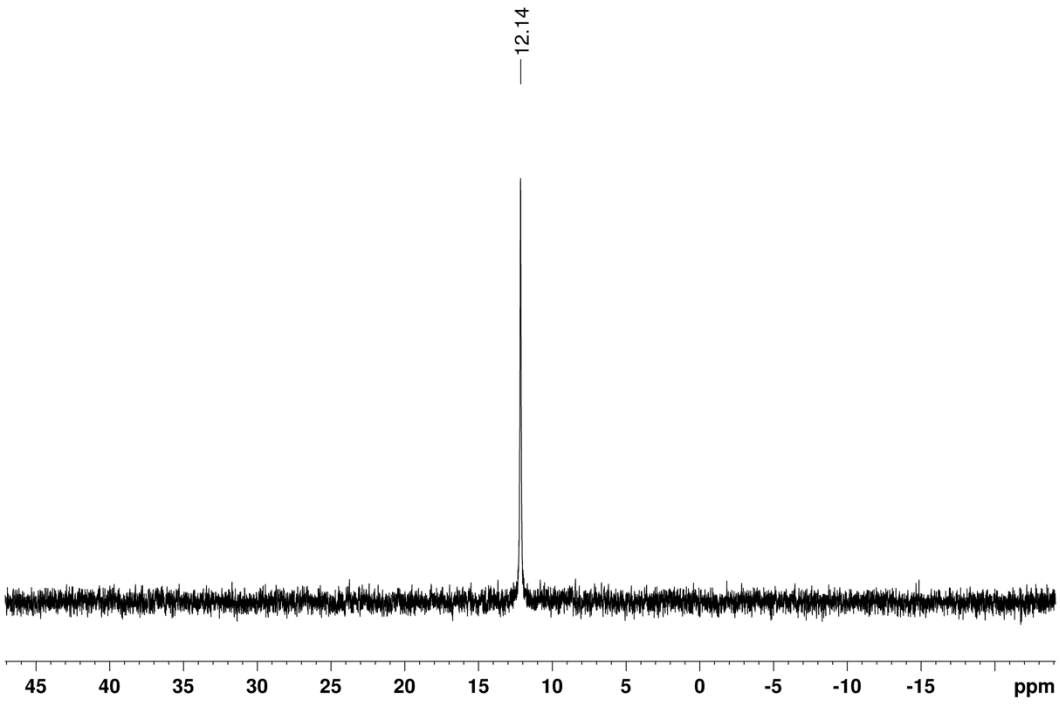

Figure 7.2.4. $^{31}P\{^{1}H\}$ NMR spectrum of **1H**[BF_4] in CD_3CN solution.

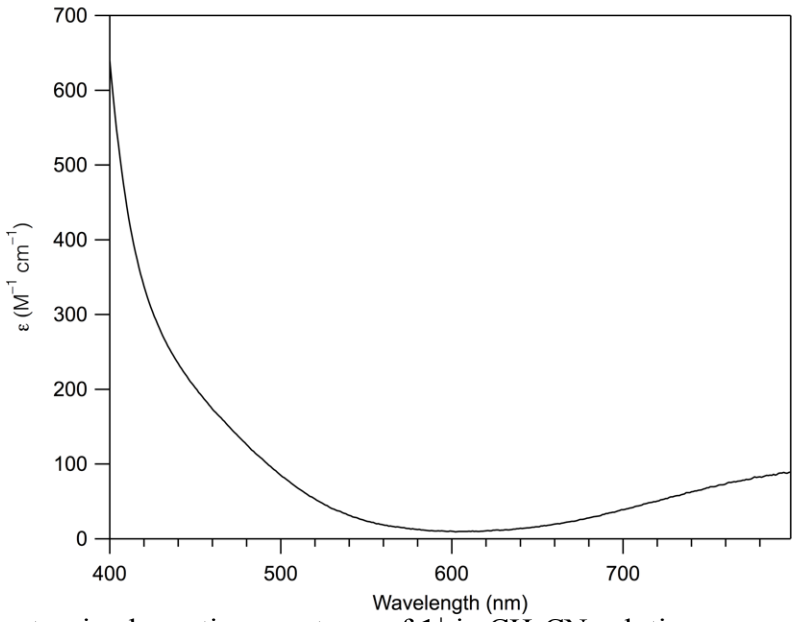

Figure 7.2.5. Electronic-absorption spectrum of $\mathbf{1}^{+}$ in CH_3CN solution.

7.2.3. Photochemical and Photophysical Experiments

Methods. Electronic-absorption spectra were obtained with a Cary 300 UV-Vis spectrophotometer of samples contained in quartz cuvettes. Photoluminescence lifetimes were measured using a custom-built pulsed-laser instrument that has been described previously.[21] Excitation was provided by an integrated Nd:YAG-optical-parametric-oscillator pulsed laser (Opotek Vibrant 355 LD; 10 Hz, 10-ns pulse width, 0.5–1.5 mJ pulse energy at sample). The luminescence from the sample was detected using a photomultiplier tube (Hamamatsu R5108) affixed to a monochromator (Horiba Scientific iHR320) and processed with a digital oscilloscope (TDS 3032C; Tektronix). Lifetimes were determined from analysis of luminescence decay traces that were the averages of 512 individual decays. Electronic-absorption spectra recorded before and after luminescence-lifetime measurements indicated that samples were photochemically stable under the experimental conditions. Preparative photolysis experiments were conducted in a sample chamber that was sealed from ambient light and contained a 455 nm Mounted High Power LED

(900 mW; ThorLabs) whose output was focused onto the sample through a bi-convex lens (ThorLabs N-BK7; f = 60.0 mm).

Luminescence quenching measurements. The luminescence quenching of $\mathbf{2}^{2+}$ by pyrrolidine, **1**[BF_4] and **1H**[BF_4] was studied by luminescence-lifetime measurements. Samples containing systematically varied concentrations of pyrrolidine (0–250 mM; Figure 7.2.11), **1**[BF_4] (0–2.0 mM; Figure 3.2), or **1H**[BF_4] (0–4.0 mM; Figure 3.6) were prepared from a CH_3CN stock solution of **2**[PF_6]$_2$ (10 μM), degassed by at least 3 freeze–pump–thaw cycles on a vacuum line, and sealed under nitrogen. The samples were excited at 455 nm and the luminescence was detected at 605 nm using the pulsed-laser instrumentation described above (see Methods). Kinetic analyses of spectra were performed using Igor Pro. The lifetime of $\mathbf{2}^{2+*}$ was determined by fitting the emission decay trace at 605 nm to a single exponential function, over a time-range of at least 3τ.

Photochemical stability studies of $\mathbf{1}^{+}$, $\mathbf{1}^{2+}$ and $\mathbf{1H}^{+}$. Photochemical studies of acetonitrile solutions of $\mathbf{1}^{+}$, $\mathbf{1}^{2+}$, and $\mathbf{1H}^{+}$ show all three to exhibit changes in their electronic-absorption spectra upon photolysis with visible light (λ_{ex} = 455 nm; Figures 7.2.6–8). For $\mathbf{1}^{+}$, a band was observed to grow in at approximately 490 nm and, concomitantly, a band at >600 nm diminished in intensity. The decay of the long-wavelength band corresponds to the consumption of 33% of the initial $\mathbf{1}^{+}$ over 24 h. This contrasts with photochemical experiments that feature $\mathbf{1}^{+}$ in the presence of $\mathbf{2}^{2+}$ and H_2, where complete decay of the same band was observed within 1 h (Figure 3.3)—indicating that background photolytic degradation of $\mathbf{1}^{+}$ is very slow in comparison to the photosensitized conversion of $\mathbf{1}^{+}$ to $\mathbf{1H}^{+}$. The photolysis of $\mathbf{1H}^{+}$ yields its partial conversion to $\mathbf{1}^{+}$, as shown by the appearance of a similar long-wavelength (>600 nm) band. It is unclear if this process is photochemically or thermally driven, as a related $[NiH(P^R_2N^{R'}_2)_2]^{+}$ species has been reported[22] to thermally decompose to the corresponding Ni(I) species with the presumed release of H_2. Given

that the reaction of photogenerated $\mathbf{1}^{2+}$ with H_2 is rapid enough to outcompete back-electron transfer, the lifetime of $\mathbf{1}^{2+}$ under the photochemical conditions of this study is assumed to be too brief to render its photolytic behavior relevant. Further, all the studies neglect to include the effect of internal filtering of $\mathbf{2}^{2+}$, which is a component of all photoredox experiments.

Photoredox-sensitized preparation of $\mathbf{1H}^+$ from $\mathbf{1}^+$ and H_2 in PhCN. A stock solution containing **2**$[PF_6]_2$ (67 μM), **1**$[BF_4]$ (1.9 mM), and PCy_3O (4.7 mM; internal ^{31}P-NMR standard) in 19:1 PhCN:CD_3CN was prepared in a flask that was shielded from light. The absorbance of the starting solution at 452 nm, after correcting for $\mathbf{1}^+$ (ε = 376 M^{-1} cm^{-1} at 452 nm, Figure 7.2.5), gives the concentration of $\mathbf{2}^{2+}$ to be 67 μM. Aliquots of this solution were dispensed into two sealable UV-Vis cuvettes and one J. Young sealable NMR tube with protection from light. Hydrogen (~2 atm) was added to the NMR tube and one of the cuvettes; this was accomplished on a vacuum line by degassing the samples via at least 3 freeze–pump–thaw cycles and then backfilling them during the final thaw process with H_2. The other cuvette remained under N_2 atmosphere as a control. Initial $^{31}P\{^1H\}$ NMR (δ 48.3 (PCy$_3$O)) and UV-Vis measurements were made at this point. All samples were then photolyzed with 455-nm light (see Methods, above). The samples under a H_2 atmosphere were monitored by UV-Vis spectroscopy every 10 min or $^{31}P\{^1H\}$ NMR spectroscopy every 20 min. The sample under N_2 atmosphere was monitored after 1 h of photolysis. Samples were shielded from light while being transported to and from the spectrometers and during measurement. The samples under H_2 atmosphere exhibited complete consumption of $\mathbf{1}^+$ over 1 h (UV-Vis, Figure 3.3) and concomitant production of $\mathbf{1H}^+$ ($^{31}P\{^1H\}$ NMR, δ 12.6, Figure 3.4); integration of the latter relative to the internal standard indicates a 94% yield based on **1**$[BF_4]$. The sample under N_2 did not exhibit appreciable change after photolysis for 1 h (Figure 7.2.12).

Photoredox-sensitized preparation of $1H^+$ and 1 from 1^+ and H_2 in CD_3CN. A CD_3CN solution of **1**[BF_4] (2 mM) and **2**[PF_6]$_2$ (70 μM) was prepared while shielded from light and transferred to a J. Young NMR tube. The sample was degassed via 3 freeze–pump–thaw cycles on a vacuum line and backfilled with H_2 (~2 atm) during the final thaw process. It was then photolyzed with 455 nm light and monitored at regular intervals by $^{31}P\{^1H\}$ and ^1H NMR; signals associated with **1H**[BF_4] appeared and increased in intensity during photolysis. A white precipitate was seen after 1 h of photolysis (Figure 7.2.13). After 3 hours of photolysis the solid was isolated by decantation. The solid was identified as **1** on the basis of its $^{31}P\{^1H\}$ NMR spectrum (C_6D_6, δ7.4).

Photoredox-sensitized preparation of 1 from $1H^+$ and pyrrolidine. A J. Young NMR tube containing a solution of **2**[PF_6]$_2$ (70 μM), **1H**[BF_4] (7.5 mM), pyrrolidine (140 mM), and PCy_3O (6.7 mM; internal ^{31}P-NMR standard) in CD_3CN was prepared in the dark and its $^{31}P\{^1H\}$-NMR spectrum recorded (δ12.1 (**$1H^+$**), 48.5 (PCy_3O), Figure 3.7). The sample was then irradiated with 455 nm light for 45 min, resulting in formation of a white precipitate (Figure 7.2.14). The $^{31}P\{^1H\}$ NMR spectrum of this sample showed that 50% of the **1H**[BF_4] had been consumed; no other signals were observed. The solvent was removed slowly from the sample under vacuum in the dark, and C_6D_6 was added to the remaining solid. The $^{31}P\{^1H\}$-NMR spectrum exhibited only signals attributable to **$1H^+$**, **1** (δ7.4), and PCy_3O. The relative integrated intensities of these signals showed that 90% of the consumed **$1H^+$** had been converted to **1**; 5% of the initial **$1H^+$** was not accounted for.

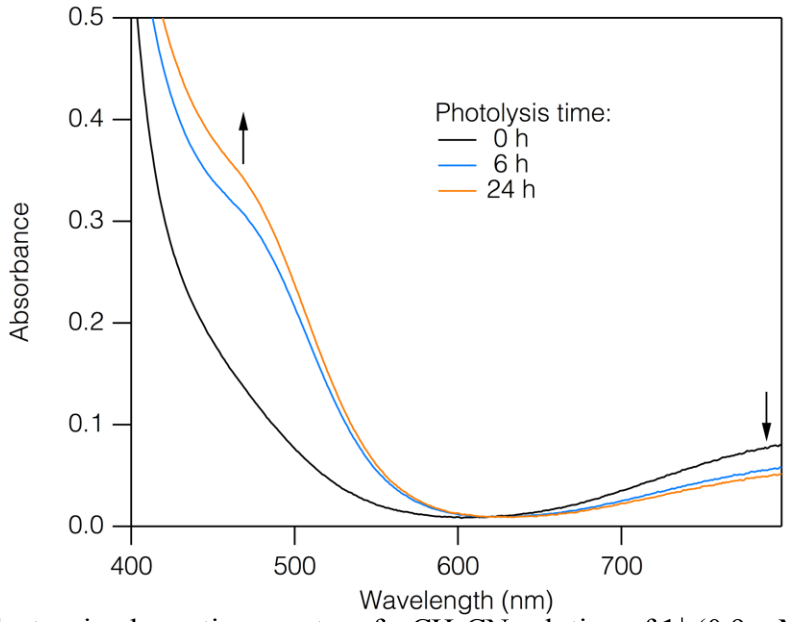

Figure 7.2.6. Electronic-absorption spectra of a CH_3CN solution of $\mathbf{1}^{+}$ (0.9 mM) during photolysis (λ_{ex} = 455 nm).

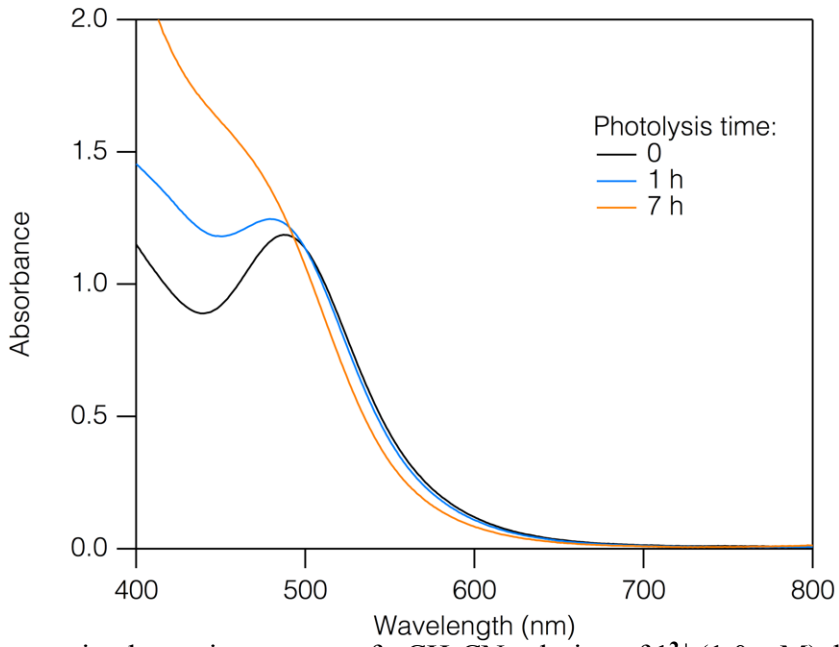

Figure 7.2.7. Electronic-absorption spectra of a CH_3CN solution of $\mathbf{1}^{2+}$ (1.0 mM) during photolysis (λ_{ex} = 455 nm).

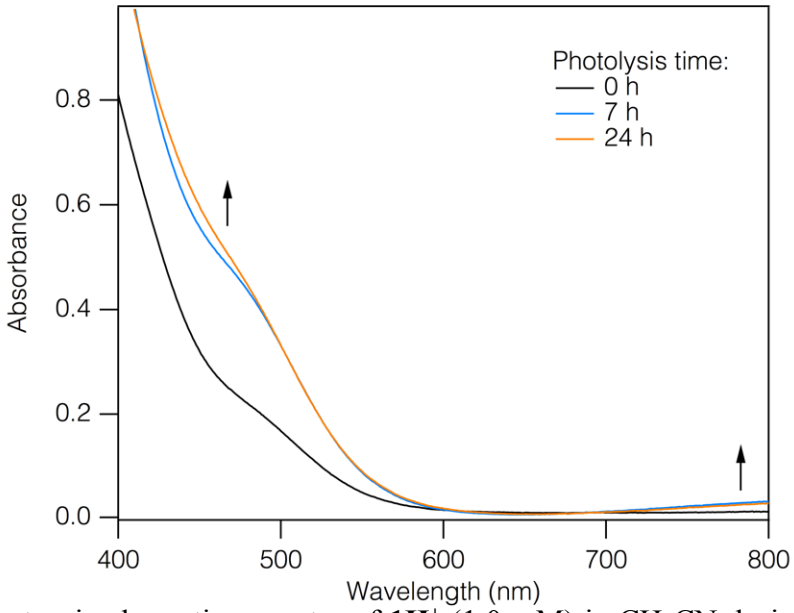

Figure 7.2.8. Electronic-absorption spectra of $\mathbf{1H}^{+}$ (1.0 mM) in CH_3CN during photolysis (λ_{ex} = 455 nm). The rising band at $\lambda \geq 700$ nm is consistent with the production of $\mathbf{1}^{+}$.

Table 7.2.1. The Emission Lifetime of $\mathbf{2}^{2+}$ in CH_3CN with Various Concentrations of Pyrrolidine.

[Pyrrolidine] (mM)	τ (ns)
0	890
100	890
250	875

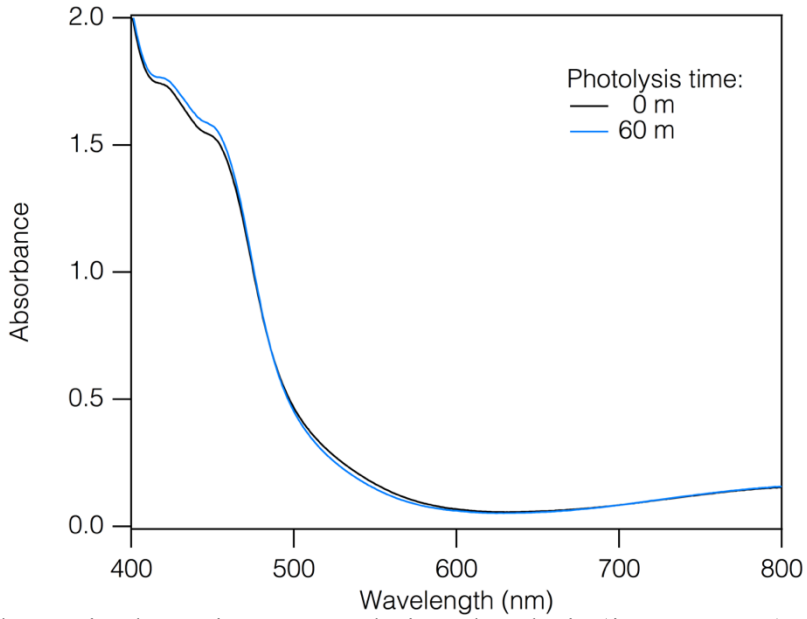

Figure 7.2.9. Electronic absorption spectra during photolysis (λ_{ex} = 455 nm) of a PhCN solution containing $\mathbf{1}^{+}$ (1.9 mM), $\mathbf{2}^{2+}$ (70 μM), and PCy_3O (4.7 mM), under N_2.

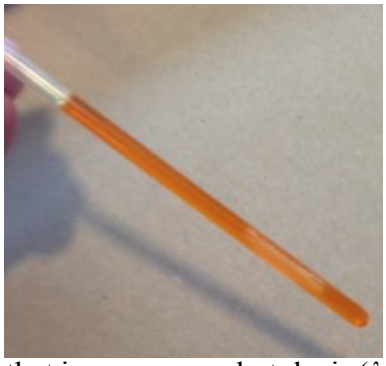

Figure 7.2.10. A white precipitate that is seen upon photolysis (λ_{ex} = 455 nm) under H_2 of a CD_3CN solution containing $\mathbf{1}^{+}$ (2.0 mM) and $\mathbf{2}^{2+}$ (70 μM).

Figure 7.2.11. A white precipitate that is seen upon photolysis (λ_{ex} = 455 nm) of a CD_3CN solution containing $\mathbf{1H}^{+}$ (7.5 mM), $\mathbf{2}^{2+}$ (70 μM) and pyrrolidine (140 mM). The addition of C_6D_6 solubilizes the precipitate and shows it to be compound **1** by $^{31}P\{^{1}H\}$ NMR.

7.2.4. Electrochemical Experiments

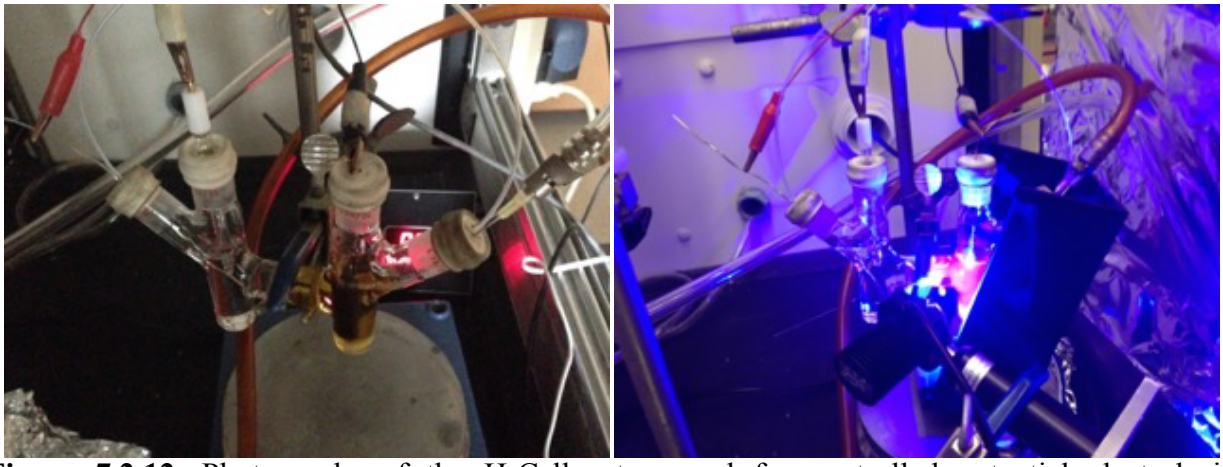

Figure 7.2.12. Photographs of the H-Cell setup used for controlled potential electrolysis experiments. (*Left*) Under ambient conditions. (*Right*) Under LED irradiation.

Table 7.2.2. Experimental Conditions Used for CPE Experiments.[a]

Exp.	[1^+] (mM)	Gas	Time (min)		Figure
			Dark	Light	
1 [b]	0 [b]	N_2 [b]	133 [b]	133 [b]	7.2.13
2	0.60	N_2	100	1500	7.2.14
3	0.40	H_2	1500	0	3.9
4	0.40	H_2	33	1310	3.9
5	0.40	H_2	See Table 7.2.3		3.9

[a] All experiments, unless otherwise stated, were conducted at –1.0 V with a PhCN working solution containing $[NBu^n_4][PF_6]$ (0.1 M), $[Ru(bpy)_3][PF_6]_2$ (70 μM) and pyrrolidine (190 mM). See Methods for complete experimental details. [b] Without $[Ru(bpy)_3][PF_6]_2$ and pyrrolidine.

Table 7.2.3. The Schedule of Illumination for CPE Experiment 5.

Time (min)	Condition
0–25	Dark
25–50	Light
50–85	Dark
85–112	Light
112–150	Dark
150–180	Light
180–298	Dark
298–321	Light
321–350	Dark

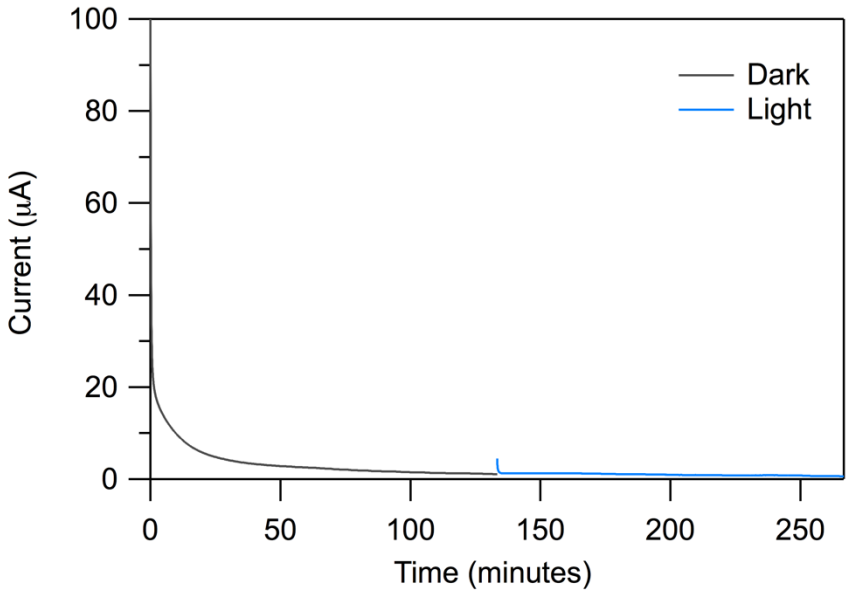

Figure 7.2.13. CPE at –1.0 V of a PhCN solution containing 0.1 M [^{n}Bu$_4$N][PF$_6$].

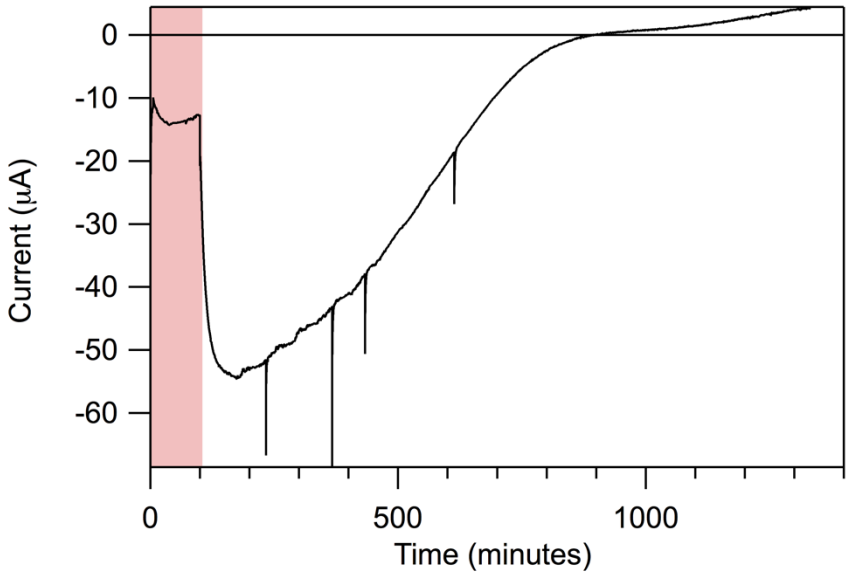

Figure 7.2.14. CPE at −1.0 V of a PhCN solution under N_2 containing 1^+ (0.6 mM), 2^{2+} (70 µM), pyrrolidine (190 mM) and [^{n}Bu$_4$N][PF_6] (0.1 M).

7.3. Chapter 4 Supplementary Information

7.3.1. Definitions.

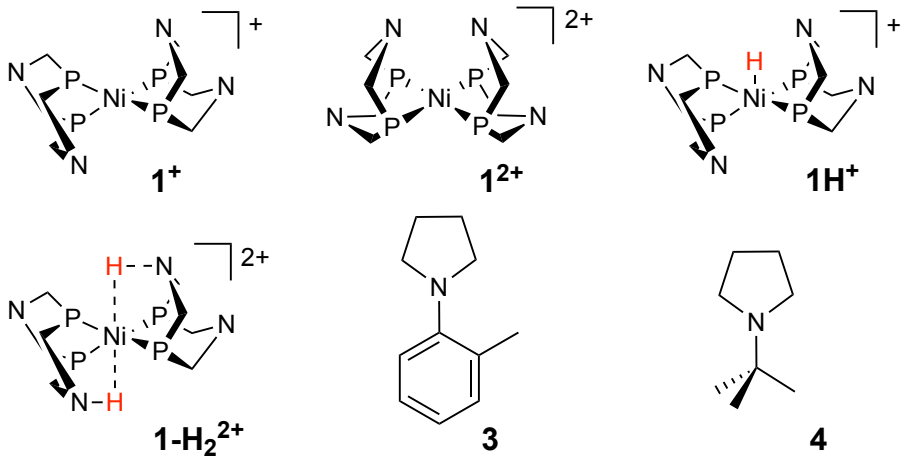

Figure 7.3.1. The compounds discussed in Section 7.3. For clarity, the phosphine (cyclohexyl) and amine (*tert*-butyl) substituents of the nickel compounds are not shown.

7.3.2. General Procedures. All solvents (HPLC grade, stored under nitrogen) were purified by passing them under nitrogen pressure through an anaerobic, stainless steel system consisting of either two 4.5 in. × 24 in. (1 gal) columns of activated A2 alumina (CH_3CN and Et_2O)

or one column of activated A2 alumina and one column of activated BASF R3-11 catalyst (pentane and toluene).[23] CD_3CN (Cambridge Isotope Laboratories) and 2,2,2-trifluoroethanol (≥99.5%, Sigma-Aldrich) were stored over activated 3A sieves under nitrogen. Pyrrolidine (≥99.5%, Sigma-Aldrich) was stored and used under nitrogen without further purification. Ethanol (anhydrous, Fisher) was used as received. HBF_4 (purum, 51–57% w/w in diethyl ether, Sigma-Aldrich) was used under nitrogen and stored at 4 °C. Phenol (unstabilized, purified by distillation, ≥99%, Sigma-Aldrich) was stored under nitrogen in the dark. Ferrocene (Sigma-Aldrich) and tetrabutylammonium hexafluorophosphate (TCI) were recrystallized twice from ethanol and dried for a minimum of 18 h under vacuum at 120 °C before use. $[Ru(bpy)_3][PF_6]_2$ (97%, Sigma-Aldrich) was recrystallized once from hot ethanol and dried for a minimum of 12 h under vacuum at 100°C before use. CO_2 (research grade, 99.9999%), H_2 (research grade, 99.9999%) and CO_2/H_2 (28:72 v/v) were purchased from Airgas and used as received. All other reagents were purchased from commercial suppliers and used as received.

NMR spectra were recorded at room temperature using a Bruker DRX 400 NMR spectrometer. Chemical shifts are reported relative to solvent resonances (^1H)[19] or an external standard of 85% H_3PO_4 in D_2O (^{31}P). J. Young NMR tubes were employed for some experiments; these tubes are topped with Teflon valves that provide an air-tight seal and enable connection to a vacuum line. Electronic-absorption spectra were obtained with a CARY 300 UV-Vis spectrophotometer of samples contained in quartz cuvettes; spectra were corrected for solvent absorption.

7.3.3. Electrochemistry. Electrochemical experiments were performed at room temperature under either a N_2 or a CO_2 atmosphere with a BAS 100B/W electrochemical workstation. All experiments used CH_3CN as solvent containing 0.1 M $[NBu^n_4][PF_6]$ as

electrolyte. Samples containing CO_2 were prepared by sparging the analyte solution with CO_2 for at least 15 min prior to measurement. Cyclic voltammetry (CV) experiments were performed in a single-compartment cell with a three-electrode configuration consisting of a glassy carbon working electrode (A = 0.07 cm^2), a platinum auxiliary electrode (A = 0.02 cm^2), and either a silver wire quasi-reference electrode or a Ag/Ag$^+$ reference electrode (BASi, 0.01 M $AgNO_3$ in CH_3CN containing 0.1 M [NBu$^n_4$][PF_6]) that was separated from the working solution by a CoralPor tip. Electrodes were polished and rinsed before use. $FeCp_2$ or $FeCp^*_2$ was used as an internal redox-potential reference; potentials are reported relative to $FeCp_2^{0/+}$ ($E_{1/2}(FeCp^*_2{}^{0/+})$ = –0.505 V *vs*. $FeCp_2^{0/+}$ in CH_3CN,[24] confirmed under our experimental conditions). Experiments in the absence of substrate (phenol and/or CO_2) were performed at multiple scan rates (0.05–0.40 V/s); other experiments were performed at a scan rate of 0.10 V/s unless otherwise stated. The reversibility of processes was assessed using Randles-Sevcik plots; peak currents were not corrected for background currents.

Controlled potential electrolysis (CPE) experiments were performed in a sealed four-neck cell (total volume = 100 mL). A three-electrode configuration was used that consisted of a reticulated vitreous carbon foam working electrode (ERG Materials & Aerospace, ca. 15 mm × 10 mm × 5 mm), a platinum wire auxiliary electrode that was separated from the working solution by a medium porosity glass frit, and a Ag/Ag$^+$ reference electrode (vide supra). The working solution (40 mL) contained a known amount of **2**, base, 0.5 M PhOH, and a stir bar. The auxiliary compartment contained 5 mL of a CH_3CN solution containing 0.1 M ferrocene (as a sacrificial reductant) and 0.1 M [NBu$^n_4$][PF_6]. After a current equivalent to at least 5.4 e$^–$ per catalyst molecule was passed, a known volume of gas within the headspace was extracted by gastight syringe and its chemical composition was characterized by gas chromatography (see Section

7.3.4). Formate was detected by ^{1}H NMR spectroscopy via a previously reported method:[25] following electrolysis and GC analysis of the headspace, D_2O (2 mL) was added to an aliquot of the reaction solution (5 mL) and the resulting aqueous mixture was vigorously stirred, washed with CH_2Cl_2 (12 mL), and acidified with one drop of concentrated HCl (aq). ^{1}H NMR (D_2O, 400 MHz, 295 K): δ 8.16 (s, 1H, *H*COOH).

7.3.4. Photochemistry. Steady-state photolysis experiments were conducted with samples contained in quartz cuvettes in a sample chamber that was sealed from ambient light and contained either a 455 nm, 565 nm, or 590 nm LED (ThorLabs) whose output was focused onto the sample through a bi-convex lens (ThorLabs N-BK7; f = 60.0 mm). Sample preparation for bulk photolysis experiments took place while shielded from ambient light. A stock CH_3CN solution of ZnTPP was prepared in a N_2-filled glovebox with an absorbance of 1.0 (± 0.05) at the maximum of the Q(0,0) band, to which various amounts (see Section 4.3.3) of **1**$^+$, **2**, base, and phenol were added. Solutions were volumetrically pipetted as 2 mL aliquots into 10 mL vials containing a stir bar and were subsequently sealed with a rubber septum and an aluminium crimp top. The vials were removed from the glovebox and sparged for at least 5 m with a H_2/CO_2 gas mixture (28:72 (v/v)). The solutions were photolyzed, with stirring, under illumination from a 590 nm LED (ThorLabs). After photolysis, 200 μL samples of the headspace were taken using a gas-tight syringe and analyzed by gas chromatography.

7.3.5. Gas Chromatography. The headspaces of photolysis and electrochemical samples were analysed on an Agilent 7890B GC system equipped with flame ionization (FID) and thermal conductivity (TCD) detectors using N_2 as a carrier gas. In front of the FID was a nickel methanizing catalyst that converted CO and CO_2 into CH_4. Gases were injected using a Hamilton 500 μL gastight syringe into a split:splitless injection port running at a 10:1 split ratio. The gases

were separated on a Supelco Carboxen 1010 PLOT column at 35°. Quantitation was performed by the Agilent software using a calibration curve generated by injecting different volumes of standard mixtures (Supelco SCOTTY Specialty Gas; 1.0% H_2, O_2, CH_4, CO, and CO_2 in N_2 or 15.0 % CO_2, 6.99% CO, 4.50% CH_4 and 4.01% O_2 in N_2).

7.3.6. Synthesis and Characterization

Synthesis of *N*-(*ortho*-tolyl)pyrrolidine (3). This compound was prepared by a procedure analogous to that for **4**.[26] To a suspension of K_2CO_3 (6.9 g, 50 mmol) in ethanol (30 mL) at 60 °C and opened to air, was added *o*-toluidine (10.7 g, 100 mmol). 1,4-Dibromobutane (21.6 g, 100 mmol) was then added dropwise with stirring. After 3 d the reaction mixture was cooled to room temperature and diethyl ether (30 mL) and saturated aqueous KOH (100 mL) were added. The pale yellow ethereal layer was separated, washed with brine (100 mL), and dried over $MgSO_4$. After decantation from the desiccant, the solvent was removed under reduced pressure giving a viscous yellow oil. The product was purified by distillation under partial vacuum (*ca*. 130 °C and 1 torr) three times, giving 4.7 g (29.2% yield) of a colorless oil that was stored and handled under N_2. The ^{1}H NMR spectrum was consistent with a prior report.[27] ^{1}H NMR ($(CD_3)_2CO$, 400 MHz, 295 K, Figure 7.3.1): δ 7.07 (m, 2H), 6.90 (m, 1H), 6.79 (m, 1H), 3.14 (m, 4H), 2.28 (s, 3H), 1.92 (m, 4H).

Synthesis of pyrrolidinium tetrafluoroborate. This procedure is adapted from a previous report.[28] To a stirred, faint-yellow solution of HBF_4 (9.52 g of 51–57% w/w solution in Et_2O, 55 mmol assuming 51% w/w) in diethyl ether (60 mL) at *ca.* –10 °C, pyrrolidine (3.83 g, 54 mmol) was added in a dropwise manner, immediately yielding a white precipitate. After 1 h and warming to room temperature, the colorless solid was collected on a sintered glass frit by filtration and washed with hexanes (3 × 20 mL). The solid was dried under reduced pressure at 100 °C overnight

(yield: 7.80 g, 91%). The ^{1}H NMR spectrum was consistent with a prior report.[28] ^{1}H NMR (CD_3CN, 400 MHz, 295 K, Figure 7.3.2): δ 6.74 (s, 2H), 3.27 (m, 4H), 1.96 (m, 4H).

Attempted preparation of 1H[BF$_4$] from 1-H$_2$[BF$_4$]$_2$ and sodium phenoxide. A red CD_3CN solution of **1[BF$_4$]$_2$** (1 mM) was prepared and a 1 mL aliquot was added to a J. Young sealable NMR tube. An initial ^{31}P{^{1}H} NMR spectrum was recorded (δ = 12.0 ppm (**1^{2+}**), Figure 4.3). Under N_2, excess sodium phenoxide (40 mM) was added, causing the solution to turn orange. Analysis by ^{31}P{^{1}H} NMR showed the presence of new features (δ = 49.9, 11.3, –23.6 ppm). H_2 (*ca*. 2 atm) was added to the NMR tube *via* degassing the sample on a vacuum line with 3 freeze-pump-thaw cycles and backfilling during the final thaw process with H_2. Final ^{31}P{^{1}H} NMR measurements showed no change (δ = 49.9, 11.4, –23.6 ppm).

Attempted preparation of 1H[BF$_4$] from 1-H$_2$[BF$_4$]$_2$ and 3. A red solution containing **1^{2+}** (1 mM) in CD_3CN was prepared and a 1 mL aliquot was added to a J. Young sealable NMR tube. An initial ^{31}P{^{1}H} NMR spectrum was recorded (δ = 12.0 ppm (**1[BF$_4$]$_2$**); Figure 4.7). H_2 (*ca*. 2 atm) was added to the NMR tube *via* degassing the sample on a vacuum line with 3 freeze-pump-thaw cycles and backfilling during the final thaw process with H_2. The solution changed color to pale yellow and analysis by ^{31}P{^{1}H} NMR showed features consistent with **1-H$_2^{2+}$** (δ = 17.4, 17.1 ppm). Subsequently excess (70 mM) **3** was added, resulting in no color change. Analysis by ^{31}P{^{1}H} NMR only showed the presence of features consistent with **1-H$_2^{2+}$** (δ = 17.1, –6.5, –8.1 ppm).

Preparation of 1H[BF$_4$] from 1-H$_2$[BF$_4$]$_2$ and 4. A red solution containing **1[BF$_4$]$_2$** (1 mM) in CD_3CN was prepared and a 1 mL aliquot was added to a J. Young sealable NMR tube. An initial ^{31}P{^{1}H} NMR measurement was taken (δ = 12.0 ppm (**1^{2+}**); Figure 4.9). H_2 (*ca*. 2 atm) was added to the NMR tube *via* degassing the sample on a vacuum line with 3 freeze-pump-thaw cycles

and backfilling during the final thaw process with H_2. The solution changed color to pale yellow and analysis by $^{31}P\{^1H\}$ NMR showed features consistent with **1-H_2^{2+}** (δ = 17.4, 17.1 ppm). Subsequently excess (70 mM) *tert*-butylpyrrolidine was added, giving a color change to yellow. Analysis by $^{31}P\{^1H\}$ NMR showed the presence of features consistent with **1H[BF_4]** (δ = 12.8 ppm).

Photosensitized preparation of 1H[BF_4] from 1[BF_4], 4 and H_2. To a stock solution of ZnTPP (*ca*. 20 μM) in CH_3CN was added **1[BF_4]** (0.8 mM), PhOH (0.5 M), and *tert*-butylpyrrrolidine (10 mM). Aliquots of the solution were dispensed into a sealable UV-vis cuvette and a J. Young sealable NMR tube, while protected from light. Initial $^{31}P\{^1H\}$ NMR and UV-Vis measurements were made at this point. A H_2-CO_2 gas mixture (*ca.* 2 atm, 28:72 (v/v)) was added to both vessels; this was accomplished on a vacuum line by degassing the samples *via* at least 3 freeze–pump–thaw cycles and then backfilling them during the final thaw process with H_2-CO_2. The samples were then photolyzed with 590 nm light (see Methods for Photolysis) and monitored regularly by UV-vis and NMR. Samples were shielded from light while being transported to and from the spectrometers and during measurement. The samples exhibited complete consumption of **1**$^+$ over 20 h (UV-Vis, Figure 4.11A) and concomitant production of **1H[BF_4]** ($^{31}P\{^1H\}$ NMR, δ 12.6, Figure 4.11B).

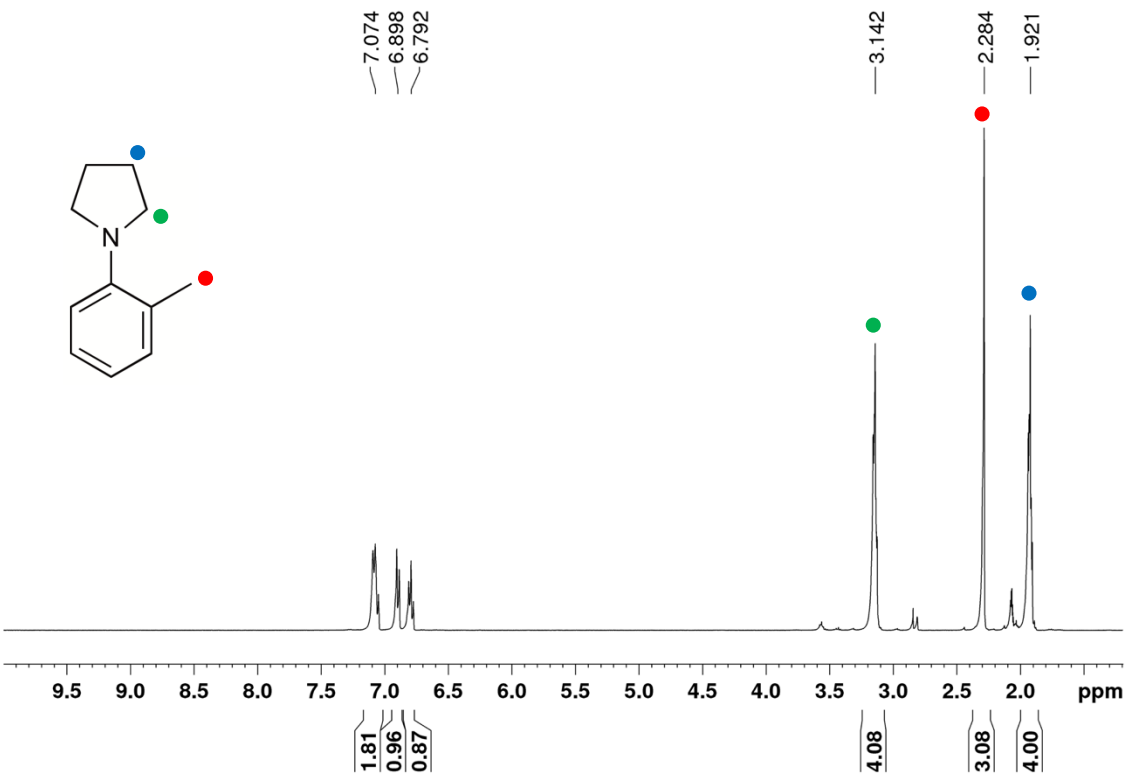

Figure 7.3.2. ^{1}H NMR spectrum of *N*-(*o*-tolyl)pyrrolidine (**3**) in $(CD_3)_2CO$.

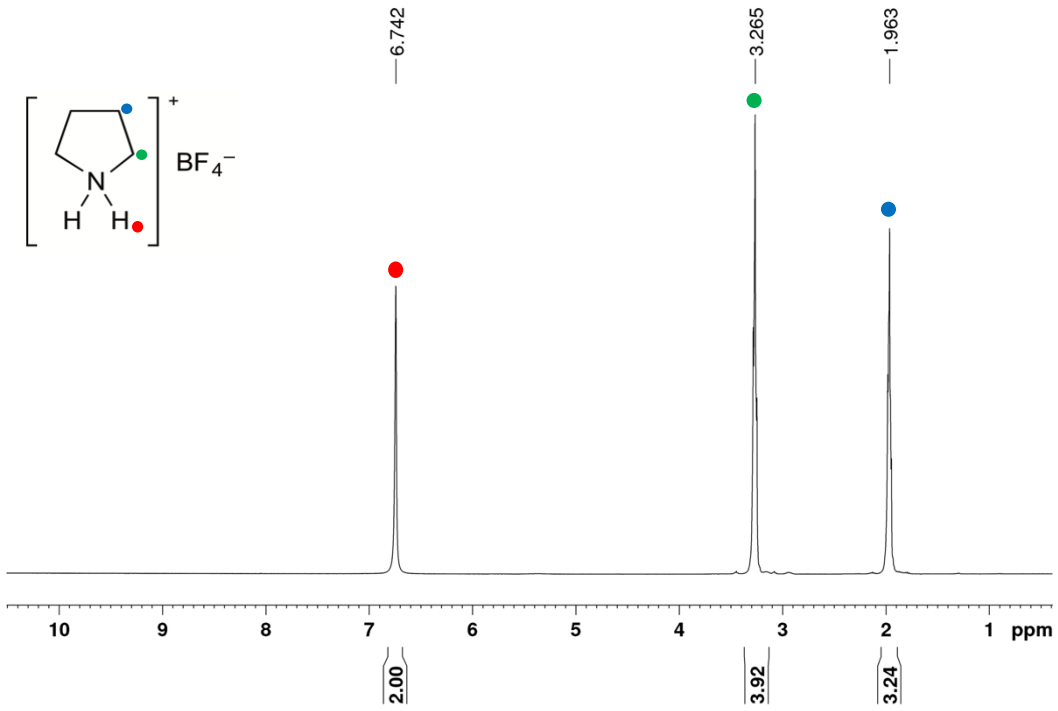

Figure 7.3.3. ^{1}H NMR spectrum of pyrrolidinium tetrafluoroborate in CD_3CN.

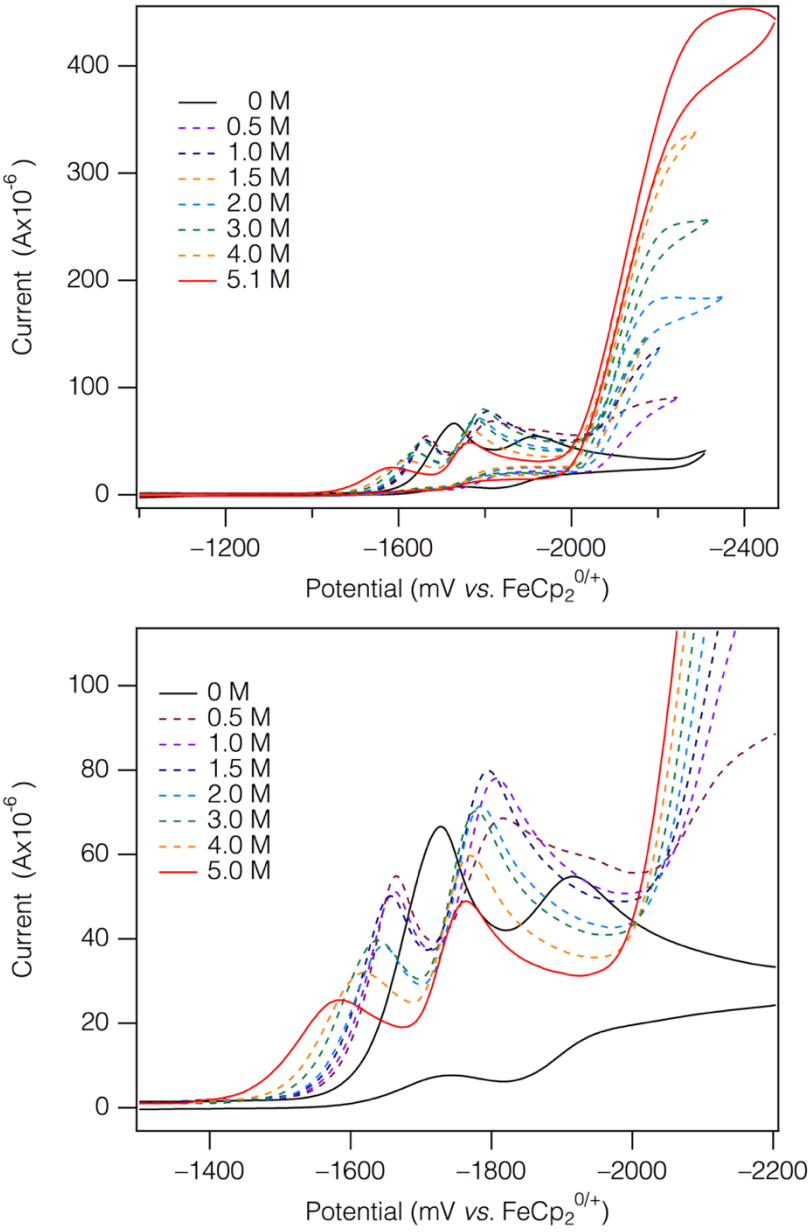

Figure 7.3.4. CV responses of 2 mM **2** in 0.1 M [NBu$^n_4$][PF_6] CH_3CN at 0.1 V/s with titration of TFE. For clarity, in the lower image only forward traces are shown for scans with added TFE.

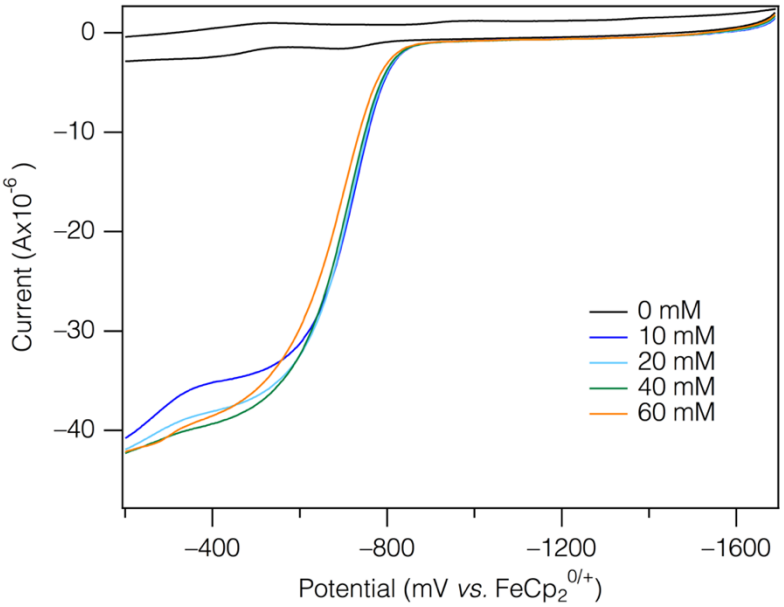

Figure 7.3.5. CV responses of 0.6 mM $\mathbf{1}^+$ with 0.5 M PhOH in 0.1 M [NBu$^n_4$][PF_6] CH_3CN at 0.1 V/s under H_2 with titration of **4**.

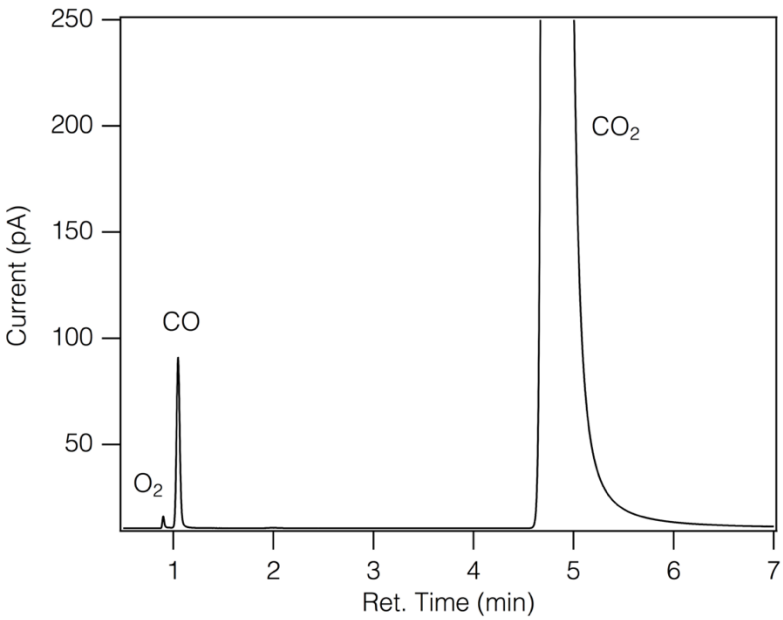

Figure 7.3.6. Example FID trace from a bulk photolysis headspace sample**.**

7.4. Supplementary Information for Chapter 5

7.4.1. Definitions.

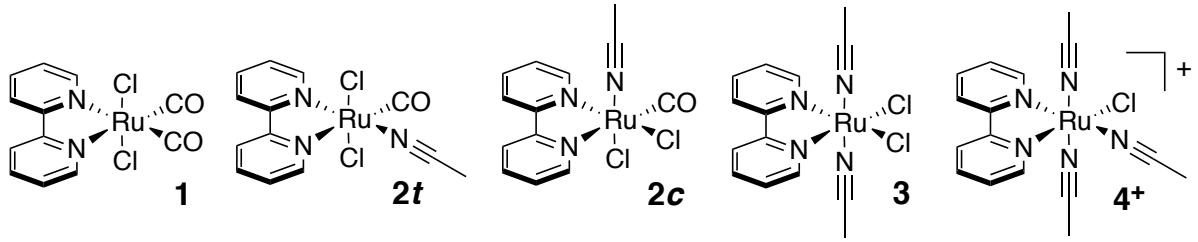

Figure 7.4.1. The compounds discussed in Section 7.4.

7.4.2. Synthesis, Characterization, and Photochemistry of Compounds.

Photochemical Instrumentation. Non-preparative photolysis experiments were conducted with samples contained in quartz cuvettes in a sample chamber that was sealed from ambient light and contained a 455 nm LED (900 mW, ThorLabs model M455L2). White LEDs used for synthetic scale experiments were from Super Bright LEDs, part no. 4NFLS-CWH24-24V-CL, 6000 K.

Synthesis of *trans(Cl)*-Ru(bpy)(CO)(CH_3CN)Cl_2 (2*t*). This procedure is based on a report that provided an outline of the synthetic route but not full details.[29] All steps were conducted with shielding from light due to the photosensitivity of the starting material and product. To a stirred, pale-yellow solution of **1** (0.100 g, 0.26 mmol) in acetonitrile (100 mL) under N_2 was added trimethylamine *N*-oxide dihydrate (0.090 g, 0.81 mmol). The solution was stirred for 15 h and the resulting orange solution then reduced to dryness under vacuum. In air, the orange residue was dissolved in a minimal volume of hot ethanol and the resulting solution filtered through a fine-porosity sintered-glass filter. Allowing this solution to stand at –20 ˚C overnight yielded an orange precipitate, which was collected via filtration and washed with cold ethanol (3 × 20 mL) and then hexane (3 × 20 mL). After drying under vacuum, 0.070 g (68% yield) of product was obtained as an orange powder. ^{1}H NMR (CD_3CN, 400 MHz, 295 K; Figures 7.4.2–3): δ 9.34 (d, 1H, J_{HH} = 6.0 Hz, bpy), 9.11 (d, 1H, J_{HH} = 6.0 Hz, bpy), 8.45 (d, 1H, J_{HH} = 8.0 Hz, bpy), 8.33 (d, 1H J_{HH} = 8.0

Hz, bpy), 8.24 (t, 1H, J_{HH} = 8.0 Hz, bpy), 7.94 (t, 1H, J_{HH} = 6.8 Hz, bpy), 7.81 (t, 1H, J_{HH} = 6.8 Hz, bpy), 7.45 (t, 1H, J_{HH} = 6.4 Hz, bpy), 2.58 (s, 3H, CH_3CN). UV-Vis (CH_3CN; Figure 7.4.4): λ_{max} (nm) = 462, 423, 350 (sh). IR (CH_3CN): ν_{CO} = 1967 cm^{-1}. The ^{1}H-NMR data for **2*t*** are compared with those for **2*c*** in Table 7.4.1; the substantially different chemical shifts for the two sets of nuclei whose chemical environment differs most significantly between **2*c*** and **2*t*** confirms that **2*t*** is a different isomer (CH_3CN: **2*t*** 2.58 ppm, **2*c*** 2.07 ppm; bpy-6-H: **2*t*** 9.34 ppm, **2*c*** 9.91 ppm).

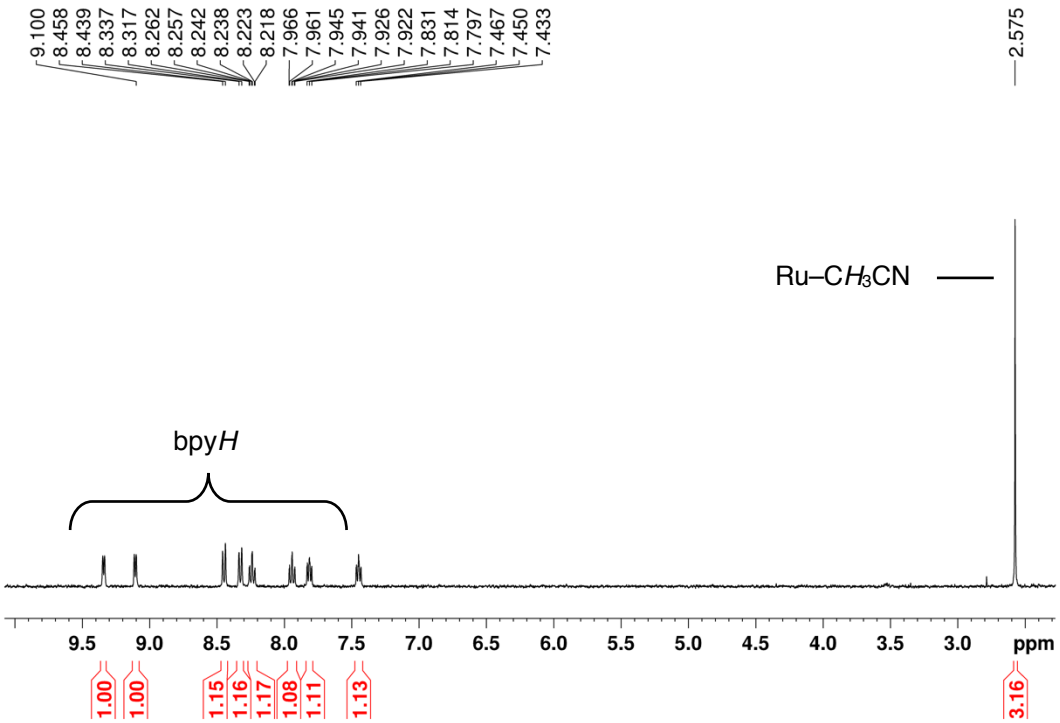

Figure 7.4.2. ^{1}H NMR spectrum of **2*t*** in CD_3CN.

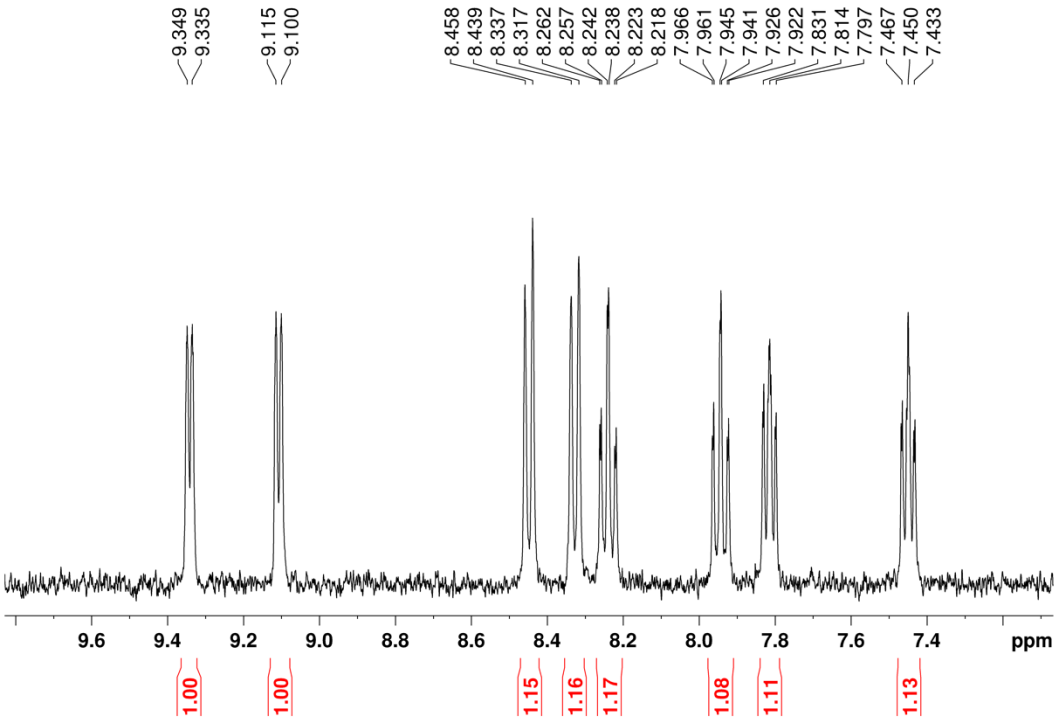

Figure 7.4.3. Expansion of the ^{1}H NMR spectrum ***2t*** in CD_3CN.

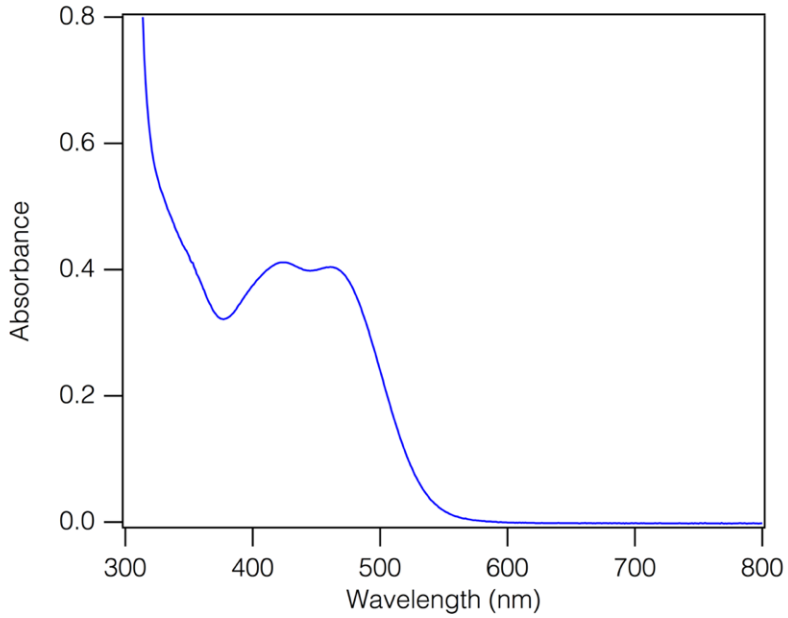

Figure 7.4.4. Electronic-absorption spectrum of ***2t*** in CH_3CN (~0.5 mM; λ_{max} (nm) = 462, 423, 350 (sh)).

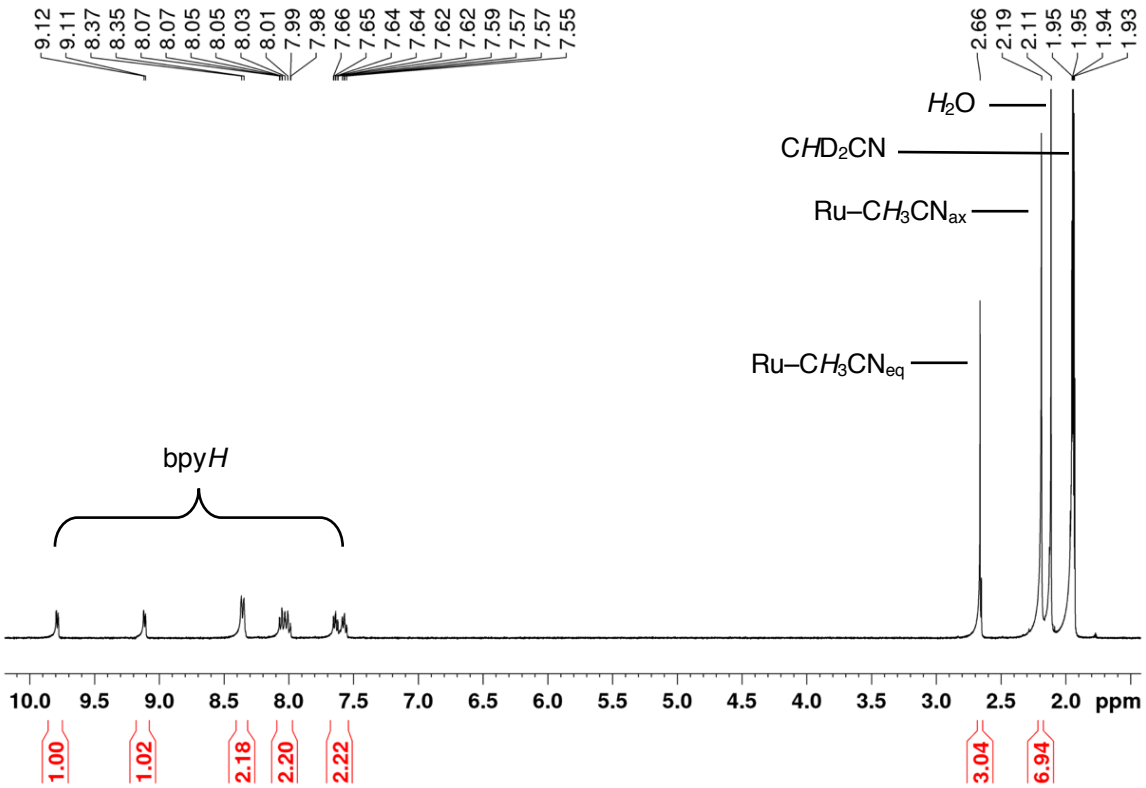

Figure 7.4.5. ^{1}H NMR spectrum of **4Cl** in CD_3CN.

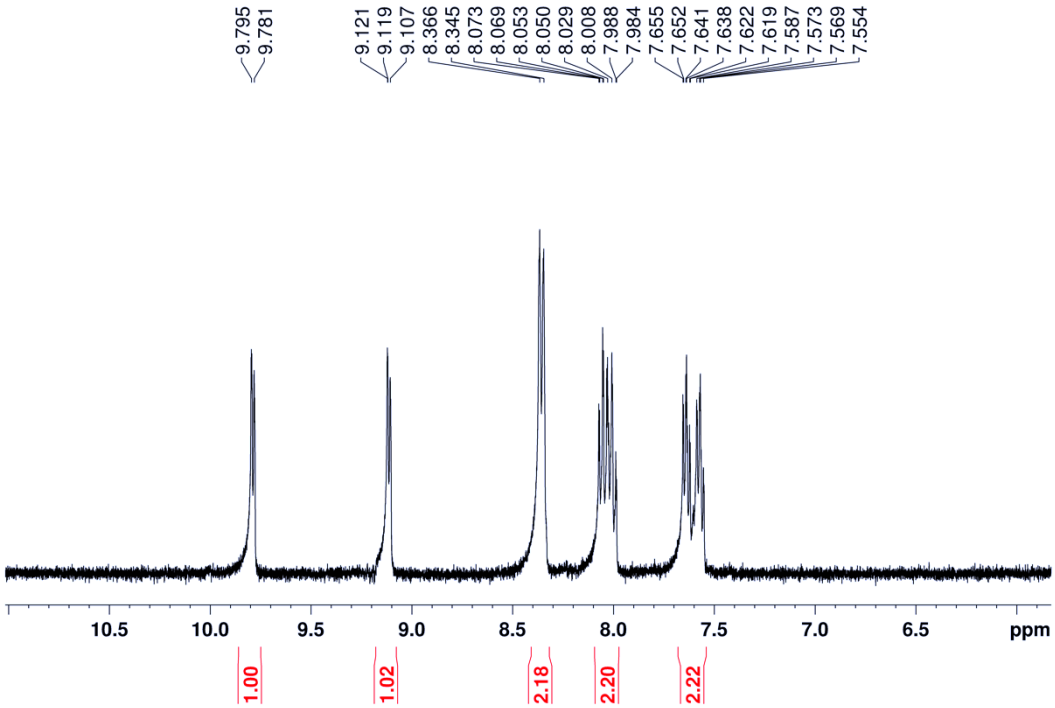

Figure 7.4.6. Expansion of the ^{1}H NMR spectrum of **4Cl** in CD_3CN.

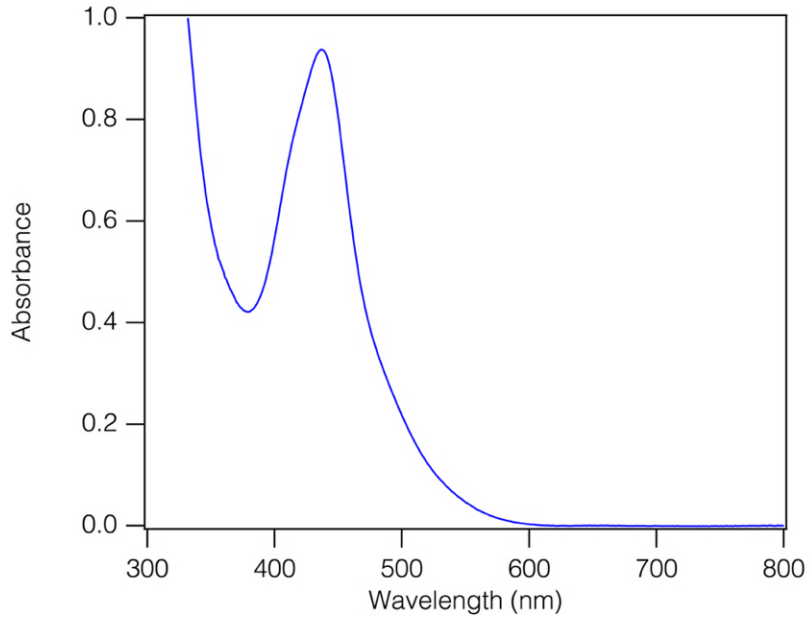

Figure 7.4.7. Electronic-absorption spectrum of **4Cl** in CH_3CN (~0.6 mM; λ_{max} = 437 nm).

Table 7.4.1. ^{1}H-NMR Chemical Shift Data for **2*c***, **2*t***, and **4Cl**.

Cmpd	Ref	bpy								CH_3CN	
2*t*	This work	9.34	9.11	8.45	8.33	8.24	7.94	7.81	7.45	2.58	
2*c*	[30]	9.91	9.09	8.44	8.34	8.24	7.95	7.84	7.44	2.07	
4Cl	This work	9.79	9.12	8.36	8.03	7.61				2.66	2.19
4Cl	[30]	9.77	9.12	8.36	8.03	7.60				2.12	2.20

7.4.3. Single Crystal X-Ray Diffraction Study of 4Cl•2H_2O.

A small brown block (0.06 mm × 0.07 mm × 0.13 mm) was mounted with Fluorolube™ oil on a Dual-Thickness MicroMount™ (MiTeGen) with 20 µm sample aperture. The diffraction data were measured at 100 K on a Bruker D8 VENTURE diffractometer equipped with a microfocus Mo-target X-ray tube (λ = 0.71073 Å) and PHOTON 100 CMOS detector. Data reduction and integration were performed with the Bruker APEX3 software package.[31] Data were scaled and corrected for absorption effects using the multi-scan procedure as implemented in SADABS.[32] The structure was solved by SHELXT[3] and refined by a full-matrix least-squares procedure using OLEX2.[4-5, 33] All atoms were refined with anisotropic thermal parameters.

Hydrogen atoms except those of water molecules were included in idealized positions for structure factor calculations. Hydrogen atoms of water molecules were located in the difference Fourier map and allowed to be refined at 0.85 Å within a default 0.02 Å standard deviation with their thermal parameters being constrained to be 1.5 times of the U_{eq} value of the O atoms. Crystallographic data and details of the data collection and structure refinement are listed in Table 7.4.2, the structure is depicted in Figure 7.4.8, bond lengths and bond angles are set out in Table 7.4.3, and selected metrical data are compared to those reported previously for a different polymorph in Table 7.4.4.

Table 7.4.2. Crystal Data and Structure Refinement for **4Cl**•$2H_2O$

Empirical formula	$C_{16}H_{21}Cl_2N_5O_2Ru$
Formula weight	487.35
Temperature/K	100(2)
Crystal system	monoclinic
Space group	$P2_1/n$
a/Å	7.0497(4)
b/Å	21.6023(12)
c/Å	13.3544(8)
α/°	90
β/°	96.449(2)
γ/°	90
Volume/Å^3	2020.9(2)
Z	4
ρ_{calc}g/cm^3	1.602
μ/mm^{-1}	1.060
F(000)	984.0
Crystal size/mm^3	0.134 × 0.067 × 0.061
Radiation	MoKα (λ = 0.71073)
2Θ range for data collection/°	4.862 to 57.53
Index ranges	$-9 \le h \le 9$, $-28 \le k \le 29$, $-18 \le l \le 17$
Reflections collected	55191
Independent reflections	5223 [R_{int} = 0.0519, R_{sigma} = 0.0381]
Data/restraints/parameters	5223/6/250
Goodness-of-fit on F^2	1.031
Final R indexes [I>=2σ (I)]	R_1 = 0.0343, wR_2 = 0.0688
Final R indexes [all data]	R_1 = 0.0549, wR_2 = 0.0742
Largest diff. peak/hole / e Å^{-3}	0.74/–0.55

$R_{int} = \Sigma \mid F_o^2 - \langle F_o^2 \rangle \mid / \Sigma \mid F_o^2 \mid$

$R1 = \Sigma \parallel F_o \mid - \mid F_c \parallel / \Sigma \mid F_o \mid$

$wR2 = [\Sigma [w (F_o^2 - F_c^2)^2] / \Sigma [w (F_o^2)^2]]^{1/2}$

Goodness-of-fit = $[\Sigma [w (F_o^2 - F_c^2)^2] / (n-p)^{1/2}$

n: number of independent reflections; p: number of refined parameters

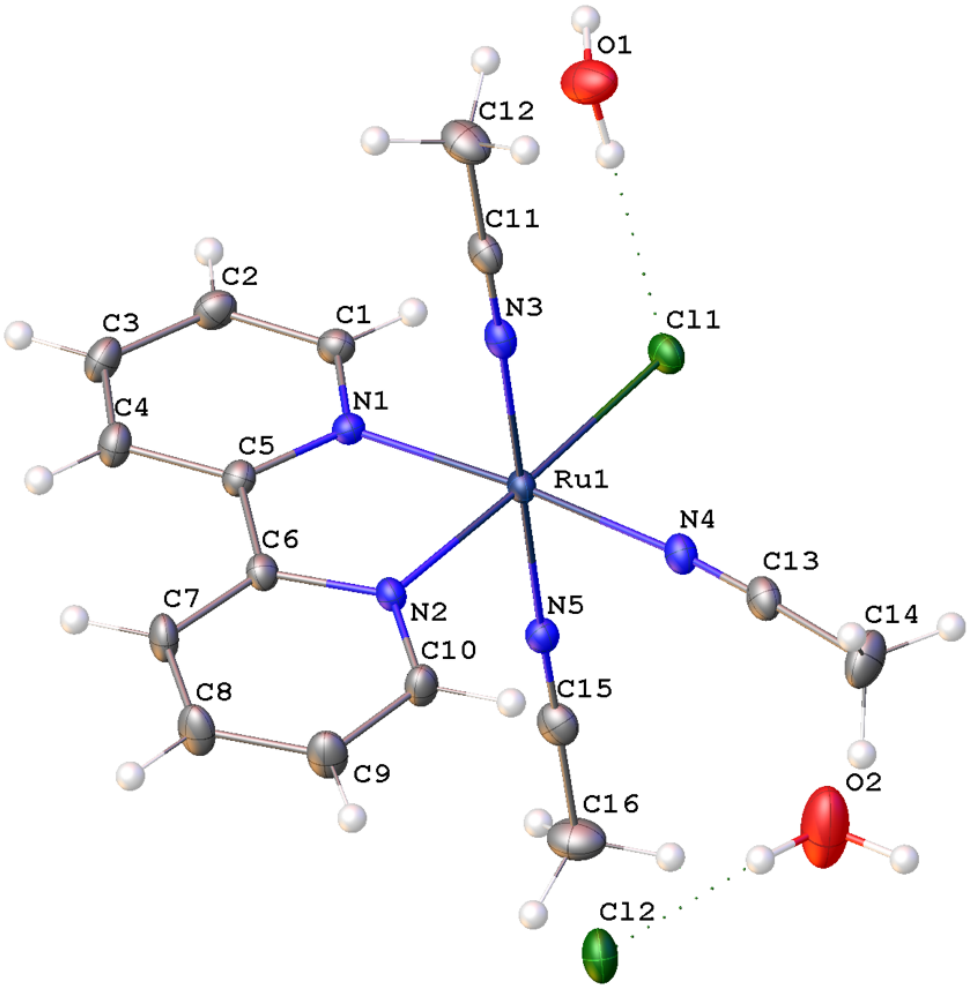

Figure 7.4.8. Thermal-ellipsoid representation (40% probability ellipsoids) of **4Cl**•2H_2O.

Table 7.4.3. Bond Lengths and Angles for **4Cl**•$_2$H$_2$O.

Atom	Atom	Length (Å)	Atom	Atom	Length (Å)
Ru1	Cl1	2.4379(6)	C1	C2	1.382(4)
Ru1	N1	2.055(2)	C2	C3	1.383(4)
Ru1	N2	2.0312(19)	C3	C4	1.376(4)
Ru1	N3	2.019(2)	C4	C5	1.390(3)
Ru1	N4	2.031(2)	C5	C6	1.475(3)
Ru1	N5	2.022(2)	C6	C7	1.384(3)
N1	C1	1.342(3)	C7	C8	1.380(4)
N1	C5	1.356(3)	C8	C9	1.382(4)
N2	C6	1.360(3)	C9	C10	1.377(4)
N2	C10	1.343(3)	C11	C12	1.456(4)
N3	C11	1.135(3)	C13	C14	1.452(4)
N4	C13	1.134(3)	C15	C16	1.453(4)
N5	C15	1.121(3)			

Atom	Atom	Atom	Angle (°)	Atom	Atom	Atom	Angle (°)
N1	Ru1	Cl1	96.82(6)	C11	N3	Ru1	177.4(2)
N2	Ru1	Cl1	176.00(6)	C13	N4	Ru1	174.8(2)
N2	Ru1	N1	79.32(8)	C15	N5	Ru1	174.1(2)
N2	Ru1	N4	94.71(8)	N1	C1	C2	122.2(2)
N3	Ru1	Cl1	91.49(6)	C1	C2	C3	119.2(2)
N3	Ru1	N1	88.57(8)	C4	C3	C2	119.1(2)
N3	Ru1	N2	89.49(8)	C3	C4	C5	119.3(2)
N3	Ru1	N4	90.78(8)	N1	C5	C4	121.6(2)
N3	Ru1	N5	179.54(8)	N1	C5	C6	114.9(2)
N4	Ru1	Cl1	89.16(6)	C4	C5	C6	123.5(2)
N4	Ru1	N1	174.01(8)	N2	C6	C5	114.5(2)
N5	Ru1	Cl1	88.96(6)	N2	C6	C7	121.6(2)
N5	Ru1	N1	91.49(8)	C7	C6	C5	123.9(2)
N5	Ru1	N2	90.07(8)	C8	C7	C6	119.2(2)
N5	Ru1	N4	89.11(8)	C7	C8	C9	119.2(2)
C1	N1	Ru1	126.29(16)	C10	C9	C8	119.1(2)
C1	N1	C5	118.6(2)	N2	C10	C9	122.4(2)
C5	N1	Ru1	115.09(16)	N3	C11	C12	178.7(3)
C6	N2	Ru1	115.96(16)	N4	C13	C14	177.4(3)
C10	N2	Ru1	125.61(16)	N5	C15	C16	179.3(3)
C10	N2	C6	118.4(2)				

Table 7.4.4. Selected Bond Lengths (Å) and Angles (˚) for **4Cl** from Two Nonisomorphous Crystal Structures.

Nuclei	**4Cl**•2(H_2O)[a]	**4Cl**•3/2(CH_2Cl_2)[b]
Ru–Cl	2.4379(6)	2.4345(15)
Ru–N(1)	2.055(2)	2.049(4)
Ru–N(2)	2.0312(19)	2.038(4)
Ru–N(3)	2.019(2)	2.012(4)
Ru–N(4)	2.031(2)	2.028(4)
Ru–N(5)	2.022(2)	2.012(4)
N(1)–Ru–N(2)	79.32(8)	79.42(17)
N(1)–Ru–N(3)	88.57(8)	89.88(15)
N(1)–Ru–N(4)	174.01(8)	173.76(18)
N(1)–Ru–N(5)	91.49(8)	91.00(15)
N(1)–Ru–Cl	96.82(6)	95.69(13)
N(2)–Ru–N(3)	89.49(8)	91.75(15)
N(2)–Ru–N(4)	94.71(8)	94.42(17)
N(2)–Ru–N(5)	90.07(8)	88.87(15)
N(2)–Ru–Cl	176.00(6)	174.89(12)
N(3)–Ru–N(4)	90.78(8)	91.28(16)
N(3)–Ru–N(5)	179.54(8)	179.00(18)
N(3)–Ru–Cl	91.49(6)	89.69(12)
N(4)–Ru–N(5)	89.11(8)	87.89(16)
N(4)–Ru–Cl	89.16(6)	90.45(12)
N(5)–Ru–Cl	88.96(6)	89.76(12)

[a] This work. [b] Ref. [30].

7.4.4. Electrochemical Experiments.

Cyclic voltammetry. Electrochemical experiments were performed at room temperature under either a N_2 or a CO_2 atmosphere with a BAS 100B/W electrochemical workstation. All experiments used CH_3CN as solvent containing 0.1 M $[NBu^n_4][PF_6]$ as electrolyte. Samples containing CO_2 were prepared by sparging the analyte solution with CO_2 for at least 15 min prior to measurement. Cyclic voltammetry (CV) experiments were performed in a single-compartment cell with a three-electrode configuration consisting of a glassy carbon working electrode (A = 0.07 cm^2), a platinum auxiliary electrode (A = 0.02 cm^2), and a silver wire quasi-reference electrode. Electrodes were polished and rinsed before use. $FeCp_2$ or $FeCp^*_2$ was used as an internal redox-potential reference; potentials are reported relative to $FeCp_2^{0/+}$ ($E_{1/2}(FeCp^*_2{}^{0/+})$ = –0.505 V *vs*. $FeCp_2^{0/+}$ in CH_3CN,[24] confirmed under our experimental conditions). Experiments in the absence of substrate (phenol and/or CO_2) were performed at multiple scan rates (0.05–0.40 V/s); other experiments were performed at a scan rate of 0.10 V/s unless otherwise stated. The reversibility of processes was assessed using Randles-Sevcik plots; peak currents were not corrected for background currents.

Controlled potential electrolysis. These experiments were performed in a sealed four-neck cell (total volume = 100 mL). A three-electrode configuration was used that consisted of a reticulated vitreous carbon foam working electrode (ERG Materials & Aerospace, ca. 15 mm × 10 mm × 5 mm), a platinum wire auxiliary electrode that was separated from the working solution by a medium porosity glass frit, and a Ag/Ag^+ reference electrode (BASi, 0.01 M $AgNO_3$ in CH_3CN containing 0.1 M $[NBu^n_4][PF_6]$) that was separated from the working solution by a CoralPor tip. The working solution (40 mL) contained a known amount of catalyst, 0.5 M PhOH, and a stir bar. The auxiliary compartment contained 5 mL of a CH_3CN solution containing 0.1 M ferrocene (as

a sacrificial reductant) and 0.1 M [NBu$^n_4$][PF$_6$]. After a current equivalent to at least 6.4 e$^-$ per catalyst molecule was passed, a known volume of gas within the headspace was extracted by gastight syringe and its chemical composition was characterized by gas chromatography (GC; Agilent 7890B with FID (CO) and TCD (H_2) detectors and a Supelco Carboxen 1010 PLOT column). Comparison with a GC calibration curve (Supelco SCOTTY Specialty Gas; 1.0% H_2, O_2, CH_4, CO, and CO_2, balance N_2) allowed quantification of the volume of each gas present at the end of the run and, from this, determination of the faradaic efficiency. Three gas samples were extracted for each run so that the standard deviation could be calculated. Formate was detected by ^{1}H NMR spectroscopy via a previously reported method:[25] following electrolysis and GC analysis of the headspace, D_2O (2 mL) was added to an aliquot of the reaction solution (5 mL) and the resulting aqueous mixture was vigorously stirred, washed with CH_2Cl_2 (12 mL), and acidified with one drop of concentrated HCl (aq). ^{1}H NMR (D_2O, 400 MHz, 295 K): δ 8.16 (s, 1H, *H*COOH).

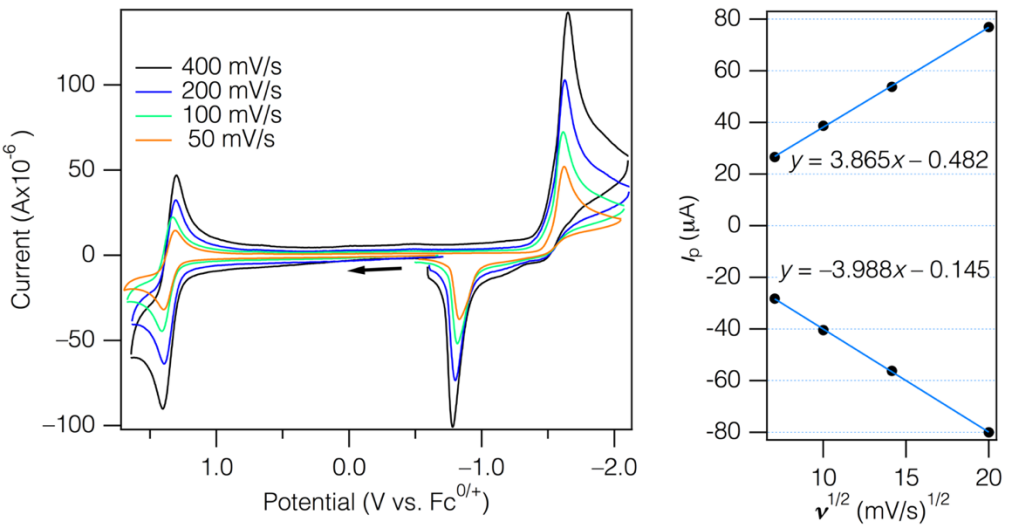

Figure 7.4.9. (*Left*) Cyclic voltammograms of 1.3 mM **1** in CH_3CN solution containing 0.1 M [NBu$^n_4$][PF$_6$]. The arrow indicates the direction of the scans. (*Right*) Randles-Sevcik plot of the reversible Ru$^{II/III}$ couple.

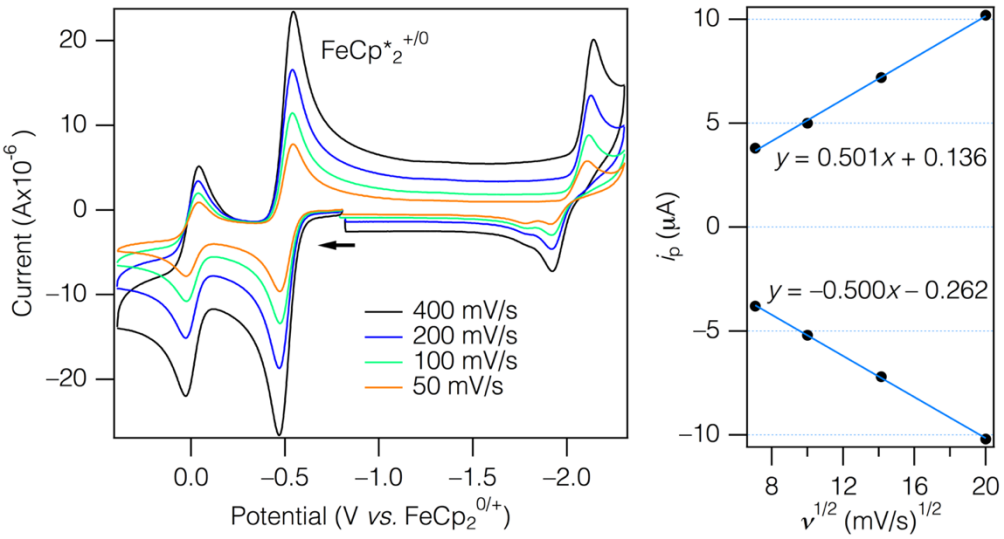

Figure 7.4.10. (*Left*) Cyclic voltammograms of 0.4 mM **3** in CH_3CN solution containing 0.1 M $[NBu^n_4][PF_6]$. The arrow indicates the direction of the scans. (*Right*) Randles-Sevcik plot of the reversible $Ru^{II/III}$ couple.

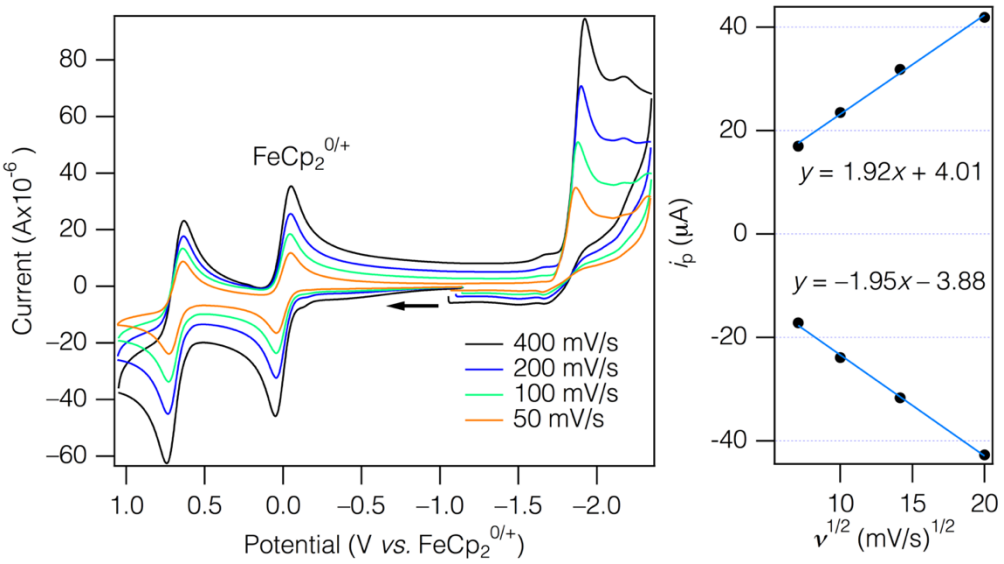

Figure 7.4.11. (*Left*) Cyclic voltammograms of 2.0 mM **4Cl** in CH_3CN solution containing 0.1 M $[NBu^n_4][PF_6]$. The arrow indicates the direction of the scans. (*Right*) Randles-Sevcik plot of the reversible $Ru^{II/III}$ couple.

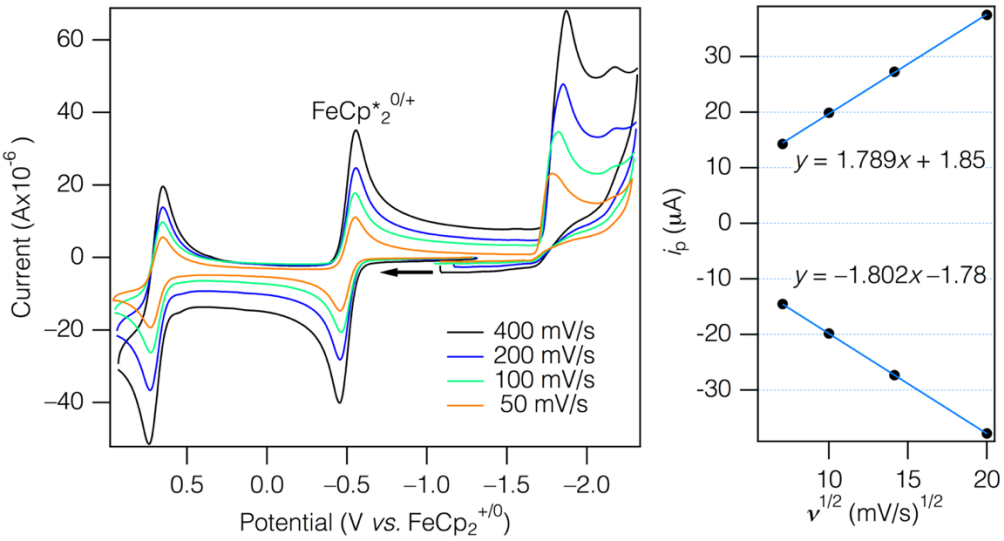

Figure 7.4.12. (*Left*) Cyclic voltammograms of **2*t*** (see Figure 5.3 in main text). (*Right*) Randles-Sevcik plot of the reversible $Ru^{II/III}$ couple.

Table 7.4.5. Comparison of Redox Potentials from This Work with Literature Values.[a]

Compound	This Work		Prior Report[b]		
	$E_{1/2}$ (Ox)	$E_p{}^c$ (Red)	$E_{1/2}$ (Ox)	$E_p{}^c$ (Red)	Ref.
1	+1.35	−1.61	+1.36	−1.59	34
2*c*	—	—	+0.66	−1.84	35
2*t*	+0.70	−1.82	—	—	
3	−0.01	−2.12	−0.01	−2.14	36
4$^+$	+0.69	−1.88	+0.64	−1.97	35

[a] Measured in CH_3CN solution containing 0.1 M $[NBu^n{}_4][PF_6]$. [b] Converted from $Ag^{0/+}$ to the $FeCp_2{}^{0/+}$ reference using $Ag^{0/+} = FeCp_2{}^{0/+} + 0.089$ V,[37] which was confirmed under our conditions. [c] E_p at scan rate 0.1 V/s.

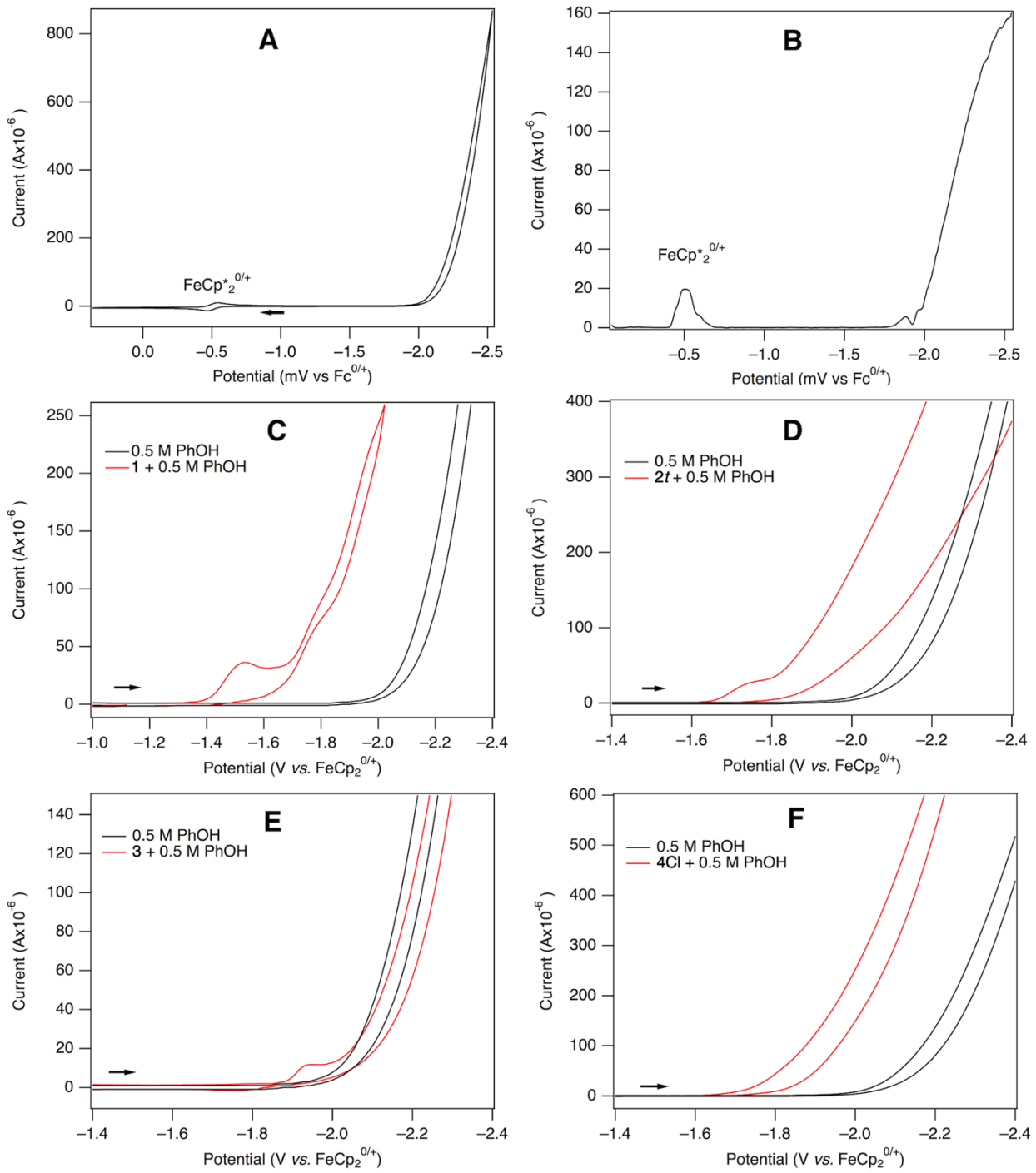

Figure 7.4.13. Cyclic-voltammetric measurements (ν = 0.1 V/s) showing proton reduction from phenol in CH_3CN (0.5 M PhOH, 0.1 M [NBu^n_4][PF_6]) in the absence (black traces) and presence (red traces) of **1**, **2*t***, **3**, and **4**$^+$: (A) no catalyst added; (C) 1 (0.8 mM); (D) 2*t* (0.8 mM); (E) 3 (0.7 mM); (F) 4Cl (1.0 mM). The differential pulse voltammogram of phenol in CH_3CN (0.5 M PhOH, 0.1 M [NBu^n_4][PF_6]) is shown in (B).

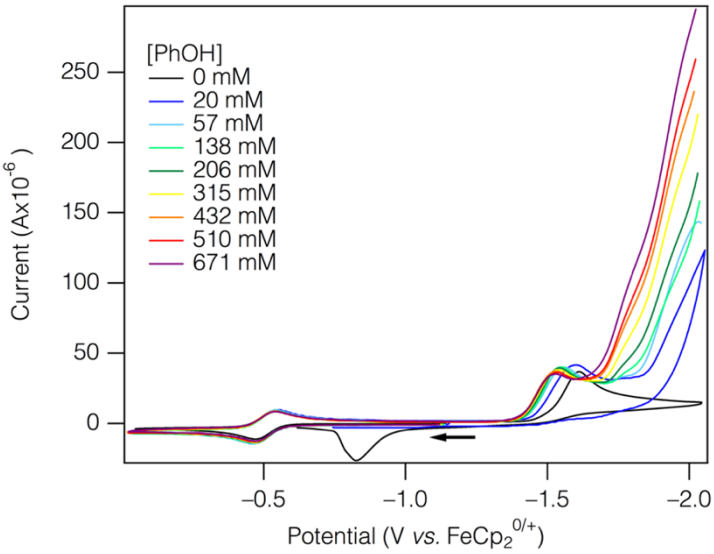

Figure 7.4.14. Cyclic voltammograms of **1** (0.8 mM) in CH_3CN containing 0.1 M $[NBu^n_4][PF_6]$ as a function of PhOH concentration (ν = 0.1 V/s). For clarity, only forward traces are shown for scans with added PhOH except for that at 20 mM PhOH, which shows the absence of the anodic feature at –0.8 V.

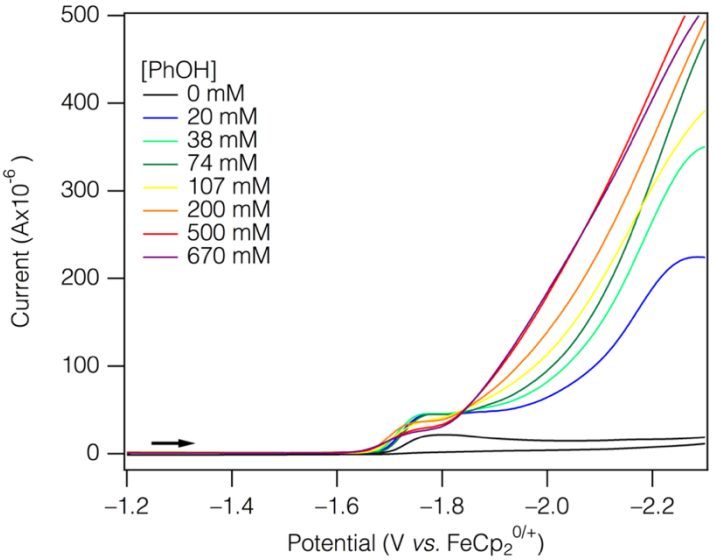

Figure 7.4.15. Cyclic voltammograms of ***2t*** (0.8 mM) in CH_3CN containing 0.1 M $[NBu^n_4][PF_6]$ as a function of PhOH concentration (ν = 0.1 V/s). For clarity, only forward traces are shown for scans with added PhOH.

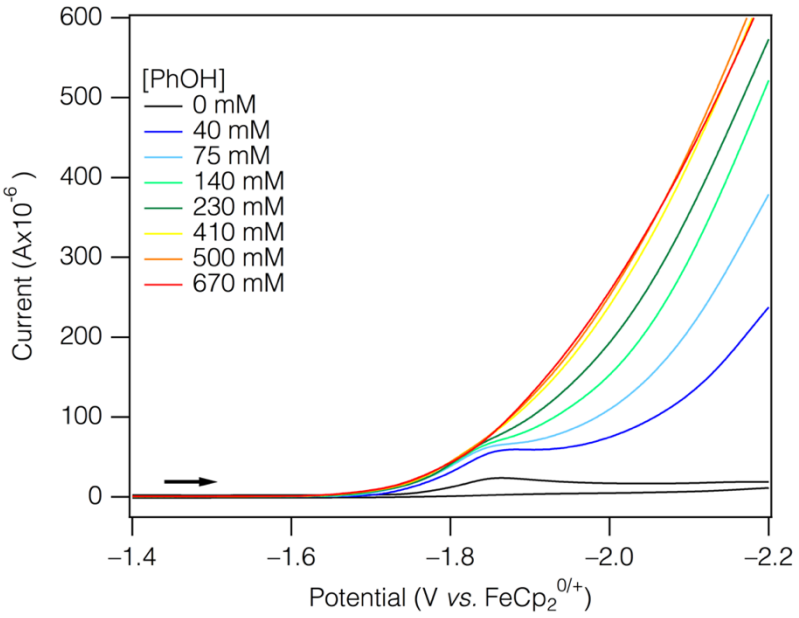

Figure 7.4.16. Cyclic voltammograms of **4Cl** (1.0 mM) in CH_3CN containing 0.1 M [NBu$^n_4$][PF_6] as a function of PhOH concentration (ν = 0.1 V/s). For clarity, only forward traces are shown for scans with added PhOH.

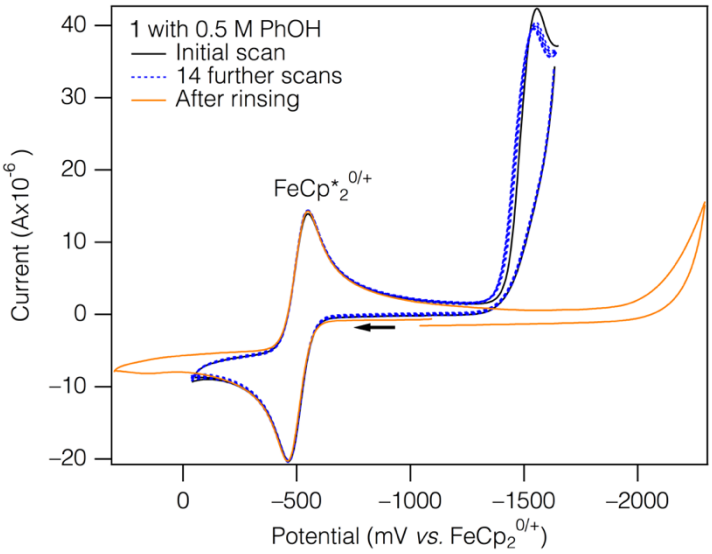

Figure 7.4.17. Cyclic voltammograms of 1 mM **1** in CH_3CN solution containing 0.1 M [NBu$^n_4$][PF_6], 0.5 M PhOH, and FeCp*$_2$ (ν = 0.1 V/s): black trace, initial scan; dotted blue traces, 14 additional scans. The orange trace is the cyclic voltammogram obtained after removing the working electrode from the solution, rinsing it with CH_3CN,[38] and immersing it in a fresh CH_3CN solution containing 0.5 M PhOH, 0.1 M [NBu$^n_4$][PF_6], and FeCp*$_2$ but not **1**. The absence of any feature other than the reduction of PhOH indicates that no Ru-containing species were deposited on the electrode during the first 15 CV scans; thus, the catalyst is homogeneous.

7.5. Chapter 6 Supplementary Information

7.5.1. Definitions

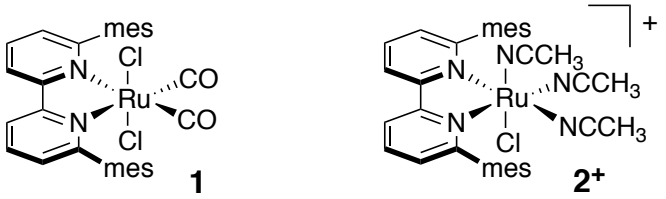

Figure 7.5.1. The compounds discussed in Section 7.5.

7.5.2. Synthesis and Characterization of Compounds

Synthesis of *fac*-[Ru(6,6′-dimesityl-2,2′-bipyridyl)(CH_3CN)$_3$Cl][PF_6] (2[PF_6]). To a stirred, orange solution of **2Cl** (0.040 g, 0.06 mmol) in CH_3CN (50 mL) was added KPF_6 (0.020 g, 0.11 mmol). A pale gray precipitate formed. After 1 h the solvent was removed under vacuum, yielding a heterogeneous dark orange and pale white residue. The mixture was extracted into $CHCl_3$ (50 mL) and the resulting orange suspension filtered through a 2 cm pad of Celite supported on a sintered glass filter. The orange filtrate was concentrated to 5 mL under reduced pressure, layered with hexane (15 mL), and allowed to stand in the dark at room temperature for 3 days, yielding yellow crystals that were isolated by decantation of the mother liquor; these crystals, of **2[PF_6]**•$CHCl_3$, proved suitable for X-ray diffraction experiments. The ^{1}H NMR spectrum of the compound in CD_3CN solution was identical to that observed for **2Cl**.

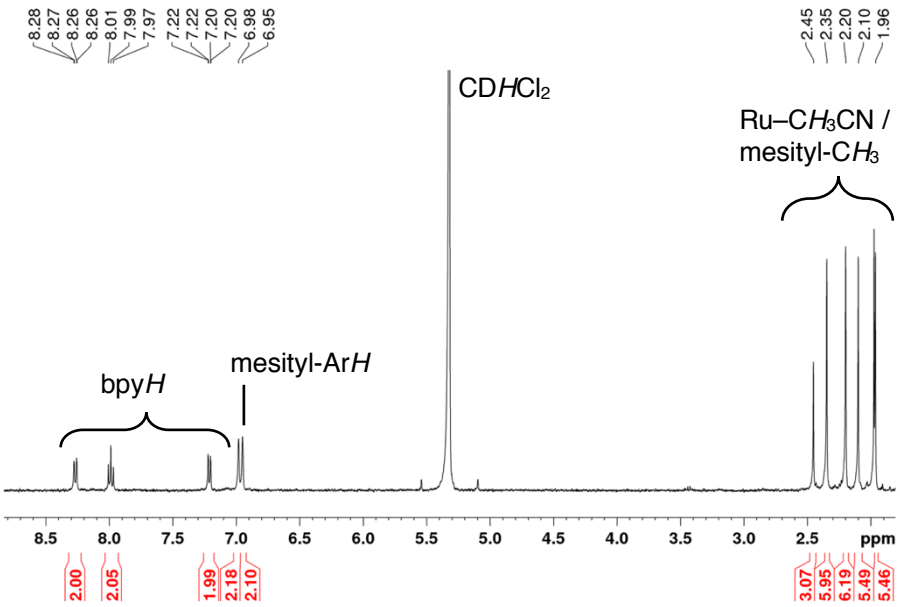

Figure 7.5.2. ^{1}H NMR spectrum of **2Cl** in CD_2Cl_2.

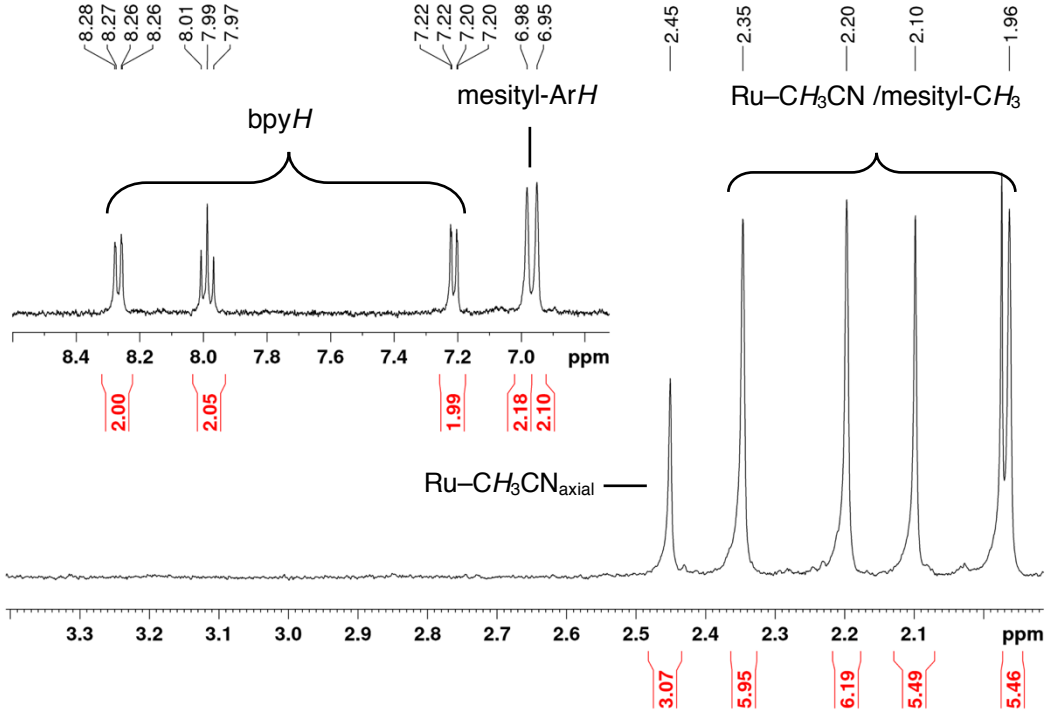

Figure 7.5.3. Expansion of the ^{1}H NMR spectrum of **2Cl** in CD_2Cl_2. The peak labeled with an asterisk is due to residual CH_3CN.

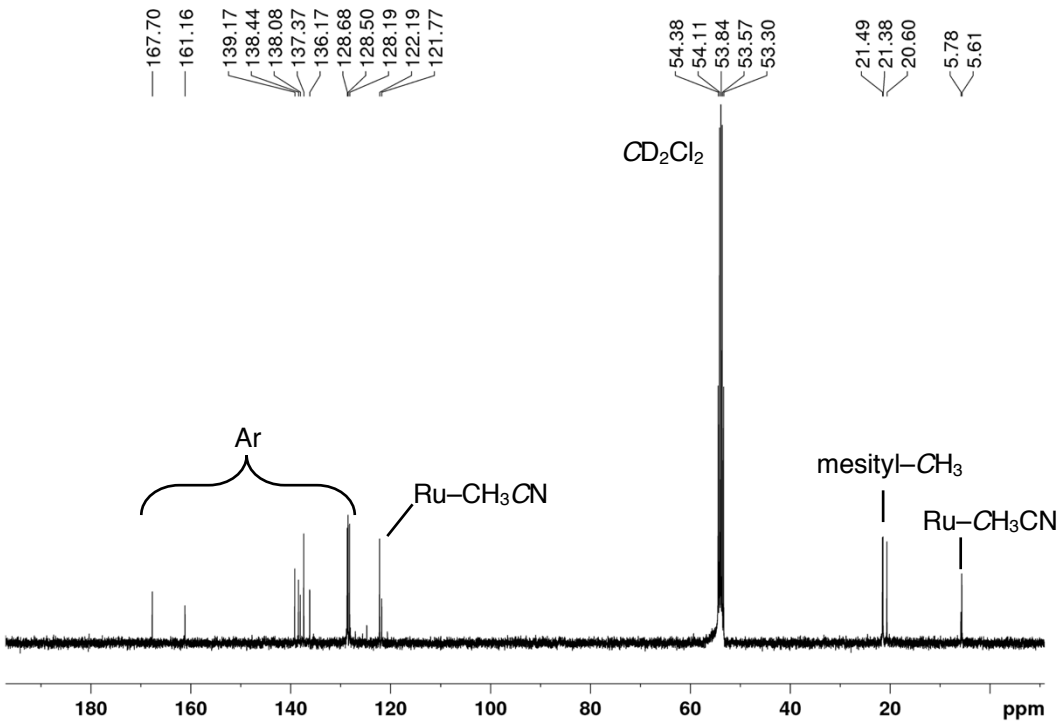

Figure 7.5.4. $^{13}C\{^{1}H\}$ NMR spectrum of **2Cl** in CD_2Cl_2.

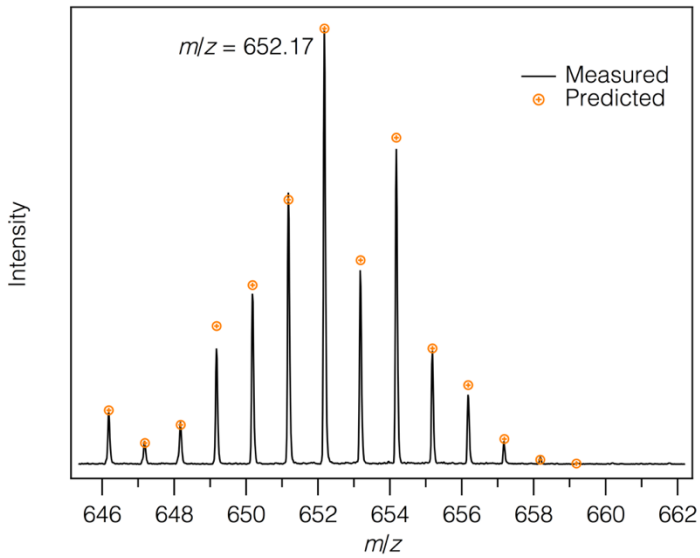

Figure 7.5.5. ESI mass spectrum of **2Cl**.

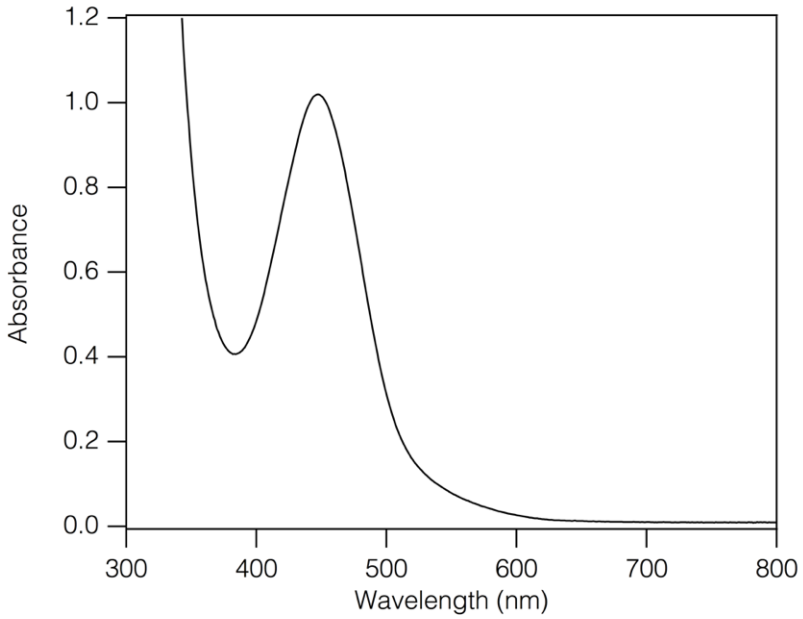

Figure 7.5.6. Electronic-absorption spectrum of **2Cl** in CH_3CN (~0.5 mM, λ_{max} = 447 nm).

7.5.3. Single Crystal X-Ray Diffraction Study of 2[PF_6]•$CHCl_3$.

A yellow thin plate (0.01 × 0.14 × 0.26 mm^3) was mounted with Fluorolube oil on a Dual-Thickness MicroMount (MiTeGen) with 30 μm sample aperture. Diffraction data were measured at 100 K on a Bruker D8 VENTURE diffractometer equipped with a microfocus Mo-target X-ray tube (λ = 0.71073 Å) and PHOTON 100 CMOS detector. Data reduction and integration were performed with the Bruker APEX3 software package.[31] The crystal appeared to be a 2-component twin. Unit-cell parameters for each component were identified using Cell_Now. Data were scaled and corrected for absorption effects using the multi-scan procedure as implemented in TWINABS[39]. The structure was solved by SHELXT[3] and refined by a full-matrix least-squares procedure using OLEX2.[4-5, 33] Crystallographic data and details of the data collection and structure refinement are listed in Table 7.5.1. TWINABS results: For component 1: wR2(int) was 0.1139 before and 0.0581 after correction. For component 2: wR2(int) was 0.1178 before and 0.0590 after correction. Final HKLF 4 output contains 98892 reflections, Rint = 0.1127 (35288 with I > 3σ(I), Rint = 0.0474). The data were first solved and refined using HKLF 4 file format. The final

refinement cycles were carried out with HKLF 5 (final refined twin value is 0.4721(14)). All atoms were refined with anisotropic thermal parameters. Hydrogen atoms were included in idealized positions for structure factor calculations. The structure of the compound is depicted in Figure 7.5.7 and bond distances and bond angles are set out in Table 7.5.3.

Table 7.5.1. Crystal Data and Structure Refinement for **2[PF_6]**•$CHCl_3$.

Empirical formula	$C_{35}H_{38}Cl_4F_6N_5PRu$
Formula weight	916.54
Temperature/K	100(2)
Crystal system	monoclinic
Space group	$P2_1/c$
a/Å	14.078(3)
b/Å	12.616(3)
c/Å	22.971(6)
α/°	90
β/°	103.36(3)
γ/°	90
Volume/Å^3	3969.4(16)
Z	4
ρ_{calc}g/cm^3	1.534
μ/mm^{-1}	0.765
F(000)	1856.0
Crystal size/mm^3	0.26 × 0.14 × 0.01
Radiation	MoKα (λ = 0.71073)
2Θ range for data collection/°	4.39 to 57.056
Index ranges	$-17 \leq h \leq 16$, $0 \leq k \leq 15$, $0 \leq l \leq 30$
Reflections collected	8139
Independent reflections	8139 [R_{int} = 0.0474, R_{sigma} = 0.0814]
Data/restraints/parameters	8139/0/479
Goodness-of-fit on F^2	1.109
Final R indexes [I>=2σ (I)]	R_1 = 0.0781, wR_2 = 0.1420
Final R indexes [all data]	R_1 = 0.1218, wR_2 = 0.1596
Largest diff. peak/hole / e Å^{-3}	1.40/-0.72

$R_{int} = \Sigma \mid F_o^2 - \langle F_o^2 \rangle \mid / \Sigma \mid F_o^2 \mid$

$R1 = \Sigma \mid \mid F_o \mid - \mid F_c \mid \mid / \Sigma \mid F_o \mid$

$wR2 = [\Sigma [w (F_o^2 - F_c^2)^2] / \Sigma [w (F_o^2)^2]]^{1/2}$

Goodness-of-fit = $[\Sigma [w (F_o^2 - F_c^2)^2] / (n-p)^{1/2}$

n: number of independent reflections; p: number of refined parameters

Table 7.5.2. Bond Lengths and Angles for **2[PF_6]**•$CHCl_3$.

Atom	Atom	Length (Å)	Atom	Atom	Length (Å)
Ru1	Cl1	2.5220(19)	C12	C18	1.582(12)
Ru1	N1	2.070(6)	C13	C14	1.457(11)
Ru1	N2	2.029(6)	C14	C15	1.423(11)
Ru1	N3	2.037(7)	C14	C19	1.460(10)
Ru1	N4	1.980(6)	C15	C16	1.360(11)
Ru1	N5	2.058(6)	C16	C17	1.556(11)
N1	C1	1.350(10)	C20	C21	1.439(11)
N1	C5	1.387(9)	C20	C25	1.355(10)
N2	C6	1.333(9)	C21	C22	1.426(12)
N2	C10	1.296(8)	C21	C27	1.467(11)
N3	C29	1.153(10)	C22	C23	1.325(12)
N4	C31	1.122(10)	C23	C24	1.424(12)
N5	C33	1.152(9)	C23	C28	1.553(12)
C1	C2	1.356(10)	C24	C25	1.446(11)
C1	C20	1.528(11)	C25	C26	1.559(11)
C2	C3	1.415(11)	C29	C30	1.436(12)
C3	C4	1.362(11)	C31	C32	1.436(12)
C4	C5	1.356(10)	C33	C34	1.522(12)
C5	C6	1.423(10)	P1	F1	1.626(6)
C6	C7	1.395(11)	P1	F2	1.621(6)
C7	C8	1.297(11)	P1	F3	1.634(8)
C8	C9	1.346(11)	P1	F4	1.549(7)
C9	C10	1.404(11)	P1	F5	1.517(6)
C10	C11	1.452(10)	P1	F6	1.528(6)
C11	C12	1.458(12)	Cl2	C35	1.757(11)
C11	C16	1.457(11)	Cl3	C35	1.640(10)
C12	C13	1.370(10)	Cl4	C35	1.820(11)

Atom	Atom	Atom	Angle (°)	Atom	Atom	Atom	Angle (°)
N1	Ru1	Cl1	89.64(17)	C13	C12	C11	113.1(8)
N2	Ru1	Cl1	80.18(19)	C13	C12	C18	120.8(8)
N2	Ru1	N1	76.4(2)	C12	C13	C14	122.1(8)
N2	Ru1	N3	101.8(2)	C13	C14	C19	119.8(7)
N2	Ru1	N5	100.0(2)	C15	C14	C13	121.8(7)
N3	Ru1	Cl1	85.51(19)	C15	C14	C19	118.3(7)
N3	Ru1	N1	175.1(3)	C16	C15	C14	119.9(8)
N3	Ru1	N5	93.2(2)	C11	C16	C17	125.5(7)
N4	Ru1	Cl1	94.88(19)	C15	C16	C11	116.4(8)
N4	Ru1	N1	102.5(2)	C15	C16	C17	117.9(7)
N4	Ru1	N2	174.9(3)	C21	C20	C1	124.3(7)

N4	Ru1	N3	78.9(2)	C25	C20	C1	117.4(7)
N4	Ru1	N5	84.9(2)	C25	C20	C21	118.0(7)
N5	Ru1	Cl1	178.75(18)	C20	C21	C27	118.6(7)
N5	Ru1	N1	91.6(2)	C22	C21	C20	124.1(7)
C1	N1	Ru1	129.2(5)	C22	C21	C27	117.1(7)
C1	N1	C5	120.8(6)	C23	C22	C21	119.2(8)
C5	N1	Ru1	109.3(5)	C22	C23	C24	116.4(8)
C6	N2	Ru1	115.3(5)	C22	C23	C28	118.9(8)
C10	N2	Ru1	128.6(5)	C24	C23	C28	124.6(8)
C10	N2	C6	114.7(7)	C23	C24	C25	126.6(7)
C29	N3	Ru1	171.6(6)	C20	C25	C24	115.6(7)
C31	N4	Ru1	170.0(6)	C20	C25	C26	118.3(7)
C33	N5	Ru1	174.2(6)	C24	C25	C26	126.1(7)
N1	C1	C2	118.0(7)	N3	C29	C30	179.2(9)
N1	C1	C20	124.1(6)	N4	C31	C32	177.9(9)
C2	C1	C20	117.9(7)	N5	C33	C34	176.0(9)
C1	C2	C3	120.4(7)	F1	P1	F3	174.4(5)
C4	C3	C2	121.7(7)	F2	P1	F1	83.9(3)
C5	C4	C3	115.9(8)	F2	P1	F3	91.1(4)
N1	C5	C6	117.1(7)	F4	P1	F1	97.9(5)
C4	C5	N1	122.9(7)	F4	P1	F2	178.1(5)
C4	C5	C6	119.8(8)	F4	P1	F3	87.1(5)
N2	C6	C5	111.1(7)	F5	P1	F1	84.4(5)
N2	C6	C7	124.7(7)	F5	P1	F2	83.9(4)
C7	C6	C5	123.8(8)	F5	P1	F3	97.8(5)
C8	C7	C6	120.5(8)	F5	P1	F4	95.5(4)
C7	C8	C9	115.3(8)	F5	P1	F6	176.2(5)
C8	C9	C10	123.3(7)	F6	P1	F1	97.0(4)
N2	C10	C9	121.1(7)	F6	P1	F2	92.7(4)
N2	C10	C11	115.2(7)	F6	P1	F3	80.5(4)
C9	C10	C11	123.3(6)	F6	P1	F4	87.8(4)
C10	C11	C12	115.6(8)	Cl2	C35	Cl4	107.1(6)
C10	C11	C16	117.3(7)	Cl3	C35	Cl2	113.4(6)
C16	C11	C12	126.6(7)	Cl3	C35	Cl4	111.0(6)
C11	C12	C18	126.1(7)				

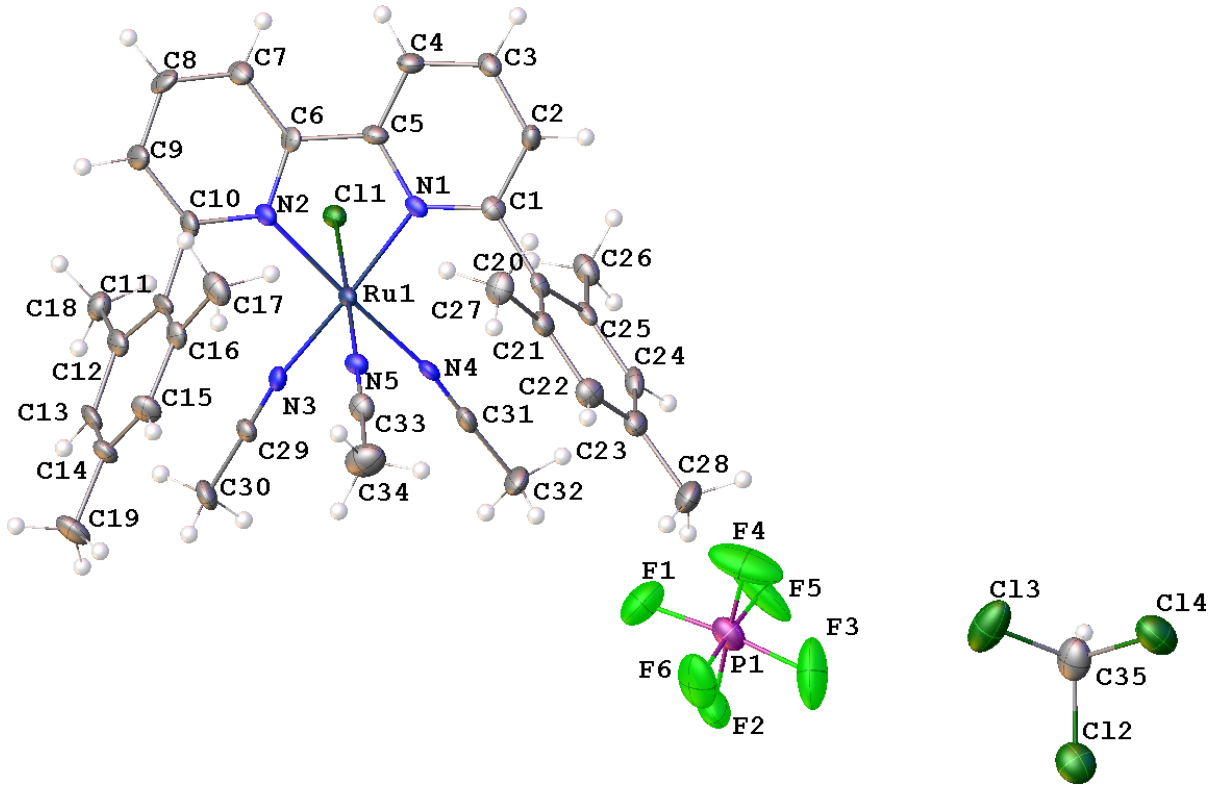

Figure 7.5.7. Thermal ellipsoid representation (40% probability ellipsoids) of **2[PF$_6$]**•$CHCl_3$.

7.5.4. Electrochemical Experiments

Cyclic Voltammetry. Electrochemical experiments were performed at room temperature under either a N_2 or a CO_2 atmosphere with a BAS 100B/W electrochemical workstation. All experiments used CH_3CN as solvent containing 0.1 M [NBu$^n_4$][PF_6] as electrolyte. Samples containing CO_2 were prepared by sparging the analyte solution with CO_2 for at least 15 min prior to measurement. Cyclic voltammetry (CV) experiments were performed in a single-compartment cell with a three-electrode configuration consisting of a glassy carbon working electrode (A = 0.07 cm^2), a platinum auxiliary electrode (A = 0.02 cm^2), and a silver wire quasi-reference electrode. Electrodes were polished and rinsed before use. $FeCp_2$ or $FeCp^*_2$ was used as an internal redox-potential reference; potentials are reported relative to $FeCp_2^{0/+}$ ($E_{1/2}(FeCp^*_2{}^{0/+})$ = –0.505 V *vs.* $FeCp_2^{0/+}$ in CH_3CN,[24] confirmed under our experimental conditions). Experiments in the absence

of substrate (phenol and/or CO_2) were performed at multiple scan rates (0.05–0.40 V/s); other experiments were performed at a scan rate of 0.10 V/s unless otherwise stated. The reversibility of processes was assessed using Randles-Sevcik plots; peak currents were not corrected for background currents.

Controlled Potential Electrolysis. These experiments were performed in a sealed four-neck cell (total volume = 100 mL). A three-electrode configuration was used that consisted of a reticulated vitreous carbon foam working electrode (ERG Materials & Aerospace, ca. 15 mm × 10 mm × 5 mm), a platinum wire auxiliary electrode that was separated from the working solution by a medium porosity glass frit, and a Ag/Ag^+ reference electrode (BASi, 0.01 M $AgNO_3$ in CH_3CN containing 0.1 M $[NBu^n_4][PF_6]$) that was separated from the working solution by a CoralPor tip. The working solution (40 mL) contained a known amount of catalyst, 0.5 M PhOH, and a stir bar. The auxiliary compartment contained 5 mL of a CH_3CN solution containing 0.1 M ferrocene (as a sacrificial reductant) and 0.1 M $[NBu^n_4][PF_6]$. After a current equivalent to at least 8 e^- per catalyst molecule was passed, a known volume of gas within the headspace was extracted by gastight syringe and its chemical composition was characterized by gas chromatography (GC; Agilent 7890B with FID (CO) and TCD (H_2) detectors and a Supelco Carboxen 1010 PLOT column). Comparison with a GC calibration curve (Supelco SCOTTY Specialty Gas; 1.0% H_2, O_2, CH_4, CO, and CO_2, balance N_2) allowed quantification of the volume of each gas present at the end of the run and, from this, determination of the faradaic efficiency. Three gas samples from each run were measured so that the standard deviation could be calculated. Formate was detected by ^1H NMR spectroscopy via a previously reported method:[25] following electrolysis and GC analysis of the headspace, D_2O (2 mL) was added to an aliquot of the reaction solution (5 mL) and the resulting aqueous mixture was vigorously stirred, washed with CH_2Cl_2 (12 mL), and acidified

with one drop of concentrated HCl (aq). ^{1}H NMR (D_2O, 400 MHz, 295 K): δ 8.16 (s, 1H, *H*COOH).

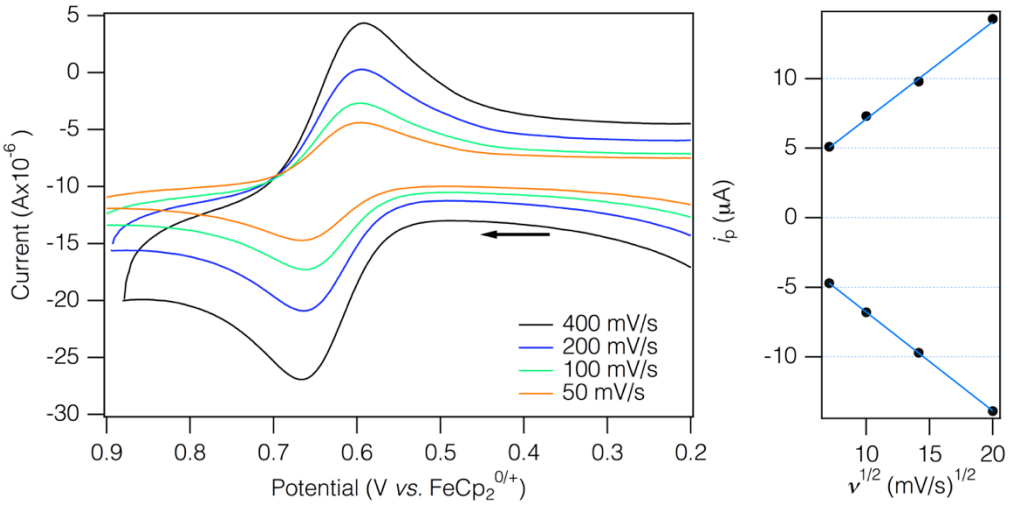

Figure 7.5.8. (*Left*) Cyclic voltammograms of **2[PF$_6$]** (0.7 mM) in CH_3CN containing 0.1 M [NBu$^n_4$][PF_6]. The figure is identical to that in Figure 5.3. (*Right*) Randles-Sevcik plot of the reversible Ru$^{II/III}$ couple.

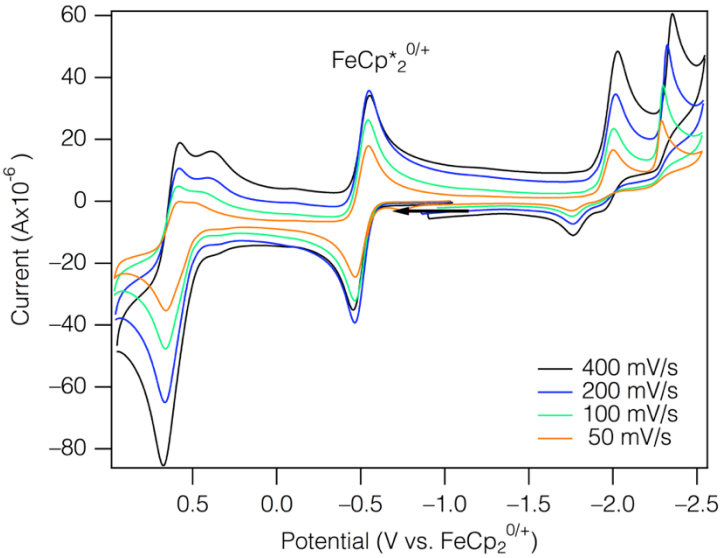

Figure 7.5.9. Cyclic voltammograms of **2Cl** (2.0 mM) in CH_3CN containing 0.1 M [NBu$^n_4$][PF_6]. The arrow indicates the direction of the scan.

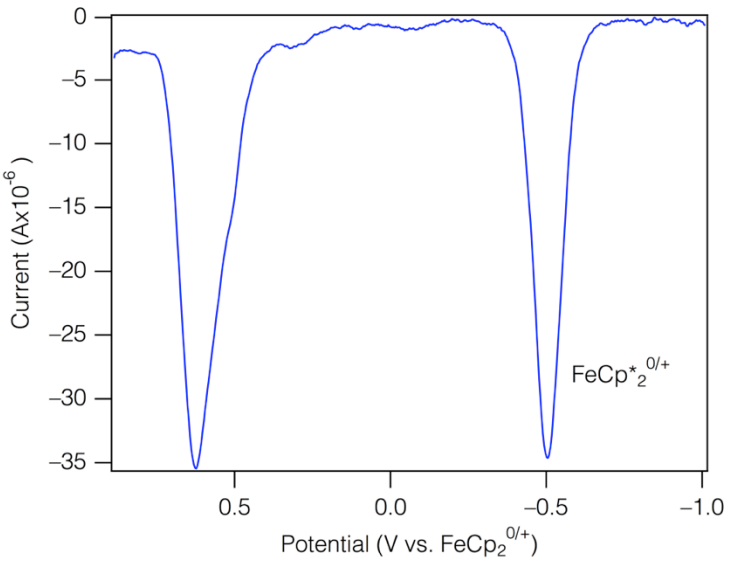

Figure 7.5.10. Differential pulse voltammogram of **2Cl** (2.0 mM) in CH_3CN containing 0.1 M $[NBu^n_4][PF_6]$.

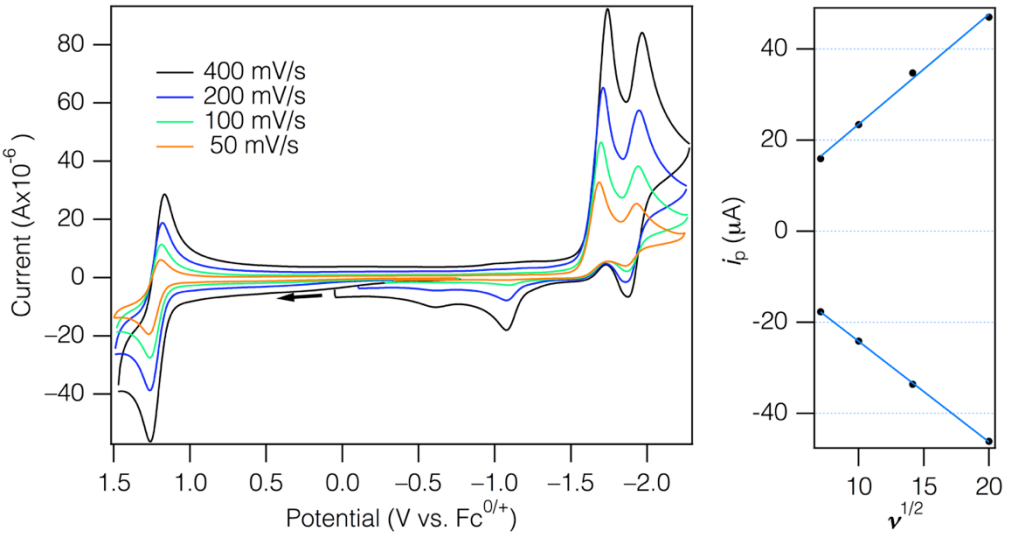

Figure 7.5.11. (*Left*) Cyclic voltammograms of **1** (1.1 mM) in CH_3CN containing 0.1 M $[NBu^n_4][PF_6]$. The arrow indicates the direction of the scans. (*Right*) Randles-Sevcik plot of the reversible $Ru^{2+/3+}$ couple.

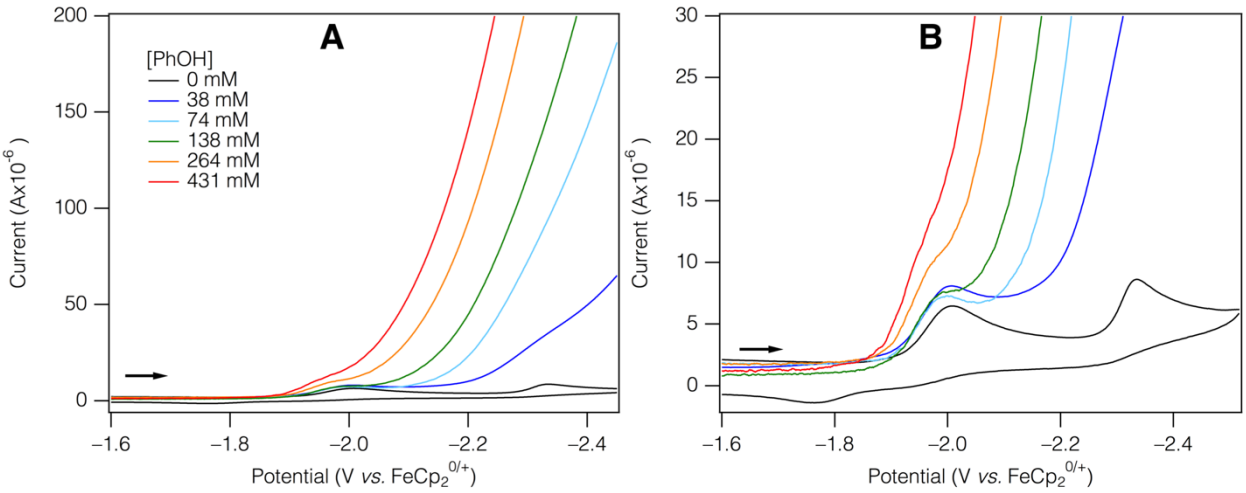

Figure 7.5.12. Cyclic voltammograms (v = 0.1 V/s) of **2Cl** (0.5 mM) in CH_3CN containing 0.1 M $[NBu^n_4][PF_6]$ and varying concentrations of PhOH. For clarity, only forward traces are shown for scans with added PhOH. Figure B is an expansion of A.

7.6. References

1. *APEX2*, 2014.9-0; Bruker AXS: Madison, WI, 2014.

2. *SADABS*, Bruker AXS: Madison, WI, 2001.

3. Sheldrick, G. M. SHELXT – Integrated Space-Group and Crystal-Structure Determination. *Acta Crystallogr.* **2015**, *A71*, 3–8.

4. Sheldrick, G. M. Crystal Structure Refinement with SHELXL. *Acta Crystallogr.* **2015**, *C71*, 3–8.

5. Sheldrick, G. M. A Short History of SHELX. *Acta Cryst.* **2008**, *A64*, 112–122.

6. Hyde, J. S.; Pasenkiewicz-Gierula, M.; Jesmanowicz, A.; Antholine, W. E. Pseudo Field Modulation in EPR Spectroscopy. *Appl. Magn. Reson.* **1990**, *1*, 483–496.

7. Weigend, F.; Ahlrichs, R. Balanced Basis Sets of Split Valence, Triple Zeta Valence and Quadruple Zeta Valence Quality for H to Rn: Design and Assessment of Accuracy. *Phys. Chem. Chem. Phys.* **2005**, *7*, 3297–3305.

8. Kutzelnigg, W.; Fleischer, U.; Schindler, M. In *Deuterium and Shift Calculation*, Diehl, P., Fluck, E., Günther, H., Kosfeld, R., Seelig, J., Eds. Springer-Verlag: Berlin, 1990; Vol. 23.

9. Wachters, A. J. H. Gaussian Basis Set for Molecular Wavefunctions Containing Third-Row Atoms. *J. Chem. Phys.* **1970**, *52*, 1033–1036.

10. Wachters, A. J. H. *IBM Technical Report RJ 584*, San Jose, CA, 1969

11. Bauschlicher, C. W.; Langhoff, S. R.; Partridge, H.; Barnes, L. A. Theoretical-Studies of the 1st-Row and 2nd-Row Transition-Metal Methyls and Their Positive-Ions. *J. Chem. Phys.* **1989**, *91*, 2399–2411.

12. Neese, F. The ORCA Program System. *WIREs Comput. Mol. Sci.* **2012**, *2*, 73-78.

13. Stephens, P. J.; Devlin, F. J.; Chabalowski, C. F.; Frisch, M. J. Ab-Initio Calculation of Vibrational Absorption and Circular-Dichroism Spectra Using Density-Functional Force-Fields. *J. Phys. Chem.* **1994**, *98*, 11623–11627.

14. Becke, A. D. Density-Functional Thermochemistry 3. The Role of Exact Exchange. *J. Chem. Phys* **1993**, *98*, 5648–5652.

15. Lee, C. T.; Yang, W. T.; Parr, R. G. Development of the Colle-Salvetti Correlation-Energy Formula into a Functional of the Electron-Density. *Phys. Rev. B* **1988**, *37*, 785–789.

16. Vosko, S. H.; Wilk, L.; Nusair, M. Accurate Spin-Dependent Electron Liquid Correlation Energies for Local Spin-Density Calculations - a Critical Analysis. *Can. J. Phys.* **1980**, *58*, 1200–1211.

17. Rega, N.; Cossi, M.; Barone, V. Development and Validation of Reliable Quantum Mechanical Approaches for the Sudy of Free Radicals in Solution. *J. Chem. Phys* **1996**, *105*, 11060–11067.

18. Barone, V. In *Recent Advances in Density Functional Methods (Part 1)*, Chong, D. P., Ed. World Scientific: Singapore, 1995; pp 287-334.

19. Fulmer, G. R.; Miller, A. J. M.; Sherden, N. H.; Gottlieb, H. E.; Nudelman, A.; Stoltz, B. M.; Bercaw, J. E.; Goldberg, K. I. NMR Chemical Shifts of Trace Impurities: Common Laboratory Solvents, Organics, and Gases in Deuterated Solvents Relevant to the Organometallic Chemist. *Organometallics* **2010**, *29*, 2176–2179.

20. Yang, J. Y.; Smith, S. E.; Liu, T.; Dougherty, W. G.; Hoffert, W. A.; Kassel, W. S.; DuBois, M. R.; DuBois, D. L.; Bullock, R. M. Two Pathways for Electrocatalytic Oxidation of Hydrogen by a Nickel Bis(diphosphine) Complex with Pendant Amines in the Second Coordination Sphere. *J. Am. Chem. Soc.* **2013**, *135*, 9700–9712.

21. La Porte, N. T.; Moravec, D. B.; Hopkins, M. D. Electron-Transfer Sensitization of H_2 Oxidation and CO_2 Reduction Catalysts using a single Chromophore. *Proc. Natl. Acad. Sci., U. S. A.* **2014**, *111*, 9745–9750.

22. Wiedner, E. S.; Yang, J. Y.; Chen, S.; Raugei, S.; Dougherty, W. G.; Kassel, W. S.; Helm, M. L.; Bullock, R. M.; Rakowski DuBois, M.; DuBois, D. L. Stabilization of Nickel Complexes with Ni 0···H–N Bonding Interactions Using Sterically Demanding Cyclic Diphosphine Ligands. *Organometallics* **2012**, *31*, 144-156.

23. Pangborn, A. B.; Giardello, M. A.; Grubbs, R. H.; Rosen, R. K.; Timmers, F. J. Safe and convenient procedure for solvent purification. *Organometallics* **1996**, *15*, 1518-1520.

24. Noviandri, I.; Brown, K. N.; Fleming, D. S.; Gulyas, P. T.; Lay, P. A.; Masters, A. F.; Phillips, L. The Decamethylferrocenium/Decamethylferrocene Redox Couple: A Superior Redox Standard to the Ferrocenium/Ferrocene Redox Couple for Studying Solvent Effects on the Thermodynamics of Electron Transfer. *J. Phys. Chem. B* **1999**, *103*, 6713–6722.

25. Machan, C. W.; Sampson, M. D.; Kubiak, C. P. A Molecular Ruthenium Electrocatalyst for the Reduction of Carbon Dioxide to CO and Formate. *J. Am. Chem. Soc.* **2015**, *137*, 8564–8571.

26. Bertrand, S.; Hoffman, N.; Pete, J.-P. Highly Efficient and Stereoselective Radical Addition of Tertiary Amines to Electron-Deficient Alkenes—Application to the Enantioselective Synthesis of Necine Bases. *Eur. J. Org. Chem.* **2000**, 2227–2238.

27. Joe, C. L.; Doyle, A. G. Direct Acylation of C(sp^3)–H Bonds Enabled by Nickel and Photoredox Catalysis. *Angew. Chem. Int. Ed.* **2016**, *55*, 4040–4043.

28. Biaggi, C.; Benaglia, M.; Raimondi, L.; Cozzi, F. Organocatalytic Synthesis of Dipyrromethanes by the Addition of N-methylpyrrole to Aldehydes. *Tetrahedron* **2006**, *62*, 12375–12379.

29. Thomas, N. C. Reactions of Ruthenium(II) Carbonyl Complexes. *Inorg. Chim. Acta* **1986**, *120*, L7–L8.

30. Eskelinen, E.; Haukka, M.; Venäläinen, T.; Pakkanen, T. A.; Wasberg, M.; Chardon-Noblat, S.; Deronzier, A. Light-Induced Decarbonylation, Solvolysis, and Isomerization of $Ru(L)(CO)_2Cl_2$ (L = 2,2'-Bipyridine and 4,4'-Dimethyl-2,2'-bipyridine) in Acetonitrile. *Organometallics* **2000**, *19*, 163–169.

31. Bruker *APEX3*, 2015.5-2; Bruker AXS, Inc.: Madison, WI, 2015.

32. Bruker *SADABS*, 2016/2; Bruker AXS, Inc.: Madison, WI, 2016.

33. Dolomanov, O. V.; Bourhis, L. J.; Gildea, R. J.; Howard, J. A. K.; Puschmann, H. OLEX2: A Complete Structure Solution, Refinement and Analysis Program. *J. Appl. Crystallogr.* **2009**, *42*, 339–341.

34. Collomb-Dunand-Sauthier, M.-N.; Deronzier, A.; Ziessel, R. Electrochemical Characterization of $[Ru^{II}(bpy)(CO)_2Cl_2]$ (bpy = 2,2'-bipyridine). *J. Electroanal. Chem* **1991**, *319*, 347–353.

35. Collomb-Dunand-Sauthier, M.-N.; Deronzier, A. Photochemical Reactivity of $[Ru^{II}(L)(CO)_2Cl_2]$ and $[Me_4N]$ $[Ru^{III}(L)(CO)Cl_3]$ (L = 2,2'-Bipyridine or 4,4'-Di(isopropoxycarbonyl)-2,2'-Bipyridine) in CH_3CN and the Redox Properties of the Resulting New Complexes. *J. Organomet. Chem.* **1993**, *444*, 191–198.

36. Chardon-Noblat, S.; Renfrew, A.; Lafolet, F.; Deronzier, A.; Jakonen, M.; Laurila, E.; Haukka, M. An Easy Electrochemical and Chemical Synthesis of $[Ru(bpy)(CH_3CN)_2Cl_2]$:

A Synthon for Heteroleptic Tris(diimine) Ru(II) Complexes. *Dalton. Trans.* **2008**, 5891–5896.

37. Elgrishi, N.; Chambers, M. B.; Wang, X.; Fontecave, M. Molecular Polypyridine-Based Metal Complexes as Catalysts for the Reduction of CO_2. *Chem. Soc. Rev.* **2017**, *46*, 761–796.

38. Artero, V.; Fontecave, M. Solar Fuels Generation and Molecular Systems: Is It Homogeneous or Heterogeneous Catalysis? *Chem. Soc. Rev.* **2013**, *42*, 2338–2356.

39. Bruker *TWINABS*, 2012/1; Bruker AXS, Inc.: Madison, WI, 2012.